

ULTRASOUND IMAGING OF NANODROPLET VAPORIZATION FOR RADIOTHERAPY MONITORING

Sophie Heymans



Arenberg Doctoral School
Faculty of Science

Supervisors:

Prof. dr. K. Van Den Abeele

Prof. dr. J. D'hooge



Erasmus MC Graduate School
Erasmus MC University Medical Center

Supervisors:

Prof. dr. ir. N. de Jong

Dr. ir. H. J. Vos

Dissertation presented in partial fulfilment of the requirements for the degree of

Doctor of Science (PhD): Physics
from KU Leuven

Doctor from the Erasmus
University Rotterdam

ULTRASOUND IMAGING OF
NANODROPLET VAPORIZATION
FOR RADIOTHERAPY
MONITORING

Sophie Heymans

Colophon

ISBN: 978-94-6421-663-9

Cover design: Sophie Heymans

Printed by: Ipskamp Printing, Enschede, the Netherlands

Copyright © 2022 Sophie Heymans

Except for the following chapters:

Chapter 3: © 2020, IOP Publishing

Chapter 4: © 2021, American Association of Physicists in Medicine

Chapter 5: © 2022, Elsevier B.V.

All rights reserved. No part of this publication may be reproduced, distributed, stored in a retrieval system, or transmitted in any other form or by any means, without prior written permission from the author, or where appropriate, from the publishers of the publications.

For a printed version please contact:

Secretary of Biomedical Engineering, Cardiology

Erasmus MC, Rotterdam, the Netherlands

or

Sophie Heymans

soph.heymans@gmail.com

Ultrasound Imaging of Nanodroplet Vaporization for Radiotherapy Monitoring

Sophie HEYMANS

Examination committee:

Prof. dr. D. Dudal, chair

Prof. dr. K. Van Den Abeele, supervisor

Prof. dr. J. D'hooge, supervisor

Prof. dr. ir. N. de Jong, supervisor

Dr. ir. H. J. Vos, supervisor

Prof. dr. ir. A. F. W. van der Steen

Prof. dr. C. Glorieux

Dr. ir. E. D'Agostino

Prof. dr. ir. E. Sterpin

Dr. K. Kooiman

Prof. dr. K. Parodi

(Ludwig-Maximilians-Universität München)

Prof. dr. E. Stride

(University of Oxford)

Dissertation presented in partial
fulfillment of the requirements for
the degree of Doctor of Science
(PhD): Physics

January 2022

© 2022 KU Leuven – Faculty of Science
Uitgegeven in eigen beheer, Sophie Heymans, Celestijnenlaan 200A box 2402, B-3001 Leuven (Belgium)

Alle rechten voorbehouden. Niets uit deze uitgave mag worden vermenigvuldigd en/of openbaar gemaakt worden door middel van druk, fotokopie, microfilm, elektronisch of op welke andere wijze ook zonder voorafgaande schriftelijke toestemming van de uitgever.

All rights reserved. No part of the publication may be reproduced in any form by print, photoprint, microfilm, electronic or any other means without written permission from the publisher.

Ultrasound Imaging of Nanodroplet Vaporization for Radiotherapy Monitoring

Ultrasonische beeldvorming van de fase- transitie van nanodruppels voor de monitoring van radiotherapie

Thesis

to obtain the degree of Doctor from the
Erasmus University Rotterdam
by command of the
rector magnificus

Prof. dr. A.L. Bredenoord

and in accordance with the decision of the Doctorate Board

The public defence shall be held on
Thursday the 24th of February 2022 at 13.00 hrs

by

Sophie Valérie Aline Heymans

born in Namur, Belgium

Doctoral Committee:

Promoters: Prof. dr. ir. N. de Jong
Prof. dr. K. Van Den Abeele
Prof. dr. J. D'hooge

Other members: Prof. dr. ir. A.F.W. van der Steen
Dr. K. Kooiman
Prof. dr. C. Glorieux
Prof. dr. K. Parodi

Co-promoter: Dr. ir. H.J. Vos



This work was supported by the European Union's Horizon 2020 research and innovation programme under grant agreement n°766456 ("AMPHORA").

Additional financial support for the printing of this thesis was kindly provided by Erasmus University Rotterdam, KU Leuven, and Bracco.



The research described in this thesis has been carried out at the Department of Physics, campus KULAK Kortrijk, Belgium, the Department of Cardiovascular Sciences, UZ Leuven, Belgium, and the Department of Biomedical Engineering, Thorax Center, Erasmus University Medical Center, Rotterdam, the Netherlands.

Preface

When I accidentally came across a PhD job opening for the Amphora project, a little more than four years ago, I had no idea how much this adventure would transform my life. I remember how tormented I felt at the idea of taking this big leap, leaving behind a comfortable job in a great company, surrounded by amazing colleagues and friends. The stars did not seem to align then: I was about to move even further away from Kulak and I had just started a new position at IBA. However, if I had known that this opportunity would allow me to finally find my place, an environment in which I feel I truly belong, I would not have hesitated for one second.

Although many say that a PhD is often associated with loneliness, mine was the complete opposite, even in these Covid times. I feel incredibly thankful to all those who shared my path during this journey, be it for a few hours or several years, virtually or in person. All of this would not have been possible without your support, encouragement, collaborative spirit and kindness.

First of all, I would like to thank my KU Leuven and Erasmus MC supervisors. **Koen**, thank you for this phone call more than four years ago, thank you for convincing me to apply and take part in this amazing project. Thank you for being exactly the supervisor I needed, for offering so much flexibility in my work arrangements, and for your trust. I truly admire how well you master the delicate balance between offering autonomy and freedom while always being available when I needed advice or support. Thank you also for your precious help when I was coming across complex mathematical or physics problems. **Jan**, I am very grateful for the way you made me feel welcome in the MIRC and immediately integrated me in the lab activities, as a full member of the team. What was supposed to be only a 'second office' turned out to be infinitely more. Your ability to think out of the box and your very broad knowledge about ultrasound imaging helped me out of difficult situations. **Nico**, thank you for agreeing to the idea of the joint PhD with Erasmus MC, for your guidance, for the numerous technical discussions, and for sharing your immense knowledge of microbubbles with me. I feel very lucky to have had the opportunity to work with you. **Rik**, thank you for your support, for your enthusiasm and for your

optimism. You were always available to help us and give us precious advice regarding experimental design or results interpretation.

Apart from my supervisors, I have also been surrounded by a fantastic supervisory and advisory team. **Christ** and **Emiliano**, thank you for agreeing to embark on this adventure for the start and for your precious advices and stimulating discussions along the way. I will also never forget the warm welcome of **Gaio** and his team in Rome. **Edmond**, thank you for always being available for a "proton talk" and for sharing your insights on proton physics; thank you **Uwe** for your support and for always welcoming me in Mosaic. **Verya**, thank you for your help in the lab, during the proton experiments in Holland PTC, and for paper writing. **Klazina**, thank you for trusting me in the Bubble lab, and for introducing me to the Coulter Counter and other equipment. I am also grateful to Prof. **Martin Verweij** for his guidance during the ProtonBubble meetings. I would like to thank my jury members, Prof. **Katia Parodi**, Prof. **Eleanor Stride**, and Prof. **Ton van der Steen** for accepting the invitation, for their time, for their interest in my work, and for the insightful discussions. I am also grateful to Prof. **David Dudal** for chairing my private defense.

I would also like to express my deep gratitude to my Amphora colleagues: the results reported in this thesis are theirs as much as they are mine. First, a very special thanks to **Bram** and **Gonzalo**, my first co-author squad, with who I shared most of my journey, many experiments, countless meetings and calls, reports, manuscript drafts, presentations, and, in the end, papers. I think all the readers of this thesis should be truly thankful for the way you condensed my writing style, which was dangerously close to graphomania. Without you, this thesis would have been far too long and would have discouraged many readers. Thank you both also for your realism, which was often necessary to keep my high expectations under control. **Bram**, thank you for bringing your enthusiasm and many innovative ideas into the project. I'll always remember the first phantom-droplets experiments, writing the "A" of Amphora in a gelatin phantom by locally vaporizing droplets, the crazily packed car rides to the Cyclotron in Louvain-la-Neuve, the excitement when we saw droplets responding to protons, and your continuous flow of hypothesis and ideas. I admire your limitless dedication, which undoubtedly helped us produce our two papers in a short time. **Gonzalo**, thank you for making me feel welcome in the Rotterdam team, inviting me to the bubble experiments, and joining our forces from the very start. I couldn't have completed the joint degree without you and your involvement in my stays in Rotterdam. Your mark is everywhere, from the elaboration of the joint project to the final paper drafts. Thank you for facing and bringing down the corona barriers with me. Thank you for your hard work in the lab when I was only able to come intermittently, and for coping with the crazy long working hours on the days of proton experiments (and forcing me to stop for a

healthy break from time to time). Your analytical mind and gift for abstract physics helped us move forward and better interpret our research results. Thank you also for the fun weekend in Boulder, for coping with the long hike in the Rocky Mountains and the dehydration (sorry!), and for the rafting experience.

Another special thanks to **Yosra**. Without you, we wouldn't have had those amazing nanodroplets to start with. Thank you for always being willing to come to Belgium, for waking up super early to go to Kulak, for teaching me very patiently how to make and handle the droplets, for quickly answering my questions and providing solutions on the fly. Your knowledge and participation was vital to the success of our experiments. When Bram and I struggled hard to find a suitable phantom recipe, you came up with the polyacrylamide solution and conducted the experiment with us. We are truly grateful for your hard work and dedication. **Sjoerd** and **Marcus**, I would like to thank you for your assistance in conducting the proton and photon experiments and for taking the lead for the ultrasound imaging part. Sjoerd, your focus, patience, and cooperative spirit are admirable. Marcus, thank you for your problem-solving mindset, your English corrections, your involvement in all aspects of Amphora, and your comeback in the team ! Thank you both also for your friendship and support. **Madalina** and **Andrea**, your assistance during the proton experiments was greatly appreciated; to Andrea, I am also grateful for your work and discussions on Monte Carlo simulations. Thank you to the other Amphora colleagues for the interesting discussions and collaboration: **Brent** for the BubbleNet project, **Ratchapol** for the microbubbles, **Mihnea** for the long hours trying to secure the future of Amphora, **Jasleen** and **Arun** for the discussions on the microbubble acoustic behaviour. Finally, I wish to acknowledge the funding for the research presented in this thesis, provided by the European Union through the Horizon 2020 research and innovation programme ("Amphora" project).

To the staff of the Physics Department in Heverlee: **Sven Villé**, **Dries Dirckx**, **Bart Moelants**, **Johan Morren** and **Valentijn Tuts**, thank you for your help in brainstorming, designing and building fantastic experimental setups for the irradiation experiments. Thank you also for coping with my French and making me feel welcome every time I visited the mechanical workshop. I also received precious help from the staff at Erasmus MC and TU Delft. **Robert**, there are no words to express how valuable your skills are to the BME department. Your ability to solve any kind of problem in record time is impressive, and your dedication to the BME family is admirable. It is fair to say that you saved a few of our proton experiments ! I am also grateful to **Alex Brouwer** and **Henry den Bok** for contributing to the design and manufacturing of the experimental setups.

The irradiation experiments could not have taken place without the help from

numerous partners, in Belgium and in the Netherlands. To **Nancy, Laurent**, and other members of the Centre de Ressources du Cyclotron in Louvain-la-Neuve, thank you for your collaborative spirit, your flexibility, and your support. To the UZ Leuven radiotherapy team: Prof. **Tom Depuydt**, thank you for trusting us and allowing us to conduct experiments with clinical Linacs, to **Laurence** and **Robin**, thank you for helping setting up the experiments and operating the beam during long evening hours. Last but not least, **Marta**, I am extremely grateful for the way you always managed to squeeze our experiments at Holland PTC in your very busy schedule, especially in corona times. Half the chapters would be missing if it weren't for you. Thank you for your good mood, your sharp mind, for feeding us during the experiments, and of course for the very long hours spent with us in the research room.

Successful irradiation experiments also require good quality nanodroplets and phantom formulations. I would like to express my very great appreciation to IRF members: **Wim Noppe** and **Inge Pareyn**, thank you for introducing me to the laboratories and answering my numerous questions. Being the only member of the WPSP group working in the IRF, your support was incredibly valuable. Thank you **Sigrid** for your availability, your patience and your help in ordering chemicals and various materials. **Katleen**, thank you for your good vibes and for the liquid nitrogen. I also would like to thank **Maarten Mees** for introducing us to his phantom formulations, and the R&D team at **Materne** for providing the Sodium Alginate phantom recipe and chemicals.

I wish to thank my former IBA colleagues, **Quentin Flandroy** and **Olivier de Wilde**, for taking the time to answer my questions about proton physics whenever needed. I also greatly appreciate the interest of **Rudi Labarbe** in our project, and his support and advice over the years, as well as the help of **Kevin Souris** who kindly provided me clinical proton therapy treatment data. I am very grateful for the opportunity provided by Prof. **Mark Borden** to spend several days in Boulder, and for insightful discussions about the behaviour of nanodroplets. I also thank **Gazendra Shakya** and **Tim Segers** for their collaboration.

During these four years, I managed to keep my administrative phobia - multiplied by the fact that I worked at 3 offices - under control thanks to the support provided by many great people. At the department of Cardiovascular Sciences, I thank **Christel**, **Ingrid** and **Annick** for helping me navigate through the UZ Leuven administrative and architectural maze. At the Arenberg Doctoral School, I thank **Graziella Del Savio** for setting up and closely following the joint PhD agreement, and **Leen Cuypers** for helping me during the final PhD phase. At Erasmus MC, my special thanks goes to **Sharon**, who had a solution for every problem and was always ready to help me with Erasmus procedures, and **Gerard**, for making sure I had the right electronic material to store heavy

ultrasound data.

For bringing fun into this PhD journey, I would like to thank my colleagues at the different institutions. In Kulak: **Adil, Kevin, Jannes, Arvid, Eef, Caroline, Wouter**, and all the others: thank you for including me in the Kulak family even though I was not there very often, for always being helpful and supportive. In Leuven, **Bidisha, João, Pedro, Alessandro, Marta, Helena, Wentao, Annette, Stéphanie, Jürgen, Dylan, Mahdi, Kate S., Kate Z., Somayeh, Mahsa, Mostafa, Paulo, Nitin, Konstantina, Andrea, Hasti, Jack**, thank you for creating and nurturing this great lab environment, for the team building events, afterwork drinks, and conferences. Finally, I am also very thankful for meeting very welcoming colleagues in Rotterdam: thank you **Simone** for your help in the Bubble lab, **Kirby** and **Inés** for the tips and tricks which helped me better manage the final phase of the PhD, **Lucy, Gerald, Jason, Lana, Bram, Jorinde, Fox, Sander, Yijing** and all the other members of the BME family for making me feel so welcome, **Floris, Agis, Xiufeng** and the ProtonBubble team for including me in the project.

I am also incredibly grateful to my master thesis supervisor, Dr **James Choi**, for his support and encouragement. James, thank you for offering me the opportunity to write my first research article, for showing me this career path and providing me enough confidence to embark on it. To Prof. **Annick Sartenaer**, thank you for taking the time to answer my questions about the academic career and its challenges, listen to my doubts, and share your experience and precious advice with me.

Pour terminer, je tiens à remercier mes amis et ma famille de m'avoir soutenu, motivé, distrait, écouté et conseillé. Je remercie particulièrement **Christine** pour nos longues discussions sur les propositions, **Olivier** et **Karim** pour avoir partagé leur expérience avec moi, **Pauline** pour m'avoir tenu compagnie quand je me suis cassé le poignet, **Hélène** pour m'avoir rejoint dans cette aventure, **Nathalie** pour nos soupers mensuels, et bien sûr tous les autres pour les bons moments passés ensemble ces dernières années. Merci à ma belle-famille, **Sofia** et **Jean-Marc**, ainsi que **Laure, David** et **Ellie**, de m'avoir intégré au sein de leur famille avec tant de bienveillance, s'être intéressés à mes recherches qui ne sont pourtant pas facile à expliquer, et pour les nombreux soupers au 31 ou au 28. A ma famille, **Florence** et **Jean-Luc, Sandrine, et Valérie**, merci de m'avoir toujours motivé à me dépasser, d'avoir accepté mes choix et permis de les réaliser, écouté mes doutes, et soutenu quoi qu'il arrive. Enfin, **François**, merci d'avoir toujours été à mes côtés, de m'avoir encouragé à entreprendre cette thèse, d'avoir affronté avec moi les hauts et les bas de ces quatre dernières années, de m'avoir nourri tous les soirs pendant la période de rédaction, et d'avoir été si patient pendant cette (très longue) phase finale. Je n'aurais pas pu arriver au bout sans ton soutien indéfectible.

As this chapter of my life is coming to an end, I am thankful for all the great encounters I have made along the way, and eager to discover what lies ahead. I hope this is only the beginning of a long story of research collaboration together.

Abstract

Almost one in two people will suffer from cancer in their lifetime, making it a major and growing health concern, especially in the context of an aging population. About half of cancer patients are treated by radiotherapy, which consists of eradicating the tumor through exposure to ionizing radiation. The success of radiotherapy depends on its ability to deliver high radiation doses to the tumor while minimizing the dose to organs at risk and healthy tissues. In the past 20 years, the accuracy of radiotherapy has been drastically boosted by major technological progress enabling the delivery of highly conformal, complex radiation fields. Moreover, the adoption of proton therapy is rapidly accelerating, as this emerging form of radiotherapy has the potential to improve healthy tissue sparing due to the finite range of protons in the body.

While those recent advances can drastically improve the treatment efficacy, the use of high dose gradients requires appropriate methods to monitor radiation delivery and prevent unacceptable toxicity and tumor miss. In conventional (photon) radiotherapy, *in vivo* dosimetry is slowly transitioning from point-based to 3D verification. However, currently, the delivered dose cannot be measured *in situ* and overlaid on the patient anatomy in real-time. In proton therapy, range uncertainties force the adoption of conservative treatment plans with excessive safety margins, especially for moving targets. In this thesis, we investigate a novel method for *in vivo* radiation monitoring, based on the vaporization of nanodroplets into echogenic microbubbles and their detection using ultrasound imaging. While potentially applicable to both conventional and proton therapy, the main focus of this work is range verification for proton therapy.

The vaporization of metastable superheated liquids (*i.e.* maintained above their boiling temperature) by ionizing radiation was discovered more than seventy years ago. In the first part of this work, we downscaled this concept to injectable perfluorobutane nanodroplets and evaluated their response to proton (Chapters 3 and 4) and photon (Chapter 9) radiation in phantoms. According to the thermal spike theory (Chapter 2), the threshold for vaporization is inversely related to the degree of superheat, and the ability of charged particles to vaporize superheated droplets depends on the density of energy they can deposit, *i.e.*

their linear energy transfer (LET). At low degrees of superheat (25 °C and 37 °C), we observed nanodroplet vaporization induced by high-LET secondary particles in proton beams. At high degrees of superheat (50 °C), vaporization by primary protons led to a peak at the proton range. In both cases, the vaporization profiles could be related to the proton range with sub-millimeter reproducibility. To obtain a vaporization response to photon radiation, extreme degrees of superheat (65 °C) were necessary. Although experimental results were globally in good agreement with the thermal spike theory, the composition of the nanodroplet shell also influenced the vaporization response and thermal stability.

Different ultrasound imaging methods were developed to detect nanodroplet vaporization in phantoms. Offline imaging allowed to retrieve the proton range accurately, but quantification of the vaporization response was hindered by the high microbubble density. Transitioning to active and passive high frame rate imaging during irradiation enabled to count and super-localize single vaporization events (by means of Ultrasound Localization Microscopy), which strongly improved the spatiotemporal resolution of the technique (Chapters 5 and 6). While active imaging is able to localize more vaporization events, especially for deep targets, passive imaging can specifically discriminate between vaporization events and flowing or collapsing microbubbles.

We present a fast statistical model to predict the number and spatial distribution of vaporization events in Chapter 7. An experimental validation with different droplet sizes and concentrations yielded vaporization counts relatively close to predicted values, except for the smallest droplets which exhibited a reduced vaporization response. The model was also used to estimate lower bounds for the range retrieval precision from vaporization maps in clinical scenarios. Moreover, an excellent range verification accuracy was demonstrated *in vitro*.

The ability to acoustically modulate the nanodroplet degree of superheat was demonstrated in Chapter 8. This option offers an alternative to the replacement of perfluorobutane by liquids with a lower boiling temperature, which comes at the cost of thermal stability. A 1.1 MHz acoustic field was applied to perfluorobutane nanodroplet dilutions flowing in a tube during proton irradiation, and vaporization by primary protons was observed at physiological temperature using a peak rarefactional pressure of 400 kPa. This finding has important implications for clinical translation, as an increased vaporization efficiency and range verification accuracy could be obtained at 37 °C using stable perfluorobutane nanodroplets.

Beknopte samenvatting

Bijna de helft van de wereldbevolking zal tijdens hun leven aan kanker lijden, waardoor het een groot en groeiend gezondheidsprobleem is, vooral in de context van een vergrijzende bevolking. Ongeveer de helft van de kankerpatiënten wordt behandeld met radiotherapie: het uitroeien van de tumor door blootstelling aan ioniserende straling. Het succes van radiotherapie hangt af van het vermogen om hoge stralingsdoses aan de tumor toe te dienen, terwijl de dosis voor risicoorganen en gezonde weefsels wordt geminimaliseerd. In de afgelopen 20 jaar is de nauwkeurigheid van radiotherapie drastisch verbeterd door grote technologische vooruitgang die de levering van zeer conforme, complexe stralingsvelden mogelijk maakt. Bovendien versnelt de acceptatie van protontherapie snel, aangezien deze opkomende vorm van radiotherapie de potentie heeft van gezond weefsel beter te sparen vanwege het eindige bereik van protonen in het lichaam.

Hoewel deze recente ontwikkelingen de effectiviteit van de behandeling drastisch kunnen verbeteren, vereist het gebruik van hoge dosisgradiënten geschikte methoden om de stralingsafgifte te controleren en onaanvaardbare toxiciteit en tumormissing te voorkomen. Bij conventionele (foton)radiotherapie gaat *in vivo* dosimetrie langzaam over van puntgebaseerde naar 3D-verificatie. Op dit moment kan de afgeleverde dosis echter niet *in situ* worden gemeten en in realtime over de anatomie van de patiënt worden gelegd. Bij protontherapie dwingen onzekerheden in het bereik tot conservatieve behandelplannen met excessieve veiligheidsmarges, vooral voor bewegende doelen. In dit proefschrift onderzoeken we een nieuwe methode voor *in vivo* stralingsmonitoring, gebaseerd op de verdamping van nanodruppels naar echogene microbellen en hun detectie met behulp van ultrasone beeldvorming. Hoewel potentieel toepasbaar op zowel conventionele als protontherapie, ligt de focus van dit werk op bereikverificatie voor protontherapie.

De verdamping van metastabiele oververhitte vloeistoffen (*d.w.z.* die boven hun kookpunt worden gehouden) door ioniserende straling werd meer dan zeventig jaar geleden ontdekt. In het eerste deel van dit werk hebben we dit concept gedownscaled naar injecteerbare perfluorbutaan-nanodruppels en hun

reactie op protonen (hoofdstuk 3 en 4) en fotonen (hoofdstuk 9) in fantomen geëvalueerd. Volgens de theorie van thermische pieken (hoofdstuk 2) is de drempel voor verdamping omgekeerd evenredig met de mate van oververhitting, en het vermogen van geladen deeltjes om oververhitte druppeltjes te verdampen hangt af van de energiedichtheid die ze kunnen afzetten, *i.e.* hun lineaire energieoverdracht (Linear Energy Transfer, LET). Bij een lage mate van oververhitting (25 °C en 37 °C), observeerden we verdamping van nanodruppels veroorzaakt door secundaire hoge-LET-deeltjes in protonenbundels. Bij een hoge mate van oververhitting (50 °C) leidde verdamping door primaire protonen tot een piek in het protonbereik. In beide gevallen kunnen de verdampingsprofielen worden gerelateerd aan het protonbereik met een reproduceerbaarheid van minder dan een millimeter. Om een verdampingsreactie op fotonstraling te verkrijgen, was een extreme mate van oververhitting (65 °C) nodig. Hoewel de experimentele resultaten globaal gezien goed overeenkwamen met de theorie van thermische pieken, had de samenstelling van de nanodruppelschil ook invloed op de verdampingsrespons en thermische stabiliteit.

Er werden verschillende ultrasone beeldvormingsmethoden ontwikkeld om de verdamping van nanodruppels in fantomen te detecteren. Offline beeldvorming maakte het mogelijk om het protonbereik nauwkeurig te achterhalen, maar kwantificering van de verdampingsrespons werd gehinderd door de hoge dichtheid van microbellen. Overgang naar actieve en passieve beeldvorming met hoge framesnelheid tijdens de bestraling (online) maakte het mogelijk om individuele verdampingsgebeurtenissen te tellen en superlokalisieren (door middel van Ultrasound Localization Microscopy), wat de ruimte-tijdresolutie van de techniek sterk verbeterde (Hoofdstukken 5 en 6). Waar actieve beeldvorming meer verdampingsgebeurtenissen kan lokaliseren, vooral voor diepe doelen, kan passieve beeldvorming specifiek onderscheid maken tussen verdampingsgebeurtenissen en bewegende of instortende microbellen.

In Hoofdstuk 7 presenteren we een statistisch model om het aantal en de ruimtelijke verdeling van verdampingsgebeurtenissen te voorspellen. Experimentele validatie met verschillende druppelgroottes en -concentraties leverde verdampingstellingen op die relatief dicht bij de voorspelde waarden lagen, behalve voor de kleinste druppels die een verminderde verdampingsrespons vertoonden. Het model werd ook gebruikt om ondergrenzen te schatten voor de nauwkeurigheid van het ophalen van het bereik van verdampingskaarten in klinische scenario's. Bovendien werd een uitstekende nauwkeurigheid van de bereikverificatie aangetoond *in vitro*.

Het vermogen om de mate van oververhitting van nanodruppels akoestisch te moduleren werd gedemonstreerd in Hoofdstuk 8. Deze optie biedt een alternatief voor de vervanging van perfluorbutaan door vloeistoffen met een lagere kooktemperatuur, wat ten koste gaat van de thermische stabiliteit. Een akoestisch

veld van 1,1 MHz werd toegepast op perfluorbutaan-nanodruppelverduunningen die in een buis stromen tijdens protonenbestraling, en verdamping door primaire protonen werd waargenomen bij fysiologische temperatuur met een piekdruk van 400 kPa. Dit heeft belangrijke implicaties voor de uiteindelijke klinische toepassing, aangezien een verhoogde verdampingsefficiëntie en nauwkeurigheid van de bereikverificatie kunnen worden verkregen bij 37°C met behulp van stabiele perfluorbutaan-nanodruppels.

Contents

Preface	i
Abstract	vii
Beknopte samenvatting	ix
Contents	xiii
List of abbreviations	xix
List of symbols	xxi
1 Introduction	1
1.1 Problem statement: the need for <i>in vivo</i> radiation therapy monitoring	1
1.2 Ultrasound imaging and contrast agents	4
1.3 <i>In vivo</i> radiation detection with ultrasound contrast agents . .	7
1.4 Research objectives and thesis outline	10
2 Metastable liquids: Limits of superheat and theory of radiation-induced vaporization	13
2.1 Introduction	14
2.2 Thermodynamics and kinetics of superheated liquids	15
2.2.1 Thermodynamic limits of superheat and overexpansion .	15
2.2.2 Kinetic limits of superheat and overexpansion	20
2.3 Radiation-induced vaporization of superheated liquids	26
2.3.1 The thermal spike theory	26
2.3.2 Extension to encapsulated nanodroplets	28
2.4 Discussion	36
2.4.1 Thermodynamic and kinetic limits of superheat	36
2.4.2 The thermal spike theory extended to encapsulated nanodroplets	38
2.5 Conclusion	40

2.6	Appendix: derivation of the saturation pressure from the generic equation of state	40
3	Proton range verification with ultrasound imaging using injectable radiation sensitive nanodroplets: a feasibility study	43
3.1	Introduction	44
3.2	Materials and methods	46
3.2.1	Theory of nucleation induced by ionizing radiation	46
3.2.2	Nanodroplet synthesis and characterization	48
3.2.3	Phantom synthesis	49
3.2.4	Irradiation protocol	50
3.2.5	Ultrasound imaging	53
3.2.6	Image processing	53
3.2.7	Statistical analyses	55
3.3	Results	56
3.3.1	Analytical evaluation of the experimental conditions	56
3.3.2	Radiation response of the nanodroplet formulation	56
3.3.3	Proton range verification	57
3.3.4	Nanodroplet sensitivity to proton dose and fluence	61
3.4	Discussion	62
3.5	Conclusion	68
3.6	Acknowledgments	68
4	Modulating ultrasound contrast generation from injectable nanodroplets for proton range verification by varying the degree of superheat	69
4.1	Introduction	70
4.2	Materials and Methods	73
4.2.1	Nanodroplet synthesis and size distribution	73
4.2.2	Phantom preparation	74
4.2.3	Irradiation protocol	74
4.2.4	Data acquisition	76
4.2.5	Data analysis	77
4.3	Results	80
4.3.1	Radiation response at physiological temperature	80
4.3.2	Primary proton sensitization (50 °C)	81
4.4	Discussion	84
4.4.1	Influence of the temperature on the ultrasound contrast generation	84
4.4.2	Influence of the temperature on the relationship between the proton range and the ultrasound contrast	85
4.4.3	Implications, limitations and future directions	88
4.5	Conclusion	90

4.6	Acknowledgments	91
5	Spatiotemporal distribution of nanodroplet vaporization in a proton beam using real-time ultrasound imaging for range verification	93
5.1	Introduction	94
5.2	Materials and Methods	96
5.2.1	Nanodroplet and phantom synthesis	96
5.2.2	Phantom irradiation	96
5.2.3	Characterization of the proton beam	97
5.2.4	Online ultrasound imaging and image processing	98
5.3	Results and discussion	100
5.3.1	Influence of the temperature on the vaporization response	100
5.3.2	Spatial quantification of the vaporization events	100
5.3.3	Temporal quantification of the vaporization events	103
5.3.4	Future directions and clinical translation	103
5.4	Conclusion	105
5.5	Acknowledgments	105
5.6	Supplementary materials	105
6	Passive Ultrasound Localization Microscopy of nanodroplet vaporization during proton irradiation	107
6.1	Introduction	108
6.2	Materials and Methods	110
6.2.1	Resolution limits of P-ULM	110
6.2.2	Experimental methods	113
6.3	Results	119
6.3.1	Resolution limits of P-ULM	119
6.3.2	Experimental comparison of the range verification accuracy of ULM and P-ULM	122
6.4	Discussion	125
6.5	Conclusion	131
6.6	Acknowledgments	131
7	A statistical model to predict superheated droplet vaporization in a proton beam: experimental validation and resolution limits for range verification	133
7.1	Introduction	134
7.2	Materials and Methods	137
7.2.1	Statistical model	137
7.2.2	Experimental validation	139
7.2.3	Simulation of the vaporization response in a clinically-relevant treatment plan	145
7.3	Results	147

7.3.1	Validation of the statistical model	147
7.3.2	Range verification performance	149
7.4	Discussion	152
7.4.1	Comparison between model predictions and experimental observations	152
7.4.2	Range verification performances	157
7.5	Conclusion	159
7.6	Appendix: Effective thickness of the acoustic imaging plane . .	159
7.7	Acknowledgments	162
8	Acoustic modulation of nanodroplet superheat enables proton detection at body temperature	163
8.1	Introduction	164
8.2	Materials and Methods	166
8.2.1	Nanodroplet formulation	166
8.2.2	Acoustic modulation transducer	166
8.2.3	Experimental setup	167
8.2.4	Acoustic modulation experiment	169
8.2.5	Ultrasound sequence	169
8.2.6	Data processing	171
8.3	Results	171
8.3.1	Sensitivity to protons at ambient conditions	171
8.3.2	Acoustically modulated sensitivity to protons	173
8.4	Discussion	174
8.5	Conclusion	179
8.6	Acknowledgments	179
8.7	Supplementary materials	180
9	Real-time ultrasound imaging of nanodroplet vaporization in a clinical photon radiotherapeutic beam: proof-of-concept	183
9.1	Introduction	184
9.2	Materials and Methods	189
9.2.1	Nanodroplet and phantom synthesis	189
9.2.2	Irradiation protocol	190
9.2.3	Online ultrasound imaging	191
9.2.4	Data processing	192
9.3	Results	194
9.3.1	Spatial quantification	196
9.3.2	Temporal quantification	198
9.4	Discussion	198
9.5	Conclusion and future directions	206
10	Discussion and conclusion	209

10.1 Summary, discussion, and future research actions	209
10.2 Future perspectives	214
10.2.1 Envisioned path towards clinical applications	214
10.2.2 Integration of this technology in the current and future radiotherapy and oncology landscape	219
10.3 Conclusion	223
Bibliography	225
Curriculum Vitae	251
List of publications	253
PhD portfolio	259

List of abbreviations

EBRT	External Beam Radiation Therapy
MV	Megavoltage
Linac	Linear Accelerator
3D-CRT	Three-Dimensional Conformal Radiotherapy
IMRT	Intensity-Modulated Radiation Therapy
VMAT	Volumetric-Modulated Arc Therapy
kV	Kilovoltage
CT	Computed Tomography
IMPT	Intensity-Modulated Proton Therapy
EPID	Electronic Portal Imaging Device
XACT	X-ray Acoustic Computed Tomography
PET	Positron Emission Tomography
PGI	Prompt Gamma Imaging
CEUS	Contrast Enhanced Ultrasound Imaging
PCCA	Phase-Change Ultrasound Contrast Agents
ADV	Acoustic Droplet Vaporization
ODV	Optical Droplet Vaporization
ULM	Ultrasound Localization Microscopy
PFB	Decafluorobutane
BGRT	Biologically Guided Radiation Therapy
LET	Linear Energy Transfer
PVA	Polyvinyl alcohol
PCDA	10,12-pentacosadyinoic acid
DLS	Dynamic Light Scattering
NMR	Nuclear Magnetic Resonance
PVC	Polyvinyl Chloride
FWHM	Full Width at Half Maximum
ROI	Region Of Interest
MC	Monte Carlo

HU	Houndsfield Unit
PSF	Point Spread Function
HPTC	Holland Proton Therapy Center
PMMA	Poly(methyl methacrylate)
RMS	Root Mean Square
P-ULM	Passive Ultrasound Localization Microscopy
TOA	Time Of Arrival
TDOA	Time Difference Of Arrival
SNR	Signal to Noise Ratio
RF	Radiofrequency
WET	Water Equivalent Thickness
PAM	Passive Acoustic Mapping
ND	Nanodroplet
PNP	Peak Negative Pressure
PZT	Lead Zirconate Titanate
AWG	Arbitrary Waveform Generator
IR	Infrared
PRF	Pulse Repetition Frequency
US	Ultrasound
OAR	Organ At Risk
SBRT	Stereotactic Body Radiotherapy
QA	Quality Assurance
IAEA	International Atomic Energy Agency
WHO	World Health Organization
MOSFET	Metal–Oxide–Semiconductor Field-Effect Transistor
CBCT	Cone-beam Computed Tomography
SSD	Source to Skin Distance
MRI	Magnetic Resonance Imaging

List of symbols

The symbols are sorted in order of first appearance.

Chapter 2:

P	Pressure [Pa]
v	Molar specific volume [m^3/mol]
T	Temperature [K]
P_r	Reduced pressure [-]
v_r	Reduced molar specific volume [-]
T_r	Reduced temperature [-]
P_c	Critical pressure [Pa]
v_c	Critical molar specific volume [m^3/mol]
T_c	Critical temperature [K]
P_s	Saturation pressure [Pa]
v_l	Molar specific volume of the liquid phase [m^3/mol]
v_v	Molar specific volume of the vapor phase [m^3/mol]
μ_l	Chemical potential of the liquid phase [J/mol] or [J/kg]
μ_v	Chemical potential of the vapor phase [J/mol] or [J/kg]
R_g	Ideal gas constant [$\text{J K}^{-1} \text{mol}^{-1}$]
$\gamma, \lambda, a_1, b_1, b_2$	Equation of state parameters
a_{r1}, b_{r1}, b_{r2}	Reduced equation of state parameters
Z_c	Critical compressibility [-]
W	Change in Gibbs free energy [J]
R	Radius [m]
P_l	Pressure in the liquid phase [Pa]
P_v	Pressure in the vapor phase [Pa]
σ	Surface tension at the perfluorocarbon interface [N/m]
ρ_l	Density of the liquid phase [kg/m^3]
ρ_v	Density of the vapor phase [kg/m^3]
$P_{v,eq}$	Pressure in the vapor phase at equilibrium [Pa]
R_{eq}	Critical radius at equilibrium [m]

W_{eq}	Work required to form a vapor embryo of critical size [J]
B	Constant factor: 2/3 for heating, 1 for cavitation [-]
n	Number of molecules [-]
N	Number of vapor embryos [m^{-3}]
N_A	Avogadro's number [mol^{-1}]
M	Molecular mass [kg/mol]
k_b	Boltzmann's constant [$\text{kg m}^2 \text{s}^{-2} \text{K}^{-1}$]
T_l	Temperature in the liquid phase [K]
J	Nucleation rate of vapor embryos of critical size [$\text{m}^{-3}\text{s}^{-1}$]
Da	Mass of a Dalton [kg]
R_c	Critical radius [m]
W_{tot}	Radiation-induced nucleation energy [J] or [keV]
ΔH	Latent vaporization heat [J/kg]
W_{irr}	Irreversible losses [J] or [keV]
σ_s	Surface tension of the nanodroplet shell [N/m]
\dot{R}	Vapor wall velocity [m/s]
D	Thermal diffusivity of the liquid [m^2/s]
k	Thermal conductivity of the liquid [$\text{W m}^{-1} \text{K}^{-1}$]
c_p	Specific heat of the liquid [$\text{J kg}^{-1} \text{K}^{-1}$]
a	Nucleation parameter [-]
E	Energy of a charged particle [keV]
$\langle \frac{dE}{dx} \rangle$	Track-averaged LET [keV/ μm]
L_{eff}	Effective length [m]
s	Reduced superheat [-]
T_b	Boiling temperature [K]
$W_{tot,enc}$	Radiation-induced nucleation energy for encapsulated droplets [J] or [keV]
$W_{s,elast}$	Elastic term for the droplet shell [J] or [keV]
$W_{s,visc}$	Viscous term for the droplet shell [J] or [keV]
$W_{m,elast}$	Elastic term for the surrounding matrix [J] or [keV]
$W_{m,visc}$	Viscous term for the surrounding matrix [J] or [keV]
p_s	Radial stress difference across the shell [Pa]
V	Volume (1: inner, 2: outer) [m^3]
V_0	Initial volume (1: inner, 2: outer) [m^3]
R_0	Initial radius (1: inner, 2: outer) [m]
ϵ	Shell thickness [m]
G_s	Shear modulus of the shell [Pa]
μ_s	Viscosity of the shell [Pa s]
κ_s	Surface dilatational viscosity of the shell [kg/s]
χ	Elastic compression modulus of the shell [N/m]
G_m	Shear modulus of the surrounding matrix [Pa]
μ_m	Viscosity of the surrounding matrix [Pa s]
P_0	Atmospheric pressure [Pa]
P_{ac}	Acoustic pressure [Pa]

ω	Acentric factor [-]
$v_{r,sp}$	Reduced molar specific volume at the spinodal [-]
$v_{r,s}$	Reduced molar specific volume at saturation [-]

Chapter 3:

R_{80}	Proton range: position corresponding to the distal 80% dose [cm]
ΔP_{lap}	Laplace pressure [Pa]

Chapter 4:

S	Magnitude spectrum of the backscattered signal [V]
G'	Gain factor [V]
f	Ultrasound frequency [MHz]
z	Ultrasound axial depth [cm]
$ P(f) $	Impulse response of the ultrasound array [-]
A	Attenuation factor [-]
B	Backscatter factor [-]
α	Attenuation coefficient [dB/cm]
B_0	Backscatter coefficient [-]
a	Intercept attenuation coefficient [dB/cm]
b	Slope attenuation coefficient [dB/(MHz cm)]
α_p	Peak attenuation coefficient [dB/cm]
f_{res}^*	Microbubble resonance frequency [MHz]
k	Nucleation parameter (= a in chapters 2 & 3) [-]

Chapter 6:

τ_i	Reception time of an acoustic signal at transducer element i [s]
c	Speed of sound [m/s]
x_0	Bubble position in lateral ultrasound direction [m]
z_0	Bubble position in axial ultrasound direction [m]
x_i	Lateral position of transducer element i [m]
z_i	Axial position of transducer element i [m]
x_{ref}	Lateral position of reference transducer element [m]
z_{ref}	Axial position of reference transducer element [m]
σ_τ	Standard deviation of measured arrival times [s]
n	Number of transducer elements [-]
Γ	Gamma matrix [s ² /m ²]
L_x	Aperture of the ultrasound array [m]
$\sigma_{\hat{x}_0}$	Lateral bubble localization error [m]
$\sigma_{\hat{z}_0}$	Axial bubble localization error [m]
σ_R	Range dispersion in the proton beam direction [m]
σ_{lat}	Proton beam lateral spot size [m]
r	Coefficient of determination [-]
y_0	Bubble position in elevational ultrasound direction [m]

Chapter 7:

L_p	Proton interaction length [m]
$P(vap)$	Probability of vaporization of a droplet by a proton [-]
R_i	Droplet radius [m]
n_i	Number concentration of droplets of size R_i [ND/m ³]
\hat{R}	Mean volume-weighted droplet radius [m]
\hat{n}	Mean volume-weighted droplet number concentration [ND/m ³]
V_{eff}	Effective volume [m ³]
N_p	Number of protons [-]
ω	Centrifugation speed [rad/s]
d_c	Nanodroplet cut-off diameter [m]
t	Centrifugation time [s]
R_{min}	Minimum rotor radius [m]
R_{max}	Maximum rotor radius [m]
L	Liquid column height [m]
$\Delta\rho$	Difference between nanodroplet and water density [kg/m ³]
μ_w	Dynamic viscosity of water [Pa s]
N_{vap}	Number of vaporization events [-]
a, b	Coefficients of the Michaelis-Menten saturation curve [-]
N_{max}	Maximum number of vaporization events [-]
\hat{R}	Proton range estimate [cm]
R_f	Geometrical focus of transducer elements in elevational direction [m]
E_H	Height of transducer elements [m]
A_f	Apodization factor of transducer elements [m]

Chapter 9:

$N_{vap,L}$	Lower plateau value of vaporization count [-]
$N_{vap,H}$	Higher plateau value of vaporization count [-]
x_m	Position of the middle of the ramp up phase [m]
x_b	Sharpness indicator for the ramp [m]
a, b	Coefficients of the Michaelis-Menten saturation curve [-]
D	Radiation dose [Gy]
k_0	Constant = $1/(4\pi\epsilon_0)$ [Nm^2/Cb^2]
e	Magnitude of the electron charge [Cb]
n_e	Number of electrons per unit volume [m^{-3}]
m_e	Electron rest mass [kg]
c	Speed of light [m/s]
β	Relative speed of the electron with respect to the speed of light [-]
v_e	Speed of the electron [m/s]
τ	Relative kinetic energy [-]
T	Electron kinetic energy [eV]
I	Mean excitation energy of the medium [eV]
Z	Atomic number [-]
A	Atomic weight [-]
r_j	Relative contribution of compound j in the molecule [-]
n_i	Number of moles of perfluorocarbon in a droplet [mol]
R	Nanodroplet radius [m]
D_i	Diffusivity of the perfluorocarbon [m^2/s]
M_w	Molecular weight of water [kg/mol]
ρ_w	Density of water [kg/m^3]
M_i	Molecular weight of perfluorocarbon [kg/mol]
ρ_i	Density of perfluorocarbon [kg/m^3]
$P_{i,s}$	Saturation pressure of the perfluorocarbon [Pa]
H_i	Henry's law constant [Pa]
P_0	Atmospheric pressure [Pa]
y_{Bi}	Mole fraction of perfluorocarbon [-]

“To live a creative life, we must lose our fear of being wrong.”

Joseph Chilton Pearce

1

Introduction

1.1 Problem statement: the need for *in vivo* radiation therapy monitoring

Cancer is a primary health concern and the second cause of mortality in the world, with 19.3 million new cases and almost 10 million deaths every year [1]. By 2040, the incidence and mortality of cancer are expected to rise to 30.2 and 16.3 million, respectively [2]. **Radiation therapy** is, together with chemotherapy and surgery, one of the main pillars in the management of cancer. The exposure of malignant tissue to ionizing radiation leads to DNA damage, which in turn induces cell death. Ionizing radiation can be delivered by external sources, as in External Beam Radiation Therapy (EBRT) or by inserting radioactive implants at or near the area requiring treatment, as in brachytherapy. The most common type of radiotherapy by far, to which we will refer as *conventional radiotherapy*, is megavoltage (MV) radiotherapy and consists in treating tumors within the body using a megavoltage photon or electron beam generated by a linear accelerator (linac) [3].

Although far less frequent than photons and electrons, light ions (proton, helium) and heavy ions (carbon) can also be used for radiotherapy. The main advantage of particle therapy is ballistic: unlike photons, which traverse the entire body,

charged particles have a finite range in the body, preceded by a narrow dose peak, called the Bragg peak (figure 1.1(a)). The range can be tuned by modifying the beam energy, thereby allowing to spare tissues located behind the tumor while delivering a high uniform tumor dose using a spread-out Bragg Peak (figure 1.1(b)) [4]. Moreover, the higher density of energy deposition of protons and heavy ions at the end of their range makes them more efficient at inducing biological damage compared to conventional radiotherapy [3, 5]. Propelled by major technological developments leading to the emergence of commercial systems, **proton therapy** has greatly expanded in the past two decades [4, 6], and is currently accessible in 110 centers worldwide [7]. However, at present, the vast majority of the patients are treated by conventional MV EBRT [8], as the cost per proton therapy treatment is much higher than for conventional therapy [9]. Clinical indications greatly vary across countries, depending on the reimbursement policy and the availability of proton therapy, but typically include pediatric patients, ocular tumors, specific types of brain or head and neck tumors, and, in some cases, hepatocellular, breast, lung, and prostate cancer [10]. Currently, approximately 1% of all radiotherapy patients benefit from proton therapy (more than 20 000 patients per year [11]), far below its suggested potential of 15% [12].

The objective of radiotherapy is to inflict maximal radiation damage to the tumor while keeping the exposure of healthy tissues to a minimum, to prevent complications such as acute effects or the onset of secondary cancer years after treatment. The total prescribed dose of *e.g.* 60 Gy is typically fractionated into daily sessions of around 2 Gy, in order to allow for repair of healthy cells while enhancing the efficacy of radiation on tumor cells [13]. In addition, the delivered radiotherapy beams are shaped to match the tumor geometry as much as possible, yielding highly conformal radiotherapy plans with steep dose gradients. In the past decades, conventional photon radiotherapy evolved from 2D to 3D conformal radiotherapy (3D-CRT) and nowadays includes intensity modulation and field shaping using multi-leaf collimators (intensity-modulated radiotherapy - IMRT) with dynamic delivery during rotation of the gantry (volumetric-modulated arc therapy - VMAT) [3, 14]. Image guidance solutions have also expanded, and while modern linacs are equipped with both kV X-ray and MV imaging devices, more elaborate imaging systems are also available, such as in-room CT or cone-beam CT integrated on the gantry [3]. As far as proton therapy is concerned, beam delivery techniques also transitioned from passive scattering to intensity-modulated proton therapy (IMPT), a technique in which a proton pencil beam is scanned across the tumor while varying its properties (such as energy or intensity) [15], yielding highly conformal dose distributions. Contrarily to conventional radiotherapy, proton therapy is currently delivered using few gantry angles to limit the normal tissue dose. However, the feasibility of proton arc therapy is being actively investigated [16–18].

The use of steep dose gradients combined with increasingly popular hypofractionated (daily dose > 2 Gy) regimes [19] requires reliable methods to verify the dose delivered to the patient, as deviations from the treatment plan can potentially lead to a lack of tumor control or unacceptable radiation damage to healthy tissues [20]. Even though pretreatment quality assurance can reduce the risk of errors, the combined impact of all sources of errors, from machine calibration and treatment planning to patient alignment and inter- and intrafractional anatomical changes, can only be verified through *in vivo* dosimetry [21, 22]. The latter was defined as "the measurement of the radiation dose received by the patient during treatment, as opposed to *ex vivo* dosimetry" [20]. While the delivered dose was traditionally verified intermittently using point detectors placed on the patient's skin (such as thermoluminescent dosimeters or silicon diodes), modern *in vivo* dosimetry in conventional radiotherapy is performed by inferring the delivered 2D or 3D dose distribution from the transmitted MV beam captured on Electronic Portal Imaging Devices (EPID) [14, 20, 23]. Recently, EPID-based *in vivo* dosimetry was implemented online, to prevent the delivery of unacceptable doses by interrupting the treatment in time [24, 25]. Although not yet used in the clinic, X-Ray Acoustic Computed Tomography (XACT) is also investigated to reconstruct the *in vivo* dose distribution by detecting thermoacoustic waves generated in the body by pulsed beams [26–28]. In addition to treatment verification, the feedback provided by *in vivo* dosimetry techniques could serve as an input for adaptive radiation therapy [23], a technique in which the treatment plan is adapted to compensate for anatomical changes happening over the course of the treatment [29].

In vivo treatment monitoring is even more essential for proton therapy, as small deviations in proton range can lead to missing part of the tumor, or to delivering the maximal prescribed dose to an organ at risk located distal to the tumor, as shown in figure 1.1(c). Uncertainties on the delivered proton range arise due to many factors in the treatment planning and delivery phases, and currently force clinicians to adopt large (several mm) safety margins and choose suboptimal beam angles [30]. ***In vivo* proton range verification** techniques are being actively developed to provide clinicians with feedback on the delivered range, thus helping proton therapy reach its full potential. The most mature solution is based on positron emission tomography (PET) of positron-emitting isotopes produced by nuclear reactions of protons with atomic nuclei of the medium [31]. As the half-life of endogenously generated positron-emitting isotopes is only a few minutes, efforts have been undertaken to transition from offline PET [32] to in-room [33, 34], or even in-beam PET [35, 36]. Prompt Gamma Imaging (PGI) also makes use of nuclear reaction products by detecting gamma rays emitted by nuclei left in an excited state [37]. The detector is typically positioned next to the patient and prompt gamma rays are detected during irradiation [38]. Recent studies demonstrated the ability

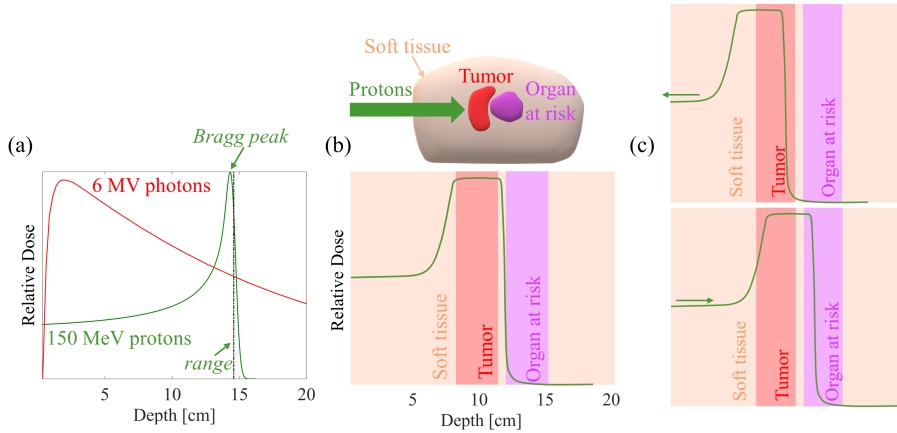


Figure 1.1: (a) Depth-dose deposition profiles of 6 MV photons and 150 MeV protons. (b) Schematic representation of a spread-out Bragg peak covering the entire tumor depth. (c) Potential impact of range uncertainties on the proton dose profile, leading to tumor miss (top) or the delivery of the tumor dose to an organ at risk (bottom).

of PGI to detect range shifts with a precision of 2 mm *in vivo* [39]. As an alternative to PET and PGI, ionoacoustics, a technique based on the detection of acoustic waves generated by thermo-elastic tissue expansion at the Bragg peak, has recently regained interest for *in vivo* range verification [40]. Several simulation and phantom studies have reported promising range verification performances [41–43], and preliminary results indicate that acoustic emissions might be further enhanced by the use of ultrasound contrast agents [44].

1.2 Ultrasound imaging and contrast agents

Ultrasound is one of the most common imaging modalities and is used routinely for diagnostic procedures in the clinic [45]. Examinations are typically carried out with a handheld probe, composed of an array (2D imaging) or matrix (3D imaging) of piezoelectric transducer elements, able to convert voltage into pressure and vice versa. To form anatomical images, several short compressional pulses at frequencies in the range 1-10 MHz, much higher than the threshold of human hearing, propagate through tissue, and are reflected back to the imaging probe at the interface of different tissues. The intensity of the reflected wave depends on differences in tissue density and stiffness. The time-of-flight information of the obtained echoes is then used to compute the location of the different anatomical structures, in a process called beamforming, yielding

brightness-mode (B-mode) images. Ultrasound imaging provides good soft tissue contrast, but does not penetrate easily through bones or gas cavities. Aside from fetal monitoring (figure 1.2), which is perhaps its best-known application, ultrasound imaging is also widely used for the cardiovascular system, as it can overlay blood flow information (using the Doppler effect) to anatomical images of *e.g.* the heart or the carotid artery, and for soft tissue imaging in the abdominal and uro-genital region. Ultrasound imaging is relatively fast, inexpensive and portable, and is considered safer than modalities relying on ionizing radiation, such as X-ray or nuclear medicine imaging.

Ultrasound can offer image guidance for different medical procedures such as radiotherapy, and is often used for the planning and guidance of brachytherapy [46]. Although the standard modality for image guidance in EBRT is X-ray or cone-beam CT imaging, ultrasound imaging is attractive for soft tissue targets, as the soft tissue contrast on X-ray images is limited and might not allow to detect daily changes in soft tissue position with respect to bony structures [47, 48]. Advantages of ultrasound for image-guided radiotherapy



Figure 1.2: Ultrasound image of a 4-months old fetus.

include its non invasiveness, spatial and temporal resolution, and relative compactness and easiness of integration. The absence of ionizing radiation dose makes ultrasound an appealing candidate for image guidance in pediatric patients [49, 50]. A commercial solution (Clarity, Elekta) was initially developed to assist daily patient setup for prostate treatments [48], as the prostate is particularly prone to interfractional motion (mm to cm) due to variations in bladder and rectal filling [51]. The technology was recently expanded to 4D intrafractional motion management, and allows to interrupt the treatment if the misalignment exceeds predefined tolerances [49, 52]. Ultrasound image guidance for breast or abdominal tumours is being investigated, but several issues, such as high inter-operator variability or tissue deformation induced by the ultrasound probe, currently limit its widespread adoption [49, 53, 54]. Research on the development of robotic arms for transducer positioning [55], flexible [56, 57] or radiolucent [58] transducers for minimal interference with the radiation beam, and fast volumetric imaging [59, 60] is ongoing, and should ultimately facilitate the adoption of ultrasound imaging in the radiotherapy room.

Microbubbles are spherical gaseous cavities surrounded by a shell made of lipids, polymers, or proteins [61]. They were introduced as intravascular ultrasound contrast agents, since their micrometer size (1 -10 μm) allows them

to pass through the capillary bed but restrains them within the vasculature [62]. Injected into the blood stream, microbubbles act as strong ultrasound scatterers, due to the high echogenicity of their gas core combined with resonant behaviour in the medical ultrasound frequency range [63]. Furthermore, when exposed to an acoustic field, microbubbles undergo radial oscillations and produce nonlinear acoustic emissions [64]. Contrast enhanced ultrasound imaging (CEUS) employs imaging sequences that can harvest the nonlinear oscillations of microbubbles to effectively suppress tissue reflection and only retain the bubble signal [62]. Another branch of ultrasound contrast agents, called nanodroplets or phase-change contrast agents (PCCA) [65], has been increasingly investigated in the past 10 years. Contrarily to microbubbles, nanodroplets have a liquid core encapsulated in a shell, with diameters ranging from a few hundreds of nanometers up to a few microns [66]. While liquid nanodroplets exhibit little echogenicity, their small size allows them to potentially extravasate through the larger endothelial junctions of (leaking) tumour vasculature and accumulate through the enhanced permeability and retention effect [67–70]. Moreover, upon external stimulation by an acoustic field (Acoustic Droplet Vaporization - ADV [71, 72]) or laser irradiation (Optical Droplet Vaporization - ODV [73, 74]), nanodroplets vaporize, either reversibly or irreversibly, and become highly echogenic microbubbles (figure 1.3).

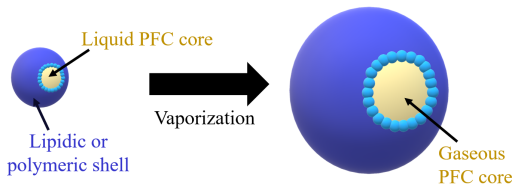


Figure 1.3: Schematic representation of the vaporization of a nanodroplet into a microbubble.

Ultrasound contrast agents have a great potential for clinical applications, as illustrated by the numerous research lines currently under investigation. Although nowadays, ultrasound contrast agents are mainly used in clinical practice for qualitative blood

perfusion studies, the ability to accommodate their shell with receptor-specific ligands, combined with the low cost of ultrasound imaging and its high sensitivity to the presence of ultrasound contrast agents, paved the way for ultrasound molecular imaging [75, 76]. Flowing microbubbles or nanodroplets, when imaged using high frame rate ultrasound, can also provide high-resolution images of the microvasculature, via a technique called Ultrasound Localization Microscopy [77, 78]. Another large body of research is dedicated to therapeutic applications of ultrasound contrast agents [79]. Combined with focused ultrasound, microbubbles can selectively release drugs at the intended location, and are able, through cavitation, to boost the delivery of drugs or genes across various biological barriers [80, 81]. Therapeutic applications include the targeted delivery of chemotherapeutic drugs in tumors [80, 82, 83], treatment of diseases of

the Central Nervous System such as Parkinson's or Alzheimer's disease [84–86], or sonothrombolysis, the disruption of blood clots [87].

Within the context of cancer diagnosis and therapy, the detection of prostate, breast and ovarian cancer by microbubbles targeted to vascular markers of neoangiogenesis was recently demonstrated in humans [88, 89]. The ability of ultrasound contrast agents to induce tumor damage through cavitation, increase tumor uptake, and selectively deliver chemotherapeutic drugs is intensively studied, and several applications have reached the clinical trial phase [79]. Importantly, acoustically-induced microbubble cavitation has been reported to enhance the efficacy of radiotherapy in tumor tissue [90–93]. Moreover, the delivery of oxygen microbubbles can improve the response to radiation therapy by reoxygenating hypoxic tumor regions in animal models [94–96], and enhance the generation of reactive oxygen species for sonodynamic therapy [97]. As major pathways leading to radiation-induced DNA damage rely on the presence of oxygen, the presence of hypoxic regions is associated with a resistance to radiotherapy [98, 99]. Enhanced oxygen delivery in hypoxic tumors was also observed using perfluorocarbon nanodroplets, presumably due to the oxygen-carrying capacity of perfluorocarbons [100]. Finally, the assessment of tumor perfusion and vasculature through CEUS is evaluated as a means to monitor the tumor response to radiotherapy [101–103].

1.3 *In vivo* radiation detection with ultrasound contrast agents

The ability to precisely target malignant tissues with highly conformal radiotherapy beams has greatly improved, owing to the development of advanced delivery techniques in conventional radiotherapy and the accelerated growth of proton therapy. As a consequence, deviations from the treatment plan can have severe repercussions, and there is a growing need to accurately monitor the dose delivered *in vivo*. In conventional radiotherapy, the delivered dose can be inferred from transmission measurements using EPID [14]. In proton therapy, transmission measurements are excluded since protons have a finite range in the body. While several techniques are being developed for *in vivo* range verification, each with its own advantages and shortcomings [104], it is worth noting that none of them has reached widespread adoption in the clinic.

The extensive research work introduced above shows that ultrasound imaging and contrast agents have a role to play in cancer diagnosis and therapy. In particular, ultrasound can provide real-time image guidance of radiotherapy, and contrast agents can synergistically enhance the damage inflicted to the

tumor. As microbubbles and nanodroplets can conquer the tumor vasculature and reach extravascular tissues, respectively, one could envision their use for radiation dosimetry by casting them into *in vivo* dose sensors that can be interrogated by ultrasound imaging. The concept of using microbubbles for *in vivo* radiotherapy dosimetry was demonstrated a few years ago [105,106], and initiated a European consortium to further explore the potential of this novel emerging technology. The Amphora¹ project brought together ten research teams with different fields of expertise from four European countries, providing a multidisciplinary approach to develop *an innovative, non-invasive, in situ dosimetry system for radiation therapy, featuring Ultrasound Contrast Agents as dose-sensing theranostic devices*. Two different research lines were defined: one focused on microbubbles coated with a radiosensitive shell, and one dedicated to superheated nanodroplets which can vaporize when exposed to ionizing radiation. Those approaches are fundamentally different, as the first relies on the detection of changes in the microbubble acoustic response following radiation exposure, while the second is based on the transition from an anechoic liquid drop into an echogenic gaseous microbubble, providing an off/on response to radiation.

This thesis is dedicated to the second research line, namely the approach based on superheated nanodroplets. The working principle is the following: nanodroplets are maintained in a metastable, superheated state, which means that the operating temperature is higher than the boiling temperature of their liquid core. Charged particles slowing down through matter deposit their kinetic energy very locally along their tracks, creating a dramatic rise in temperature and pressure confined within a few nanometers, called thermal spike [108,109]. This causes explosive boiling of the superheated liquid along the particle track. The ability of ionizing radiation to nucleate gas bubbles in superheated liquids was discovered more than seventy years ago, when Donald Glaser invented the bubble chamber [110]. Since then, bubble chambers and superheated drop detectors have been exploited for



Figure 1.4: Charged particle tracks in a liquid hydrogen bubble chamber (John Wood, 1954). ©The Regents of the University of California, Lawrence Berkeley National Laboratory. Image reprinted with permission [107].

¹The Amphora (*Acoustic Markers for Enhanced Remote Sensing of Radiation Doses*) project is funded by a Horizon 2020 FET-Open grant. See also <https://www.amphora-project.eu/>

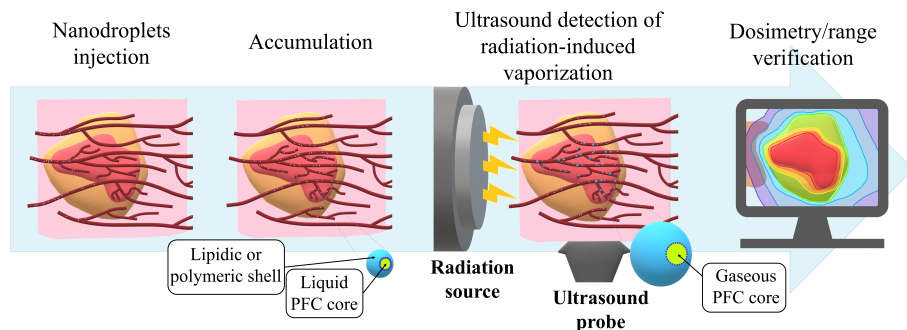


Figure 1.5: Overview of the envisioned workflow for radiotherapy dosimetry or proton range verification using superheated nanodroplets.

radiation detection in space applications [111,112], neutron spectrometry and dosimetry [113,114], dark matter search [115], and medical physics [116,117]. In 1998, the idea of using injectable, superheated droplets for *in vivo* radiation detection was patented by Robert Apfel [118] but, to the best of our knowledge, was never pursued. Intensive research on the development of stable nanodroplet formulations in the past ten years, combined with the fact that their liquid core is typically superheated at physiological temperature, finally brings the concept envisioned by Apfel within reach.

The foreseen clinical implementation of the nanodroplet dosimeter concept is illustrated in figure 1.5. A few minutes before beam delivery, a solution of nanodroplets is injected intravenously to the patient. Nanodroplets could be targeted to preferentially accumulate at the area of interest, *i.e.* the tumor and/or surrounding organs at risk. During radiotherapy or proton therapy delivery, irradiated nanodroplets vaporize into echogenic microbubbles, and this phase-change can be detected using online or offline ultrasound imaging. The number and spatial distribution of vaporization events is then used to determine the delivered dose distribution and/or the proton range. This novel technique has the potential to offer competitive advantages with respect to other *in vivo* dosimetry/proton range verification solutions already established or under development. Real-time volumetric ultrasound imaging of the target, coupled with nanodroplet vaporization detection, would enable intrafractional image guidance with superior soft tissue contrast, in addition to dosimetry/range verification. Furthermore, molecular imaging of the target with targeted nanodroplets could be used for biologically guided radiation therapy (BGRT) strategies [20] and adaptive radiotherapy. As far as proton range verification is concerned, the technological complexity and cost would be reduced compared to PET and PGI, as ultrasound imaging systems are affordable and portable.

Contrarily to ionoacoustics, this method is applicable to continuous proton beams as well as pulsed beams, and is unlikely to suffer from signal to noise ratio limitations, as single bubbles can be detected by ultrasound. The main drawback of using an ultrasound-based approach is its inapplicability to cranial or pulmonary tumours, as an acoustic window is required for ultrasound imaging. However, it could be applicable to breast cancer and tumours in the abdominal and pelvic region, for which range uncertainties are particularly large due to tumour depth and organ mobility [15].

1.4 Research objectives and thesis outline

The research presented in this thesis focuses on the **ultrasound-based detection and quantification of radiation-induced nanodroplet vaporization**, aiming at **monitoring of radiation therapy** delivery. In particular, the specific application of *in vivo* range verification for proton therapy is emphasized.

We first seek to determine the conditions under which nanodroplets can be vaporized by different types of charged particles, and which theoretical or empirical models best describe their vaporization response. To answer those research questions, this work starts with a theoretical and experimental exploration of the mechanisms behind the vaporization of superheated nanodroplets by ionizing radiation. In **Chapter 2**, the thermodynamic and kinetic limits of superheat are presented, together with the semi-empirical theory of radiation-induced vaporization of superheated liquids. Modifications of the existing theoretical framework are introduced to account for specific features of injectable superheated nanodroplets, such as the encapsulation of the superheated liquid in a viscoelastic shell. The feasibility of using superheated nanodroplets for proton range verification is investigated experimentally in **Chapter 3** and **Chapter 4**, using offline ultrasound imaging of aqueous phantoms with dispersed nanodroplets. The influence of the shell composition and the degree of superheat is studied, and the potential for *in vivo* use is demonstrated at the physiological temperature of 37 °C.

The next objective is to determine the most efficient imaging method to record the vaporization response, and to develop techniques to translate the latter into clinically-relevant information on the treatment delivery. Therefore, a transition to online imaging is made, enabling the quantification of single nanodroplet vaporization events using high frame rate active (**Chapter 5**) or passive (**Chapter 6**) ultrasound imaging. This drastically increases the resolution of vaporization maps. By enabling an accurate quantification of the

vaporization response, experimental results can be compared to a statistical model predicting the number and spatial distribution of vaporization events, in **Chapter 7**. In order to anticipate achievable clinical performances, this chapter contains a calibration of the vaporization response and an investigation of the effect of droplet size, concentration, and proton fluence on the vaporization response. Furthermore, it provides theoretical resolution limits for proton range verification in clinically-relevant scenario.

As only an indirect response to proton radiation was observed at physiological temperature, **Chapter 8** explores the potential of actively sensitizing nanodroplets to primary protons at 37 °C by means of an external acoustic field. This principle, called acoustic modulation, enables a high vaporization yield and direct correspondence between the peak of vaporization events and the proton range. After an extension of the application of radiation-induced nanodroplet vaporization to dosimetry of conventional EBRT in **Chapter 9**, the findings presented in this thesis and their impact for short-term and long-term clinical applications are discussed in **Chapter 10**.

Overall, this thesis lays the foundations of the ultrasound-based detection of nanodroplet vaporization by ionizing radiation for therapy monitoring purposes, through a collection of *in vitro* studies. It aims at providing the reader with a detailed understanding of the conditions under which radiation-induced vaporization takes place, the available ultrasound imaging strategies to efficiently detect and quantify those vaporization events, and the potentially achievable performances.

“We can know only that we know nothing. And that is the highest degree of human wisdom.”

Leo Tolstoy

2

Metastable liquids: Limits of superheat and theory of radiation-induced vaporization

*Sophie V. Heymans, Gonzalo Collado-Lara, Yosra Toumia, Bram Carlier,
Hendrik J. Vos, Jan D’hooge, Nico de Jong and Koen Van Den Abeele*

Bubble chambers, superheated drop detectors, and injectable nanodroplets can be used to detect ionizing radiation owing to the formation of bubbles along the track of charged particles. This phenomenon is due to a common property: that of being maintained in a metastable liquid state. In this chapter, we first derive the temperature and pressure limits of this metastable state, with a particular focus on the decafluorobutane liquid, as the latter is used as liquid core for the nanodroplet formulations investigated in this thesis. Then, we present the semi-empirical theory of radiation-induced nucleation, first proposed by Seitz in 1958. Finally, modifications of this theoretical framework are introduced to account for the encapsulation of superheated nanodroplets in a viscoelastic shell.

2.1 Introduction

This thesis investigates the vaporization of injectable nanodroplets by ionizing radiation, aiming at exploiting this phenomenon for ultrasound-based *in vivo* monitoring of radiation therapy. To prepare and complement experimental studies (Chapters 3-9), the problem must be approached from a theoretical point of view. Indeed, a theoretical framework can help to determine the conditions under which radiation-induced vaporization can take place, in order to predict the vaporization response to different types of charged particles. As radiation-induced vaporization requires the liquid to be superheated, we start by introducing important concepts related to superheated states.

Superheating is not a commonly observed phenomenon, and is only reached in certain situations. In the majority of encountered situations, phase-change is initiated preferentially on heterogeneous nucleation sites (impurities, solid container surfaces) rather than in the bulk of the liquid [119,120]. However, in the absence of heterogeneous nucleation sites, the liquid can be heated beyond its boiling temperature (superheat) or depressurized below its saturation pressure (overexpansion) without undergoing phase transition. This is the case when the liquid is encapsulated to form small (sub-millimeter) droplets, as the liquid entirely wets its surrounding phase and is not in contact with any bulk vapor phase [121]. Phase-change contrast agents, also called nanodroplets, have been shown to reach a superheated state. For instance, despite the low boiling point of decafluorobutane (PFB, b.p. $-2\text{ }^{\circ}\text{C}$), PFB nanodroplets have been extensively used for ultrasound imaging applications at (and above) body temperature while remaining in the droplet liquid state [72,122,123]. This exceptional stability is due to the presence of an energy barrier for homogeneous nucleation [119].

In order to initiate nanodroplet vaporization into a microbubble, the homogeneous nucleation barrier must be overcome by supplying energy to the system. This energy may come from a laser, as in Optical Droplet Vaporization [73], or, as demonstrated in this thesis, can be deposited along their track by a charged particle (radiation-induced vaporization) [124]. Moreover, nanodroplets can be vaporized using an acoustic source (Acoustic Droplet Vaporization [71,125,126]), owing to a pressure decrease inside the superheated liquid during the rarefactional phase of the acoustic wave.

In this chapter, we first review the pressure and temperature limits inside which metastable liquids can exist. If these limits are transgressed, the metastable liquid spontaneously vaporizes. For the sake of completeness, we approach the limits of superheat and overexpansion from a thermodynamic point of view, using the equation of state, and from a kinetic point of view, using homogeneous nucleation theory. Next, we present the existing theoretical framework behind

radiation-induced vaporization of superheated liquids. Finally, we extend this theory to superheated nanodroplets by accounting for the encapsulation of the superheated liquid in a viscoelastic shell. The theoretical derivations presented in this chapter are applied to PFB, which is the liquid core used in all nanodroplet formulations investigated in this thesis.

2.2 Thermodynamics and kinetics of superheated liquids

In this section, the limits of superheat are derived using two approaches, one using the thermodynamic equation of states, called *thermodynamic limit of superheat*, and the other from dynamic considerations on the rate of homogeneous nucleation, called *kinetic limit of superheat* [127]. The thermodynamic limit of superheat represents the maximum degree of superheat (or negative pressure) that the liquid can withstand in the metastable state before evaporating, in a situation in which there would be no disturbances or imperfections in the system [128]. In general, the temperatures that can actually be reached by superheated liquids are lower than those predicted by thermodynamics. Therefore, the real limit for homogeneous nucleation in superheated or overexpanded liquids is better represented by the kinetic limit of superheat.

2.2.1 Thermodynamic limits of superheat and overexpansion

Thermodynamic equations of state, the most popular being the van der Waals equation, are used as models to represent real fluids. The suitability of a given equation of state depends on how well it can approximate the real behaviour of the fluid (saturation properties, critical point, etc) [128,129]. Expressed in reduced units, these equations form laws of corresponding states. The reduced pressure, molar volume and temperature are expressed as $P_r = P/P_c$, $v_r = v/v_c$, and $T_r = T/T_c$, respectively, where P_c , v_c , and T_c define the critical point of the substance, which represents the boundary between the region where the liquid and vapor phase can coexist and the region where there is no longer any distinction between the liquid and vapor phase ($P > P_c$, $T > T_c$ and $v_l = v_v$). Above the critical point, the fluid is said to be supercritical [130].

Pressure-volume (p-V) diagrams obtained from the equation of state are useful to represent the superheated state and derive the limits of superheat/overexpansion. In figure 2.1, the p-V diagram is represented in reduced units and an isotherm is drawn for a reduced temperature $T_r = 0.85$ (dashed-dotted blue line). The liquid ($v_r < 1$) and vapor ($v_r > 1$) saturation curves, in dotted red, show the

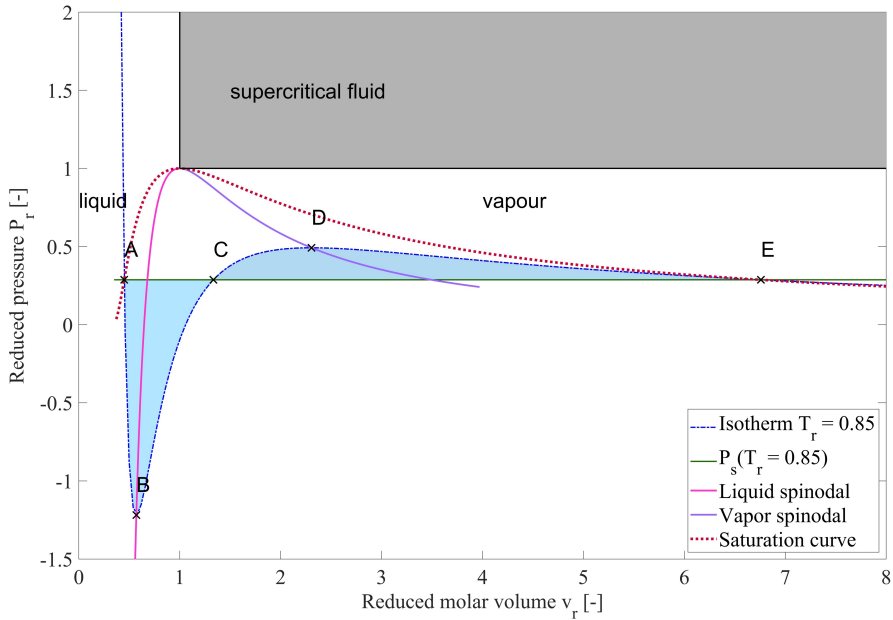


Figure 2.1: Pressure-volume diagram in reduced units for a reduced temperature $T_r = 0.85$. The Maxwell condition imposes that the two shaded areas are equal.

states for which the liquid and vapor phases are at equilibrium, and meet at the critical point. For the considered temperature ($T_r = 0.85$), the intersection of the isotherm with the liquid saturation curve (point A) represents the (P, v) properties of the saturated liquid, and the intersection of the isotherm with the vapor saturation curve (point E) corresponds to the saturated vapor. The liquid and vapor state coexist at the saturation pressure (horizontal green line). As a consequence of liquid-vapor equilibrium, the chemical potentials of the saturated liquid (point A) and saturated vapor (point E) are equal ($\mu_l = \mu_v$, no driving force for mass transfer). This translates in the p-V diagram by the condition that the two areas bounded by the isotherm and the horizontal line corresponding to the saturation pressure are equal: $ABCA = CDEC$ (Maxwell's rule) [127, 131]. Points A and E, and hence the saturation pressure, are found by applying Maxwell's rule (see appendix 2.6). Then, the saturation curve (dotted red) is built by repeating this process for all isotherms.

Classical equilibrium thermodynamics predicts that phase transition from liquid to vapor occurs when the equilibrium saturation conditions are reached, i.e. the liquid reaches points A and vaporizes to point E [127]. However, real fluids

have more complex behaviours and can exist in metastable states, beyond limits predicted by classical equilibrium thermodynamics. The liquid phase boundary can be transgressed in two ways: either the temperature can be increased along a constant pressure path, or the pressure can be reduced at constant temperature [120]. Both situations bring the liquid into a metastable state, called superheat in the former case and that we choose to qualify as overexpansion in the latter. The metastability indicates an unstable equilibrium, as the entropy of the system is at a local maximum rather than an absolute maximum [120]. Therefore, if a sufficiently high perturbation is applied, the system will spontaneously evolve towards stable equilibrium (i.e., the liquid will vaporize) [127].

The criterion for mechanical stability (derived from the condition that the system should be at an entropy maximum) imposes that the fluid lies on the part of the isotherm which has a negative slope [127]. The points where the isotherm slope changes sign (minimum and maximum points, B and D in figure 2.1) therefore represent the maximum deviations from equilibrium conditions under which the system can remain metastable. By connecting the minima of different isotherms, the liquid spinodal line (pink line in figure 2.1) can be constructed. The vapor spinodal line (purple line in figure 2.1) is obtained in the same way, connecting this time the isotherms maxima. Therefore, starting from point A, metastable liquids at temperature $T_r = 0.85$ can withstand negative pressure down to point B (overexpansion), or they can be heated isobarically ($P = P_s(T_r = 0.85)$) until they reach the liquid spinodal (superheat). The spinodal lines represent the absolute limits of superheat or overexpansion [132], also called thermodynamic limit of superheat for the liquid (and supersaturation for the vapor).

Equation of state for the C_4F_{10} liquid

In order to determine the location of the spinodal lines, and therefore the thermodynamic limit of superheat, an equation of state must first be chosen to model the fluid under consideration. A great variety of equation of states have been presented in the literature, such as the van der Waals, Redlich-Kwong, or Berthelot equation of state, to cite a few [133]. The validity of an equation of state to describe a given real fluid can be assessed by comparing the predicted behaviour of the fluid to experimental P , v , T values [134]. The critical compressibility, Z_c , is often used for that purpose [134]:

$$Z_c = \frac{P_c v_c}{R_g T_c}. \quad (2.1)$$

P_c , T_c and v_c are the pressure, temperature and molar volume, respectively, at the critical point, and R_g is the ideal gas constant. Instead of using popular formulations (such as van der Waals), equations of states can also be built from parametric equations, such as the virial equations of state [133] or parametric equations of state in cubic form [127, 132]. The parameter values are in this case determined by applying the critical conditions (see below) and using experimental data such as the critical constants of the fluid (P_c, v_c, T_c) [134], or saturation data [132].

Here, rather than opting for a well-known equation of state, we chose to derive an equation of state specific to PFB, starting from a general parametric equation of state [127]. In reduced units, this parametric equation is given by [127, 135]:

$$P_r = \frac{\gamma T_r}{v_r - b_{r1}} - \frac{a_{r1}}{T_r^\lambda v_r (v_r + b_{r2})} \quad (2.2)$$

The parameters, in reduced units, are γ , λ , a_{r1} , b_{r1} , and b_{r2} . In dimensional units, this family of equations corresponds to the following:

$$P = \frac{R_g T}{v - b_1} - \frac{a_1}{T^\lambda v (v + b_2)} \quad (2.3)$$

with $Z_c = 1/\gamma$, $b_1 = b_{r1} v_c$, $b_2 = b_{r2} v_c$ and $a_1 = a_{r1} P_c v_c^2 T_c^\lambda$. Attributing different values to the parameters in the cubic equation yields well-known equations of state [127]. For instance, the van der Waals equation of state is obtained for $\gamma = 8/3$, $\lambda = 0$, $a_{r1} = 3$, $b_{r1} = 1/3$ and $b_{r2} = 0$.

The equation of state must satisfy the critical conditions, defining the critical point as an horizontal inflection point [134]:

$$P_r = 1 \quad \left(\frac{\partial P_r}{\partial v_r}\right)_{T_c} = 0 \quad \left(\frac{\partial^2 P_r}{\partial v_r^2}\right)_{T_c} = 0 \quad (2.4)$$

These conditions form a system of three equations, which can be used to determine three constants in the parametric equation of state. In order for the equation of state to best fit the real characteristics of a given fluid (here, PFB), other parameters of this generalized equation of state can be chosen to match experimental measurements of thermodynamic properties of the fluid, such as the saturation curve [132]. Here, we chose to determine the three parameters a_r , b_{r1} , and b_{r2} , using the critical conditions, and to optimize the parameters λ and γ by fitting the liquid saturation properties predicted by the thermodynamic equation of state to the known saturation properties, extracted from the NIST database [136], at moderate temperatures. This required to solve the following non linear optimization problem (with the subscript s represents values at

saturation):

$$\min_x \sum_i (\hat{F}(x, T_i) - F_{meas}(T_i))^2$$

$$x = [\lambda \quad \gamma] \quad (2.5)$$

$$F_{meas}(T_i) = [P_{r,s,meas}(T_i) \quad v_{r,s,l,meas}(T_i)] \quad (2.6)$$

$$\hat{F}(T_i) = [\hat{P}_{r,s}(T_i) \quad \hat{v}_{r,s,l}(T_i)] \quad (2.7)$$

It is important to note that by applying the three critical conditions and allowing γ to vary, the critical compressibility condition $Z_c = 1/\gamma$ is no longer fulfilled and the ideal gas constant in equation 2.3 is replaced by $R'_g = \gamma Z_c R_g$ [134]. Alternatively, γ could have been fixed using the experimental value of the critical compressibility for PFB. The Matlab function *lsqcurvefit* [137] was employed to solve this optimization problem, in the range $T_i = 0^\circ\text{C}$ to $T_c/3$. The choice of fitting saturation data away from the critical point was made in order to match closely the liquid boiling temperature and avoid fitting molar volume data close to the critical point, as measurements of the critical molar volume suffer from remarkably larger uncertainties compared to the critical pressure and temperature [138]. The estimation \hat{F} of the saturation properties of the fluid from the reduced equations of state is explained in the appendix (section 2.6). Solving the optimization problem yielded values of $\lambda = 0.93$ and $\gamma = 2.83$, while applying the critical conditions led to $a_{r1} = 3.38$, $b_{r1} = 0.30$ and $b_{r2} = 0.12$. The obtained saturation pressures and molar volumes are compared to experimentally measured values in figure 2.2.

Derivation of the spinodal line and saturation properties from the thermodynamic equation of state

The liquid and vapor spinodal lines can be obtained by differentiating the equation of state, in order to find the extrema of the isotherms in the p-V diagram:

$$\left(\frac{\partial P_r}{\partial v_r}\right)_{T_r} = 0 \quad (2.8)$$

which becomes, for the generic equation of state introduced above [127]:

$$T_{r,sp} = \left[\frac{a_{r1}(2v_r + b_{r2})(v_r - b_{r1})^2}{\gamma v_r^2 (v_r + b_{r2})^2} \right]^{\frac{1}{\lambda+1}} \quad (2.9)$$

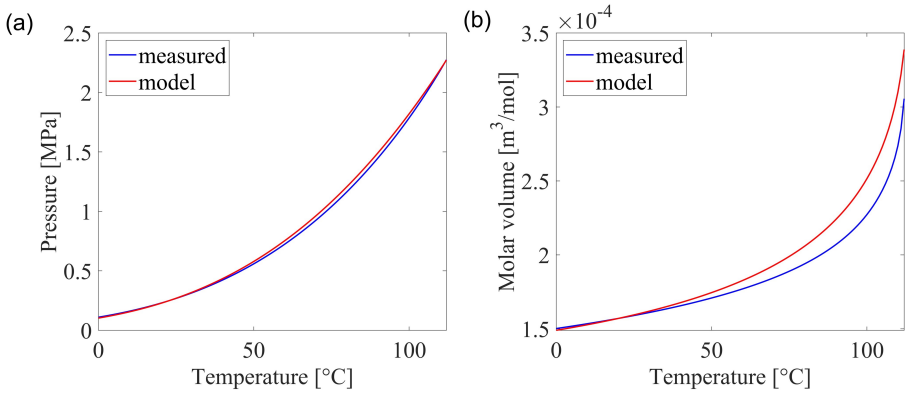


Figure 2.2: Comparison between the C_4F_{10} measured saturation properties and the saturation properties predicted by the optimized equation of state. (a) Saturation pressure as a function of temperature and (b) molar volume as a function of temperature. Curve fitting was implemented for the temperature interval $(0^\circ\text{C}, T_c/3)$.

To determine the saturation lines, the Maxwell condition of equal areas was applied, and we followed the procedure described in [129] (see appendix 2.6).

The p-V diagram (in reduced units) of the optimized equation of state is displayed in figure 2.3, showing both spinodal and saturation curves. As the model was fitted to the saturation curve at relatively low temperatures, discrepancies between the modelled and experimental saturation curves increase for high temperatures. The liquid spinodal line is presented in figure 2.4. Black dashed-dotted lines represent atmospheric pressure and physiological temperature. At atmospheric pressure, the optimized equation of state predicts that the superheat limit is reached for $T_r = 0.92$, which corresponds to 82°C , while the limit of overexpansion at body temperature is $P_r = -2.3$, which is -5.4 MPa.

2.2.2 Kinetic limits of superheat and overexpansion

In this section, starting from the energy required for homogeneous nucleation in the bulk of a superheated liquid, we extract the conditions under which those vapor embryos can spontaneously grow, and derive the rate at which vapor embryos are formed, from which the kinetic limit of superheat can be obtained.

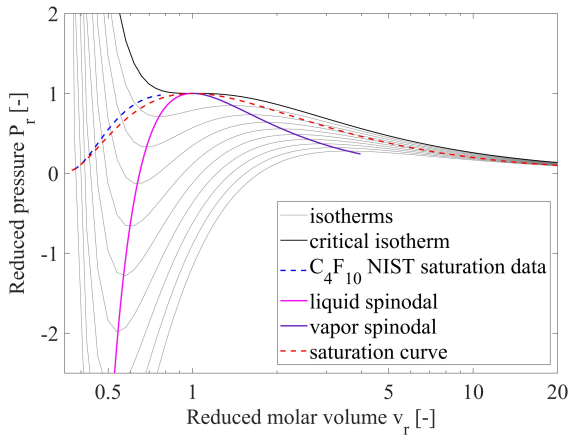


Figure 2.3: Reduced pressure as a function of reduced volume for the optimized thermodynamic model.

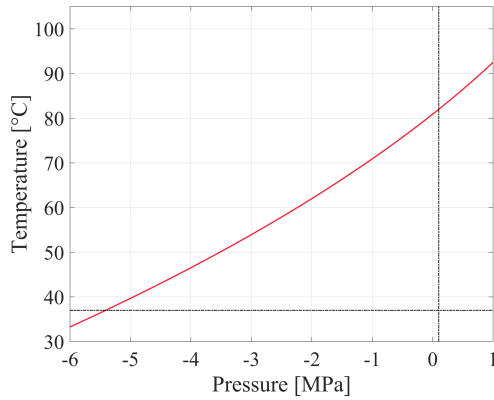


Figure 2.4: Thermodynamic limit of superheat derived from the optimized equation of state.

Homogeneous nucleation and critical radius

We consider a droplet made of superheated liquid which entirely wets its shell. The liquid molecules are constantly in motion and induce local fluctuations of molecular density and energy [127, 128]. These result in the growth and collapse of small vapor embryos within the liquid. In the following, we study the conditions for growth of such a vapor embryo, at constant temperature. The minimum work (i.e., along an isothermal, reversible path) required to form a vapor embryo is given by nucleation theory [121]:

$$W = \sigma 4\pi R^2 - \frac{4}{3}\pi R^3(P_v - P_l) + \frac{4}{3}\pi R^3 \rho_v(\mu_v - \mu_l) \quad (2.10)$$

This is equivalent to the change in Gibbs free energy associated with the formation of a vapor embryo of radius R . P_v and P_l are the pressure in the vapor and liquid phase, respectively, μ_v and μ_l are the vapor and liquid chemical potentials, expressed per unit mass, and σ is the surface tension at the interface between the vapor and liquid phase. When the vapor embryo is in mechanical equilibrium with its surroundings, the pressure in the vapor embryo can be written by the Young-Laplace equation [127]:

$$P_{v,eq} = P_l + \frac{2\sigma}{R_{eq}} \quad (2.11)$$

Moreover, at equilibrium, the chemical potentials are equal [139]:

$$\mu_v = \mu_l \quad (2.12)$$

The energy required to form a vapor embryo at equilibrium is therefore given by:

$$W_{eq} = \frac{4}{3}\pi\sigma R_{eq}^2 = \frac{16\pi\sigma^3}{3(P_{v,eq} - P_l)^2} \quad (2.13)$$

It can be shown that W_{eq} is a local maximum of W [127], which indicates an unstable equilibrium (figure 2.5). As any evolution away from this unstable equilibrium will further reduce the Gibbs free energy of the system (by reducing W), the system will spontaneously evolve towards either the shrinkage of the embryo (for all embryos whose radius $R < R_{eq}$) or its growth leading to homogeneous nucleation of the vapor phase (for all embryos whose radius $R > R_{eq}$). Therefore, W_{eq} represents the energy barrier that must be exceeded for homogeneous nucleation, and R_{eq} is also known as the critical embryo radius. The height of the energy barrier for homogeneous nucleation increases with the surface tension at the interface, and decreases with increasing degree of superheat.

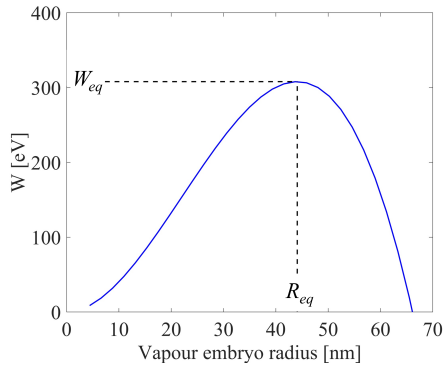


Figure 2.5: Work, or change in Gibbs free energy, required to nucleate a vapor embryo as a function of the embryo radius, for PFB at body temperature. If $R > R_{eq}$, the vapor embryo will spontaneously grow, else, it will shrink.

The expression of W around equilibrium can be simplified by performing a Taylor expansion around $R = R_{eq}$. This leads to the following expression [121]:

$$W \approx \frac{4}{3}\pi\sigma R_{eq}^2 - 4\pi\sigma B(R - R_{eq})^2 \quad (2.14)$$

This simplification requests to assume either mechanical (equation 2.11) or chemical (equation 2.12) equilibrium to approximate W , which is reflected in the value of the factor B . For cavitation, the assumption of chemical equilibrium is more appropriate, as the embryo radius might not rapidly adjust to variations in applied pressure, and B is equal to 1. When mechanical equilibrium is assumed, B is equal to $2/3$ [121,127].

Embryo growth rate

Due to thermal agitation and fluctuations, vapor embryos are continuously being formed and collapsing within the superheated liquid. The limit of superheat will be attained when a small temperature increase or pressure decrease will be enough to nucleate a sufficient number of growing vapor embryos, within an observable time frame [120]. The number of embryos containing n molecules, expressed per unit volume, is related to the work require to create the embryo by the following formula [121,127]:

$$N_n = N_A \frac{\rho l}{M} e^{\frac{W(R)}{k_b T_l}} \quad (2.15)$$

with M the molecular mass of the liquid, N_A Avogadro's number, k_b Boltzmann's constant, and T_l the temperature of the liquid phase. $W(R)$ is the work, or the

change in free energy, required to form the vapor embryo of radius R , given by equation 2.10.

Embryo growth is dictated by evaporation and condensation processes at the liquid-vapor interface. By subtracting the rate of condensation at the interface (from $n+1$ molecules to n) to the rate of vaporization (from n to $n+1$ molecules), one can obtain the net excess rate of growing embryos (going from n to $n+1$ molecules) per unit volume of liquid, J . The complete derivation is available in [127] for the interested reader. The final expression for J is the following:

$$J = N_A \frac{\rho_l}{M} \left(\frac{2\sigma}{\pi MB} \right)^{1/2} e^{\frac{-16\pi\sigma^3}{3k_b T_l (P_v - P_l)^2}} \quad (2.16)$$

Because J is assumed to be independent of n (steady-state condition), J is also the rate at which vapor embryos of critical size are generated [121, 127]. The units of J are $[\text{m}^{-3}\text{s}^{-1}]$. The factor B , which comes from the approximation of $W(R)$ around the equilibrium radius R_{eq} (equation 2.14), should be taken as $2/3$ if mechanical equilibrium is assumed, and equal to 1 for cavitation [121]. Avedisian developed a slightly different expression [140]:

$$J = N_A \frac{\rho_l}{M} \frac{8P_v\sigma}{(P_v - P_l)^2} \left(\frac{2\pi}{MDak_b T_l} \right)^{1/2} e^{\frac{-16\pi\sigma^3}{3k_b T_l (P_v - P_l)^2}}, \quad (2.17)$$

in which Da is the mass of a Dalton in kg. Lienhard suggested to replace the factor $k_b T_l$ inside the exponent by $k_b T_c$, arguing that using the critical temperature would yield more accurate limits of superheat especially for low negative pressures [132, 141].

The pressure inside the vapor bubble embryo P_v can be related to the saturation pressure $P_s(T_l)$ by means of different correction factors, which are relatively equivalent. Carey [127] and Avedisian [142] use the expression (obtained by applying the ideal gas law and the condition of equal chemical potential at equilibrium, equation 2.12):

$$P_v = \eta P_s(T_l) = P_s(T_l) e^{\frac{P_l - P_s(T_l)}{\rho_l R T_l}} \quad (2.18)$$

while Blander [121] and Lienhard [132] use the following Poynting correction [139]:

$$P_v - P_l = \delta(P_s(T_l) - P_l) = \left(1 - \frac{\rho_v}{\rho_l} + \frac{1}{2} \left(\frac{\rho_v}{\rho_l}\right)^2\right) (P_s(T_l) - P_l) \quad (2.19)$$

The nucleation rate is shown in figure 2.6 for two situations: (a) limit of superheat at atmospheric pressure and (b) limit of overexpansion (also called tensile strength) at body temperature. The fluid under consideration is

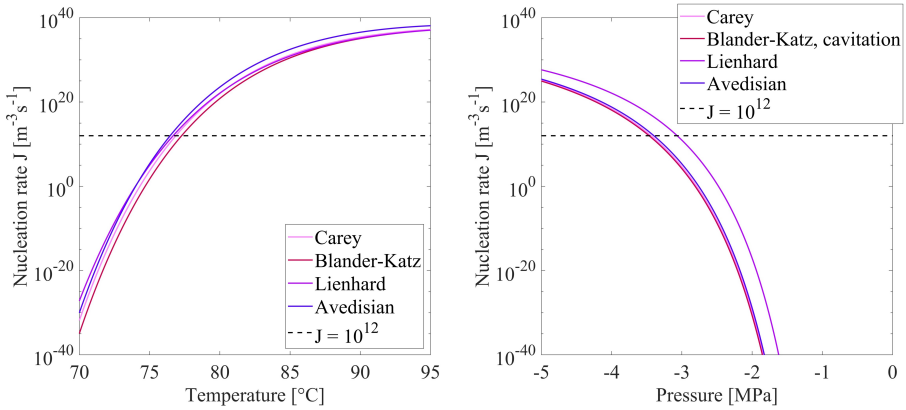


Figure 2.6: (a) Nucleation rate as a function of temperature for the C_4F_{10} liquid at atmospheric pressure. (b) Nucleation rate as a function of negative pressure for the C_4F_{10} liquid at body temperature.

decafluorobutane. The surface tension, as well as the liquid and vapor densities, are evaluated from the saturation properties of the fluid at the liquid temperature T_l [136]. At constant pressure, the nucleation rate varies by several orders of magnitude over a very narrow temperature range. For cavitation, the nucleation rate is a strong function of the negative pressure, therefore we call the negative pressure required to induce homogeneous nucleation the tensile strength of the liquid [121]. The nucleation rate corresponding to the limit of superheat (or tensile strength) is generally taken close to or equal to 10^{12} [bubbles/(m^3s)] [121, 127, 140]. At atmospheric pressure, the different expressions for the limit of superheat agree within 1°C, and yield a predicted temperature for homogeneous nucleation of around 76.5°C, which corresponds to $T = 0.9T_c$. For the tensile strength at body temperature, the models of Carey [127], Blander [121] and Avedisian [142] predict a negative pressure of -3.4 MPa, while the one of Lienhard [132, 141] indicates that homogeneous nucleation might already occur at a negative pressure of -3 MPa.

2.3 Radiation-induced vaporization of superheated liquids

2.3.1 The thermal spike theory

Since the discovery of the vaporization of superheated liquids along the trajectory of charged particles by Glaser in the 1950s [110], numerous researchers have attempted to derive a theoretical framework to describe radiation-induced nucleation [108, 113, 139, 143]. The very local (nm scale) and rapid (femto- to nanoseconds) energy deposition by charged particles makes any experimental validation extremely challenging. To date, radiation-induced nucleation has been modelled using a semi-empirical theory, based on the principle, first proposed by Seitz [108], that radiation energy deposition occurs through the formation of thermal spikes (i.e., the thermal spike theory). The term "thermal spike" refers to the highly localized temperature increase induced by radiation energy deposition along the charged particle track. A charged particle slowing down in matter interacts with the medium and, upon reaching the end of its range, transfers the majority of its remaining energy to secondary electrons, which in turn leads to atomic vibrations and consequently heat [108, 109]. Simulations have estimated the temperature increase to be $>300\text{K}$ in a radius of 1 nm around the ion track [109]. Due to these extremely high temperatures, exceeding the limit of superheat described in section 2.2 by far, the liquid along the charged particle path explodes to form small gas embryos. According to the homogeneous nucleation theory, those embryos will grow if their radius exceeds the critical radius, leading to complete evaporation of the superheated liquid, or shrink otherwise. Therefore, the vaporization condition is dictated by the thermodynamics of homogeneous nucleation, and the total energy W_{tot} required to nucleate a critical radius R_c through radiation-induced nucleation is given by [113, 139]:

$$R_c = \frac{2\sigma}{(P_s - P_l)(1 - \rho_v/\rho_l)} \quad (2.20)$$

$$W_{tot} = \frac{16\pi\sigma^3}{3(P_s - P_l)^2(1 - \rho_v/\rho_l)^2} \times \left[1 + \frac{2\Delta H}{(P_s - P_l)(1 - \rho_v/\rho_l)} - 3\frac{T}{\sigma} \frac{d\sigma}{dT} \right] + W_{irr} \quad (2.21)$$

In these expressions, P_s is the saturation pressure, P_l is the pressure inside the superheated liquid, and ρ_v and ρ_l are the densities of the vapor and liquid phases, respectively. σ is the surface tension of the superheated liquid, not to be

mistaken with the surface tension of the nanodroplet shell (σ_s , not accounted for in this section), and ΔH is the latent vaporization heat of the fluid. The equation for the critical radius, equation 2.20, is identical to equation 2.11 with the first two terms of the correction given by equation 2.19. The first term in equation 2.21 is the work required for isothermal homogeneous nucleation of a critical gas embryo at equilibrium, equivalent to equation 2.13 [113]. The second term represents the work required to vaporize the liquid using the heat generated by the thermal spike, as in radiation-induced nucleation the liquid is maintained below its limit of superheat. The third term is linked to the assumption that vaporization initiation is adiabatic [113, 144], as the time scale for heat transfer is much longer than the time scale at which radiation energy is being deposited. Indeed, gas embryo formation must occur before the heat deposited by the charged particle has been dissipated in the medium. As radiation-induced vaporization occurs far from equilibrium conditions, the energy W_{tot} is 1-1.5 orders of magnitude above W_{eq} [139], as the majority of the energy is spent by vaporization, heat conduction, or irreversible processes (generation of a shock wave, work against viscous forces, etc.) [113]. The last term, W_{irr} is an upper limit approximation for the work lost to viscous forces and to the transfer of kinetic energy of the liquid due to the vapor wall motion and is given by [113, 145]:

$$W_{irr} = 2\pi\rho_l R_c^3 \dot{R}^2 \quad (2.22)$$

$$\dot{R} = \frac{4D(\rho_l/\rho_v)^{1/3}}{R_c} \quad (2.23)$$

$$D = \frac{k}{\rho_l c_p} \quad (2.24)$$

\dot{R} is the vapor wall velocity, while the thermal diffusivity of the liquid, D , is given by the ratio of its thermal conductivity, k , and the product of the liquid density and specific heat c_p .

Both W_{tot} and R_c decrease with increasing degree of superheat, which is the temperature excess above the liquid boiling point, meaning that the more the liquid is superheated, the easier it is to vaporize. In order for the thermal spike energy to lead to nucleation of a critical gas embryo, it must be deposited within a scale comparable to the critical embryo diameter, yielding an effective track length $L_{eff} = aR_c$, where a is the dimensionless nucleation parameter [113, 146, 147]. Therefore, to vaporize a superheated drop, a charged particle of energy $E \geq W_{tot}$ must also satisfy the condition [146]:

$$\left\langle \frac{dE}{dx} \right\rangle_{L_{eff}} \geq \frac{W_{tot}}{aR_c} \quad (2.25)$$

The left-hand side of this expression represents the density of energy deposited by the charged particle per unit length, averaged over L_{eff} . In radiation physics, this quantity is called linear energy transfer (LET). The right-hand side of the nucleation condition decreases with increasing degree of superheat. Consequently, the LET threshold for vaporization is inversely related to the degree of superheat of the liquid.

The radiation-induced nucleation theory has been compared to experimental results of superheated liquid vaporization by various types of charged particles, such as high LET recoil ions generated by e.g. neutrons [148], heavy ions [149,150], alpha particles [151], protons [114,152], and electrons [116,153]. While a relatively good agreement was found between theoretical and experimental LET thresholds, the estimates of the nucleation parameter, a , were found to vary in a wide range, between 2 and 12.96 [146,154]. For high degrees of superheat, the nucleation parameter is close to 2, while it increases for lower degrees of superheat (i.e., higher values of W_{tot}) [154]. Therefore, the relationship between the effective length and the critical radius might be more complex than a direct proportionality [150,154].

Interestingly, when expressed in reduced superheat, defined as

$$s = \frac{T - T_b}{T_c - T_b}, \quad (2.26)$$

the sensitization threshold to different types of charged particles was found to coincide for different halocarbons [113,154]. T_b is the boiling temperature, T the operating temperature and T_c the critical temperature of the liquid. Figure 2.7 shows the LET threshold for vaporization of PFB as a function of reduced superheat, assuming a nucleation parameter $a=2$. Horizontal dotted lines represent the approximate peak LET values reached by oxygen recoil ions, alpha particles, protons, and electrons in water, at their individual Bragg peaks. The corresponding predicted sensitization thresholds, expressed in reduced superheat, are 0.15, 0.31, 0.39 and 0.59, while $s = 0.65$ corresponds to the limit of superheat.

2.3.2 Extension to encapsulated nanodroplets

The radiation-induced nucleation theory introduced in the previous section was developed for bubble chambers, in which a large volume of liquid is transiently brought into a superheated state, and for superheated drop detectors, which consist in uniform dispersions of small (2-1000 μm) drops of superheated liquid in a gel, each drop representing a miniaturized version of the bubble chamber [143,155]. The use of superheated nanodroplets for radiation detection differs

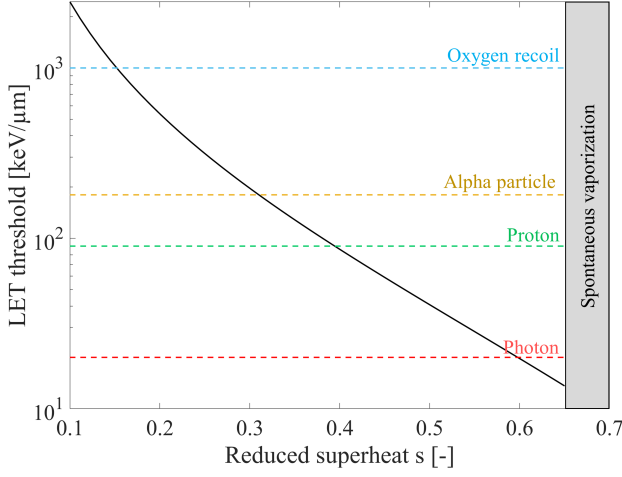


Figure 2.7: LET threshold, given by $W_{tot}/(2R_c)$, as a function of reduced superheat, for the perfluorobutane liquid. The approximate peak LET reached by oxygen recoils, alpha particles, protons, and secondary electrons produced in photon beams is shown.

from those situations, as nanodroplets are encapsulated in a viscoelastic shell, to enhance their *in vivo* stability. When a critical vapor embryo is formed inside a nanodroplet, the resulting displacement of the surrounding liquid also leads to an expansion of the nanodroplet shell, which requires an additional energy input. The importance of this effect is expected to increase as the droplet radius decreases, due to a higher relative change in volume induced by the critical embryo formation. In addition, most experiments reported in this thesis were performed using nanodroplets encapsulated in a viscoelastic matrix. Therefore, we propose to add four terms to the total energy required for radiation-induced nucleation (equation 2.21):

$$W_{tot,enc} = W_{tot} + W_{s,elast} + W_{s,visc} + W_{m,elast} + W_{m,visc} \quad (2.27)$$

The terms $W_{s,elast}$ and $W_{s,visc}$ are related to the elasticity and viscosity of the shell, respectively, while $W_{m,elast}$ and $W_{m,visc}$ are related to the surrounding matrix.

In order to derive theoretical expressions for the first two terms, we integrate the radial stress difference across the shell p_s , due to viscoelastic forces in the shell, for an increase in nanodroplet inner volume from $V = V_{01}$ to $V = V_1$:

$$W_{s,elast} + W_{s,visc} = \int_{V_{01}}^{V_1} p_s dV_1 \quad (2.28)$$

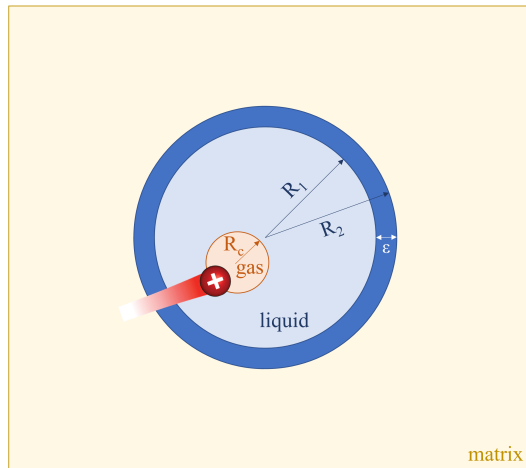


Figure 2.8: Nucleation of a critical embryo by a charged particle, inside a nanodroplet of final inner radius R_1 , outer radius R_2 , and thickness ϵ .

The nanodroplet volume expansion due to the formation of a critical vapor embryo of radius R_c by a charged particle in a nanodroplet of initial inner radius R_{01} (figure 2.8) is given by:

$$V_1 = \frac{4\pi R_1^3}{3} = \frac{4\pi R_{01}^3}{3} + \frac{4\pi R_c^3}{3}. \quad (2.29)$$

The equation above assumes that the initial volume of liquid converted into a critical vapor embryo is negligible compared to the initial droplet volume ($4\pi R_{01}^3/3$). Such an assumption holds as the vapor specific volume is two orders of magnitude higher than that of the liquid phase. The final inner droplet radius, R_1 , can be isolated:

$$R_1 = R_{01} \sqrt[3]{\frac{R_c^3}{R_{01}^3} + 1}. \quad (2.30)$$

The radial stress difference p_s is extracted from microbubble shell models, which have been vastly described in the literature [156,157]. A distinction is made between thick shells (e.g. polymeric shells of thickness ϵ) and thin shells (e.g., an encapsulation by a phospholipidic monolayer, $\epsilon \rightarrow 0$). The Marmottant model [158] was chosen for the latter case, while thick shells have been modelled by the Church model [159].

Thick shell model

Applying equation (11) of [159] for a thick, incompressible shell, and assuming zero initial surface tension, the stress across the shell for a final inner droplet radius R_1 is:

$$p_s(R_1) = 4 \frac{R_2^3 - R_1^3}{R_2^3 R_1} [G_s(R_1 - R_{01}) + \mu_s \dot{R}_1] \quad (2.31)$$

R_2 is the final outer radius of the droplet, G_s is the shear modulus in [Pa], μ_s is the viscosity in [Pa·s], and \dot{R}_1 is the radial speed of the inner wall [m/s]. The velocity at the droplet surface can be derived from the conservation of mass assuming incompressibility, yielding [159, 160]:

$$\dot{R}_1 = \frac{R_c^2}{R_1^2} \dot{R}_c \quad (2.32)$$

We also introduce the shell thickness ϵ :

$$R_2 = R_1 + \epsilon \quad (2.33)$$

Substituting equations 2.32 and 2.33 into 2.31, and integrating using equation 2.28 yields, after applying a Taylor approximation around $R_c^3/R_{01}^3 \rightarrow 0$:

$$W_{s,elast} + W_{s,visc} = \left(\frac{8}{9} \pi G_s \epsilon \frac{R_c^6}{R_{01}^4} + \frac{16}{3} \pi \mu_s \epsilon \dot{R}_c \frac{R_c^5}{R_{01}^4} \right) \left[\frac{3 + 3\epsilon/R_{01} + \epsilon^2/R_{01}^2}{(1 + \epsilon/R_{01})^3} \right] \quad (2.34)$$

Thin shell model

For a thin shell, as $\epsilon \rightarrow 0$, there is no distinction between the inner and outer radius, i.e. $R_1 = R_2 = R$ and $R_{01} = R_{02} = R_0$. Applying the Marmottant model [158], we have:

$$p_s(R) = \frac{2\sigma_s(R)}{R} + 4\kappa_s \frac{\dot{R}}{R^2} \quad (2.35)$$

with σ_s the surface tension of the shell in [N/m] and κ_s the surface dilatational viscosity from the monolayer in [kg/s]. Assuming that the initial surface tension of the droplet $\sigma_s(R_0)$ is equal to 0, and that the shell remains in the elastic regime during expansion, we obtain the following expression for the surface tension:

$$\sigma_s(R) = \chi \left(\frac{R^2}{R_0^2} - 1 \right). \quad (2.36)$$

χ is the elastic compression modulus, in [N/m]. Inserting equations 2.35 and 2.36 into equation 2.28, and using 2.30 to apply a Taylor approximation around $R_c^3/R_0^3 \rightarrow 0$, we obtain the final expression for the work required to expand the droplet shell:

$$W_{s,elast} + W_{s,visc} = \frac{8}{9}\pi\chi\frac{R_c^6}{R_0^4} + \frac{16}{3}\pi\kappa_s\dot{R}_c\frac{R_c^5}{R_0^4} \quad (2.37)$$

In both equations 2.34 and 2.37, the vapor wall velocity, \dot{R}_c , can be derived from equation 2.23, which assumes that the phase change is governed by heat transfer from the surrounding liquid [113].

Nanodroplets immobilized in an aqueous matrix

When a critical embryo is formed within a droplet, the volume increase in the droplet also leads to a deformation of the viscoelastic matrix surrounding the droplet. The work associated with this deformation is again given by equation 2.28, this time integrated over the change in outer shell volume V_2 . Keeping the same assumptions of shell incompressibility, and applying the generalized Hooke's law (linear elasticity) [161] and constitutive equations for a Newtonian fluid yields, for a displacement of the outer shell from R_{02} to R_2 :

$$p(R_2) = \frac{4G_m}{R_2}(R_2 - R_{02}) + 4\mu_m\frac{R_1^2}{R_2^3}\dot{R}_1 \quad (2.38)$$

In this expression, G_m is the shear modulus [Pa] of the viscoelastic matrix, while μ_m represents its shear viscosity in [Pa·s]. Since the shell is incompressible, equation 2.29 also describes the relationship between R_{02} and R_2 . Inserting equation 2.38, 2.29, and 2.32 into equation 2.30 and applying a Taylor approximation around $R_c^3/R_{02}^3 \rightarrow 0$ yields the following expression for the work required to expand the surrounding matrix:

$$W_{m,elas} + W_{m,visc} = \frac{8}{9}\pi G_m\frac{R_c^6}{R_{02}^3} + \frac{16}{3}\pi\mu_m\dot{R}_c\frac{R_c^5}{R_{02}^3} \quad (2.39)$$

Impact on the LET threshold of superheated nanodroplets

Applying the formulas derived above to different nanodroplet formulations requires the knowledge of the shell thickness (for the thick shell model), shear modulus and viscosity. For the **thick shell model**, as viscoelastic shell properties and shell thickness have not been measured on nanodroplets with a polyvinyl alcohol shell (PVA-PFB) used in this thesis, we used shell

parameters measured on air-filled PVA-shelled microbubbles. For the shear modulus, values between 3-10 MPa have been reported in the literature, while reported viscosities are in the range 0.2-0.6 Pa·s [162, 163]. As far as shell thicknesses are concerned, values between 100 and 700 nm have been measured, for microbubble outer diameters in the range 2.5-6 μm [162–164]. Here, we considered a PVA-PFB nanodroplet of 800 nm outer diameter and 70 nm shell thickness, with a shear modulus of 10.5 MPa and viscosity of 0.6 Pa·s. The chosen parameters for the **thin shell model** were $\chi = 2 \text{ N/m}$ and $\kappa_s = 3 \times 10^{-8} \text{ kg/s}$, and are in the range of values reported in the literature for ultrasound contrast agents with a phospholipidic shell [158, 165–169]. For the **aqueous matrix**, we consider gelatin as an example. For concentrations similar to those used in our experiments [124], the shear modulus for gelatin matrices is in the range 2-10 kPa, and the viscosity is 0.6 Pa·s [170].

Figure 2.9 (a) shows the total nucleation energy, W_{tot} , together with individual contributions $W_{s,elast}$, $W_{s,visc}$, both for a thin and thick shell, and $W_{m,elast}$, $W_{m,visc}$ for the surrounding matrix, while figure 2.9 (b) represents the corresponding LET thresholds. For the chosen shell parameters and a nanodroplet outer diameter of 800 nm (which is the mean diameter of PVA-PFB nanodroplets), the increase in nucleation energy and consequently LET threshold due to encapsulation of the superheated liquid in a thick shell is superior to that of a thin shell. In both cases, however, the effect of the encapsulation decreases as the degree of superheat increases. The elastic contribution, $W_{s,elast}$, falls more rapidly with temperature compared to the viscous term. Similar observations can be made for the effect of the surrounding matrix.

For low degrees of superheat, the impact of the shell and the surrounding matrix on the LET threshold is significant (figure 2.9 (b)), and can raise the degree of superheat required for vaporization by high LET particles such as heavy recoil ions. Figure 2.10 (a) shows the separate effects of the nanodroplet shell and the surrounding matrix on the LET threshold at 37 °C, as a function of the nanodroplet outer diameter. For nanodroplet diameters higher than 1 μm , the impact of the shell and of the surrounding matrix are negligible. As the nanodroplet diameter decreases, the LET threshold increases very rapidly. Figure 2.10 (b) illustrates this impact on the sensitization temperature to different types of charged particles, for a nanodroplet encapsulated in a thick shell. The lower the degree of superheat, the higher the nanodroplet diameter at which deviations from the uncoated droplet model start to appear, and the higher the raise in sensitization temperature. This has important implications for experiments performed with polydisperse nanodroplet populations, as depending on the temperature, the smallest droplets might be below the sensitization threshold to a particle type, while only the largest droplets will be vaporizable by this charged particle.

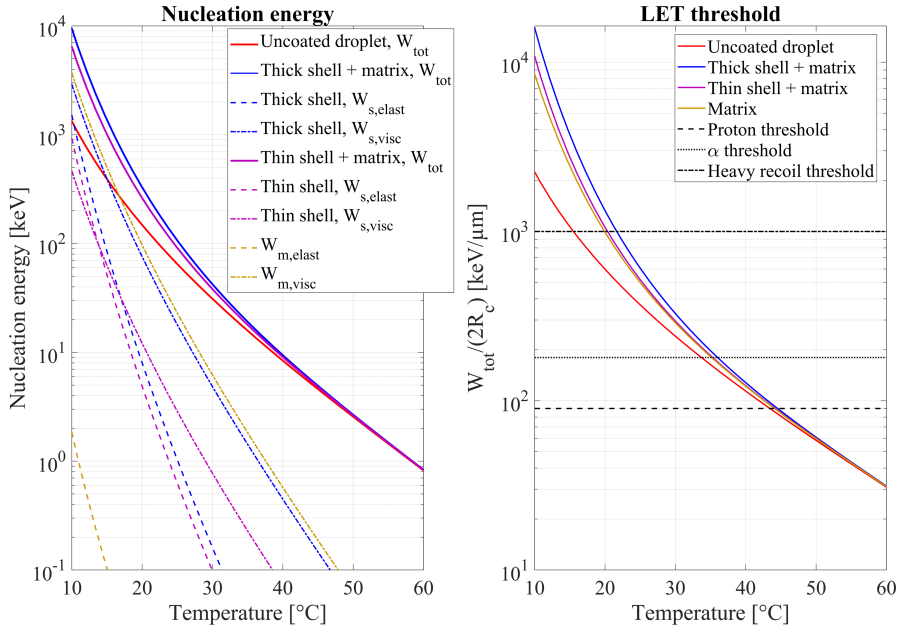


Figure 2.9: (a) Energy required to nucleate a critical embryo, W_{tot} for a naked 800 nm diameter droplet, and corresponding values for a nanodroplet encapsulated in a thin or thick shell. The contributions from the work required to counteract elastic ($W_{s,elast}$) and viscous ($W_{s,visc}$) forces are shown, as well as the work required to stretch the surrounding matrix ($W_{m,elast}$ and $W_{m,visc}$). (b) Corresponding values of the LET threshold as a function of temperature. Horizontal lines are representative LET values for protons, alpha particles, and heavy recoils (such as oxygen). The shell parameters were the following: $R_0 = R_{02} = 400$ nm, $\epsilon = 70$ nm, $G_s = 10.5$ MPa, $\mu_s = 0.6$ Pa·s (thick shell), $\chi = 2$ N/m, $\kappa_s = 3 \times 10^{-8}$ kg/s (thin shell), and the liquid was C_4F_{10} . The shear modulus of the matrix was $G_m = 10$ kPa, and its viscosity was $\mu_m = 0.6$ Pa·s.

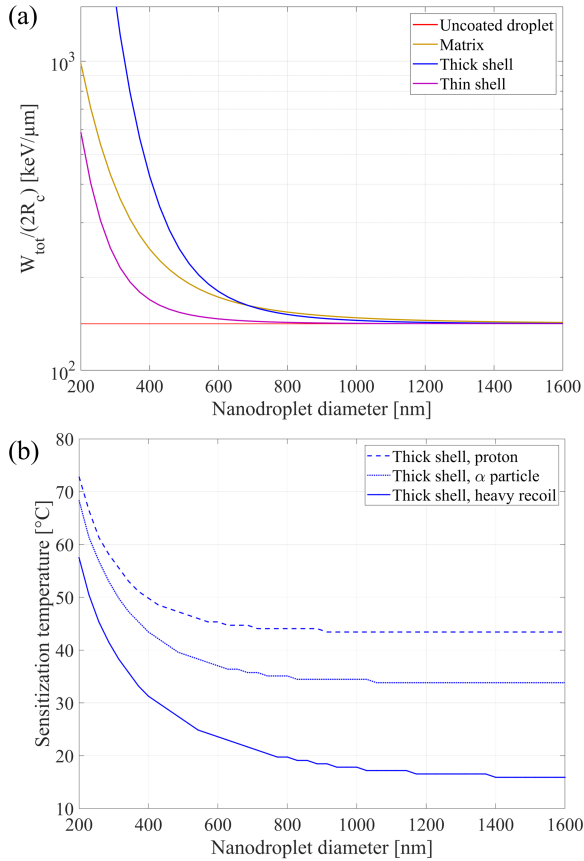


Figure 2.10: (a) Impact of the nanodroplet outer diameter on the LET threshold for vaporization at 37°C , for an uncoated nanodroplet, an uncoated nanodroplet dispersed in a viscoelastic matrix, and a nanodroplet encapsulated in a thick or thin shell (no matrix). (b) Impact of the nanodroplet outer diameter on the sensitization temperature to different charged particles, for a nanodroplet encapsulated in a thick shell. The liquid core is perfluorobutane and shell parameters are the same as in figure 2.9.

2.4 Discussion

2.4.1 Thermodynamic and kinetic limits of superheat

In this chapter, the theoretical thermodynamic and kinetic limits of superheat and overexpansion were derived for the decafluorobutane liquid. The former was obtained by determining the liquid spinodal line using a parametric equation of state optimized to fit the saturation curve of PFB at low temperatures, while the latter was established from the nucleation rate of embryos of critical size. The thermodynamic limit of superheat predicted a spontaneous vaporization temperature of 82 °C at atmospheric pressure, and a tensile strength of -5.4 MPa at body temperature. In contrast, the spontaneous vaporization temperature predicted by kinetics was 76.5 °C while the predicted tensile strength was between -3 and -3.5 MPa.

The limit of superheat at atmospheric pressure was measured by Dr. Yosra Toumia at the University of Rome Tor Vergata using Differential Scanning Calorimetry on PFB nanodroplets encapsulated in a PVA shell (800 nm mean diameter). Vaporization was initiated at 76 °C and peaked at 78 °C (private communication). This is in excellent agreement with the kinetic limit of superheat derived above. Mountford [119] reported a spontaneous vaporization temperature of 74 °C for PFB nanodroplets (800 nm mean diameter) coated with a lipidic shell. The difference in reported temperature could be explained by a combination of the effect of the lower atmospheric pressure in Boulder, CO (83.8 kPa) and an increased resistance against vaporization attributed to the thick PVA shell, in comparison to a lipid monolayer.

The tensile strength, or limit of overexpansion, can be estimated by applying an acoustic field of increasing intensity on superheated drops until vaporization is observed [120]. During the rarefactional phase of the acoustic wave, the pressure in the superheated liquid drops to $P_l = P_0 - P_{ac}$. However, homogeneous nucleation theory does not account for the dynamic effects of a pressure field as it assumes a constant liquid pressure. Therefore, the nucleation threshold measured by means of an acoustic field is better characterized as the acoustic cavitation threshold [171], or for nanodroplets, the threshold for acoustic droplet vaporization (ADV). Since vapor embryos may grow during the rarefactional phase only to collapse in the subsequent compressional phase, the acoustic cavitation threshold may exceed the true tensile strength of the liquid, assuming static pressure conditions [171]. To leave enough time for vapor cavities to grow, low acoustic frequencies, such as 50 kHz, are preferred and give a good agreement with theoretical predictions [120].

For nanodroplets, the ADV threshold is generally measured at frequencies

relevant for ultrasound imaging, in the MHz range. Within this frequency range, other effects come into play such as superharmonic focusing [172] and resonance [173]. Therefore, ADV thresholds cannot be directly compared to theoretical limits of overexpansion. A recent study reviewed the ADV thresholds reported in the literature, showing large variations in reported thresholds for PFB at physiological temperature (from -1.2 to -3.8 MPa), which is not surprising as the ADV threshold depends on many parameters, such as the ultrasound frequency, pulse length, nanodroplet size and concentration [126].

When comparing experimental to theoretical limits of superheat, the kinetic approach yields predictions closer to experimental values, while the thermodynamic limit appears to overestimate the spontaneous vaporization temperature and the tensile strength. The model accuracy was shown to be limited, as it led to a mismatch between the real compressibility factor at the critical point ($Z_c = 0.29$) and the one predicted by the optimized thermodynamic equation of state ($Z_c = 1/\gamma = 0.35$). To improve the model accuracy, more complex equations of state can be sought, such as the Soave modification to the Redlich-Kwong equation of state [174], which introduced a more elaborate temperature dependence relying on the acentric factor, ω . Indeed, fluids made of nonspherical molecules, with a non-zero acentric factor, will not be accurately represented by an equation of state of the Redlich-Kwong type [174, 175]. For PFB, the acentric factor is 0.371 [175]. Alternatively, the van der Waals equations of state can be generalised by including the influence of the molecular shape on the spinodal lines [135]. However, reviewing the vast literature surrounding the thermodynamic equations of state is outside the scope of this work.

The encapsulation of nanodroplets in a viscoelastic shell might further enhance their resistance against spontaneous vaporization, as (i) the viscoelastic shell offers an increased resistance against vaporization (section 2.3.2) and (ii) the pressure inside the nanodroplet core could be increased by the Laplace pressure [119]. While the former effect was shown to be negligible at high degrees of superheat, the latter might lead to an increase of the limit of superheat. As an example, for a shell surface tension value of $\sigma_s = 0.02$ N/m, a nanodroplet of 600 nm diameter would have an elevated inner pressure of $P_l = P_0 + 2\sigma_s/R = 235$ kPa. However, multiple reasons point towards a relatively low contribution of the Laplace pressure. First, the good agreement between predicted and measured (both on polymeric and lipidic droplets) spontaneous vaporization temperatures at ambient pressure indicates that the effect of the Laplace pressure does not significantly affect the vaporization temperature. Second, nanodroplets under significant Laplace pressure are expected to dissolve within a few minutes [119], while the PVA nanodroplets exhibited long term stability (shelf life of several days). Therefore, we hypothesize that the nanodroplet surface tension is negligible, and therefore, so is the internal pressure elevation

due to the Laplace pressure.

2.4.2 The thermal spike theory extended to encapsulated nanodroplets

This chapter also presented an overview of the semi-empirical radiation-induced nucleation theory, which postulates that the vaporization of the superheated liquid is induced by highly localized temperature spikes along the track of charged particles. Applied to PFB at atmospheric pressure, this theory predicts sensitization temperatures of $\sim 15^\circ\text{C}$ for heavy ions, $\sim 33^\circ\text{C}$ for alpha particles, $\sim 43^\circ\text{C}$ for protons, and $\sim 63\text{-}67^\circ\text{C}$ for electrons.

As the thermal spike theory only considers the bulk of the superheated liquid, and does not account for its encapsulation in a viscoelastic shell, we added two terms to the total energy required for radiation-induced nucleation of a critical embryo (equation 2.21) to account for the work required to expand the nanodroplet viscoelastic shell. We considered both the effect of encapsulation in a thick (e.g. polymeric) shell and in a thin (e.g. lipid monolayer) shell. Moreover, as nanodroplets were often encapsulated in an aqueous gel for *in vitro* experiments reported in this thesis, additional terms were included to account for the expansion of the surrounding matrix as well, assuming it behaves as a viscoelastic solid.

To quantify the potential impact of the shell and surrounding matrix on the LET threshold for vaporization, we used shell parameter values found in the literature (both for PVA microbubbles and phospholipidic microbubbles), and considered nanodroplets embedded in gelatin. Both the nanodroplet shell and matrix effects were found to decrease with increasing degree of superheat (figure 2.9). This is due to the fact that as the degree of superheat decreases, the critical embryo radius R_c increases, and therefore the nucleation of a critical vapor embryo induces a larger deformation of the nanodroplet shell and surrounding matrix. As the elastic contribution was proportional to R_c^6 while the viscous contribution was proportional to R_c^4 (\dot{R}_c is inversely proportional to R_c , equation 2.23), the elastic contribution decreased faster with increasing degree of superheat. With the assumed parameters, the shell and matrix contribution can increase the LET threshold by up to 1 order of magnitude at low degree of superheat ($T=10^\circ\text{C}$), while the effect at high degree of superheat ($T>40^\circ\text{C}$) is negligible. The effect on the LET threshold is expected to increase linearly with the shell elasticity, viscosity and thickness, and with the matrix elasticity and viscosity. The nanodroplet diameter also has a large impact on the LET threshold, as shown in figure 2.10. Both the shell and matrix contribution to the LET threshold drastically increase with decreasing droplet diameter. Indeed, the relative

volume increase due to the nucleation of a critical embryo is inversely related to the nanodroplet size. The LET threshold increase translates into higher sensitization temperatures to different types of charged particles for smaller nanodroplets, especially at low degrees of superheat.

The presented theoretical model suffered from some limitations. Variations of elastic and viscous parameters were not accounted for, but might affect the relative impact of the shell and matrix at different degrees of superheat. Moreover, both the nanodroplet shell and matrix were assumed to behave as linear viscoelastic solids. Experimental evidence suggests that the behaviour of encapsulated ultrasound contrast agents would be better predicted by more complex models [156, 157]. Similarly, not all aqueous matrices used in this thesis can be described by linear viscoelastic models (for instance, gels made of Carbopol, used in Chapters 5, 6, 7 and 9, behave as non-Newtonian fluids). Importantly, the effect of the initial surface tension of the shell was neglected. The surface tension can potentially impact both the critical radius (by raising the pressure inside the nanodroplet liquid core) and the nucleation energy. As the Laplace pressure is inversely proportional to the droplet radius, this effect is expected to increase for small nanodroplets. However, we expect the initial surface tension of nanodroplets used in this thesis to be negligible, for reasons already exposed above. Nevertheless, this assumption should be ideally validated by measuring the nanodroplet initial surface tension.

While the importance of the effect of the surrounding matrix for *in vivo* applications is limited, the increase in LET threshold due to the nanodroplet shell should be validated as it has important implications for clinical applications. On the one hand, small nanodroplets (diameter $< 1 \mu\text{m}$) might be desirable for *in vivo* use, in order to enable nanodroplet extravasation and to avoid vessel occlusion by large microbubbles. On the other hand, a decrease in nanodroplet diameter is associated with an increase in LET threshold, which affects the vaporization efficiency as only part of the nanodroplet population might be sensitive to a given charged particle. Therefore, the optimal nanodroplet size distribution for *in vivo* applications might be the result of a compromise between extravasation potential and radiation sensitivity.

Therefore, the shell models developed in this chapter should be experimentally validated in future studies. To that aim, viscoelastic shell properties should be estimated from measurements on the considered nanodroplet formulations. However, measuring such properties on nanodroplets is difficult, as shell parameters are usually estimated from acoustic or optical measurements performed on oscillating microbubbles. As there is no guarantee that the shell retains its viscoelastic properties, let alone its integrity, upon vaporization, shell parameters should be characterized using alternative techniques [176–180]. Once the shell parameters are known, the models could be validated by measuring

the radiation-induced vaporization threshold at low degrees of superheat, where the impact of the shell is expected to be the highest. This could be done by irradiating PFB nanodroplets with neutrons, carbon ions, or even protons (looking only at the radiation response from high-LET secondary particles), while increasing the temperature in the range 15-25 °C, in order to determine the sensitization temperature. To validate the impact of the nanodroplet radius on the LET threshold, the sensitization temperature of size-sorted nanodroplet populations with different mean radii should be compared.

2.5 Conclusion

This chapter introduced the theory of metastable superheated liquid, with a particular focus on radiation-induced vaporization of encapsulated nanodroplets. The thermodynamic and kinetic limits of superheat were derived and compared to the measured spontaneous vaporization temperature of PFB nanodroplets, showing a good agreement with the kinetic limit and an overestimation by the thermodynamic limit. The thermal spike theory developed for bubble chambers and superheated drop detectors was extended to encapsulated nanodroplets. As a result of the encapsulation, the LET threshold was predicted to increase by up to one order of magnitude at low degrees of superheat, particularly for nanodroplet diameters below 800 nm.

2.6 Appendix: derivation of the saturation pressure from the generic equation of state

The saturation pressure was determined from the equations of state using the procedure developed in [129] for van der Waals fluids. This technique employs the Maxwell condition of equal areas (see section 2.2.1). The procedure consists in the following steps, applied to each isotherm:

1. For the considered isotherm, obtain the two volumes at the isotherm minimum (liquid spinodal) $v_{r,sp,l}$ and at the isotherm maximum (vapor spinodal) $v_{r,sp,v}$ by solving equation 2.8 for v .
2. Find the pressure $P_r(v_{r,sp,v})$ corresponding to the vapor spinodal point (isotherm maximum) by using the equation of state 2.2, then obtain the corresponding reduced volume in the liquid phase $v_{r,l}(P_r(v_{r,sp,v}))$ by solving the equation of state for v .

3. Determine the liquid and vapor reduced volumes corresponding to saturation ($v_{r,s,l}$ and $v_{r,s,v}$) by solving the following system of equation:

$$P_r(T_r, v_{r,l}) = P_r(T_r, v_{r,v}) \quad (2.40)$$

$$\int_{v_{r,l}}^{v_{r,v}} (P_r(T_r, v) - P_r(T_r, v_{r,l}))dv = 0 \quad (2.41)$$

The first equation implies that at saturation, both the liquid and vapor phase in equilibrium have the same pressure (i.e. the saturation pressure), and the second equation is Maxwell's rule of equal areas (which stems from the condition of equal chemical potential in the liquid and vapor phase). The starting points are chosen such as $v_{r,start,l} = v_{r,l}(P_r(v_{r,sp,v}))$ (obtained in the step 2) and $v_{r,start,v} = 1.1v_{r,sp,v}$ (obtained in step 1). The *fsolve* Matlab function was employed.

4. The corresponding saturation pressure $P_{r,s}(T_r)$ is found using the equation of state 2.2 with either the liquid or vapor saturation volume obtained in the step 3.

Examples of saturation pressures for different reduced temperatures are presented in figure 2.11. Once saturation pressure and liquid and vapor molar volumes are found for all temperatures, those points can be linked to form the saturation curves presented in figure 2.3.

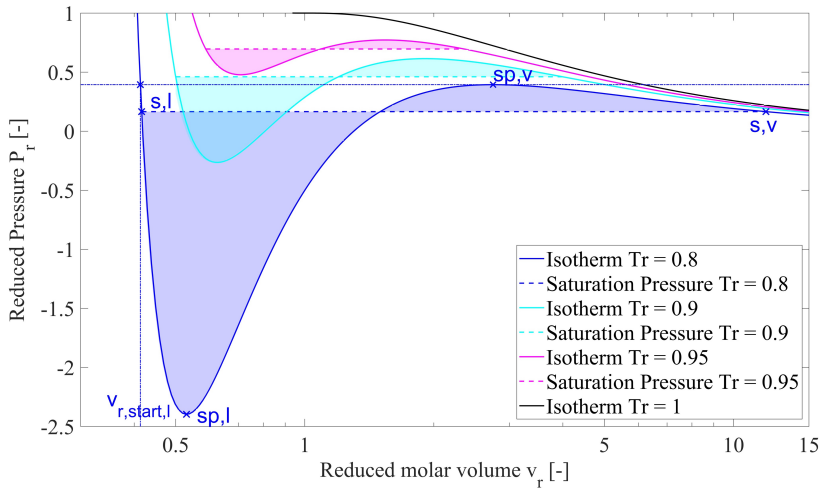


Figure 2.11: Isotherms and saturation pressures satisfying Maxwell’s rule for different reduced temperatures. For $T_r = 0.8$, the technique to obtain the saturation pressure is depicted: from the vapor spinodal point, the corresponding liquid reduced volume is found and used as starting point ($v_{r,start,l}$) of the optimizer.

“Optimism is the faith that leads to achievement.
Nothing can be done without hope and
confidence.”

Helen Keller

3

Proton range verification with ultrasound imaging using injectable radiation sensitive nanodroplets: a feasibility study

*Sophie V. Heymans**, *Bram Carlier**, *Sjoerd Nooijens*, *Yosra Toumia*, *Marcus Ingram*, *Gaio Paradossi*, *Emiliano d’Agostino*, *Uwe Himmelreich*, *Jan D’hooge*, *Koen Van Den Abeele*, and *Edmond Sterpin*

Published in *Physics in Medicine and Biology*, 65(2020) 065013.

Technologies enabling *in vivo* range verification during proton therapy are actively sought as a means to reduce the clinical safety margins currently adopted to avoid tumor underdosage. In this contribution, we applied the semi-empirical theory of radiation-induced vaporization of superheated liquids to coated nanodroplets. Nanodroplets are injectable phase-change contrast agents that can vaporize into highly echogenic microbubbles to provide contrast in ultrasound images. We exposed nanodroplet dispersions in aqueous phantoms to monoenergetic proton beams of varying energies and doses. Ultrasound imaging

*joint first author

of the phantoms revealed that radiation-induced droplet vaporization occurred in regions proximal to the proton Bragg peak. A statistically significant increase in contrast was observed in irradiated regions for doses as low as 2 Gy and found to be proportional to the proton fluence. The absence of enhanced response in the vicinity of the Bragg peak, combined with theoretical considerations, suggest that droplet vaporization is induced by high linear energy transfer (LET) recoil ions produced by nuclear reactions with incoming protons. Vaporization profiles were compared to non-elastic cross sections and LET characteristics of oxygen recoils. Shifts between the ultrasound image contrast drop and the expected proton range showed a sub-millimeter reproducibility. These early findings confirm the potential of superheated nanodroplets as a novel tool for proton range verification.

3.1 Introduction

The increasingly growing fleet of proton therapy facilities, owing to substantial cost reduction and compactness improvements over the past ten years, has contributed in making proton therapy accessible to a variety of clinical indications [6]. The favorable depth-dose distribution of protons implies that excellent dose conformality and therefore healthy tissue sparing could be achieved. However, taking full advantage of the physical selectivity of protons, e.g. to preserve organs-at-risk, is hampered by uncertainties in their *in vivo* range, which arise from inaccuracies of the stopping power calculation from computed tomography (CT) scans, imaging artifacts, setup errors, patient motion and anatomical changes throughout the treatment [30,181]. Additionally, to avoid tumor underdosage due to these range uncertainties, considerable safety margins (up to several millimeters), conservative planning strategies (sub-optimal choice of beam angles), or a substantial value of the range uncertainty parameter used in robust optimizers (around 3%) have been adopted in most proton therapy facilities [30]. In order to reduce these margins and gather more insight into the influence of different factors on the range, an urgent need for accurate *in vivo* range verification techniques exists.

Several methods for *in vivo* range verification have been proposed, however, none of them are routinely employed in the clinic. The most investigated technology relies on positron emission tomography (PET) imaging of positron-emitting isotopes activated by proton nuclear interactions [30]. The measured activity distribution is correlated with the actual proton range through Monte Carlo simulations. PET imaging can be performed offline [182], in-room [33] or in-beam [35,183]. While in-room and in-beam acquisitions benefit from shorter scan times and higher resolution compared to offline PET imaging,

they require bespoke detectors and may affect the throughput in the treatment room [15]. Alternatively, prompt gamma imaging (PGI) makes use of gamma rays emitted by nuclei excited by the incoming proton beam for real-time range verification [37, 184]. PGI has been recently tested to assess range shifts in a patient with brain cancer and demonstrated a shift retrieval precision of 2 mm [39], but its translation towards clinical applications is hampered by technological limitations and detector cost [181, 185]. Range probe (1D) and proton radiography (2D/3D) require high energy protons completely traversing the body in the low-dose plateau [181, 186, 187]. The stopping power of the body tracks is then determined from the residual ranges of the transmitted protons. However, typical proton energies used cannot ensure the beam traverses the patient at all beam angles, especially in the abdomen [15].

Detection of ionizing radiation by means of the vaporization of superheated droplets, i.e. metastable droplets operated at a temperature above their boiling point, was achieved in the 1950s by Donald Glaser [110]. Since then, the use of superheated emulsions significantly expanded to different fields such as space applications, medical physics, neutron dosimetry or dark matter search [155]. These detectors typically feature superheated drops of dimensions ranging from tens to thousands of microns, embedded in a compliant polymeric or aqueous matrix [113]. Upon exposure to radiation, the drops vaporize into bubbles which can be detected either by visual inspection, volumetric measurement or acoustic readout [113, 188]. Two decades ago, Apfel envisioned the use of injectable superheated emulsions as *in vivo* dosimeter [118], but to our knowledge, the idea has never been pursued.

Over the past ten years, nanodroplets, or phase-change contrast agents (PCCAs), have become increasingly popular as versatile contrast agents for ultrasound imaging and therapy [65]. They consist of a perfluorocarbon liquid core surrounded by a stabilizing lipidic or polymeric shell, whose diameter typically ranges from hundreds of nanometers to a few microns [66]. Nanodroplets can be injected intravenously and circulate inside the patient's vasculature, where the smallest sizes (< 200 nm) are able to extravasate. Additionally, the shell can be functionalized to target tissues of interest, making them suitable for molecular imaging and targeted therapy [189]. Localized nanodroplet vaporization can be achieved with ultrasound waves at moderate to high intensities [71, 72] or through laser heating [73], yielding micrometer-sized echogenic bubbles readily imaged with Contrast Enhanced Ultrasound Imaging (CEUS). In order to minimize potential tissue damage from cavitation or heating, droplet vaporization should be achieved with moderate levels of acoustic or thermal energy [190]. Therefore, the droplet liquid core is generally designed to be in a metastable superheated state.

Here, the applicability of the radiation-induced nucleation theory to submicron-sized superheated droplets is evaluated. Specifically, we upgraded the naked superheated emulsions used in dosimetry into injectable nanodroplets similar to the ones employed for CEUS. First, we give a brief overview of the generally accepted theory of superheated droplet vaporization induced by ionizing radiation. Then, we demonstrate the existence of a radiation response and assess the suitability of these radiation sensors for proton range verification. To this aim, tissue-mimicking phantoms with entrapped nanodroplets were irradiated with varying proton energies and the relationship between the resulting ultrasound signals and the predicted proton range was investigated. Finally, the potential dose sensitivity was examined and the feasibility of the presented approach at clinically-relevant doses is shown.

3.2 Materials and methods

3.2.1 Theory of nucleation induced by ionizing radiation

The nucleation of bubbles along particle tracks in a metastable liquid is a complex physics problem involving time and length scales spanning several orders of magnitude and different fields such as thermodynamics and radiation physics, for which a complete analytical description is still lacking. The most widely accepted semi-empirical model combines the thermal spike theory developed by Seitz [108] with the isothermal spontaneous nucleation thermodynamics. In Seitz's theory, the kinetic energy of charged particles is transferred to the medium by a multitude of highly localized temperature spikes forming along their track [143,147]. The thermal spikes occur within a time scale so small compared to thermal diffusion that the liquid explodes into vapor embryos [113,188] along the particle track. These vapor embryos then combine and form spherical bubbles, which can grow indefinitely provided that the initial bubble size exceeds a critical radius, determined from the thermodynamics of phase equilibrium,

$$R_c = \frac{2\sigma}{(P_s - P_l)(1 - \rho_v/\rho_l)} \quad (3.1)$$

where σ is the surface tension of the superheated liquid, P_s is the saturation pressure, P_l is the pressure inside the superheated liquid drop, and ρ_v and ρ_l are the densities of the vapor and liquid phases, respectively. The energy required to nucleate a critical vapor bubble is obtained from homogeneous nucleation

theory, with additional terms specific to radiation-induced nucleation [113].

$$W_{tot} = \frac{16\pi\sigma^3}{3(P_s - P_l)^2(1 - \rho_v/\rho_l)^2} \times \left[1 + \frac{2\Delta H}{(P_s - P_l)(1 - \rho_v/\rho_l)} - 3\frac{T}{\sigma} \frac{d\sigma}{dT} \right] + W_{irr} \quad (3.2)$$

$$W_{irr} = 2\pi\rho_l R_c^3 \dot{R}^2 \quad (3.3)$$

$$\dot{R} = \frac{4D(\rho_l/\rho_v)^{1/3}}{R_c} \quad (3.4)$$

$$D = \frac{k}{\rho_l c_p} \quad (3.5)$$

where ΔH is the latent vaporization heat of the fluid, and W_{irr} accounts for the irreversible energy losses from the action of viscous forces and the transfer of kinetic energy to the surrounding liquid [113]. \dot{R} is the vapor wall velocity, D is the thermal diffusivity of the liquid, and k and c_p are its thermal conductivity and specific heat, respectively.

In order to nucleate a vapor bubble of dimensions larger than the critical radius, the energy deposited by the charged particle along an effective path length (L_{eff}) must exceed W_{tot} [154]. The effective path length is often assumed proportional to the critical radius, yielding $L_{eff} = aR_c$. However, a single value of the proportionality constant (a), also called nucleation parameter, is insufficient to describe the behavior of superheated drop detectors for all degrees of superheat [154]. Moreover, the linear relationship between the effective length and the critical radius remains questionable [150]. Nevertheless, most authors assume a constant value of the nucleation parameter that typically ranges from 2 to 13 [146].

The energy transferred by a charged particle per unit track length in a medium is given by its linear energy transfer (LET) [15]. The nucleation condition is given by:

$$\int_0^{L_{eff}} \frac{dE}{dx} dx \geq W_{tot} \quad (3.6)$$

and can be further expressed in terms of track-averaged LET [146]:

$$\left\langle \frac{dE}{dx} \right\rangle_{L_{eff}} \geq \frac{W_{tot}}{aR_c} \quad (3.7)$$

The left hand side of the equation is only dependent on the energy deposition characteristics of the radiation, while the right hand side obeys

the thermodynamic properties of the superheated fluid. Since the nucleation energy drops when the superheat increases, the LET threshold of superheated drop detectors is inversely proportional to the degree of superheat.

The "reduced superheat" parameter is commonly used to describe the operating point of a superheated liquid with respect to the temperature boundaries of the superheated state [154], and is defined as:

$$s = \frac{T - T_b}{T_c - T_b} \quad (3.8)$$

T_b is the boiling temperature at atmospheric pressure, and T_c is the critical temperature of the fluid above which the liquid phase can no longer exist. By appropriately tuning the degree of superheat of the liquid core, one can tailor the droplet sensitivity to different types of radiation. Typically, neutron dosimeters operate at $s = 0.2$, as the droplets are vaporized by high-LET secondary charged particles produced by nuclear reactions [113]. To sensitize bubble detectors to low-LET radiation such as photons and protons, higher degrees of superheat are required, which comes at the cost of decreased droplet stability. The practical limit of superheat is reached for $s = 0.65$, when the metastable liquid spontaneously vaporizes [153, 191]. Detection of proton radiation in the vicinity of the Bragg peak with superheated drops was reported by several groups [114, 149, 152], indicating that the threshold for proton detection lies between $s = 0.35$ and $s = 0.42$, corresponding to an LET threshold of 70-90 keV/ μm , typically reached by protons at the end of their range. Proton irradiation of bubble detectors with lower degrees of superheat revealed that high-LET nuclear reaction products (heavy recoils) induce uniform vaporization tracks [111, 148, 149, 192].

3.2.2 Nanodroplet synthesis and characterization

Nanodroplet composition and synthesis

The nanodroplets employed in this study are comprised of a perfluorobutane (C_4F_{10} , boiling point of -2°C) liquid core encapsulated by a polymerizable fatty acid monolayer of 10,12-pentacosadiynoic acid (PCDA). The complete nanodroplet synthesis is described elsewhere [72] and can be performed with standard laboratory equipment. Moreover, feasibility of production was observed to be reproducible and laboratory-independent, as nanodroplets were initially developed in the University of Rome Tor Vergata, and subsequently prepared in the KU Leuven campus KULAK. In brief, decafluorobutane was fluxed for a few seconds into an empty glass vial sealed with a rubber septum and immersed in liquid nitrogen to ensure liquefaction. Afterwards, injection of 6 ml of PCDA

aqueous suspension (1 mM) in the vial, followed by a 10-minute sonication in an ice-cold ultrasound bath, yielded a milky suspension of nanodroplets. Non-encapsulated decafluorobutane vaporized during sonication, filling the headspace of the glass vial. After addition of surfactant (Pluronic F127) and photoinitiator solutions (Irgacure 2959), nanodroplets were exposed to 352 nm UV-light (UV lamp model ENF-260C, Spectroline Corporation, Westbury, NY) for 30 minutes, to polymerize the PCDA shell through the diacetylene moieties, resulting in formation of a blue color and enhanced nanodroplet stability. Finally, the vial was stored at 4 °C for three days before use, and the droplets were washed with distilled water by centrifugation (1000 g-force, 6 minutes) prior to phantom preparation.

Nanodroplet size and concentration

The size distribution of the nanodroplets was measured by Dynamic Light Scattering (DLS), as described in [72]. The median diameter of the nanodroplets (intensity-weighted) was found to be 842 nm \pm 12 nm (n=4) and the polydispersity index was 0.25 \pm 0.02. The concentration of nanodroplets was evaluated using ^{19}F NMR spectroscopy (400 MHz Avance II, Bruker Biospin GmbH, Rheinstetten, Germany) referenced against 5 mM fluorocytosine.

3.2.3 Phantom synthesis

Gelatin was chosen to fix the droplets as it has a low gelling temperature and excellent tissue-mimicking ultrasonic properties [193]. The gelatin powder (6% vol., ITW Reagents) was added to deionized water at room temperature to prevent flocculation and then boiled to ensure complete dissolution and removal of entrapped air bubbles. Afterwards, the mixture was poured in rectangular phantom containers (inner dimensions: length = 54 mm, width = 26 mm, depth = 31 mm, 43.5 ml in volume, figure 3.1). Different volumes of nanodroplets were added (see table 3.1) using an 18G needle when the gelatin solution reached 32 °C to reduce spontaneous vaporization due to large injection pressure and temperature fluctuations. After manual homogenization, phantoms were quickly cooled on ice to minimize nanodroplet sedimentation during solidification. Due to the observed limited stability of the nanodroplets in gelatin over time (figure 3.2), the phantoms were always made less than three hours before irradiation.

3.2.4 Irradiation protocol

Irradiation setup

Proton irradiation was carried out at the Centre de Ressources du Cyclotron (UCLouvain, Louvain-la-Neuve, Belgium), an experimental research facility. The cyclotron (CYCLONE 110) produced a monoenergetic, passively scattered proton beam at 62 MeV. The proton range was modulated in discrete steps by inserting different thicknesses of degrader material in front of the irradiated sample. A brass aperture of 40 mm diameter was positioned in front of the phantoms to limit the field size. The phantoms were fixed in a water tank heated to 25 °C and equipped with temperature control (feedback provided by an immersed thermocouple, temperature accuracy of ± 0.5 °C), as illustrated in figure 3.1(a-b). Each phantom was irradiated twice, first in the configuration of figure 3.1(a), and then the phantom was rotated by 180° to irradiate the other side (figure 3.1(b)). Since the proton range was shorter than half of the phantom length, we assumed each irradiation independent of the other. In both configurations, the protons traveled a certain depth before penetrating the gelatin phantoms. Due to the asymmetric design of the phantom containers, the path traveled by the proton beam before penetrating the gelatin differed for the forward and reverse positions. This difference, as well as the presence of PVC material in the beam path (water tank entrance window and PVC phantom container walls), was accounted for when estimating the Bragg peak position in the phantom. The impact of a sub-millimeter thin acoustic window sheet on one side of the phantom container (figure 3.1) was assumed to be negligible.

Absolute range measurement

Two beam energies were employed during the experiments (62 MeV and 46.8 MeV). For each energy, we performed an absolute measurement of the proton range with a bespoke setup consisting of a water tank equipped with a thin 23 μm polyethylene terephthalate entrance window. An automated 1D linear stage was employed to move a dosimetry diode (1.33 mm water equivalent thickness (WET), model PR60020, PTW, Freiburg, Germany) along the depth of the proton beam with a step size of 1 mm. The measured depth-dose curve was fitted to an analytical approximation of the Bragg profile [194] to determine the range (defined here as the distal 80% dose point, R_{80} , as recommended in [30]) and the skin-to-peak dose ratio for the dose calculation. To account for the PVC layers of the water tank and phantom container, we measured the beam profile with and without a 5-mm thick PVC plate in front of the water tank. Relying on these range measurements and the phantom geometry, the

R_{80} values for both the forward and reverse positions were calculated (figure 3.1(c)).

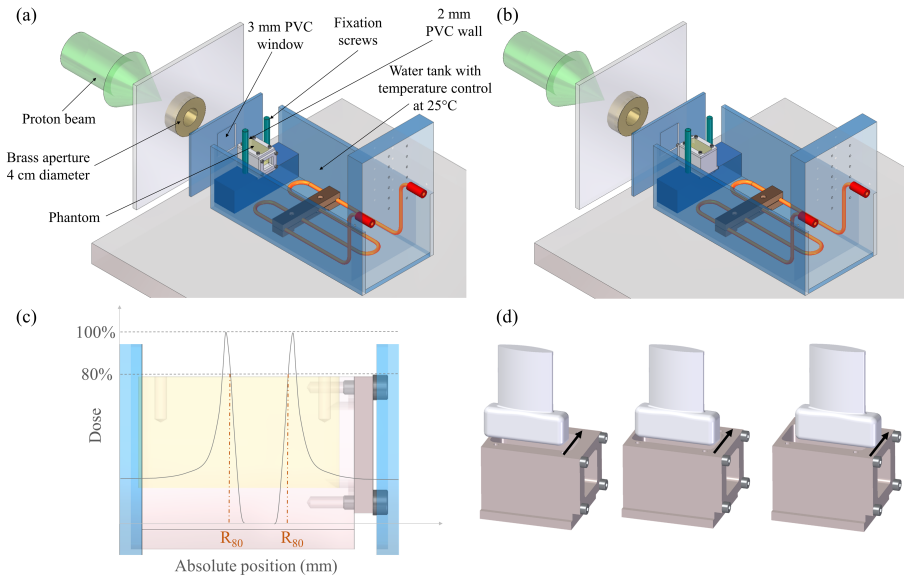


Figure 3.1: Schematics of the irradiation setup, for phantoms in forward (a) and reverse position (b). (c) Position of the Bragg peaks inside the gelatin phantoms. (d) Imaging of the phantoms with an ultrasound probe on three different positions to cover the entire phantom length. The lateral ultrasound axis is parallel to the direction of the proton beam, and the axial ultrasound axis corresponds to the phantom depth. Eleven images were acquired at each position by moving the ultrasound probe across the phantom width (elevational axis).

Irradiation conditions

The irradiation conditions of each phantom are recorded in table 3.1. Three phantoms with $25 \mu\text{M}$ PCDA droplets were irradiated with 62 MeV protons on both sides, 10 Gy in forward position and 20 Gy in reverse. A gelatin phantom without nanodroplets was also irradiated with the same parameters to verify that the gelatin matrix itself does not exhibit any dose response detectable via ultrasound imaging. Three phantoms with the same nanodroplet concentration were not irradiated and acted as controls. These phantoms were made simultaneously with their irradiated counterparts and immersed in a separate water tank at 25°C for ten minutes to mimic the thermal conditions of

Phantom composition	Number of phantoms	Forward phantom position			Reverse phantom position			Ultrasound imaging
		Dose [Gy]	Dose rate [Gy min ⁻¹]	Energy [MeV]	Dose [Gy]	Dose rate [Gy min ⁻¹]	Energy [MeV]	
6% Gelatin No NDs	1	10	2	62	20	4	62	Pre-irradiation Post-irradiation
6% Gelatin 25 μ M NDs	3	10	2	62	20	4	62	Pre-irradiation Post-irradiation
6% Gelatin 25 μ M NDs	3	-	-	-	-	-	-	Pre-immersion (25 °C) Post-immersion (25 °C)
6% Gelatin 50 μ M NDs	3	10	2	46.8	2	2	62	Post-irradiation

Table 3.1: Irradiation conditions.

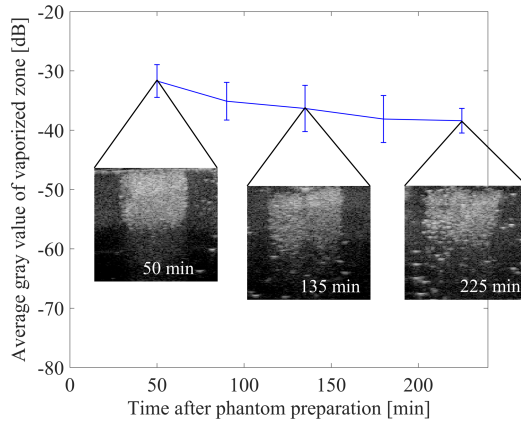


Figure 3.2: Nanodroplet vaporization potential over time (mean \pm standard deviation over five phantoms), represented as the average gray value in 16 mm² regions of acoustically vaporized nanodroplets (25 μ M nanodroplets in 6% gelatin phantoms). Although densely packed microbubbles were generated at each time point, the slowly decreasing gray value indicated a limited stability of nanodroplets in gelatin over time.

the irradiated phantoms. Additionally, three phantoms received a dose of 10 Gy at a different energy (46.8 MeV) in forward position, and a clinically-relevant dose of 2 Gy at 62 MeV in reverse position. For these phantoms, the nanodroplet concentration was doubled. The reported doses and dose rates are evaluated at the Bragg peak, and dose calculations were performed using a peak-to-skin dose ratio equal to five, in agreement with the measured beam profiles. The proton entrance flux was measured by a calibrated ionization chamber present in the beam path.

3.2.5 Ultrasound imaging

Each phantom was immersed in water at room temperature and imaged with an experimental ultrasound scanner (DiPhAS, Fraunhofer IBMT, Germany) driving a 7.5 MHz linear array (L7-Xtech, Vermon, France). The lateral and axial resolution of the ultrasound system were evaluated as described elsewhere [195]. Briefly, the full width at half maximum (FWHM) of the point spread function of an 80 μm -diameter wire acting as point scatterer was determined at varying depths. This resulted in a representative lateral resolution of 1.18 mm and axial resolution of 0.29 mm along the depth of the phantom container.

The ultrasound probe was mounted on a manual 1D linear stage and moved to scan the phantom parallel to the proton beam direction, yielding up to 11 independent images per phantom (figure 3.1(d)). Because the probe's lateral field of view (38.5 mm) was smaller than the sensitive zone (54 mm), we acquired three different views of each phantom (figure 3.1(d)) aligned with either end or the center of the gelatin. Low pressure, plane wave imaging was employed, which was verified not to cause acoustic droplet vaporization. All phantoms except the last three phantoms in table 3.1 (due to time constraints) were imaged twice, before and after forward and reverse irradiation (or immersion in 25 °C water tank for controls), with identical ultrasound parameters.

3.2.6 Image processing

Bubble localization and counting

Ultrasound images of the phantoms were divided in three zones: the region irradiated in the forward direction, the one irradiated in the reverse direction, and the space in between, distal to both forward and reverse irradiations (figure 3.1(c)). For each zone, a rectangular isometric region of interest (ROI) was defined, with a size of 7 mm parallel to the proton beam and 17 mm parallel to the phantom depth. These ROI sizes maximized bubble counts, while still ensuring complete containment in the respective zone and preventing artifacts from phantom wall reflections as well as irregularities at the gelatin surface. Bubbles were counted with an in-house developed algorithm, based on peak detection and thresholding on the pixel gray value. Bubbles were localized as the position of the brightest pixel of their point spread function, resulting in a lateral localization precision of 0.25 mm (one pixel). This approach showed sub-pixel agreement with the intensity-weighted center of mass calculation [78] for the 80 μm -diameter wire scatterer and was expected to provide an improved robustness in dense bubble zones. Additionally, an ellipsoidal inclusion zone

was defined around each detected microbubble, with dimensions defined by the previously described FWHMs in the respective axial and lateral direction. If multiple microbubbles were detected in this zone, they were assumed to be originating from a single microbubble with the average position as its center. Depth-dependent thresholding was used to counteract the decrease of the mean gray value due to attenuation of the ultrasound wave (especially in regions with high bubble density).

Bubble count profiles

Bubble count profiles along the proton beam path were derived from the ultrasound images as illustrated in figure 3.3. Each microbubble detected by the bubble-counting algorithm (figure 3.3(a)) was assigned to a single pixel (brightest spot). Then, the bubble positions in the 11 frames per phantom view were combined (figure 3.3(b)). All bubbles in a rectangular bin of dimensions equal to the ROI depth in the depth direction and seven pixels in the lateral direction were summed and the resulting count was assigned to the central lateral pixel position. This ensured sufficient count statistics and smoothed out strong fluctuations, while preventing loss of profile information. Consecutively, the vertical bin was moved pixelwise along the lateral axis (parallel to the proton beam direction, see figure 3.3(c)) and the resulting lateral intensity profile was divided by the number of frames ($n=11$). To provide full coverage of the lateral view, bubble count profiles derived from the three different probe positions were aligned and combined (figure 3.3(d)). Finally, to translate the pixel position into an absolute position in the phantom, the middle of the non-vaporized zone in the phantoms (figure 3.3(f)), defined as the center point between the two 50% drops in bubble count (figure 3.3(e)), was aligned with the position equidistant from the forward and reverse range (R_{80}) values (figure 3.3(f)). The exact position of the 50% drop was determined as follows. First, the profiles were smoothed to decrease the impact of bubble count fluctuations. Then, the position corresponding to the peak value of the square of the first differential of the bubble count profile was detected. In a 10 mm-interval around this position, the minimum and maximum bubble count was determined and the position corresponding to the bubble count closest to their average was assigned as 50% drop. The proton range in the phantom was then compared with the end of the vaporization zone, defined as the position at which the bubble count drops by 50%.

To evaluate the accuracy of the proposed algorithm to detect the actual position of the 50% drop in bubble count, 1000 artificial vaporization maps (figure 3.3(b)) for which the positions of the irradiated zones were fixed were generated and tested. In particular, bubble densities were derived from the experimental

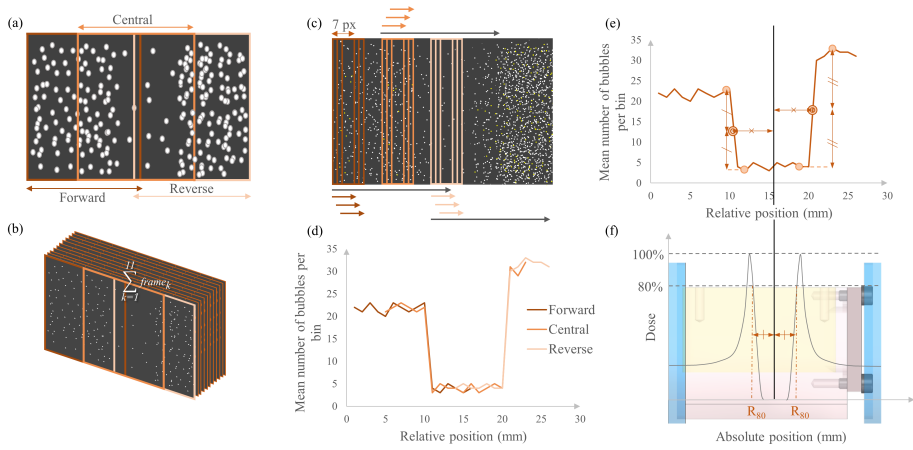


Figure 3.3: Schematic overview of the image processing. (a) Bubbles were identified in every frame of each view (forward, reverse, central) and their central position was stored. (b) For each view, all frames were combined. (c) Then, bubbles were counted in rectangular bins (width of seven pixels) and divided by the number of frames. The resulting bubble count was assigned to the central lateral position of the bin. Afterwards, the bin was moved pixelwise across the image's lateral axis to obtain a full bubble count profile. (d) The obtained bubble count profiles for the three views were aligned by template matching and combined by a weighted average to obtain a single profile across the entire phantom length. (e) The position of 50% drop in bubble count was identified in the forward and reverse transition zones. (f) The midpoint between the two transition zones was aligned with the midpoint between the forward and reverse R_{80} positions in the phantom to enable comparison with the proton range.

measurements for each dose (0, 2, 10 and 20 Gy). The artificial vaporization maps were fed to the image processing algorithms (steps (c) to (f) of figure 3.3) and the 50% drop position was deduced. In order to quantify the uncertainties introduced by the image processing steps, we characterized the error between the obtained 50% drop position ($n=1000$) and the known position of the transition zone (between vaporized and non-vaporized areas) in the artificial vaporization maps.

3.2.7 Statistical analyses

Statistical data were calculated as mean \pm standard deviation. Differences in bubble count between the three ROIs (forward, reverse and central distal regions) in phantoms of the same condition (irradiated or control) were examined using two-tailed Student's t-tests. Increases in bubble count between images acquired

before and after irradiation were assessed for control and irradiated samples using one-tailed paired Student's t-tests on the corresponding ROIs. Finally, the difference in bubble count increase between irradiated and control groups was evaluated with a one-tailed Student's t-test. All tests were performed in Matlab (R2018b, The Mathworks, Natick, MA, USA) with a significance level (α) of 0.05.

3.3 Results

3.3.1 Analytical evaluation of the experimental conditions

In this study, the radiation response of nanodroplets with a decafluorobutane core at 25 °C was evaluated. The necessary physical quantities to estimate the required vaporization energies are listed in table 3.2. Using these values in equations 3.1-3.5 results in a nucleation energy W_{tot} of 66 keV and a critical radius R_c of 89 nm. In order to compute the LET threshold from the semi-empirical nucleation theory, we set the nucleation parameter equal to two, in agreement with the experimental findings of d'Errico [154] for moderate (\ll 1 MeV) values of the critical nucleation energy W_{tot} . This led to a calculated track-averaged LET threshold of 370 keV/ μ m. At 25 °C, the reduced superheat value of the nanodroplet dispersion was 0.23.

Property	Symbol	Value [unit]
Surface tension	σ	7.19×10^{-3} [N · m ⁻¹]
Saturation pressure	P_s	2.68×10^5 [Pa]
Latent vaporization heat	ΔH	8.75×10^4 [J · kg ⁻¹]
Liquid pressure	P_l	1.01×10^5 [Pa]
Heat conductivity	k	4.27×10^{-2} [W · m ⁻¹ · K ⁻¹]
Gas density	ρ_v	28.9×10^{-2} [kg · m ⁻³]
Liquid density	ρ_l	1.5×10^3 [kg · m ⁻³]
Specific heat capacity	c_p	1.08×10^3 [J · kg ⁻¹ · K ⁻¹]

Table 3.2: Physical properties of C_4F_{10} at 25 °C.

3.3.2 Radiation response of the nanodroplet formulation

Examples of ultrasound images aligned to the center of the phantom are displayed in figure 3.4(a-f). Before irradiation, the two phantoms with dispersed nanodroplets are similar, with only a few visible microbubbles (figure 3.4(c,e)). The microbubbles appear bright due to the large acoustic impedance mismatch

between the surrounding water-equivalent matrix and the microbubble gaseous core. On the contrary, the liquid core of the nanodroplets is invisible on the ultrasound images. As microbubbles are too small to be resolved by ultrasound imaging, their shape on the image is dictated by the point spread function of the ultrasound system. The irradiated phantoms (figure 3.4(d)) exhibit spatially confined zones of higher bubble count inside the primary proton beam path compared to the area beyond the Bragg peak (middle zone). The number of bubbles is higher for the 20 Gy region compared to 10 Gy. After immersion at 25 °C, the control phantoms (figure 3.4(f)) displayed an increased, homogeneous bubble density similar to the one observed in the middle zone of the irradiated phantoms. No bubbles were detected before or after irradiation in the phantom without nanodroplets (figure 3.4(a-b)).

Bubble signals were counted as described in section 3.2.6 and a typical identification result is displayed in figure 3.5. Afterwards, phantoms were grouped per condition, irradiated with 62 MeV protons in forward and reverse positions (n=3, pre and post) and control (n=3, pre and post). Potential differences between the three ROIs (spatial differences in bubble density) were assessed with Student's t-tests for each condition. Only the irradiated group, post-irradiation, exhibited a statistically significant difference in bubble count between the three zones ($p < 0.05$). This confirmed the homogeneous dispersion of the droplets in the phantom, as the bubble density in non-irradiated samples was spatially uniform. Then, the increase in bubble count between pre and post images for irradiated and control groups was evaluated with a one-tailed paired t-test. For both irradiated and control groups, we observed a significant increase ($p < 0.05$) in bubble count, indicating that all phantoms exhibit a certain degree of spontaneous vaporization over time. Finally, we investigated whether the bubble count increase was more pronounced in the irradiated group. The mean and standard deviation of the difference in bubble count between images acquired before and after irradiation are displayed in figure 3.6 for each ROI of the control and irradiated groups. Statistically significant ($p < 0.01$) differences in bubble count were observed between irradiated and control phantoms for the left and right ROIs, corresponding to the 10 Gy and 20 Gy zones, respectively. No significant difference between irradiated and control groups was found for the zone distal to the Bragg peaks.

3.3.3 Proton range verification

Lateral bubble count profiles (figure 3.4(g-h)) were derived from the ultrasound images (figure 3.4(c-f)) as explained in section 3.2.6. Figure 3.7 shows the profile of two individual phantoms irradiated with 62 MeV and 46.8 MeV protons, as well as the corresponding absolute range measurements. For both beam

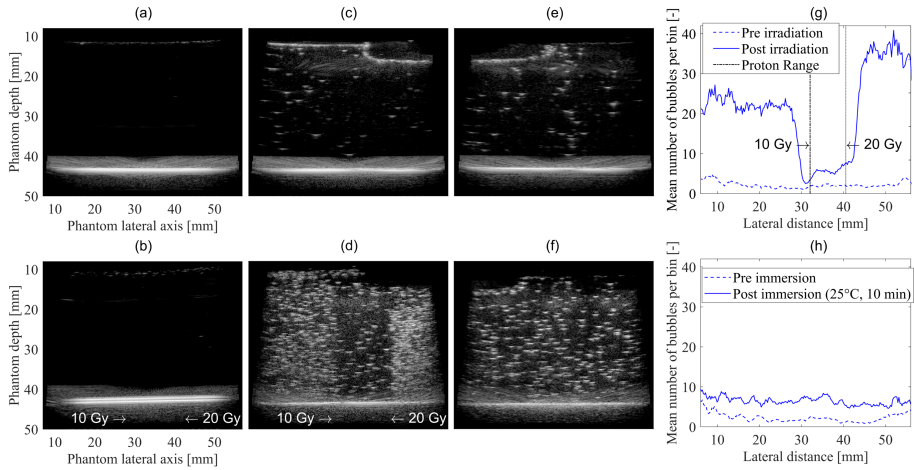


Figure 3.4: Ultrasound images of a phantom made of pure gelatin before (a) and after (b) exposure to 62 MeV protons (10 Gy dose delivered in the forward position, 20 Gy in the reverse position). Gelatin phantom with dispersed nanodroplets before (c) and after (d) an identical irradiation scheme. Corresponding images for a control phantom with dispersed nanodroplets before (e) and after (f) immersion at 25 °C (no irradiation). (g) Bubble count profile across the irradiated phantom with nanodroplets (c-d), averaged over 11 imaging frames. (h) Bubble count profile for the control phantom with nanodroplets (e-f).

energies, the bubble count profiles did not follow the characteristic Bragg profile, but instead appeared as step functions, with higher bubble counts for 20 Gy irradiations compared to 10 Gy (figure 3.4(g)). Additionally, for each phantom, the bubble count abruptly dropped a few millimeters proximal to the dose maximum position. Signal shifts, calculated as the difference between the R_{80} value obtained from the absolute range measurements and the position corresponding to a 50% drop in bubble count (star in figure 3.7), are listed in table 3.3 together with the measurement uncertainties estimated as described in section 3.2.6. One of the phantoms irradiated with 46.8 MeV was discarded due to high background signal (elevated by 9 dB with respect to other phantoms), hampering profile extraction. To compensate for this, an additional phantom containing 6% gelatin and 25 μM nanodroplets (not included in table 3.1), was irradiated with 46.8 MeV protons during a follow-up experiment. A signal shift of 2.79 ± 0.26 mm was obtained for irradiation with 62 MeV protons and a shift of 2.98 ± 0.22 mm was observed for 46.8 MeV protons. However, due to measurement variability and uncertainty on the 50% drop position, we cannot establish whether there is a difference between the signal shifts observed with 62 MeV and 46.8 MeV protons. The distance between the end of the dense bubble

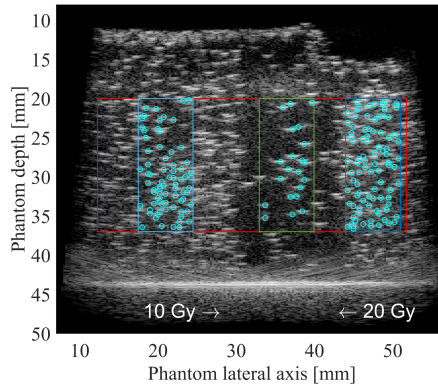


Figure 3.5: Delineation of regions of interest in the two irradiated regions and in the zone distal to both Bragg peaks, on a post-irradiation ultrasound image. The round markers indicate bubble counts. The vaporization profiles across the image lateral axis are computed over the red region of interest.

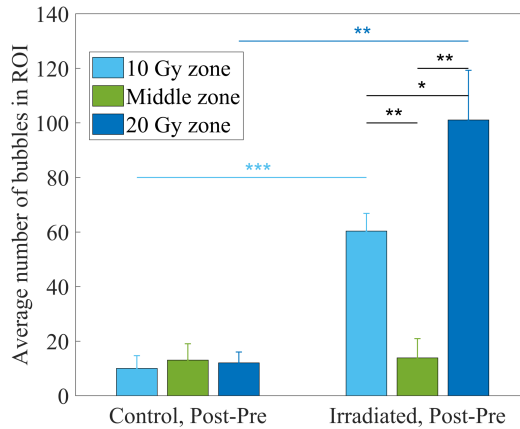


Figure 3.6: Difference between post-irradiation and pre-irradiation bubble count in the three ROIs, for the irradiated ($n=3$, 62 MeV) and control (no irradiation) group ($n=3$). Statistical significance is indicated by the presence of stars: $p < 0.05$ (*), $p < 0.01$ (**) and $p < 0.001$ (***).

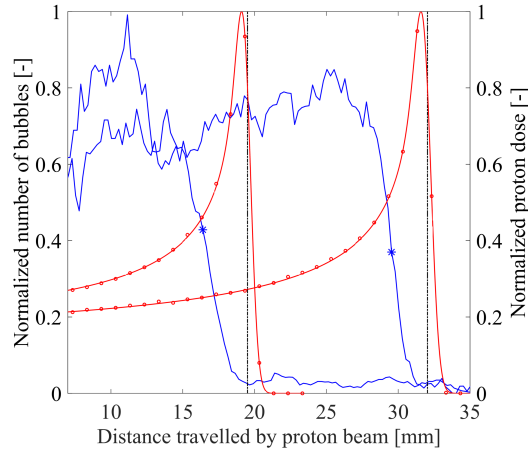


Figure 3.7: Comparison of bubble vaporization profiles along the lateral direction of ultrasound images (parallel to the proton beam) and measured proton dose deposition with depth, for delivered doses of 10 Gy and beam energies of 62 and 46.8 MeV. The position of the 50% drop in bubble count is marked by a star, and the dotted vertical lines represent R_{80} values.

Phantom	Beam Energy	Signal shift	Bubble localization error	Error on the bubble count drop localization
				Mean \pm standard deviation
6% Gelatin 25 μ M NDs	62 MeV	2.87 mm	<0.25 mm	0.11 \pm 0.09 mm
	62 MeV	3.00 mm		
	62 MeV	2.50 mm		
6% Gelatin 50 μ M NDs	46.8 MeV	3.11 mm	<0.25 mm	0.34 \pm 0.39 mm
	46.8 MeV	3.11 mm		
6% Gelatin 25 μ M NDs	46.8 MeV	2.73 mm	<0.25 mm	0.32 \pm 0.37 mm

Table 3.3: Signal shifts experimentally determined for six irradiated phantoms and estimated measurement uncertainties. The bubble localization error was determined by comparing the in-house developed algorithm with super-resolution techniques. The error on the position of the 50% drop in bubble count was estimated from artificial vaporization maps (n=1000).

region and the proton range was measured with sub-millimeter repeatability for both energies.

3.3.4 Nanodroplet sensitivity to proton dose and fluence

After evaluating the radiation response for large proton doses (10 and 20 Gy), we assessed whether the same results could also be obtained for clinically-relevant doses. Since less vaporization events were expected, the droplet concentration in the phantoms was doubled. An ultrasound image acquired after delivery of a 2 Gy dose in the Bragg peak with 62 MeV protons is displayed in figure 3.8. Again, a distinct zone of high bubble density was observed proximal to the Bragg peak, confirming the capability of the superheated nanodroplets to detect clinically-relevant doses.

The relationship between the dose and the resulting bubble counts is depicted in figure 3.9. As before, isometric ROIs were defined in zones irradiated with 2, 10 and 20 Gy as well as the corresponding zones distal to the Bragg peak. The latter served as internal reference and the resulting bubble counts were subtracted from the values obtained from the irradiated zones to account for spontaneous droplet vaporization. The 0 Gy data points were analogously obtained from the control phantoms. A linear regression line was fitted through the 0, 10 and 20 Gy data points, which were all acquired for the same droplet concentration. Bubble counts for the 2 Gy irradiation were rescaled by a factor of 0.5 to account for the double droplet concentration. However, since we ignore potential concentration dependent effects, these data points were not used for curve fitting. Nevertheless, the 2 Gy bubble counts were located well within the calculated confidence interval of the fit.

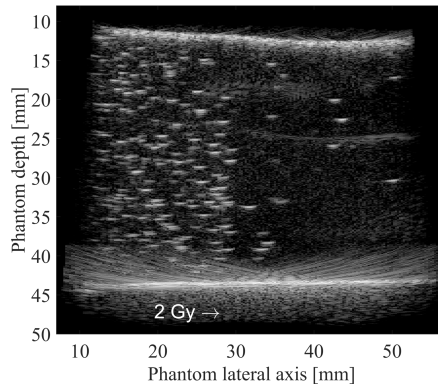


Figure 3.8: Ultrasound image acquired after phantom irradiation with clinically-relevant parameters (dose: 2 Gy, dose rate: 2 Gy/min and beam energy of 62 MeV).

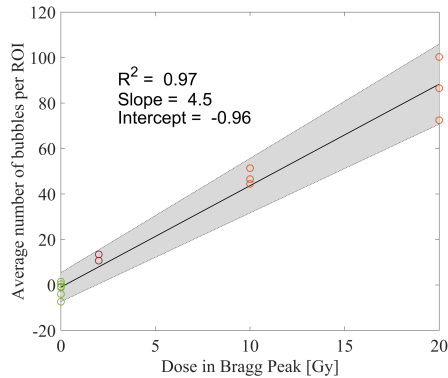


Figure 3.9: Evolution of the number of vaporization events with proton dose. Circles represent experimental data, and the black line is the linear regression fit. The 95% confidence interval on the linear regression is shown by the shaded area.

3.4 Discussion

In this study, we evaluated the radiation sensitivity of submicron-sized superheated droplets in proton beams, assessing their potential for proton dosimetry and range verification. First, we verified the radiation response of the gelatin matrix in terms of ultrasound contrast generation. As displayed in figure 3.4(a-b), the gelatin phantom without nanodroplets resulted in a background-free ultrasound image after irradiation, demonstrating that the radiation-induced contrast generation was attributed to the presence of nanodroplets. The background signal present in phantoms before irradiation (figure 3.4(c,e)) was due to spontaneous vaporization of a small fraction of superheated nanodroplets either already in the nanodroplet vial or during phantom preparation. The increase in bubble count was significantly higher for irradiated phantoms, in regions proximal to the proton range, compared to non-irradiated phantoms, confirming that the observed response (figure 3.4(d)) is induced by proton irradiation.

The theoretical threshold LET value for droplet vaporization was determined to be $370 \text{ keV}/\mu\text{m}$. Hence, sensitivity to neither the primary proton beam (exhibiting a maximum LET of $70\text{-}90 \text{ keV}/\mu\text{m}$ at the distal end of the Bragg peak) nor to secondary alpha particles (LET ranging from $130 \text{ to } 190 \text{ keV}/\mu\text{m}$) [196] was expected. This was confirmed by the nearly flat bubble count profiles observed, with no enhancement in the Bragg peak location, which would have been observed for both protons and alpha particles. Instead, we hypothesize

that bubble vaporization was caused by nuclear recoils, whose LET can range from several hundreds to a thousand $\text{keV}/\mu\text{m}$ [196], created from interactions with either the primary proton beam or secondary neutrons. However, the contribution of the latter was assumed negligible as we did not observe a significant increase of bubbles in the region distal to the Bragg peak.

To confirm that bubble vaporization was induced by recoil ions, we extracted nuclear reaction cross sections of C, N, O and F (atoms present in the gelatin matrix and nanodroplets) from the TENDL-2014 database, which rely on the advanced nuclear reaction simulation software TALYS [197], and displayed them together with a bubble count profile in figure 3.10(a). The average proton energy at each depth was determined based on the PSTAR [198] residual continuous slowing down approximation (CSDA) range in water and used to evaluate the reaction cross section at these positions. For each atom, the reaction cross section drops – similarly to the bubble profile – proximal to the Bragg peak. This is due to the Coulomb barrier of the nucleus, which has to be overcome for a non-elastic nuclear reaction to take place [4]. For oxygen, this threshold energy is 8 MeV, which corresponds to a residual range in water of 0.83 mm. In section 3.3.3, the distance between the 50% drop in bubble count and the range of 62 MeV protons measured in water was estimated to be 2.79 ± 0.26 mm. We measured a difference of 1.8% in density between pure water and a 6% gelatin matrix, leading to a CSDA range decrease of 0.59 mm [198] that is accounted for in figure 3.10. However, a small discrepancy between the steep drop in oxygen recoil production and the experimentally determined vaporization profile remains. This indicates that the presence of recoil nuclei is insufficient for droplet vaporization. Indeed, superheated drop detectors are LET-dependent, and the maximal amount of energy transferred to recoil nuclei decreases with the energy of incident protons [199]. Therefore, we also evaluated the track-averaged LET of oxygen recoils produced along the phantom depth. The average energy transferred to heavy recoils ($A > 4$) from proton-oxygen nuclear interactions was extracted from the ICRU report n°63 [200]. For these energies, the range of an oxygen ion in water with a density of $1.018 \text{ g}/\text{cm}^3$ was determined with SRIM [201] and used to calculate the track-averaged LET. The result is depicted in figure 3.10(b), together with the theoretical threshold of $370 \text{ keV}/\mu\text{m}$, and a bubble count profile. The depth at which the track-averaged LET of oxygen recoils drops below the LET threshold coincides with the start of the drop in bubble count. The latter provides evidence that only recoils of sufficient LET can trigger nanodroplet vaporization. This is in agreement with the radiation-induced nucleation theory (section 3.2.1). Moreover, this can also explain why no bubbles were detected at or closely in front of the Bragg peak (figure 3.10). The measurement uncertainties are displayed in figure 3.10(a) and (b) as shaded areas. Uncertainties in the absolute range position arise from potential measurement and fitting errors, whose combined

effect was estimated to be less than ± 0.5 mm. This uncertainty propagates towards the estimated position of the non-elastic cross sections and track-averaged LET of recoil ions, which depend on the residual proton energy. The 95% confidence interval in the position of the drop in bubble count, extracted from the measured signal shifts ($n=3$, see table 3.3) observed in phantoms irradiated with 62 MeV protons, is represented as a gray area. Furthermore, longitudinal range straggling of 62 MeV protons in water was simulated using TRIM [201] and determined to be $508 \mu\text{m}$. As the initial energy dispersion of the proton beam is unknown, we did not account for range straggling in figure 3.10. Despite the aforementioned uncertainty arising from the limited resolution of the experimental measurements, these results suggest that the features of the observed bubble count profiles can be related to the non-elastic reaction cross section and the energy deposition characteristics of oxygen recoils. This supports the hypothesis that the radiation-induced nucleation theory is applicable to droplets of nanometer size.

The transition from drops of several microns, commonly used in superheated drop detectors, to nanometer-sized droplets has two important implications. Firstly, the assumption that the recoil ions responsible for droplet vaporization are only formed within the superheated liquid [113] no longer holds, as the nanodroplet diameters are several times smaller than the mean range of recoil ions. Hence, both recoils produced inside the droplets and in the surrounding gelatin matrix can induce droplet vaporization. For this reason, we considered oxygen as the dominant recoil ion, given its relative abundance in the phantom matrix. Secondly, while negligible in micro-emulsions, the contribution of the Laplace pressure to the pressure inside the droplet (P_l) becomes important for small droplet radii as described in equation 3.9.

$$\Delta P_{lap} = \frac{2\sigma_s}{R} \quad (3.9)$$

Here, σ_s denotes the surface tension at the droplet interface and therefore depends on the polymerized PCDA layer. A positive Laplace pressure will decrease the degree of superheat of the droplets, and hence raise the LET threshold for droplet vaporization. Since we did not experimentally measure the surface tension, nor could values be adapted from the literature, we did not account for the Laplace pressure. Theoretical considerations and experimental observations support the assumption of a negligible surface tension. Indeed, the nanodroplets employed in this study have an outstanding in-vial stability [72], while models predict a fast dissolution of nanodroplets with a positive surface tension [119]. Additionally, it has been described that perfluorocarbons can decrease the overall surface tension of droplets [202]. Moreover, due to the large polydispersity of the droplets used (polydispersity index of 0.25), it is reasonable to assume that part of the population (i.e., the large droplets) will be

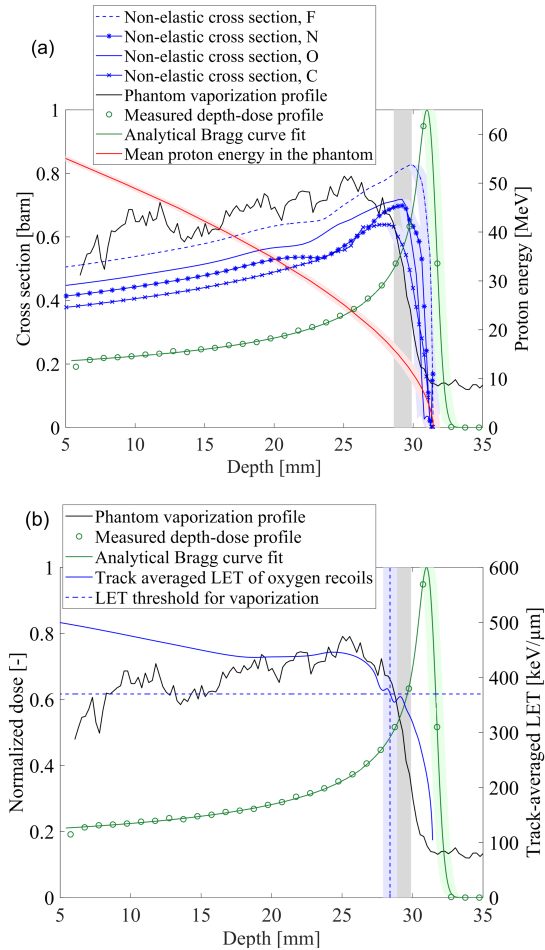


Figure 3.10: (a) Overlay of the droplet vaporization profile in one phantom with the non-elastic nuclear interaction cross sections for relevant atoms and the proton depth-dose profile. (b) Overlay of the droplet vaporization profile in the phantom with the average track-averaged LET of oxygen recoils and the proton depth-dose profile. The shaded area surrounding the Bragg peak represents measurement uncertainties on the proton range, which propagate to uncertainties on the residual proton energy in the phantom (in red) and on the non-elastic cross section and track-averaged LET estimates (in blue). Uncertainties on the position of the 50% drop in bubble count are represented by the gray area.

relatively unaffected by the Laplace pressure, while only the smallest droplets might experience a decreased superheat.

In addition to proton range verification, we also evaluated whether the bubble count profiles were correlated with the radiation dose. No direct sensitivity to the primary proton beam was established due to the limited degree of superheat of the nanodroplets. Nevertheless, a linear relationship between bubble counts and irradiation dose was obtained for high proton doses of 10 and 20 Gy. We explain this relationship by the fact that the number of nuclear reactions and thus recoil ions is dependent on the proton fluence. As a rule of thumb, the primary proton fluence decreases by 1% for every centimeter of tissue traversed [203] due to nuclear reactions. Hence, for the limited size of the ROIs (7 mm) along the proton beam, the fluence can be assumed constant. To double the dose from 10 to 20 Gy, the fluence was also doubled, which is captured by the linear relationship in figure 3.9. This linear response tends to hold for clinically-relevant doses (2 Gy), although further work is required to assess the validity of this relationship at smaller fluences.

Consequently, the experimental findings presented in this contribution show that superheated nanodroplets can provide indirect information on the proton range and fluence, by generating ultrasound contrast upon interaction with high-LET nuclear recoils. The latter provides one of the major advantages of the presented approach over current state-of-the-art range verification tools such as PGI and PET imaging, which are also based on nuclear reactions. Since this technique is not relying on specific reaction channels, like prompt gamma emitting channels or channels in which positron emitting isotopes are generated, it has the potential to detect a larger number of nuclear events. Moreover, the detection of nuclear recoils via individually detectable microbubbles provides a strong, inherent signal enhancement.

To accurately relate the observed signals to the primary proton beam, Monte Carlo (MC) simulations are required. Apart from providing a means for *in vivo* range verification, these could potentially be employed for *in vivo* proton dosimetry by taking advantage of the fluence dependency. To assess this hypothesis and better understand the LET vaporization thresholds, we are currently implementing comprehensive MC simulations describing individual nanodroplets as detectors. However, MC simulations of nuclear interactions suffer from uncertainties arising from the limited amount of experimental data available to describe interaction cross sections for biologically-relevant targets [30].

Alternatively, increasing the degree of superheat to sensitize nanodroplets to the primary proton beam might be beneficial, as the vaporization profiles could be directly related to the proton range and dose distribution. Additionally, nuclear

recoils only represent a very small percentage of all interactions, leading to a low fraction of nanodroplets undergoing vaporization. For *in vivo* applications, a high yield might be recommended to minimize the required droplet concentration and related potential side-effects. However, highly superheated droplets will be more prone to spontaneous vaporization. Hence, the appropriate choice of degree of superheat will depend on the achievable signal-to-noise ratio.

One could argue that the temperature of 25 °C chosen for this study is unsuitable as it does not fully reflect the response of the nanodroplets at physiological temperature, due to the high dependence of the radiation response on the degree of superheat. At 37 °C, the reduced degree of superheat for C_4F_{10} droplets, $s = 0.33$, is theoretically still insufficient to expect a response to the primary proton beam. However, the proton range would have to be inferred from vaporization profiles related to secondary radiation products, comprised not only of heavy recoil ions, but potentially also of light secondaries such as alpha particles and deuterons, as the track-averaged LET threshold would drop to 145 keV/ μm . Moreover, the composition of the nanodroplets superheated liquid core can be altered to appropriately tune the degree of superheat to the desired LET thresholds. Indeed, a variety of perfluorocarbons with different boiling points have been employed to formulate nanodroplets [204].

The use of ultrasound imaging to noninvasively evaluate vaporization events has numerous advantages for clinical applications such as its inexpensiveness, small footprint, portability, short examination times and real-time capabilities. In our study, we did not employ an ultrasound pulse sequence tailored for microbubble contrast agent imaging, and the limited image quality and resolution affected the accuracy of the estimation of the absolute position of the drop in bubble count. Additionally, the algorithm developed for bubble detection was not optimal for zones of high bubble density. To verify that the bubble counting algorithm did not introduce any bias in the results, we compared it with results obtained by considering the mean gray value as the relevant metric for vaporization (instead of the number of bubbles) and found no noticeable difference. In order to benefit from the improved ultrasound image resolution in the axial direction, the axial ultrasound axis should coincide with the proton beam direction. Further research should be conducted to obtain the optimal droplet concentration and maximize the contrast between irradiated and non-irradiated regions.

Proton irradiations were performed in an experimental research facility, with a passively-scattered monoenergetic beam whose characteristics differ from clinical proton beams. In particular, the features of the vaporization profiles, with a steep drop in front of the proton range, might be altered in a spread-out Bragg peak. Future studies aim to establish the response of the superheated nanodroplets in clinical proton beams, including scanned beams.

3.5 Conclusion

In this contribution, the potential use of nanodroplets for proton dosimetry and range verification was investigated. Downscaling radioresponsive micro-emulsions used in superheated drop detectors to injectable phase-change contrast agents produced ultrasonically detectable radiation sensors with potential for *in vivo* use, provided that a similar radiation response would be observed under clinical proton therapy conditions. Applying radiation-induced nucleation theory to our experimental conditions revealed that the decafluorobutane liquid core vaporizes when exposed to high-LET secondary particles generated during nuclear reactions of the proton beam. Nanodroplet dispersions exposed to monoenergetic proton beams of 62 MeV and 46.8 MeV, at 25 °C, exhibited spatially confined bubble vaporization regions proximal to the Bragg peak. While ultrasound signals dropped before the actual proton range due to LET dependencies, the resulting signal shift was determined with sub-millimeter precision. Additionally, the bubble count was linearly related to the proton fluence. Lastly, the potential of the developed technique was shown at a clinically-relevant dose of 2 Gy. Future work aims to confirm these early findings and refine the range estimates accuracy. Proton irradiations at 37 °C will be carried out to assess the relevance of these proof-of-concept data at physiological temperatures. Finally, the nanodroplet design will be optimized to ensure sensitivity to the primary proton beam, enabling direct *in vivo* proton range verification and potentially *in vivo* proton dosimetry.

3.6 Acknowledgments

The authors would like to acknowledge the team of the "Centre de Ressources du Cyclotron" of UCLouvain for their precious assistance in operating the proton beam and performing absolute range measurements. The authors also thank Fraunhofer IBMT for providing the ultrasound readout system, and the mechanical and electrical staff of the Physics Department of KU Leuven for the design and conception of the water tank heating system and phantom containers. This work has been supported by the European Union's Horizon 2020 research and innovation programme under grant agreement n°766456 ("AMPHORA"). BC received a PhD fellowship fundamental research from the Research Foundation Flanders (n°11A9520N).

“Research is formalised curiosity. It is poking and prying with a purpose.”

Zora Neale Hurston

4

Modulating ultrasound contrast generation from injectable nanodroplets for proton range verification by varying the degree of superheat

*Sophie V. Heymans**, *Bram Carlier**, *Yosra Toumia*, *Sjoerd Nooijens*, *Marcus Ingram*, *Andrea Giammanco*, *Emiliano d’Agostino*, *Wouter Crijns*, *Alexander Bertrand*, *Gaio Paradossi*, *Uwe Himmelreich*, *Jan D’hooge*, *Edmond Sterpin* and *Koen Van Den Abeele*

Published in *Medical Physics*, 48(4), 2021, pp. 1983-1995.

Purpose: Despite the physical benefits of protons over conventional photon radiation in cancer treatment, range uncertainties impede the ability to harness the full potential of proton therapy. While monitoring the proton range *in vivo* could reduce the currently adopted safety margins, a routinely applicable range verification technique is still lacking. Recently, phase-change nanodroplets were proposed for proton range verification, demonstrating a reproducible relationship between the proton range and generated ultrasound contrast

*joint first author

after radiation-induced vaporization at 25 °C. In this study, previous findings are extended with proton irradiations at different temperatures, including the physiological temperature of 37 °C, for a novel nanodroplet formulation. Moreover, the potential to modulate the linear energy transfer (LET) threshold for vaporization by varying the degree of superheat is investigated, where the aim is to demonstrate vaporization of nanodroplets directly by primary protons.

Methods: Perfluorobutane nanodroplets with a shell made of polyvinyl alcohol (PVA-PFB) or 10,12-pentacosadyinoic acid (PCDA-PFB) were dispersed in polyacrylamide hydrogels and irradiated with 62 MeV passively-scattered protons at temperatures of 37 °C and 50 °C. Nanodroplet transition into echogenic microbubbles was assessed using ultrasound imaging (gray value and attenuation analysis) and optical images. The proton range was measured independently and compared to the generated contrast.

Results: Nanodroplet design proved crucial to ensure thermal stability, as PVA-shelled nanodroplets dramatically outperformed their PCDA-shelled counterpart. At body temperature, a uniform radiation response proximal to the Bragg peak is attributed to nuclear reaction products interacting with PVA-PFB nanodroplets, with the 50% drop in ultrasound contrast being $0.17 \text{ mm} \pm 0.20 \text{ mm}$ (mean \pm standard deviation) in front of the proton range. Also at 50 °C, highly reproducible ultrasound contrast profiles were obtained with shifts of $-0.74 \text{ mm} \pm 0.09 \text{ mm}$ (gray value analysis), $-0.86 \text{ mm} \pm 0.04 \text{ mm}$ (attenuation analysis) and $-0.64 \text{ mm} \pm 0.29 \text{ mm}$ (optical analysis). Moreover, a strong contrast enhancement was observed near the Bragg peak, suggesting that nanodroplets were sensitive to primary protons.

Conclusions: By varying the degree of superheat of the nanodroplets' core, one can modulate the intensity of the generated ultrasound contrast. Moreover, a sub-millimeter reproducible relationship between the ultrasound contrast and the proton range was obtained, either indirectly via the visualization of secondary reaction products or directly through the detection of primary protons, depending on the degree of superheat. The potential of PVA-PFB nanodroplets for *in vivo* proton range verification was confirmed by observing a reproducible radiation response at physiological temperature, and further studies aim to assess the nanodroplets' performance in a physiological environment. Ultimately, cost-effective online or offline ultrasound imaging of radiation-induced nanodroplet vaporization could facilitate the reduction of safety margins in treatment planning and enable adaptive proton therapy.

4.1 Introduction

Proton dose deposition profiles are characterized by a low entrance dose and a narrow Bragg peak, followed by a sharp distal dose fall-off. These physical

features have provided a strong impetus for the development of proton centers for cancer treatment in the past decades [6]. However, even with the availability of powerful Monte Carlo engines allowing the development of highly accurate treatment plans a priori, the exact proton range *in vivo* remains unknown [181]. Indeed, considerable range uncertainties arise from the ambiguous conversion of Hounsfield Units (HU) to stopping powers, patient motion, setup inaccuracies and anatomical changes over the course of the treatment [181]. This is accounted for by the addition of substantial safety margins on the original treatment plan and the choice of suboptimal beam arrangements, preventing full exploitation of the ballistic advantage of protons [30, 205, 206]. To solve this problem, several *in vivo* range verification techniques have been investigated. PET imaging detects coincident gamma rays emitted by certain isotopes produced by nuclear reactions of the proton beam with atomic constituents of the tissue being irradiated [31, 33, 35, 182]. However, complex models and simulations are required to relate the obtained PET signals to the actual proton range and limited accuracy is achieved [205, 207]. Prompt gamma imaging has the potential to provide real-time range feedback by detecting the prompt gamma radiation released from similar nuclear interactions [37–39], but the lack of suitable and cost-effective detectors has prevented its translation to standard clinical practice [181, 185]. Recently, ionoacoustic imaging has emerged as a novel approach to determine the proton range by probing the ultrasound signals arising from the thermo-elastic tissue expansions induced by localized dose deposition at the Bragg peak [40, 208–211]. While the Bragg peak location was detected in phantom experiments with sub-millimeter resolution, the technique is limited to pulsed proton accelerators given its transient nature [41, 42]. Finally, radiation-induced changes of tissue properties detected by magnetic resonance imaging can be used as a post-treatment range verification approach as demonstrated for spinal and liver tissues [212, 213]. However, an important constraint is that those changes occur weeks after irradiation, preventing the compensation of range errors over the course of the treatment [212]. In general, due to the aforementioned limitations, none of the presented technologies are routinely adopted in the clinic [104].

The European Horizon 2020 project "Amphora" recently revisited superheated emulsions as an alternative means to measure the proton range [124]. Superheated emulsions typically comprise micrometer or millimeter-sized drops dispersed in an immiscible aqueous matrix [113]. Owing to the absence of heterogeneous nucleation sites, these droplets can be operated at temperatures above their boiling point, in a metastable superheated state, without vaporizing [119, 147]. However, when charged particles with sufficient linear energy transfer (LET) traverse these droplets, small vapor embryos are created that can eventually trigger complete vaporization of the drops into gaseous bubbles as described by Seitz's thermal spike theory [108, 143, 154]. These

highly echogenic bubbles can then be detected via optical, acoustic or volume measurements [113, 188]. For the past half century, this principle has been exploited by bubble chambers and superheated drop detectors in a variety of fields ranging from radiation spectrometry and dosimetry to space applications and dark matter search [111, 115, 116, 155, 214]. Furthermore, it was envisioned for *in vivo* applications two decades ago [118].

To apply this concept to *in vivo* non-invasive radiation dosimetry and proton range verification, the aforementioned emulsions were downscaled to phase-change nanodroplets and stabilized by a lipidic shell [124]. This was facilitated by recent developments in the field of ultrasound imaging and therapy [65, 66, 215, 216], which led to the emergence of several injectable superheated nanodroplet formulations able to provide ultrasound contrast on demand when triggered by acoustic [71, 72] or optical [73] sources. A first proof-of-concept study was recently performed with nanodroplets made of a 10,12-pentacosadiynoic acid shell encapsulating a liquid decafluorobutane core (PCDA-PFB, boiling point = -2°C) [72], demonstrating radiation-induced vaporization in a proton beam at room temperature (25°C) [124]. Moreover, a highly reproducible ($< 1\text{ mm}$) relationship between the proton range and the generated ultrasound contrast was observed, thereby disclosing the potential of superheated nanodroplets for ultrasound-guided *in vivo* range verification. The presence of a shift was explained by the LET threshold for perfluorobutane droplets at 25°C ($370\text{ keV}/\mu\text{m}$) predicted by the thermal spike theory [113] (figure 4.1). This indicates that only secondary recoil nuclei generated by non-elastic interactions carried sufficient LET to trigger droplet vaporization, harnessing only a small fraction of the radiation for ultrasound signal generation.

In this contribution, those previous findings are extended by exploring the potential to modulate I) the overall ultrasound contrast generation and II) its relationship to the proton range, by varying the degree of superheat, s , defined as:

$$s = \frac{T - T_b}{T_c - T_b} \quad (4.1)$$

with T the ambient temperature and T_b and T_c the boiling and critical temperature of the nanodroplets' liquid core, respectively. Due to the limited thermal stability of the PCDA-PFB nanodroplets, the lipidic shell was replaced by a more resistant polyvinyl alcohol (PVA) shell for the experiments in this study. First, the radiation response of these PVA-PFB nanodroplets was evaluated in phantoms at physiological temperature, taking the next step towards the eventual *in vivo* application. Afterwards, irradiations at 50°C were performed to investigate whether nanodroplet vaporization induced by the primary proton beam could be achieved, as predicted by the radiation-induced nucleation theory [113, 154] (figure 4.1). Ultrasound imaging was employed to

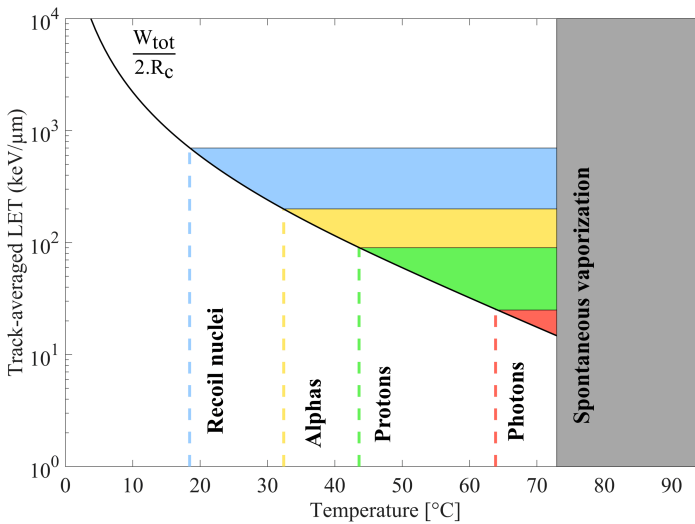


Figure 4.1: LET threshold, obtained from the thermal spike theory as the ratio between the nucleation energy (W_{tot}) and twice the critical radius (R_c), for perfluorobutane droplets as a function of temperature. Shaded areas highlight the temperature zones where droplets are sensitized to the respective particles. Above 76 °C, the superheated metastable state can no longer exist and spontaneous vaporization takes place.

evaluate nanodroplet vaporization profiles, which were subsequently compared to the proton range. Finally, the observations at different degrees of superheat were compared and explained by the theory of radiation-induced nucleation of superheated emulsions.

4.2 Materials and Methods

4.2.1 Nanodroplet synthesis and size distribution

Unless described otherwise, all chemicals were obtained from Sigma-Aldrich (Darmstadt, Germany). The PVA-PFB nanodroplet preparation was performed as follows. First, 1 g of fully hydrolyzed PVA was dissolved in 50 ml Milli-Q water at 80 °C. After complete dissolution, heating was stopped and 95 mg of sodium periodate were added and stirred for 1 hour to oxidize the PVA chains. Separately, an empty glass vial sealed with a rubber septum was immersed in liquid nitrogen and injected with gaseous perfluorobutane (F2 Chemicals Ltd, United Kingdom), which immediately condensed, for a few seconds. Afterwards,

5 ml of the oxidized PVA solution was added to this vial and the mixture was sonicated in an ice-cold water bath (Elmasonic X_{TRA} 30H, Elma Schmidbauer GmbH, Germany) for 15 minutes. After an additional 1 hour incubation at 4 °C, the nanodroplet solution was washed by a two-step centrifugation. First, the glass vial was centrifuged for 5 minutes at 1200 g (Thermo Scientific SL 16, Thermo Electron LET GmbH, Germany). The supernatant was transferred to a plastic Falcon tube and underwent a second centrifugation at 4700 g for another 5 minutes. Finally, both pellets were resuspended in Milli-Q water and combined. PCDA-PFB nanodroplets were prepared as described previously [72,124]. The resulting nanodroplet solutions were stored in the fridge and used within 1 week after preparation.

Dynamic light scattering (NanoBrook Omni, Brookhaven Instruments, Corporation, NY) was used to measure the PVA-PFB nanodroplet size distribution, and yielded an intensity-weighted median diameter of 799 nm \pm 25 nm (n=7, repetitions over two different vials) and a polydispersity index of 0.3 \pm 0.01. The PCDA-PFB nanodroplets have an intensity-weighted median diameter of 842 nm \pm 12 nm (n=4) and a polydispersity index of 0.25 \pm 0.02 [124].

4.2.2 Phantom preparation

Phantoms were prepared in bespoke containers of inner dimensions L = 38 mm, W = 24 mm and H = 25 mm. First, the 30% acrylamide-bisacrylamide (Am/Bis) stock solution (29:1, Bio-Rad Laboratories NV, Belgium) was diluted to 5% in Milli-Q water and degassed via sonication. Next, 22.2 ml of this solution was poured into the phantom container and mixed with 570 μ l of 8.5% (w/v) ammonium persulfate in Milli-Q water. Afterwards, the required volume of nanodroplets was added to achieve a final perfluorobutane concentration of 25 μ M in the phantom. Perfluorobutane concentration of the nanodroplet solution was previously quantified using NMR spectroscopy (400 MHz Avance II, Bruker Biospin GmbH, Rheinstetten, Germany). Then, 28.5 μ l of TEMED was added and the mixture was homogenized, before allowing gelation for 30 minutes at room temperature. Finally, the phantoms were heated to the desired temperature in a water bath, just prior to irradiation (figure 4.2).

4.2.3 Irradiation protocol

Phantom irradiation

Proton irradiations were performed at the Centre de Ressources du Cyclotron (UCLouvain, Louvain-la-Neuve, Belgium), equipped with a cyclotron (CY-

CLONE 110) producing a passively-scattered proton beam with a nominal energy of 62 MeV. Phantoms were placed in a heated water tank equipped with temperature control ($\pm 0.5^\circ\text{C}$) and aligned in the proton beam (figure 4.2). The orange pipes depicted in the irradiation setup are metallic heating elements, connected to a temperature controller. The proton beam was collimated by a 4 cm diameter brass aperture and covered the entire phantom cross section. The phantoms were heated to two temperatures, 37°C in order to mimic physiological conditions, and 50°C aiming at nanodroplet vaporization by the primary proton beam. At 37°C , six PVA-PFB phantoms received each a dose of 10 Gy at a dose rate of 2 Gy/min (doses and dose rates are reported at the Bragg peak location), while four others were irradiated at 50°C (dose rate of 4 Gy/min): three phantoms received a dose of 10 Gy and one phantom received 2 Gy. For all irradiations, the beam energy was 62 MeV. Control phantoms underwent the same temperature conditions, but were not irradiated. Additionally, PCDA-PFB phantoms were irradiated at 37°C , but were not included for further analysis because the radiation response was indistinguishable from the initial background.

Absolute range measurement

The dose deposition profile of 62 MeV protons was measured by scanning a diode (model PR60020, PTW, Freiburg, Germany) by steps of 1 mm parallel to the beam direction in a water tank (entrance window of 23 μm polyethylene terephthalate), with a 3 mm thick polyvinyl chloride plate positioned in front, to mimic the entrance wall of the water tank used for the phantom irradiations. The range was determined as the distal point where the dose drops to 80% of the peak dose [30], R_{80} , and obtained by fitting the depth-dose profile to an analytical approximation of the Bragg curve [194]. The impact of the phantom container wall (1.5 mm plexiglas) on the proton range was simulated with TRIM [201]. To account for the different density of polyacrylamide aqueous phantoms compared to water, rectangular Gafchromic EBT3 films (15 mm by 54 mm) were immersed in water and polyacrylamide phantoms at room temperature ($n=3$ and 4, respectively), with an angle of 32° relative to the beam direction (to prevent in-film slowing down of the protons). Films were converted to dose [217] and the relative range difference between water and polyacrylamide was obtained after correcting for quenching effects at the Bragg peak location, following the procedure described by Fiorini et al [218].

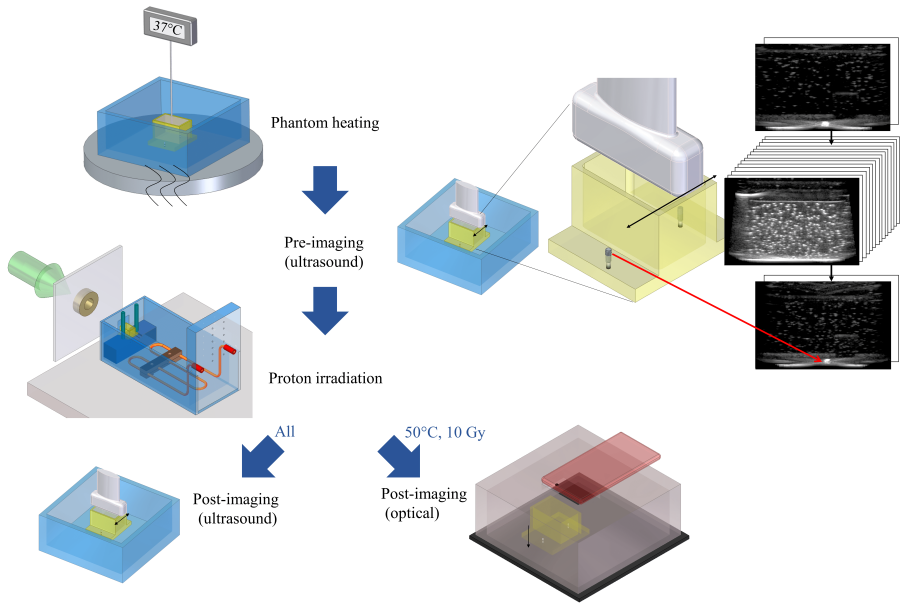


Figure 4.2: Flowchart of the experimental protocol. After preparation, the phantoms were immersed in a water bath equipped with temperature control until they reached the intended temperature (37 °C or 50 °C). Then, all phantoms were imaged with an ultrasound scanner before being irradiated with 62 MeV protons. Afterwards, ultrasound images of all phantoms were acquired again, and optical images of phantoms that were irradiated at 50 °C (10 Gy) were taken from the top with a mobile phone camera.

4.2.4 Data acquisition

Ultrasound images of the phantoms were acquired just prior to and immediately after proton irradiation (or immersion in a heated water bath for control phantoms) by means of an ultrasound research scanner (DiPhAS, Fraunhofer IBMT, Germany). The system was connected to a 7.5 MHz linear array (L7-Xtech, Vermon, France) mounted on a 1D linear stage to scan the phantoms parallel to the proton beam. Plane wave, low acoustic pressure imaging was adopted in order to prevent acoustic droplet vaporization. The axial and lateral resolution of the DiPhAS system was 0.20 mm and 0.63 mm, respectively, as determined by the full width at half maximum (FWHM) of microbubble point scatterers.

In order to match the ultrasound images of the phantom to an absolute position, external fiducials (M2 screws) were incorporated in the phantom containers,

as shown in the magnification in figure 4.2. Phantom scanning consisted of acquiring two frames of the metallic screw on the front side first, then up to 20 parallel images of the phantom across its width, and finally two frames of the metallic screw on the back side.

Additionally, for the three phantoms irradiated at 50 °C that received a dose of 10 Gy, three optical images per phantom were captured with a smartphone camera (12 million pixels, Iphone 8, Apple Inc., United States) in a dedicated light box (figure 4.2). The pictures were acquired one day after the experiment.

4.2.5 Data analysis

Ultrasound gray value analysis

Firstly, a region of interest (ROI) was determined in the ultrasound images to exclude reflections from the phantom walls and surface, as shown in figure 4.3(a). Then, gray value profiles (representative of the microbubble density) were extracted in the ultrasound lateral direction (parallel to the proton beam) by averaging the gray values across the image depth. The obtained profiles were further averaged over the different image slices (approximately 20 per phantom). The 50% drop in gray value was extracted from the profiles as described previously [124], by applying a moving average filter, followed by a derivative filter to locate the slope maximum, in the transition zone, and finally taking the midpoint between the highest and lowest gray values in a 3.6 mm-wide interval surrounding the position of maximum slope (figure 4.3(a)). The intensity-weighted center-of-mass of the fiducials was used to relate the image coordinates to an absolute position. The absolute proton range was compared to the ultrasound contrast by calculating the difference between the R_{80} value and the 50% drop in gray value. Results are presented as mean \pm standard deviation, describing inter-phantom variability.

Ultrasound attenuation analysis

In the presence of a large microbubble density, the actual ultrasound contrast could not be determined accurately along the complete phantom depth due to acoustic shadowing [219, 220]. While both the scattering (hence the image gray value) and the attenuation coefficient (expressed in dB/cm) are proportional to the microbubble concentration [221], estimating the attenuation coefficient might prove more robust against acoustic shadowing artifacts. We therefore modified a recently described approach to evaluate tissue attenuation [222]), as an alternative analysis for the phantoms irradiated at 50 °C, where non-

negligible acoustic shadowing was observed. The methodology involves fitting a known attenuation model to ultrasound beamformed radiofrequency data in the frequency domain. The magnitude spectrum of the backscattered signal can be modelled as:

$$|S(f, z)| = G'|P(f)|A(f, z)B(f, z) \quad (4.2)$$

In this expression, f is the frequency and z is the ultrasound axial depth. $|P(f)|$ is the impulse response or pulse-echo transfer function of the ultrasound array, which can be determined by a pulse-echo reflector measurement, and G' is an unknown gain factor. The impulse response variation across the different transducer elements was considered negligible. Diffraction effects were neglected as plane wave imaging was employed [223] and the attenuation coefficient was estimated along a line, assuming a 1D propagation. $A(f, z)$ denotes the attenuation of the medium and can be described by a function exponentially decaying with depth: $A(f, z) = e^{-2\alpha(f)z}$, where $\alpha(f)$ is the frequency-dependent attenuation coefficient and the factor of two accounts for the two-way travel of the ultrasound wave in the sample. Finally, $B(f, z)$ represents the backscatter coefficient of the medium and was assumed independent of frequency and depth for simplicity, hence $B(f, z) = B_0$. Although the assumption of frequency independence is not strictly correct for bubbly media [169], it has been shown to hold at frequencies above resonance [224, 225]. The equation can be linearized in terms of the parameters to be optimized by applying the logarithmic operator:

$$\log|S(f, z)| = \log|P(f)| + \log|G| - 2\alpha(f)z \quad (4.3)$$

G is a constant which absorbs the backscatter coefficient B_0 and the original gain factor G' . For soft tissues, the attenuation is often assumed proportional to frequency, i.e. $\alpha(f) = \alpha f$. However, the behavior of microbubbles in an ultrasound field is more complex and leads to a resonance peak in the MHz frequency range [226]. Therefore, the frequency-dependent attenuation coefficient of PVA-PFB microbubbles entrapped in polyacrylamide was determined using the reference phantom method [169, 227, 228]. This demonstrated that beyond resonance and within the bandwidth of the ultrasound probe (3 - 9 MHz, see figure 4.3(b)), the attenuation coefficient could be approximated by a linear decrease with frequency, i.e.:

$$\alpha(f) = a - bf \quad (4.4)$$

Substitution of the latter in the linearized equation resulted in a linear least squares optimization problem, which can be simultaneously solved for G , a , and b using a single-shot solver [222]. The peak attenuation $\alpha_p = a - bf_{res}$ was chosen as an estimation of the true bubble density profile as an increase in microbubble density results in a higher resonance peak (figure 4.3(b)). The

measured backscattered spectrum was obtained after having applied coherent beamforming (delay-and-sum followed by plane wave compounding [229]) to the radiofrequency (RF) channel data, and averaged in the frequency domain over the 20 ultrasound frames. Lateral profiles of α_p , parallel to the proton beam, were obtained by solving the optimization problem for 128 positions (corresponding to the center of individual transducer array elements) and the 50% drop in the attenuation profile was determined and compared to the proton range in the same way as for the gray value profiles (see section 4.2.5).

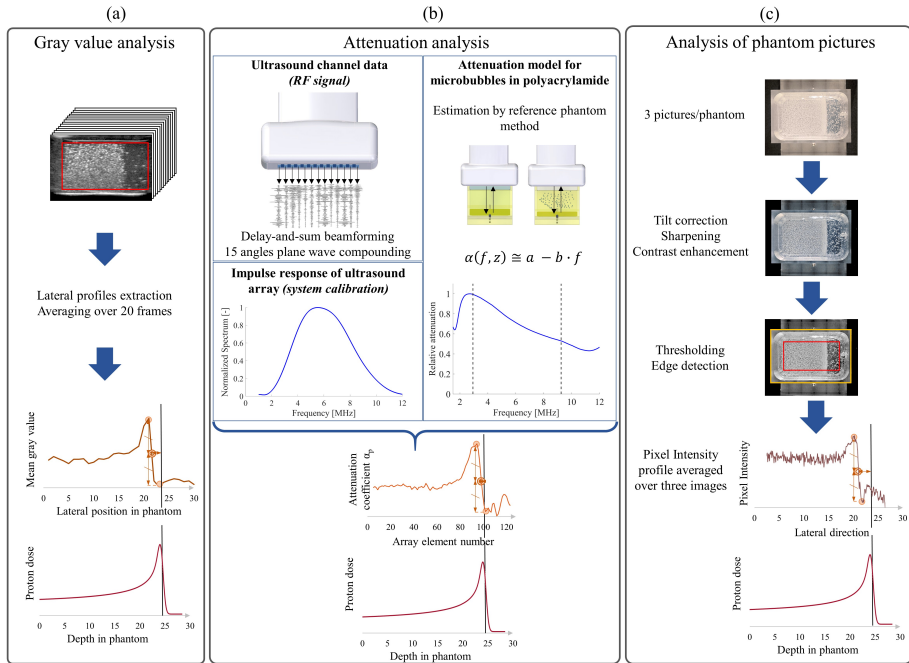


Figure 4.3: Image processing workflow for three different types of analysis based on (a) the ultrasound gray value, (b) the ultrasound attenuation coefficient, and (c) pictures of the phantoms (for 50°C phantoms, 10 Gy). For all three methods, vaporization profiles as a function of the distance traveled by the proton beam were extracted, and related to the proton depth-dose profile and the proton range. The displayed gray value, attenuation and pixel intensity profile schematics do not represent experimental data and are for illustrative purposes.

Analysis of phantom pictures

As an independent method (with respect to the aforementioned ultrasound-based analyses) to locate the distal edge of the microbubble contrast zone, pixel intensity profiles were derived from phantom pictures as depicted in figure 4.3(c). First, tilts in the image plane were removed and the contrast and sharpness were enhanced. Then, images were processed in Matlab (R2019a, MathWorks, NA, USA) and the outer edges of the phantom container were delineated using thresholding followed by edge detection, in order to derive a pixel-to-mm conversion factor based on the known phantom length. Afterwards, an ROI was defined within the polyacrylamide gel, and pixel intensity profiles across the lateral direction were extracted by averaging intensity values along the phantom width. The individual profiles of the three images per phantom were averaged. Finally, the position of the 50% drop in pixel intensity was determined as described earlier (section 4.2.5) and compared with the proton range. The photographic analysis was intended as a semi-quantitative analysis, as the pixel intensity was not expected to be linearly related to the microbubble concentration. However, the sharp drop in bubble concentration could be accurately located on the images and compared to the proton range.

4.3 Results

4.3.1 Radiation response at physiological temperature

Ultrasound images of polyacrylamide phantoms with dispersed PCDA-PFB and PVA-PFB nanodroplets heated to 37 °C prior to irradiation are presented in figure 4.4, and show that a substantial fraction of PCDA-PFB nanodroplets already vaporizes at 37 °C before irradiation (figure 4.4(b)). Due to the large background signal in ultrasound images of PCDA-PFB phantoms, no difference in contrast could be observed between zones proximal and distal to the proton range after irradiation. This lack of thermal stability explains the necessity to shift to PVA-PFB droplets in these experiments at elevated degrees of superheat. Indeed, figure 4.4(a) demonstrates the superior stability of PVA-PFB droplets at temperatures well above the PFB boiling point (-2 °C), resulting in a limited background signal. For PVA-PFB phantoms, a strong increase in contrast was observed proximal to the proton range after irradiation, as shown in figure 4.5(a). Gray value profiles are displayed in figure 4.5(b) for the six irradiated PVA-PFB phantoms and the three control phantoms, together with the proton depth-dose deposition profile. The gray value profiles indicate a rather uniform bubble density, dropping close to the proton range. The signal shift, calculated

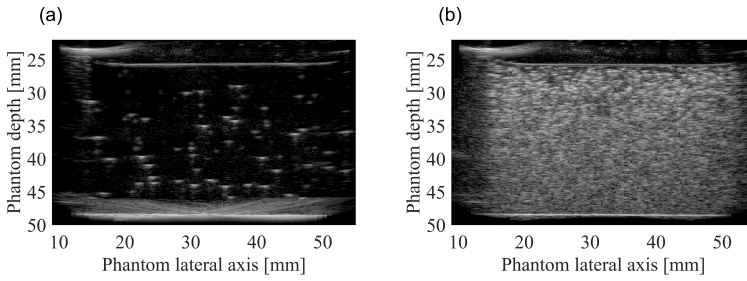


Figure 4.4: Ultrasound images of polyacrylamide gels with (a) dispersed PVA-PFB nanodroplets or (b) PCDA-PFB nanodroplets, after heating to 37 °C through immersion in a warm water bath (no irradiation).

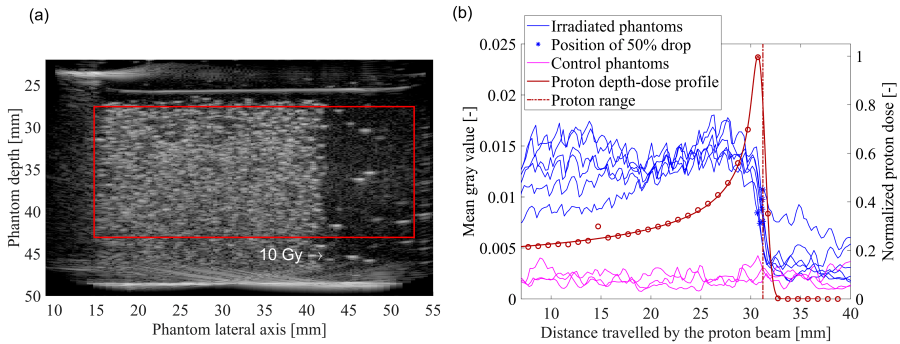


Figure 4.5: Ultrasound image of a polyacrylamide gel phantom with dispersed PVA-PFB nanodroplets, after irradiation by a 62 MeV proton beam (10 Gy dose) at 37 °C. The red rectangle (online version only) is the ROI used to derive gray value profiles. (b) Gray value profiles for six irradiated and three control PVA-PFB phantoms along the lateral axis of the ultrasound image, with the proton Bragg curve and range position superimposed. The position of the 50% drop in mean gray value is indicated by a star on each profile post-irradiation.

as the difference between the proton range (R_{80}) and the position of the 50% drop in ultrasound gray value, was $0.17 \text{ mm} \pm 0.20 \text{ mm}$.

4.3.2 Primary proton sensitization (50 °C)

Ultrasound images of phantoms with dispersed PVA-PFB nanodroplets, heated to 50 °C, are displayed in figure 4.6 before (a) and after proton irradiation with a dose of 10 Gy (b). The small number of background microbubbles

before irradiation (figure 4.6(a)) confirms the thermal stability of PVA-PFB nanodroplets for high degrees of superheat. For irradiated phantoms, a contrast increase was observed in the proton path, with an additional enhancement around the Bragg peak location (figure 4.6(b)), which was also observed visually (figure 4.6(c)). The strength of the induced contrast resulted in acoustic shadowing, particularly in the Bragg peak region. Hence, only the upper rectangular ROI, bounded by the red line (figure 4.6(b)), was used to derive the gray value profiles. For the estimation of the attenuation parameter, the complete ROI was employed (magenta rectangle in figure 4.6(b)). Three different profiles were derived from ultrasound and optical images, as described in section 4.2.5, in order to estimate the microbubble density along the proton path and compare the end of the vaporized zone with the proton range. The profiles are displayed in figure 4.6(d-f) together with the Bragg curve and the proton range. Qualitatively, all three analysis methods yield similar vaporization profiles, with an increase around the location of the Bragg peak and a sharp drop distal to the proton distal dose fall-off. The ratio between the vaporization profiles proximal to the Bragg peak (in the plateau region) and the peak value is higher than the measured skin-to-peak dose ratio of the protons (0.2). Ultrasound attenuation and gray value profiles agree with each other with similar peak-to-plateau ratios, although the ROIs used for the two techniques differ. This demonstrates that the ultrasound attenuation analysis is not adversely impacted by acoustic shadowing, as a full ROI could be employed. For all phantoms, the width of the zone with higher bubble density at the end of the proton range appeared larger than the Bragg peak width. The signal shifts between the proton R_{80} value and the 50% drops in gray value or α_p were $-0.74 \text{ mm} \pm 0.09 \text{ mm}$ and $-0.86 \text{ mm} \pm 0.04 \text{ mm}$, respectively. As an independent evaluation of the relationship between the proton range and the microbubble generation, signal shifts were also derived from phantom pictures and yielded a value of $-0.64 \text{ mm} \pm 0.29 \text{ mm}$.

Finally, an ultrasound image of the phantom irradiated with a clinical dose of 2 Gy is displayed in figure 4.7, together with the corresponding gray value and attenuation profiles. Although less pronounced compared to 10 Gy irradiations, acoustic shadowing is also observed in the Bragg peak vicinity, where the largest microbubble density was found. The signal shifts were -0.52 mm for the gray value profile, and -0.78 mm for the attenuation profile. The peak-to-plateau ratios were higher than for the 10 Gy case, both for the gray value and attenuation profile. The fact that the contrast peak-to-plateau ratio displayed in figure 4.7 is very similar to the peak-to-plateau ratio of the proton dose deposition profile is coincidental, as the microbubble density is not expected to follow the depth-dose deposition profile, but should rather depend on the fluence of the different particles that can trigger vaporization (primary protons and secondaries) and their local LET.

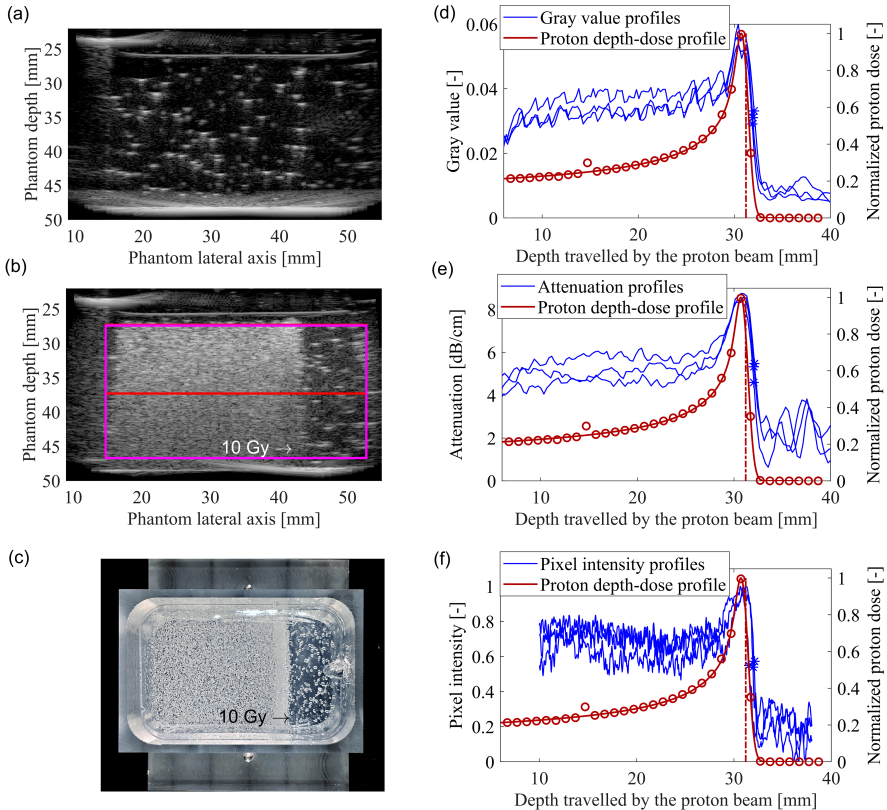


Figure 4.6: Ultrasound images of PVA-PFB nanodroplets dispersed in polyacrylamide hydrogel phantoms and heated to 50 °C, (a) before irradiation, and (b) after proton irradiation with a dose of 10 Gy. The ROI used for ultrasound gray value analysis is displayed in red, and the ROI for attenuation analysis is shown in magenta (online version only). (c) Picture of an irradiated phantom. (d) Gray value and (e) attenuation profiles were derived from the ultrasound images, and the position of the 50% distal profile drop was identified (stars). Additionally, phantom pictures were analyzed to extract pixel intensity profiles (f) and corresponding 50% drop (stars). The proton depth-dose deposition profile is displayed in red (online version only), and the proton range (R_{80}) is the vertical dashed line.

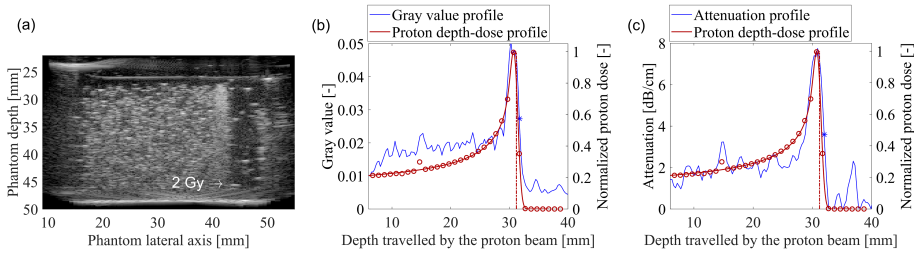


Figure 4.7: (a) Ultrasound image of a polyacrylamide phantom with dispersed PVA-PFB nanodroplets after irradiation with 62 MeV protons (dose of 2 Gy) at 50 °C. (b) Gray value and (c) attenuation profiles derived from the ultrasound images, with the Bragg curve superimposed (in red, online version only) and a vertical line representing the proton range. The stars indicate the 50% distal drop position of the ultrasound-based profiles.

4.4 Discussion

For both temperatures, a noticeable increase in ultrasound contrast was observed after irradiation with 62 MeV protons, confirming the potential of superheated injectable nanodroplets for *in vivo* proton range verification. Comparison between PCDA-PFB and PVA-PFB nanodroplets highlighted the critical role of the encapsulating shell to stabilize the nanodroplets at elevated temperatures, well above the superheated liquid boiling point.

4.4.1 Influence of the temperature on the ultrasound contrast generation

The average ultrasound gray value in the plateau region (and peak region at 50 °C) is shown in figure 4.8(a) for the tested temperatures and compared to our earlier findings at 25 °C [124], demonstrating an increase of the generated ultrasound contrast with temperature. The radiation-induced nucleation theory [113] predicts a temperature-dependent LET threshold given by:

$$\left\langle \frac{dE}{dx} \right\rangle_{L_{eff}} = \frac{W_{tot}}{kR_c} \quad (4.5)$$

where W_{tot} is the total energy required to nucleate a critical embryo of radius R_c in the superheated liquid, and the effective length is given as $L_{eff} = kR_c$. The semi-empirical nucleation parameter k is assumed to be equal to 2, a reasonable assumption for nucleation energies well below 1 MeV [154] (e.g. W_{tot} is 13 keV at 37 °C). Both at 25 °C and 37 °C, the LET thresholds (370 and 145 keV/ μ m,

respectively) are above the maximum LET reached by protons or secondary electrons. Therefore, nucleation is expected to be induced by heavy recoil nuclei generated by non-elastic interactions of protons with the phantom matrix or the nanodroplets themselves, as well as by similarly released alpha particles, whose LET lie in the range 130-190 keV/ μm [196], for the 37°C case. At 50°C, the predicted threshold drops further down to 60 keV/ μm , allowing sensitization to primary protons that reach an LET up to 70-90 keV/ μm at the very end of their range [149], while being too high to observe vaporization induced by secondary electrons (LET of 25-30 keV/ μm [154]). This sensitization to the primary proton beam is clearly demonstrated by the strong contrast increase at the end of the vaporization curves and could even be observed visually (figure 4.6 and 4.7).

The contrast increase with temperature in the plateau region can thus be explained by the decrease of the LET threshold with temperature, making nanodroplets sensitive to a broader range of charged particles. Furthermore, the higher the temperature, the longer the track length over which charged particles have a sufficient LET to induce nanodroplet vaporization, and consequently the higher the likelihood of vaporization. In contrast to the 25°C and 37°C case, a strong increase in gray value was observed at the end of the proton range at 50°C. As shown in figure 4.8(a), the contrast difference between the plateau region and the peak ultrasound contrast is rather small compared to the fluence ratio between primary protons and secondary particles (as only 1% of the primary protons undergo non-elastic nuclear interactions per cm [203]), which would predict a stronger contrast increase upon proton sensitization. The relatively low contrast increase observed at the end of the proton range could be attributed to the imaging modality, as the microbubble concentration was high enough to induce signal saturation and acoustic shadowing. Moreover, the large microbubble density observed in the peak might have caused a drop of the local nanodroplet concentration over the course of the irradiation, leading to a progressive decrease of the probability of a proton-droplet interaction. These hypotheses are further supported by the lack of proportionality observed between the peak contrast and the proton peak dose, as shown by the 2 Gy and 10 Gy bars of figure 4.8(a).

4.4.2 Influence of the temperature on the relationship between the proton range and the ultrasound contrast

Both at 37°C and 50°C, a reproducible relationship was obtained between the proton depth-dose deposition profile and the generated ultrasound contrast, as evidenced by the sub-millimeter reproducible shift between the 50% signal drop and the proton R_{80} value. Interestingly, despite small (<0.3 mm) variations on

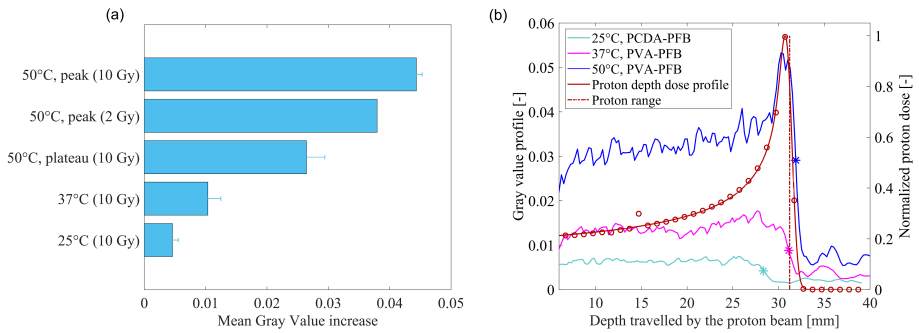


Figure 4.8: (a) Gray value increase observed on ultrasound images due to nanodroplet vaporization at different temperatures. The 25 °C data correspond to a previous study with PCDA-PFB nanodroplets. Error bars correspond to the standard deviation in gray value increase, for available phantoms at each temperature (b) Ultrasound gray value profiles for three temperatures were superimposed on a Bragg curve. The 50% drop in contrast position is indicated by a star.

the exact signal shift, a high reproducibility of the signal curves at 50 °C was achieved, irrespective of the applied analysis method. Comparing the profiles at 37 °C and 50 °C with our earlier findings at 25 °C (figure 4.8(b)), one can notice that the drop in ultrasound contrast shifts deeper into the phantom with increased degree of superheat. This is also caused by the drop in LET threshold with temperature. Indeed, at 25 °C, the energy of the primary protons in the final few millimeters of their range was too low to produce recoil nuclei with sufficient LET to trigger vaporization events [124]. At 37 °C, most secondary particles will have a sufficient LET, and the signal generation is expected to be solely dependent on the occurrence of nuclear reactions. Hence, the proton beam needs to have enough energy to exceed the Coulomb barrier. The most important elements in the phantom are C, N, O and F (apart from H), with approximate Coulomb barriers between 3-5 MeV [230]. The corresponding residual proton range explains why the ultrasound contrast drops earlier than in the 50 °C case, where the primary proton sensitization ensures contrast generation until the very end of their range. Both at 25 °C and 37 °C, the shape of vaporization profiles is dictated by the production cross-sections of relevant secondary particles as well as their likelihood to traverse a droplet while having a sufficient LET.

At 50 °C, the end of the vaporization profile is expected to coincide with the end of the proton range. Due to the energy dispersion of the proton source combined with range straggling, the range spread was modeled as a Gaussian with a sigma value of 0.54 mm (based on the analytical fit of the measured

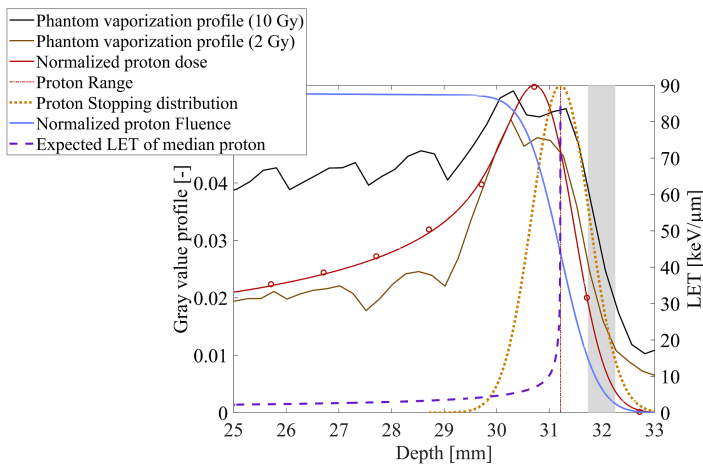


Figure 4.9: Representative gray value profiles at 50 °C (2 Gy and 10 Gy) superimposed on the proton depth-dose deposition profile, proton fluence and Gaussian distribution of proton stopping positions. The shaded area represents the confidence interval on the position of the 50% drop in ultrasound gray value (extracted from the three phantoms which received a dose of 10 Gy). The LET of a proton stopping at the R_{80} position is also illustrated (dashed curve).

proton depth-dose deposition). Figure 4.9 overlays ultrasound gray value profiles after irradiation (doses of 2 Gy and 10 Gy) with the estimated proton stopping distribution, indicating that the ultrasound contrast profile is broader and peaks slightly earlier than expected. Indeed, the contrast profile was expected to peak at the R_{80} position, where the density of stopping protons is the highest (dotted curve). The broadening of the peak could be attributed to the potential ultrasound contrast saturation, which results in the true contrast peak being cropped, and by the fact that the gray value profiles are modulated by the Point Spread Function (PSF) of the ultrasound system (0.63 mm FWHM). These also contribute to the negative signal shift of $-0.74 \text{ mm} \pm 0.09 \text{ mm}$. The slight offset ($< 1 \text{ mm}$) between the contrast peak and the proton range is believed to arise from measurement uncertainties elaborated later. While for lower temperatures the signal shift between the 50% drop and R_{80} value was preferred (maximal slope at 50% drop makes this characteristic value more robust to fluctuations on the profile), the 50% drop is less relevant when proton sensitization occurs. A more interesting relationship would in this case be between the ultrasound signal peak and the proton range, as these are expected to be aligned. However, due to a presumed saturation of the signal, we opted not to do so here.

4.4.3 Implications, limitations and future directions

In this study, the radiation-induced vaporization of superheated, injectable nanodroplets was validated at physiological temperature. As shown in figure 4.4, it was crucial to ensure the stability of the nanodroplet formulation at increased temperatures. While PCDA-PFB droplets were unsuitable, PVA-PFB droplets showed promising thermal stability *in vitro*. This also demonstrates the robustness of the concept to different chemical formulations. Indeed, while we expect that the shell viscoelastic properties and surface tension have an influence on the LET threshold for vaporization (the influence of the surrounding polyacrylamide matrix was found to be negligible), the latter is mainly defined by the superheated core liquid. This knowledge, in combination with the versatility of nanoplatforms under development in different fields of biomedical research, allows the further development of these or similar particles towards an *in vivo* application where additional modifications of the shell (e.g. pegylation) might be required to secure biocompatibility and reasonable circulatory lifetimes [231]. Moreover, functionalization of the shell with targeting ligands (e.g. antibodies, peptides, etc.) could achieve nanodroplet accumulation inside the tumor volume, ensuring signal generation at the location of primary interest and possibly counteracting biological wash-out. However, potential particle detachment due to vaporization remains to be assessed. On the long-term, we can even envision targeted, radiation-induced release of chemotherapeutics by upgrading these functionalized contrast agents towards drug delivery vehicles [232]. On a shorter term, also non-targeted droplets could serve *in vivo* applications either in combination with online imaging, visualizing vaporization events in real-time, or for proton therapy of liver tumors, as particles of this size are expected to spontaneously accumulate in the liver (clearance by the reticulo-endothelial system [232]).

The strong ultrasound contrast resulting from the phase transition of nanodroplets into echogenic microbubbles enables the extraction of vaporization profiles whose sharp fall-off could be related to the proton range with sub-millimeter accuracy, both through gray value analysis and attenuation estimation. This was confirmed independently, for the 50 °C phantoms, by optical images. Uncertainties in the alignment of vaporization profiles with the proton depth-dose profile were estimated to be 0.22 mm (the standard deviation of the alignment fiducials' lateral ultrasound coordinate used for image registration, see figure 4.2) for ultrasound-based analysis (gray value and attenuation), and 0.36 mm (the inter-phantom standard deviation of the phantom container length retrieved from the images) for optical images. Additionally, as microbubbles could not be counted individually due to the large bubble densities, the image resolution was limited by diffraction [233] and the microbubble localization accuracy was characterized by the lateral Gaussian PSF of the ultrasound

system (0.63 mm). Moreover, the reported signal shifts also rely on the accuracy of the absolute R_{80} value, which suffers from uncertainty (± 0.5 mm) related to the limited resolution of the diode and Gafchromic film measurements, as well as TRIM simulation accuracies. Overall, the three evaluation methods (gray value, attenuation, optical) agreed on the level of the respective image resolution, cross-validating each other. However, this sub-millimeter accuracy was reported in idealized *in vitro* conditions. The signal shift retrieval performance remains to be determined in physiological conditions, with heterogeneous tissue densities, and might be influenced by different factors such as inhomogeneities in nanodroplet distribution, speed of sound mismatch, multiple scattering or acoustic shadowing. While attenuation estimation could help reduce the effects of acoustic shadowing by dense microbubble populations, online high frame rate imaging (up to thousands of frames per second) could be beneficial to minimize the impact of ultrasound contrast saturation or multiple scattering, for instance. Besides, online ultrasound imaging (either active or passive, relying on the detection of individual acoustic signals emitted during phase-change [234]) enables real-time feedback over the course of the irradiation, and could greatly improve the microbubble localization accuracy through super-resolution ultrasound imaging [235]. While targeted microbubbles could potentially be imaged offline a few minutes post-irradiation (expecting their *in vivo* lifetime to be sufficient [236]), online high frame rate imaging would allow to perform range verification both for targeted or non-functionalized, freely-flowing contrast agents, by means of differential imaging and microbubble tracking [235].

Similarly to PET and Prompt Gamma Imaging, at 37 °C, the radiation-induced nanodroplet response is expected to rely solely on nuclear reaction products, only indirectly visualizing the proton irradiation. While the vaporization profiles could qualitatively be explained by means of the radiation-induced nucleation theory, comprehensive Monte Carlo simulations should be the next step towards a full understanding of the relationship between different features of the vaporization profiles and the proton range. Moreover, nanodroplet vaporization was evaluated in a mono-energetic, broad proton beam, and should be assessed for clinically-relevant treatment plans, where the ultrasound contrast relationship to the proton range is expected to become more complex. The contrast generation was evaluated for a limited range of doses (2 and 10 Gy) and the minimum dose for which the proton range can be accurately detected remains to be determined. The impact of the generated gaseous microbubbles on the proton treatment delivery was estimated to be negligible (shift in range well below 1 mm) for clinically-relevant doses. In comparison with other range verification techniques currently under investigation, ultrasound-based detection of nanodroplet vaporization for range verification would be particularly suitable for treatment sites of sonic accessibility, such as the prostate, breast or liver, where tissue motion and anatomical changes tend to lead to large range

uncertainties [15, 206]. The advantage of using ultrasound for conventional imaging would be that it enables direct co-registration of the proton range with tissue anatomy [40, 237].

Interestingly, at 50 °C, we demonstrated that a sufficient degree of superheat sensitizes the superheated core to protons, motivating further exploration of this technique for application to proton dosimetry. Nevertheless, achieving such a degree of superheat at body temperature would require additional modifications of the nanodroplet design. One possibility would be to change the core to a lower-boiling point liquid, e.g. octafluoropropane (b.p. = −37 °C). However, the reduced stability makes these droplets difficult to handle [122]. Recently, endoskeletal droplets with highly tunable vaporization properties were introduced [238], potentially bringing direct *in vivo* proton detection and range verification within reach.

4.5 Conclusion

The ultrasound contrast generation from phase-change nanodroplets after proton irradiation at 37 °C and 50 °C was evaluated in tissue-mimicking phantoms. This elucidated the importance of the nanodroplet design to ensure stability at elevated temperatures and demonstrated the feasibility of the concept for a different nanodroplet formulation. Our recent proof-of-concept study, which showed radiation-induced vaporization of superheated nanodroplets in proton beams at 25 °C, was extended to physiological temperature, taking the next step towards an *in vivo* application. Raising the temperature further to 50 °C led to a strong contrast increase at the Bragg peak location attributed to the vaporization of the nanodroplets by primary protons at the end of their range. Comparison of the radiation-induced contrast generation at different temperatures showed that the overall contrast increases with increasing degree of superheat and that the contrast profiles shift closer towards the proton range. This was explained by the radiation-induced nucleation theory, as the LET threshold decreases with temperature, resulting in vaporization by heavy recoil nuclei only at 25 °C, lighter nuclei such as alpha particles at 37 °C, and proton detection at 50 °C. The positions of the 50% drop in contrast were retrieved from ultrasound images (at 37 °C and 50 °C) and optical images (50 °C) and were related to the proton range with sub-millimeter reproducibility. Overall, these findings further confirm the potential and tunability of injectable phase-change nanodroplets as a proton range verification technique in an indirect (through secondary reaction products) mode and unveil the possibility of reaching direct range verification through detection of primary protons.

4.6 Acknowledgments

The authors thank the "Centre de Ressources du Cyclotron" of UCLouvain for the irradiation experiments, absolute range measurements and fruitful discussion. The authors also thank Fraunhofer IBMT for lending the DiPhAs ultrasound scanner, and the mechanical and electrical staff of the Physics Department of KU Leuven for manufacturing phantom containers as well as the water tank with temperature control. This work has been supported by the European Union's Horizon 2020 research and innovation programme under grant agreement n°766456 ("AMPHORA"). BC received a PhD fellowship fundamental research from the Research Foundation Flanders (n°11A9520N).

“We do not need magic to transform our world.
We carry all the power we need inside ourselves
already.”

J. K. Rowling

5

Spatiotemporal distribution of nanodroplet vaporization in a proton beam using real-time ultrasound imaging for range verification

*Gonzalo Collado-Lara**, *Sophie V. Heymans**, *Marta Rovituso*, *Bram Carlier*,
Yosra Toumia, *Martin Verweij*, *Gaio Paradossi*, *Edmond Sterpin*, *Hendrik J.*
Vos, *Jan D’hooge*, *Nico de Jong*, *Koen Van Den Abeele*, and *Verya Daeichin*

Published in *Ultrasound in Medicine & Biology*, 48(1), 2022, p. 149-156.

The potential of proton therapy to improve the conformity of the delivered dose to the tumor volume is currently limited by range uncertainties. Injectable superheated nanodroplets have recently been proposed for ultrasound-based *in vivo* range verification, as these vaporize into echogenic microbubbles upon proton irradiation. In previous studies, offline ultrasound images of phantoms with dispersed nanodroplets were acquired after irradiation, relating the induced vaporization profiles to the proton range. However, the aforementioned method did not enable the counting of individual vaporization events, and offline imaging

*joint first author

cannot provide real-time feedback. In this study, we overcame these limitations using high frame rate ultrasound imaging with a linear array during proton irradiation of phantoms with dispersed perfluorobutane nanodroplets at 37 °C and 50 °C. Differential image analysis of subsequent frames allowed to count individual vaporization events and to localize them with a resolution beyond the ultrasound diffraction limit, enabling spatial and temporal quantification of the interaction between ionizing radiation and nanodroplets. Vaporization maps were found to accurately correlate with the stopping distribution of protons (at 50 °C) or secondary particles (at both temperatures). Furthermore, a linear relationship between the vaporization count and the number of incoming protons was observed. These results show the potential of real-time high frame rate contrast enhanced ultrasound imaging for proton range verification and dosimetry.

5.1 Introduction

Proton therapy is emerging as an advanced radiation therapy modality for tumors in critical locations [239]. Since protons deposit most of their dose in a narrow (few millimeters wide) peak at the end of their range, called the Bragg peak, followed by a sharp distal dose fall-off, the spatial dose distribution can be better conformed to the tumor volume than in conventional radiotherapy, thereby improving healthy tissue sparing [104]. In practice, however, the physical benefits of protons cannot be fully exploited since deviations from the planned dose distribution may arise from different sources of range uncertainty, including treatment planning, setup errors, or patient and organ motion [30,181]. Therefore, substantial safety margins are included in the treatment plan [30,206], reducing the potential improvement compared to conventional radiotherapy. The benefits of proton therapy could be maximized if deviations during the treatment were detected and corrected through real-time spatial verification, especially in moving targets [240–242]. Although several *in vivo* range verification techniques are being investigated [34,39–41,43,182], none of them has been widely adopted in clinical practice.

The detection of charged particles, amongst which protons, can be achieved in superheated liquids [111,113,115], which can remain in a metastable liquid phase above their boiling point owing to the removal of heterogeneous nucleation sites [147]. The only mechanism remaining for vaporization is homogeneous nucleation, occurring when a gas embryo grows larger than a critical size [119]. Consequently, a charged particle can induce vaporization of the superheated liquid if it deposits a sufficient amount of energy to nucleate such a critical embryo within a length comparable to the embryo size [113]. Accordingly, the

condition for vaporization of superheated liquids depends on the density of energy deposited by the charged particle per unit length, namely its Linear Energy Transfer (LET). Furthermore, the energy necessary to nucleate a critical embryo decreases with the temperature excess above the liquid boiling point, i.e. the degree of superheat [113].

Superheated nanodroplets have been introduced as a novel injectable ultrasound contrast agent capable of turning into echogenic microbubbles upon controlled energy deposition, e.g. acoustic or thermal [71–74, 243]. It was only recently reported that the phase-change mechanism holds for superheated encapsulated nanodroplets irradiated by protons [124, 244]. The combination of the long-standing knowledge of radiation-induced nucleation with the recent developments in producing stable, injectable nanodroplets opens the door to ultrasound-based detection and monitoring of ionizing radiation *in vivo*.

Previous studies of nanodroplet vaporization using a passively scattered proton beam have demonstrated a sub-millimeter reproducibility of the shift between the proton range and vaporization profiles derived from the ultrasound grey value or attenuation coefficient [124, 244]. However, offline ultrasound imaging does not enable real-time verification and, potentially, compensation of deviations during treatment delivery. Moreover, those studies revealed the presence of acoustic shadowing and image saturation, which led to a complex relation between ultrasound contrast and proton fluence [219], limiting the performance for dosimetry and range verification. Indeed, obtaining a sufficient response for accurate range verification and dosimetry *in vivo* will require high bubble concentrations, which precludes individual bubble counting on offline ultrasound images. Moreover, real-time verification during proton therapy would allow to stop the beam during the treatment in case of deviation. Online imaging would be performed with the patient in the treatment position, and could be more robust to potential errors induced by nanodroplets and microbubbles biological washout, compared to offline, post-irradiation imaging. Therefore, in this study, we transition to real-time high frame rate ultrasound imaging during irradiation in a proton beam in order to detect individual vaporization events and localize them with an accuracy beyond the ultrasound diffraction limit. This allowed temporal and spatial quantification of the interaction between charged particles and superheated nanodroplets.

5.2 Materials and Methods

5.2.1 Nanodroplet and phantom synthesis

Nanodroplets with a perfluorobutane core (boiling point -2°C) and a crosslinked polymeric shell made of polyvinyl alcohol (PVA) were prepared according to the protocol described in [244]. Briefly, gaseous perfluorobutane was injected in an empty vial and liquefied by immersion in liquid nitrogen. After addition of an aqueous telechelic PVA solution (2% w/v PVA, 0.2% w/v sodium metaperiodate), the vial was sonicated in an ice-cold water bath for 15 minutes. The resulting nanodroplets were then washed by a two-step centrifugation. Dynamic light scattering measurements yielded intensity-weighted size distributions with a median nanodroplet size of 799 nm and a polydispersity index of 0.3 [244]. The droplets were dispersed in an aqueous polymer gel, which entrapped their position, in order to achieve a homogeneous distribution within the phantom. The phantom matrix was made of a carbomer solution (0.1% w/v) and prepared according to [245]: after diluting Carbopol 2050 powder (Lubrizol, Wickliffe, USA) in Milli-Q water, the solution pH was adjusted to 7 by adding NaOH while monitoring with a pH meter (Consort C830, Turnhout, Belgium). This non-Newtonian fluid was able to entrap the nanodroplets and resulting microbubbles, keeping the dispersion of contrast agents homogeneous throughout the experiment, but did not impede the microbubble oscillations [246]. Prior to nanodroplet dispersion, the carbomer solution and phantom containers (54x26x31 mm) were first heated to the desired temperature (37°C or 50°C). Then, the carbomer solution was poured in phantom containers (54x26x31 mm), and a given volume of nanodroplets was dispersed homogeneously in the gel by manual stirring. The phantoms were subsequently immersed in a water tank preheated to 37°C or 50°C for irradiation. The perfluorobutane concentration in the phantom was assessed with NMR spectroscopy (400 MHz Avance II, Bruker Biospin GmbH, Rheinstetten, Germany) on the day following the proton experiments and was $19\ \mu\text{M}$. For this concentration, the impact of both liquid-filled nanodroplets and gas-filled microbubbles on proton therapy treatment delivery (i.e., the proton range) is expected to be negligible.

5.2.2 Phantom irradiation

The phantoms were irradiated in the research beam line of the Holland Proton Therapy Center in Delft (HPTC). The water tank was aligned in order to have its outer wall positioned at the beam isocenter and the phantom traversed by the proton beam through its center (Fig. 5.1(a)). Reproducibility of phantom

positioning with respect to the proton range was ensured with a locking pin. The distance between the water tank's outer wall and the phantom entrance was 13.3 cm. The R&D proton room of HPTC has an horizontal, fixed beam line which provides therapeutic beam from 70 up to 250 MeV with beam intensities from 1 up to 800 nA at beam extraction. A beam energy of 154 MeV was chosen to ensure that the proton range would approximately correspond to the phantom mid-length, as shown in figure 5.1(a). As the accelerator produced a single pencil beam, the lateral beam profile was a 2D Gaussian. For each irradiation, the total number of protons was counted with an ionization chamber (beam monitor, DE.TEC.TOR, Turin, Italy) inserted in the beam path (Fig. 5.1(a)). The beam currents, total number of protons, irradiation durations and phantom doses are given in Table 5.1. The radiation dose used at 50 °C was relatively close to the typical dose delivered in a proton therapy session (~ 2 Gy), while a higher dose was used at 37 °C to account for the fact that at this temperature, nanodroplets are only sensitive to high-LET secondary particles, which are relatively rare [244].

	Temperature	Cyclotron current	Number of incoming protons	Irradiation time	Peak dose	Averaged dose across the Gaussian FWHM at the Bragg peak
Phantom 1	37 °C	80 nA	$7.96 \cdot 10^9$	4.93 s	14.19 Gy	9.25 Gy
Phantom 2	50 °C	25 nA	$2.61 \cdot 10^9$	5.20 s	4.65 Gy	3.03 Gy

Table 5.1: Irradiation settings.

5.2.3 Characterization of the proton beam

The spatial dimensions of the proton beam were independently characterized after the experiment. The depth-dose distribution was measured using a multi-layer ionization chamber (QubeNext, 2.43 mm spacing, DE.TEC.TOR, Turin, Italy) and fit to an analytical expression of the Bragg curve [194] to obtain the proton range R_{80} (i.e. distal position at which the dose has dropped to 80% of its peak value [15, 30]). The impact of the in-beam ionization chamber, water tank entrance wall (9.5 mm, PMMA) and phantom container entrance wall (2 mm, PVC) on the range was estimated by calculating their water equivalent thickness [247]. The phantom was considered water equivalent, as it was made of 99.9% water. As nanodroplets are vaporized by individual charged particles at the end of their range (i.e., where the LET is maximal), the distributions of their ranges (also called "stopping distributions") was computed to be compared to nanodroplet vaporization maps. The stopping distribution of primary protons in the beam direction was modelled as a Gaussian centered on the R_{80} position, defined as "the depth at which half the surviving primaries (...) have stopped" [15]. The standard deviation, characterizing the range

dispersion, was obtained from the analytical Bragg curve fit. The entrance lateral spot profile was measured at the isocenter with a scintillating screen detector (LynxPT, IBA Dosimetry, Schwarzenbruck, Germany). Lateral spot spreading in water was modelled using a Gaussian approximation and applying the Highland formula [15, 248]. The combination of the beam model and online proton count enabled to compute the 3D proton stopping distribution and absorbed dose for each phantom. Aside from protons, nanodroplets can also be vaporized by heavy secondary particles, which are produced by nuclear reactions between primary protons and atomic nuclei from the medium. As those secondary particles have a very limited range (few microns), contrarily to protons, their stopping distribution was assimilated to their production distribution. The spatial distributions of secondary reaction products generated from the nuclear reaction $p+^{16}\text{O}$ were also derived from the production cross-section of relevant particles [200].

5.2.4 Online ultrasound imaging and image processing

Real-time ultrasound imaging during proton irradiation was achieved by fixing a linear ultrasound array (ATL L12-5, 38 mm aperture) outside the water tank (acoustic coupling was ensured through ultrasound gel and a 20 μm polyester window) (Fig. 5.1(a)). The side of the phantom facing the ultrasound probe was also covered with an identical acoustically-transparent window. The array was connected to a research platform (Verasonics Vantage 256, Kirkland, USA) to image phantoms at 1000 frames per second during irradiation, by use of a plane wave (0° , no angle compounding) imaging sequence. The ultrasound center frequency was 9 MHz, and the peak negative pressure of the plane waves was 370 kPa (characterized with a 0.075 mm needle hydrophone, Precision Acoustics, Dorchester, England), well below the threshold for acoustic droplet vaporization [249]. The ultrasound RF data was beamformed offline using the Verasonics beamformer. Differential imaging was performed by subtracting subsequent frames (Fig. 5.1(b)), allowing to identify newly formed echogenic microbubbles (radiation-induced vaporized nanodroplets), which appeared as bright spots in the subtracted frames (Fig. 5.1(c)). As the vaporization events per frame were sparse, they could be individually detected as in Ultrasound Localization Microscopy [195, 250], with a resolution overcoming the ultrasound diffraction limit ($<50 \mu\text{m}$) [77, 78]. The events were detected in the differential images by intensity thresholding and localized by the weighted average centroid of their Point Spread Function. To determine the distance between the ultrasound probe and the entrance of the proton beam, a fiducial object of known absolute position was imaged between irradiations. This step provided us with an absolute reference in the direction parallel to the beam in order to compare

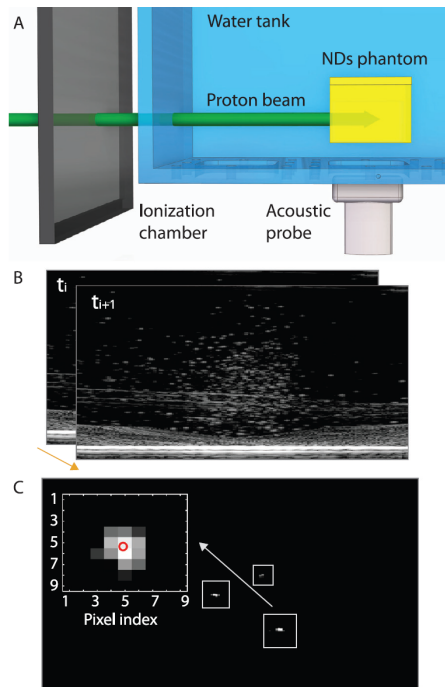


Figure 5.1: (a) Schematic representation of the setup: the proton beam was used to irradiate nanodroplets (NDs) dispersed in a phantom (yellow), which was imaged in real-time with an ultrasound array. Simultaneously, an ionization chamber counted the incoming protons. (b) Subsequent frames were subtracted to isolate vaporization events. (c) Example of differential imaging result, showing three sparse microbubbles. The weighted average centroid of each newly formed bubble was localized.

range estimates from the obtained vaporization maps to ionization chamber measurements. In the direction orthogonal to the beam, the distance between the beam axis and the probe was not measured. Therefore, the vaporization counts and the beam profile in the orthogonal direction were aligned during post-processing.

5.3 Results and discussion

5.3.1 Influence of the temperature on the vaporization response

Movies of the ultrasound B-mode frames acquired during proton irradiation of both phantoms are available online as supplementary materials, together with the corresponding movies of the differential images and accumulated vaporization events. The 2D maps of the vaporized nanodroplets detected during proton irradiation at 37 °C and 50 °C are shown in figure 5.2. A considerable difference in vaporization density and location can be observed for the two temperatures, with the presence of sparse vaporization events mostly in front of the Bragg peak (dose peak) at 37 °C (Fig. 5.2(a)), and a high vaporization density close to the proton range at 50 °C (Fig. 5.2(b)). We attribute this difference to the variation of the LET threshold for vaporization with temperature, leading to the detection of different charged particles. It was previously shown for the droplets used in these experiments that at moderate degrees of superheat, vaporization is induced by high-LET secondary particles only [124, 244], which can be produced by nuclear reactions up until the proton energy drops below the Coulomb barrier (the energy barrier that protons should overcome to trigger a nuclear reaction with an atom from the medium). Only at high degrees of superheat is the vaporization threshold sufficiently low ($< 70 \text{ keV}/\mu\text{m}$) for protons to directly vaporize nanodroplets at their individual Bragg peak [244]. This explains the enhancement observed in figure 5.2(b) at the proton range (where the majority of the primary protons stop), just beyond the dose maximum. The difference in number of vaporization events stems from the fact that non-elastic nuclear reactions are relatively rare events (1% per cm [203]), yielding a number of secondary particles much lower than primary protons. At 50 °C, the bubble density within the peak zone after irradiation was too high to allow the localization of single bubbles on post-irradiation images, highlighting the need for high frame rate differential imaging.

5.3.2 Spatial quantification of the vaporization events

Since vaporization events were not expected to be directly proportional to the absorbed dose, but rather to be related to the number of stopping primary protons and secondaries, the spatial distribution of bubble count was compared to these beam features in figure 5.3. 2D maps are represented in Figs 5.3(a1) and 5.3(b1) for 37 °C and 50 °C, respectively. Vaporization count profiles were obtained by binning the location of all vaporization events in the direction

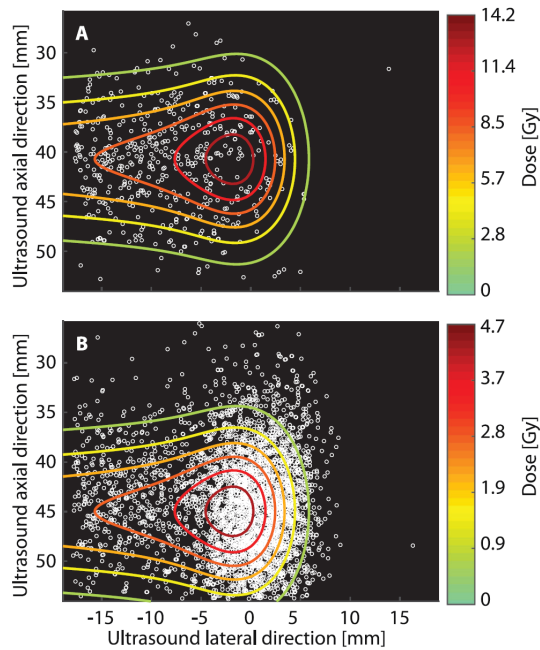


Figure 5.2: Vaporization maps at 37 °C (a) and 50 °C (b) overlaid with the beam dose distribution (the field of view limits match the phantom dimensions). The same nanodroplet concentration was employed in both phantoms, while the maximum dose was higher at 37 °C.

parallel (Figs 5.3(a2), 5.3(b2)) and orthogonal (Figs 5.3(a3), 5.3(b3)) to the proton beam. Here, the red color was used to display the spatial distribution of the stopping positions of individual protons inside the phantom, and the blue color represents the spatial density of relevant secondary particles.

At 37 °C, the microbubble count profiles are compared to the spatial distribution of heavy secondaries ($Z > 1$), as those are expected to have a sufficient LET to vaporize nanodroplets [244]. Qualitatively, bubble count profiles closely resemble the secondaries distribution (Fig. 5.3(a2-3)). In order to compare the lateral spot spreading to the bubble count profile (Fig. 5.3(a3)), a Gaussian fit was applied to the latter, yielding a standard deviation ($\sigma = 5.33$ mm) close to the dispersion of secondaries ($\sigma = 5.14$ mm). At 50 °C, the projection of the microbubble counts on the axis parallel to the proton beam (Fig. 5.3(b2)) clearly illustrates that vaporization is induced both by primary protons at the end of their range, responsible for the observed Gaussian peak, and by secondaries ($Z \geq 1$, including secondary protons), responsible for the plateau proximal to the proton range.

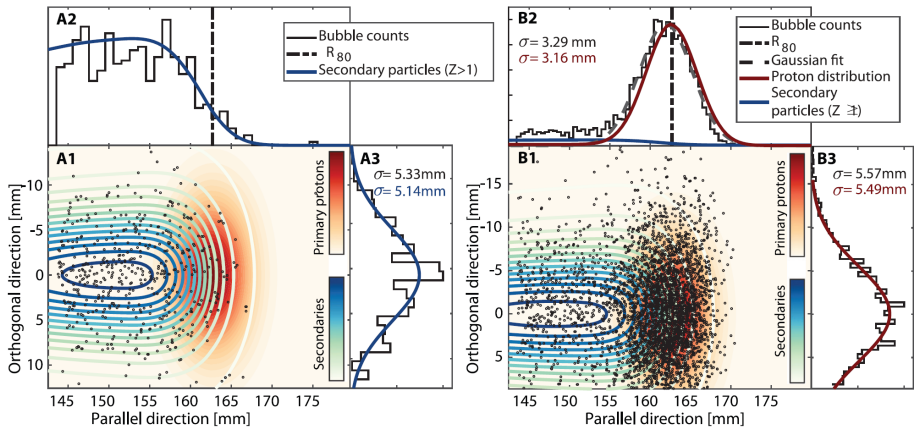


Figure 5.3: Nanodroplet vaporization distribution at 37°C (a1) and 50°C (b1) superimposed on the distribution of the stopping positions of primary protons (red color scale) and heavy secondaries ($Z > 1$ (a1) or $Z \geq 1$ (b1), blue color scale). The vaporization counts were projected in the direction parallel (a2,b2) and orthogonal (a3,b3) to the proton beam, and compared to the corresponding projections of the stopping distribution of secondary particles (a2,a3) and primary protons (b2,b3). The proton range is displayed with a dashed vertical line (a2 and b2). The standard deviations (σ) are displayed for both the bubble count profiles (Gaussian fit) and the charged particles profiles.

This is further supported by the sub-millimeter distance (0.8 mm) between the peak in bubble count (161.9 mm) and the peak in stopping protons (162.7 mm, R_{80} position), which we attribute to experimental uncertainties. Importantly, the position of the vaporization count peak, including an uncertainty window of $\pm 3\sigma$, was within ± 0.5 mm of its final value from 575 events on, indicating that for the tested nanodroplet concentration, a dose of 0.7 Gy (dose maximum reported at the spot center) would have been sufficient to obtain a range estimate with a ± 0.5 mm precision. Moreover, the standard deviation for the bubble count (Gaussian fit) was within 0.2 mm of that of the range (Fig. 5.3(b2)) and within 0.1 mm of the beam lateral standard deviation (Fig. 5.3(b3)).

Overall, the profiles displayed in figure 5.3 illustrate the ability of the obtained vaporization maps to accurately represent different spatial features of the proton beam, depending on the temperature. This has implications not only for range verification, as bubble count profiles can be directly (50°C) or indirectly (37°C) related to the proton range, but also for dosimetry, as both the number of activated droplets and their spatial distribution can be accurately quantified. The ratio between the microbubble peak and its plateau at 50°C (9.31) is

smaller than the ratio between primary protons and secondaries (25.5), which might be due to the fact that the vaporization efficiency depends on the charged particle type [154]. Also, the standard deviation of the microbubble Gaussian distribution only slightly exceeds the proton stopping dispersion (by 4%), while it was largely overestimated (by more than 100%) on previous post-irradiation offline recordings [244]. To summarize, online high frame rate imaging was shown to be a reliable tool to characterize the interaction of nanodroplets with ionizing radiation.

5.3.3 Temporal quantification of the vaporization events

Next to spatial quantification, online ultrasound imaging allowed to examine the temporal vaporization rate and assess the relationship between the vaporization counts and the proton fluence. Figure 5.4(a) compares the cumulative number of vaporization events recorded during irradiation to the number of stopping protons in the field of view of the ultrasound probe (the elevational plane thickness was approximated to a quarter of the elevational aperture [251]). We assumed a constant proton flux during irradiation, neglecting any small deviation in beam current. The results indicate a linear relationship between the number of vaporization events and the number of protons, with a coefficient of determination of 0.9947 at 37 °C and 0.9997 at 50 °C. Comparing both temperatures, a 25-fold increase in the number of generated microbubbles was observed, from 460 bubbles per 10^9 stopping protons at 37 °C to $11.6 \cdot 10^3$ bubbles per 10^9 stopping protons at 50 °C. The residuals are displayed in Fig 5.4(b-c), and show an RMS error of 10 events at 37 °C and 19.5 at 50 °C. The maximum deviation occurred at the start of the irradiation in both cases, which could be caused by the beam "ramp-up". The linearity of these curves shows a straightforward relationship between proton and vaporization count which could potentially be exploited for dosimetry. However, the influence of the nanodroplet concentration and proton dose on the linearity should be addressed in future studies, as both acoustic shadowing and a gradual decrease in nanodroplet concentration (due to radiation-induced vaporization) in regions with high densities of vaporization events might reduce the count rates.

5.3.4 Future directions and clinical translation

Two scenarios are presented in this letter: sensitivity only to high-LET secondaries (37 °C) and sensitivity to primaries and secondaries (50 °C). The current nanodroplets were sensitive to secondary reaction products at physiological temperature, which could be used to indirectly measure the range

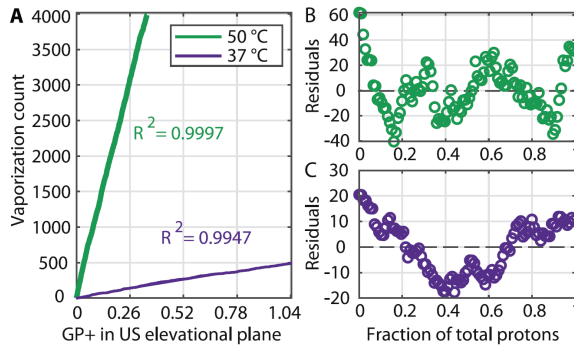


Figure 5.4: (a) Vaporization count as a function of number of stopping protons in the ultrasound field of view (GP+ symbol refers to 10^9 protons). The R^2 values and residual counts of a linear fit are shown both at 50 °C (b) and 37 °C (c).

in vivo with an approach similar to PET and Prompt Gamma Imaging. However, the number of vaporization events were multiplied by a factor of 25 at 50 °C, once they became sensitive to primary protons. A larger number of events will utterly result in a refined resolution for both dosimetry and range verification. Moreover, vaporization by primary protons leads to a direct relationship between the peak in vaporization count and the proton range. Therefore, even though the indirect response observed at 37 °C for our nanodroplet formulation might enable proton range verification, increasing the degree of superheat of the nanodroplets to transpose the direct response to physiological temperature would be desirable [244]. This could be achieved by modifying the nanodroplet liquid core using lower boiling point perfluorocarbons [119] or mixed compounds [238].

This *in vitro* study was performed in ideal conditions as a proof of concept, thus future research should cover different aspects regarding clinical translation. The effect of both tissue and nanodroplet distribution inhomogeneities on the accuracy of the localization method should be assessed and compared to the homogeneous dispersions used here. In particular, the use of acoustic droplet vaporization as a calibration tool could be considered, to infer potential nanodroplet distribution inhomogeneities. Furthermore, analytical models need to be developed in order to estimate the nanodroplets response for complex treatment plans, and the integration of the ultrasound system in the proton therapy room should be examined. Ultimately, we envision that this online range verification method could benefit several sites of sonic accessibility such as the prostate, breast, liver, etc. In the longer term, the dosimetric use of nanodroplets could be complemented with their ability to mechanically (through cavitation) or chemically (through drug or oxygen delivery) enhance the tumor response to radiation therapy [90, 94].

Finally, even though the detection and localization of vaporization events was performed offline, the necessary operations were not too computationally-intensive. Thus, future research could focus on the optimization and implementation of the algorithm in real-time [252, 253] in order to provide direct feedback over the course of irradiation.

5.4 Conclusion

In conclusion, we have developed and implemented a method for detecting and super-localizing superheated nanodroplet vaporization events in a proton pencil beam using high frame rate contrast enhanced ultrasound imaging. This allowed to quantify the spatial and temporal distribution of droplet activation events, which have been related to the proton range as well as to spatial features of primary protons and secondary particles. The presented method allows to derive microbubble count profiles directly representing the interaction between nanodroplets and charged particles, even for large vaporization concentrations for which offline ultrasound assessment would only provide indirect information. Ultimately, online imaging could provide real-time feedback during proton therapy, potentially enabling to compensate for deviations in treatment delivery.

5.5 Acknowledgments

This study was funded by the European Union's Horizon 2020 research and innovation program under grant agreement n°766456 ("AMPHORA") and by the Dutch Research Council under the grant NWA 1160.18.095. The authors thank A.A. Brouwer (Erasmus MC), R. Beurskens (Erasmus MC) and H. den Bok (TU Delft) for their help in designing and building the experimental apparatus.

5.6 Supplementary materials

Supplementary material associated with this article can be found in the online version at [doi:10.1016/j.ultrasmedbio.2021.09.009](https://doi.org/10.1016/j.ultrasmedbio.2021.09.009).

“Silence is sometimes the best answer.”

Dalai Lama

6

Passive Ultrasound Localization Microscopy of nanodroplet vaporization during proton irradiation

*Sophie V. Heymans**, *Gonzalo Collado-Lara**, *Marta Rovituso*, *Hendrik J. Vos*,
Jan D’hooge, *Nico de Jong*, *Koen Van Den Abeele*

In preparation for submission

Perfluorobutane nanodroplets have recently been presented as a potential candidate for ultrasound-based *in vivo* proton range verification. In the previous chapter, online high frame rate ultrasound imaging during proton irradiation allowed to count and super-localize individual vaporization events in static hydrogel phantoms. However, in the presence of flow, *i.e.* in physiological conditions, the specific detection of vaporization events might be compromised by the dynamic behavior of the microbubbles resulting from nanodroplet vaporization. Those microbubbles might remain in the extravascular space, quickly dissolve, or circulate in the vasculature. This latter incidence could lead to false detections, as differentiating microbubbles entering or exiting the ultrasound probe’s field of view from radiation-induced vaporization events

*joint first author

might be a difficult task, especially for 2D imaging. Therefore, inspired by Ultrasound Localization Microscopy (ULM), we propose to specifically detect vaporization events by exploiting the acoustic signatures emitted by vaporizing nanodroplets. When sparse vaporization events are passively detected by an ultrasound array during proton irradiation, their position can be determined using the time difference of arrival between channels. We called this method Passive Ultrasound Localization Microscopy (P-ULM). In this chapter, the resolution limits of P-ULM and ULM were obtained and compared for our acoustic system, both theoretically and in phantoms irradiated by protons. The lateral resolution of ULM and P-ULM were found to be comparable, while the axial resolution of P-ULM was degraded compared to ULM. Nevertheless, P-ULM allowed to detect vaporization events with high specificity in the presence of flow and localize the proton range with sub-millimeter accuracy.

6.1 Introduction

Recently, the vaporization of injectable, superheated nanodroplets by ionizing radiation was demonstrated and proposed for ultrasound-based *in vivo* dosimetry and range verification during proton therapy [124, 244]. Real-time image guidance and range verification could be combined by interleaving conventional ultrasound imaging sequences with ultrasound monitoring of radiation-induced nanodroplet vaporization in the tumor and surrounding tissues [104]. By detecting and compensating potential errors in treatment delivery in real-time, this technique could greatly improve the accuracy of proton therapy of tumors in the abdominopelvic region. These locations suffer from substantial range uncertainties and intrafractional motion [30, 206], which are further enhanced by the interplay effect between the scanned beam and physiological motion [254, 255]. While proof-of-concept studies used offline ultrasound imaging to assess nanodroplet vaporization (Chapters 3 and 4, [124, 244]), the quantification of the radiation response was hindered by the large microbubble densities on post-irradiation images. In a subsequent publication (see also Chapter 5), online high frame rate imaging was used during proton irradiation, enabling the detection and localization of individual nanodroplet vaporization events. We showed that different spatiotemporal characteristics of the proton beam, amongst which the range, could be retrieved from vaporization maps [256].

In this previous study [256], individual vaporization events were localized by means of Ultrasound Localization Microscopy (ULM). ULM exploits the sparsity of acoustic scatterers to overcome the wave diffraction limit, which had bounded the resolution of ultrasound images for decades, forcing clinicians to compromise between image resolution and penetration depth. In ULM, high frame rate

ultrasound imaging is applied to sparse microbubbles. After differential imaging and filtering, microbubbles appear as individual point reflectors and can be super-localized by *e.g.* finding the centroid of their point spread function. The microbubbles can be subsequently tracked to create anatomical and functional (velocity maps) images of the vasculature at the micrometer scale [77, 78, 257, 258]. Foreseen applications comprise cancer diagnosis and monitoring, brain imaging for a better understanding of certain pathologies such as Alzheimer’s disease, or intervention monitoring [235]. As the sparsity condition demands low microbubble concentrations, which lengthens the acquisition time [259], nanodroplets were proposed for super-resolution imaging, taking advantage of their ability to generate contrast on demand through Acoustic Droplet Vaporization. Indeed, higher concentrations of nanodroplets can be injected, while only a small fraction at a time are activated and deactivated by the ultrasound probe, leading to rapid accumulation of microbubble signals and faster image construction [195, 260]. As an alternative to ultrasound activation, nanodroplets have also been vaporized by laser [261] and ionizing radiation [124]. The super-resolution capabilities offered by ULM could be exploited to improve the achievable range verification accuracy, especially in deep tumors for which low ultrasound frequencies are required.

In aforementioned studies [124, 244, 256], nanodroplets were dispersed in hydrogel phantoms, in order to easily extract spatial features and correlate them with the proton dose deposition profile. However, this simplified setup with immobilized nanodroplets is not representative of *in vivo* conditions, where the presence of flowing contrast agents might impede the selective detection and localization of vaporization events. Therefore, an imaging sequence whose aim is to find the proton range position by locating radiation-induced vaporization events will have to account for the presence of other flowing microbubbles, either vaporized spontaneously during injection or circulating in the vasculature after radiation-induced vaporization. Online high frame rate imaging on a conventional (2D) ultrasound array followed by ULM postprocessing might not allow to discriminate between newly formed microbubbles and existing microbubbles flowing in and out of the imaging plane, particularly in the elevational direction.

Here, we propose an alternative approach. As vaporizing nanodroplets undergo a volume expansion, they emit characteristic acoustic signatures with a narrowband frequency content [234]. Previously, sparse vaporization signals from Acoustic [262, 263] or Optical [264, 265] Droplet Vaporization were also detected by means of ULM. However, in both cases, the time of flight could be determined from the laser or ultrasound transmit time, allowing for traditional two-way beamforming. Instead, for many proton therapy systems delivering a continuous beam, the time of flight cannot be determined *a priori*. Therefore,

the source must be localized by the Time Difference of Arrival (TDOA) of the acoustic wave to the different piezoelectric elements of the ultrasound array.

In this contribution, we introduce a technique, named Passive Ultrasound Localization Microscopy (P-ULM), in which individual radiation-induced nanodroplet vaporization signals are passively detected by an ultrasound array. Without knowledge of the time of flight, the vaporization events can be super-localized by computing the TDOA between channels and fitting it to a one-way wave propagation model [266–269]. Adapting the formalism introduced by Desailly et al. [270], we determined the theoretical resolution limits of P-ULM and compared them with conventional ULM. The resolution of P-ULM was then measured experimentally in aqueous phantoms with dispersed nanodroplets, by interleaving active and passive imaging during proton irradiation. The super-localized vaporization maps obtained from passive recordings (P-ULM) were compared to super-resolution maps obtained from ULM. In addition, the range verification accuracy of ULM and P-ULM were evaluated. Finally, in order to validate the ability of P-ULM to discriminate between flowing microbubbles and vaporizing droplets, a dispersion of nanodroplets in water was also irradiated while being simultaneously stirred.

6.2 Materials and Methods

6.2.1 Resolution limits of P-ULM

Theoretical derivation

ULM is an application of the Time of Arrival (TOA) problem. An ultrasound wave is actively transmitted, and the reception time τ_i of a microbubble located at a position (x_0, z_0) for a transducer element i located in (x_i, z_i) is given by (assuming a linear array, figure 6.1 (a)):

$$\tau_i = \frac{z_0}{c} + \frac{\sqrt{(x_i - x_0)^2 + (z_i - z_0)^2}}{c} \quad (6.1)$$

c is the speed of sound in the medium (assumed homogeneous) and z and x are the axial and lateral directions, respectively. Contrarily to ULM, the activation (transmit) time is unknown in P-ULM, making it a TDOA problem (figure 6.1 (b)). The reception times τ are substituted by the differences in reception time $\Delta\tau$:

$$\Delta\tau_i = \frac{\sqrt{(x_i - x_0)^2 + (z_i - z_0)^2}}{c} + \frac{\sqrt{(x_{ref} - x_0)^2 + (z_{ref} - z_0)^2}}{c} \quad (6.2)$$

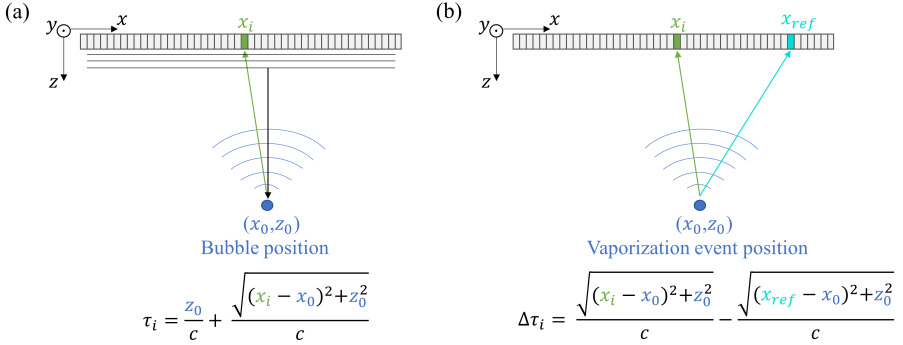


Figure 6.1: (a) Schematic representation of the determination of the pulse-echo time of a single acoustic source in ULM, using zero-angle plane wave transmit (equation 6.1). (b) Representation of the one-way travel of a nanodroplet vaporization signal and determination of the time difference of arrival between a transducer element i and the reference transducer element (equation 6.2).

with (x_{ref}, z_{ref}) the lateral and axial coordinates of a chosen reference channel. For simplicity, we set $z_i = z_{ref} = 0$.

Desailly *et al.* [270] introduced a theoretical model to estimate the resolution limits of ULM, depending both on the configuration of the ultrasound imaging system (number of channels, center frequency, etc) and the signal to noise ratio (SNR). Single microbubbles are assimilated to point sources whose echo is received by a transducer array. In the time domain, the RF echo appears as a pressure hyperboloid. The model separates the error sources in two contributions: first, the error in determining the arrival time of the echo for all channels is estimated, and then this error is propagated to the fitting of those arrival times to a time-of-flight equation.

In P-ULM, the initial step is identical to ULM, and the arrival time of the vaporization signal is extracted from the RF channel data. The Cramer-Rao lower bound, which gives the standard deviation σ_τ of the measured arrival times $\hat{\tau}$ (with respect to the theoretical arrival time τ) can be used [271]. As P-ULM has a different fitting than ULM, the standard deviation of the arrival time σ_τ will propagate differently. Following the same approach as Desailly [270], an asymptotic model is used to characterize the backpropagation of the residuals of the non-polynomial curve fitting step to the estimated bubble location. The standard deviation of vaporization signal position estimates can be obtained from the covariance matrix:

$$Covar(\hat{x}_0, \hat{z}_0) = \frac{1}{n} \sigma_\tau^2 \Gamma^{-1} \quad (6.3)$$

with $\Gamma_{k,l} = \lim_{n \rightarrow +\infty} \frac{1}{n} \sum_{i=1}^n \frac{\partial}{\partial k} \Delta\tau_i(x_0, z_0) \frac{\partial}{\partial l} \Delta\tau_i(x_0, z_0)$ and (k, l) is any pair of axes ($k = x$ or z and $l = x$ or z). The covariance matrix is derived assuming that the vaporization events occur in the far-field, i.e. $z_0 \gg L_x$, which allows to simplify the partial derivatives of the time difference equation by making a Taylor expansion around the points $(x_i - x_0)/z_0 \approx 0$ and $(x_{ref} - x_0)/z_0 \approx 0$. In those expressions, n is the number of elements in the 1D array, and L_x is the array aperture.

The localization errors in x and z for P-ULM are the following:

$$\sigma_{x_0} = \frac{2c\sigma_\tau z_0}{\sqrt{n}L_x} \sqrt{\frac{3L_x^4 + 40L_x^2(2x_0^2 + 2x_0x_{ref} - x_{ref}^2) + 240x_{ref}^2(4x_0^2 - 4x_0x_{ref} + x_{ref}^2)}{L_x^4 - 8L_x^2x_{ref}^2 + 80x_{ref}^4}} \quad (6.4)$$

$$\approx \frac{2\sqrt{3}c\sigma_\tau z_0}{\sqrt{n}L_x} \quad (6.5)$$

$$\sigma_{z_0} = \frac{8\sqrt{5}c\sigma_\tau z_0^2}{\sqrt{n}L_x} \sqrt{\frac{L_x^2 + 12x_{ref}^2}{L_x^4 - 8L_x^2x_{ref}^2 + 80x_{ref}^4}} \quad (6.6)$$

$$\approx \frac{8\sqrt{5}c\sigma_\tau z_0^2}{\sqrt{n}L_x^2} \quad (6.7)$$

In contrast, the localization errors for ULM are the following:

$$\sigma_{x_0} \approx \frac{2\sqrt{3}c\sigma_\tau z_0}{\sqrt{n}L_x} \quad (6.8)$$

$$\sigma_{z_0} \approx \frac{c\sigma_\tau}{2\sqrt{n}} \quad (6.9)$$

The lateral localization error has the same approximated expression for ULM and P-ULM. Contrarily to ULM, the axial localization error of P-ULM is strongly dependent on the axial distance (proportional to z_0^2) and the array features (dependence in $1/(\sqrt{n}L_x^2)$). Consequently, vaporization events occurring at large axial distances from the probe are expected to suffer from higher localization errors compared to events occurring closer to the probe.

Monte Carlo simulations

To validate the theoretical derivation of the resolution limits, we generated theoretical TDOAs (using equation 6.2) for different bubble positions ($x_0 = -10$ to 10 mm and $z_0 = 20$ to 70 mm), added random delays, and fitted the

resulting TDOAs to a hyperboloid function to estimate the bubble position, using different choices of the reference channel. The delays added to the theoretical TDOAs were normally distributed with a standard deviation given by the experimental error $\sigma_{\tau,exp}$, corresponding to the median of the absolute value of the residuals after curve fitting. By repeating the process 500 times, 500 different bubble position estimates were obtained for each initial set of parameters. The standard deviations of the bubble lateral and axial positions were compared to the theoretical resolution limits, using array parameters corresponding to the P4-2v array used for the experiments (64 elements, 0.3 mm pitch).

Synthetic data generation

In order to validate the localization algorithms of both P-ULM and ULM, a synthetic dataset was simulated with the acoustic simulation work-package field II [272,273]. The transducer geometry and impulse response were modelled based on the datasheet provided by the manufacturer (P4-2v, Verasonics, Kirkland, WA, USA), and the acoustic excitation was identical to what is used in the experiments. We simulated the pulse-echo response of a single linear scatterer whose position was varied in the axial (15 to 70 mm), lateral (0 to 10 mm), and elevational (0 to 8 mm) direction. For P-ULM, the time traces were down-sampled to the sampling frequency used in the experiments (10.8 MS/s) and the localization algorithm was applied. For ULM, the down-sampled data was beamformed using the Verasonics reconstruction tool before the localization algorithm was applied.

6.2.2 Experimental methods

Nanodroplet and phantom preparation

Nanodroplets with a perfluorobutane core and a polyvinyl alcohol shell (PVA-PFB nanodroplets) were prepared two days before the proton experiment, following the protocol described in [244]. Aqueous phantoms (0.1% w/v Carbopol 2050, Lubrizol, Wickliffe, USA [245]) were used to disperse and immobilize nanodroplets without impeding their vaporization, as shown in [256]. Briefly, a few minutes before irradiation, 60 μ L nanodroplets were poured and mixed in the phantom matrix (phantom container dimensions 54 x 26 x 51 mm) preheated to the desired temperature. Four Carbopol phantoms were used in total: two were heated to 37°C and two to 50°C. In order to evaluate the ability of P-ULM to distinguish vaporization signals from moving microbubbles,

Phantom	Temperature	Cyclotron current [nA]	Irradiation time [s]
Carbopol	50 °C	5	2.1
		10	2.3
		20	2.2
Carbopol	50 °C	5	2.0
		10	2.0
		20	2.2
Water	50 °C	20	2.5
Carbopol	37 °C	20	2.6
		40	2.2
		80	2.0
Carbopol	37 °C	20	1.4
		40	2.4
		80	1.8

Table 6.1: Phantom irradiation parameters

a fifth phantom made of nanodroplets dispersed in water heated to 50 °C was irradiated. The phantom was continuously stirred by a magnetic rod during irradiation. The nanodroplet concentration in the phantoms was 21.5 μM and was determined by NMR spectroscopy (400 MHz Avance II, Bruker Biospin GmbH, Rheinstetten, Germany) of the nanodroplet vial on the day following irradiation experiments.

Phantom irradiation settings

The phantoms were immersed in a heated water tank equipped with temperature control and irradiated in the experimental room of the Holland Proton Therapy Center (Delft, The Netherlands), using a monoenergetic 154 MeV horizontal pencil beam. The reproducibility of the phantom positioning was ensured by means of a locking pin, and alignment with the beam was performed using the in-room lasers. The entrance of the water tank was located at isocenter, and the depth of the phantom center corresponded approximately to the proton range (figure 6.2(a)). The irradiation conditions for each phantom are displayed in table 6.1. Each phantom was irradiated three times, using increasing beam currents, except for the phantom containing nanodroplets dispersed in water. The irradiation start and end were triggered manually, which explains the slight variability in irradiation times. For each irradiation, incident protons were counted by a transmission ionization chamber (beam monitor, DE.TEC.TOR, Turin, Italy).

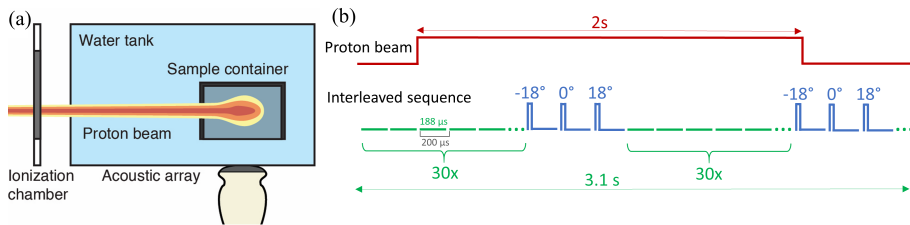


Figure 6.2: (a) Schematics of the experimental setup for proton irradiation and simultaneous ultrasound imaging. (b) Interleaved passive and active ultrasound pulse sequences.

Ultrasound imaging

A low frequency ultrasound array (P4-2v, -6dB bandwidth: 1.71-3.73 MHz, 64 elements, Verasonics) was used to image the phantoms during irradiation, through an acoustically transparent window facing the side of the phantoms (figure 6.2 (a)). The probe was positioned parallel to the phantom and driven by a programmable ultrasound research unit (Verasonics Vantage 256, Kirkland, USA). Registration of ultrasound image coordinates with room coordinates was achieved by imaging a fiducial object (point reflector) of known absolute position. As the cyclotron delivered a quasi-continuous proton flux (72 MHz), ultrasound acquisitions could not be synchronized with proton beam delivery. Instead, long ultrasound acquisition lengths (3.1 s) were used to cover the entire irradiation. Phantoms were imaged by interleaving active imaging frames between series of passive acquisitions (figure 6.2 (b)). The latter consisted in setting the system to passively record acoustic signals quasi-continuously (the transmit voltage was set to 0V), acquiring 188 μs -long frames over a period of 200 μs . Every 30 passive frames, an imaging sequence was introduced, which consisted in successively transmitting three low amplitude (4V) diverging waves (-18°, 0°, 18°). Therefore, the effective frame rate for imaging was 152 Hz. The insertion of the active imaging frames reduced the percentage of the irradiation time captured by passive ultrasound recordings to 77%.

Characterization of the proton beam

The characterization of the proton beam is described in details in Chapters 5 [256] and 7. Briefly, the proton range (R_{80}) and range dispersion (σ_R) were derived from an analytical fit of the measured depth-dose distribution [194]. The water-equivalent thickness (WET) of the water tank and phantom container walls was accounted for [247]. The entrance spot size was measured in air, and

spot spreading in water (σ_{lat}) was modelled by the Highland formula [15, 248]. The spatial distribution of nuclear interactions in the phantom was obtained using the non-elastic interaction cross-section of protons in oxygen [200]. The stopping distribution of primary protons was modelled as a Gaussian centered on the proton range (R_{80}) and with a standard deviation equal to the range dispersion parameter of the analytical fit (σ_R) [194].

Data processing and analysis

Active frames:

Active imaging frames were processed using the same methods as in Chapter 5 [256]. After beamforming, differential imaging was applied to isolate sparse vaporization events, which were counted and super-localized using ULM.

Passive frames:

The radiofrequency (RF) data of passive acquisitions were processed in Matlab (R2019a, The Mathworks, Natick, MA, USA). Since passive frames were interleaved with active imaging frames, the first three passive frames following each active imaging sequence were discarded, as the RF data contained residual acoustic reflections from the previous active acquisition. A Butterworth low-pass filter (3 MHz cut-off frequency, order 8) was first applied to the raw RF data (figure 6.3 (a)) in order to remove frequency components above the expected bandwidth of nanodroplet vaporization signals. Next, the SNR was enhanced with a 2D Wiener filter (figure 6.3 (b)). To detect vaporization events, peaks were first identified in the RF data, and the coherence of the signal was then verified by comparing the different channels. The signal was considered a vaporization signal if peaks were present in 90% of the channels.

For every detected vaporization signal, the time difference of arrival between channels was determined as follows. After resampling to increase the time resolution of the RF data, all 64 channels were cross-correlated. The cross-correlation kernel was taken as the RF signal of a reference channel, which was varied from channel 4 to channel 60 by steps of 8 channels, as shown in figure 6.3 (b). Cross-correlation was computed for the 8 neighbouring channels. Potential errors (*e.g.* at the junctions between TDOAs computed from different reference channels) were compensated for by computing the derivative of the TDOAs and patching large discontinuities.

Finally, the vaporization events axial and lateral coordinates were estimated using a two-step fitting procedure. First, we only retained TDOAs of channels for which (i) the correlation was higher than 20% of the maximum correlation score observed across all channels, and (ii) the TDOA compared to adjacent

channels was lower than an empirically determined threshold (to further avoid outliers). Then, those retained TDOAs were fitted to the TDOA equation (equation 6.2), using a non-linear least squares curve fitting approach (figure 6.3 (c), top panel). The reference channel ($\Delta\tau_i = 0$) was chosen to be the channel with the highest vaporization signal amplitude. If the coefficient of determination was too low ($r^2 < 0.7$), the event was discarded. Otherwise, the residuals of the fit were computed, and all channels for which the absolute value of the residuals was below $\mu + 1.5\sigma$ were included in the second curve fitting step (figure 6.3 (c), middle and bottom panels). Finally, only the localization of vaporization events with a sufficiently large coefficient of determination ($r^2 > 0.96$) were retained. In order to extract the acoustic signatures of single nanodroplet vaporization events, the channel data were coherently delayed and summed using the fitted one-way time of flight equation.

Comparison between vaporization event positions extracted using ULM and P-ULM:

As active and passive imaging sequences were interleaved during proton irradiation, vaporization event positions extracted using ULM and P-ULM were compared on corresponding frames. For each frame containing both passively and actively detected vaporization events, the nearest events were determined using the Matlab function *dsearchn*, while ensuring that each active event had at most one corresponding passive event and vice versa. If the difference between the positions of two events was superior to 8 mm, those positions were assumed to originate from two different vaporization events, and were thus not matched. The axial and lateral localization differences between matched events were computed to evaluate the localization performances.

Determination of the proton range and spot size from vaporization maps:

The locations of the detected vaporization events were binned using a 0.5 mm by 0.5 mm grid, and summed to create 1D profiles in the directions parallel and transverse to the proton beam. The spot size σ_{lat} was estimated by fitting the 1D vaporization profile transverse to the beam direction to a Gaussian. At 50 °C, the 1D vaporization profile parallel to the proton beam was also fitted to a Gaussian to determine the range dispersion σ_R . The proton range, R_{80} , was estimated by determining the shift between the 1D vaporization profile parallel to the proton beam direction and a predicted vaporization curve, which differed depending on the temperature. At 37 °C, vaporization profiles were fitted to the 1D projection of the non-elastic reaction cross section of protons in oxygen. At 50 °C, the predicted vaporization profile was made of the sum of the 1D non-elastic cross section profile (as at 37 °C) and the Gaussian distribution of proton stopping positions at the end of their range.

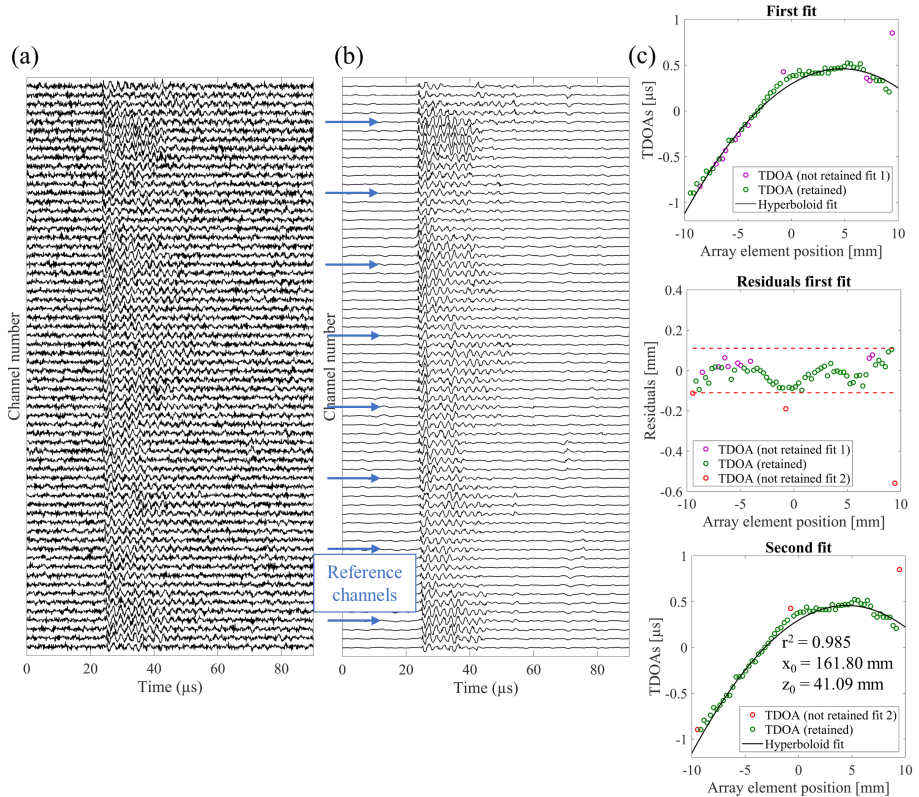


Figure 6.3: Channel data showing a nanodroplet vaporization signal detected during proton irradiation, before (a) and after (b) filtering and denoising. The TDOAs were computed using eight reference channels distributed across the array. (c) Two step fitting procedure to extract the position of the vaporization event. A first fit is performed with a subset of TDOAs (top panel, green dots). Then, the residuals distribution (middle panel) is used to discard channels for which the residual exceeds the $\pm 1.5\sigma$ limit. Finally, a second fit is performed with retained channels from the second step only (middle panel, hence potentially including again channels that were not used in the first fit), yielding the final estimate of the vaporization event location (bottom panel).

6.3 Results

6.3.1 Resolution limits of P-ULM

We applied the P4-2v array geometry and the experimental error on arrival times estimates ($\sigma_{\tau,exp} = 37$ ns) to the theoretical expressions of σ_{x_0} and σ_{z_0} introduced in section 6.2.1 (equations 6.4 and 6.6) and obtained expressions for the lateral and axial resolution limits as function of the bubble position and reference channel location (figure 6.4). Both lateral and axial resolution limits vary with the axial position of the vaporization event and the location of the reference channel. The error is lower at the array center and extremities. The lateral localization error increases for vaporization events located away from the array center, and both errors increase with the depth of the vaporization event. As a comparison, for an identical σ_{τ} of 37 ns, using the same probe and vaporization event positions, the lateral and axial resolution limits of ULM are 26-90 μm and 3.5-16 μm , respectively. Therefore, the theoretical lateral and axial resolution limits of P-ULM are larger by up to one (20-900 μm) and up to two (100-2500 μm) orders of magnitude, respectively.

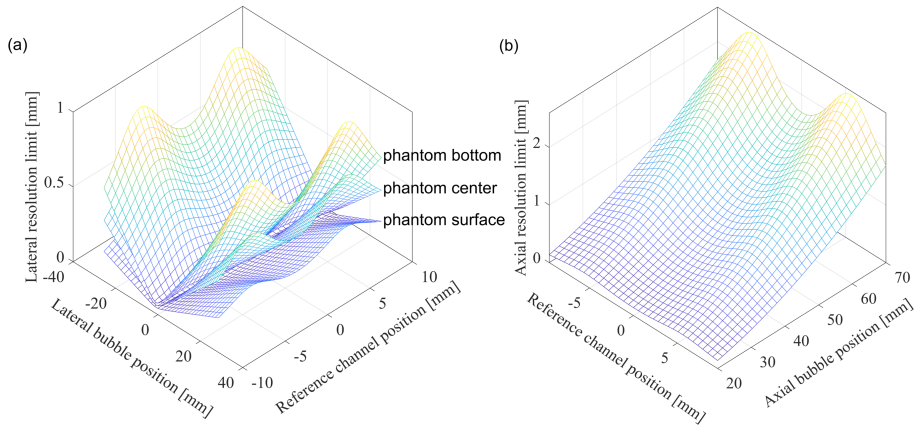


Figure 6.4: Theoretical resolution limits of P-ULM corresponding to the experimental conditions of this study. (a) Lateral resolution limit as a function of the lateral bubble position x_0 and the reference channel x_{ref} , for three different axial depths ($z_0 = 20, 45,$ and 70 mm). (b) Axial resolution limit as a function of the reference channel and the axial bubble position z_0 .

The theoretical resolution limits are compared to Monte Carlo simulation results in figure 6.5, for different combinations of x_0 , z_0 , and x_{ref} . A good agreement was found between simulated and theoretical resolution limits, which confirms

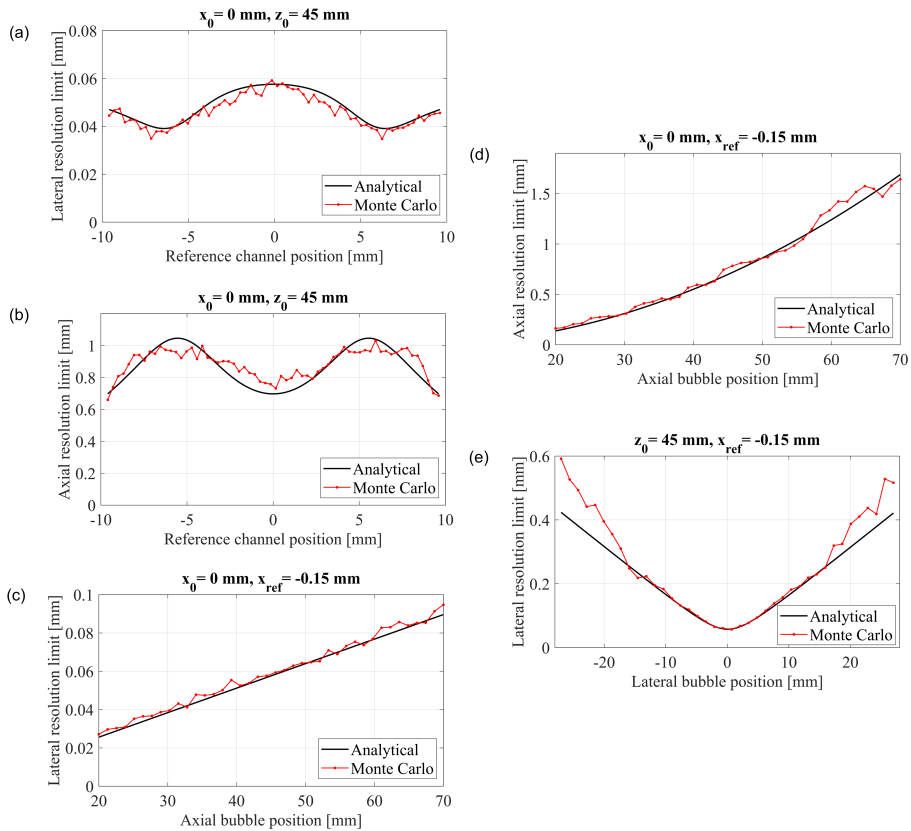


Figure 6.5: Monte Carlo simulation results overlaid on theoretical resolution limits of P-ULM for different situations: (a) lateral and (b) axial resolution limit as a function of x_{ref} , (c) lateral and (d) axial resolution limit as a function of the z_0 , and (e) lateral resolution limit for different values of x_0 . Each dot in the red curve represents the standard deviation of the localization error extracted from 500 repetitions.

the validity of the simplifying assumptions, except for values of x_0 far from the array center (figure 6.5(e)). The assumptions used to justify the Taylor expansion, $(x_i - x_0)/z_0 \approx 0$ and $(x_{ref} - x_0)/z_0 \approx 0$, fail for large values of x_0 .

The impact of the P4-2v array diffraction characteristics and the bubble elevational position on the localization precision of ULM and P-ULM was evaluated by applying both localization algorithms on synthetic data. The distribution of localization errors, *i.e.* the difference between the estimated and true bubble position, is shown on figure 6.6, for bubbles located at the center of

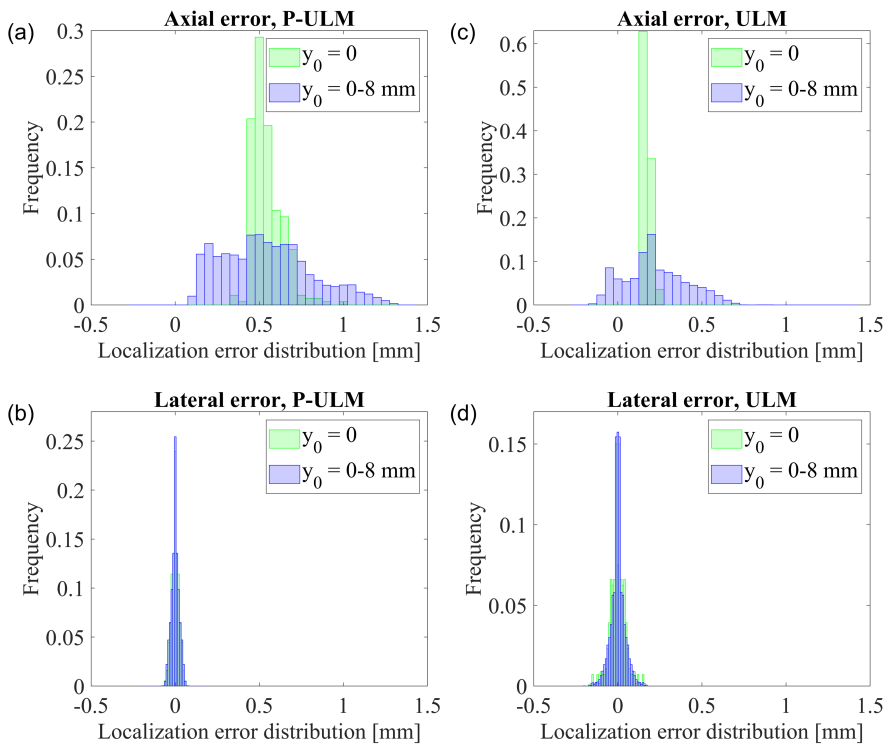


Figure 6.6: Comparison between ULM and P-ULM localization accuracy using synthetic data. (a) Axial and (b) lateral localization error distribution for P-ULM, both for scatterers located at $y_0 = 0$ and at different elevational positions. (c)-(d) Corresponding values for ULM. The scatterer lateral and axial position was varied between 0-10 mm and 15-70 mm, respectively

the elevational axis ($y_0 = 0$) and for all bubbles ($y_0 = 0$ to 8 mm). Contrarily to the lateral localization error (figure 6.6 (b),(d)), the axial localization error is strongly affected by the scatterer elevational position, both for ULM and P-ULM (figure 6.6 (a),(c)). The two localization methods introduce a constant positive bias in the axial direction (0.22 mm for ULM and 0.55 mm for P-ULM). The standard deviations of the localization errors were 0.04 and 0.02 mm in the lateral direction and 0.18 and 0.27 mm in the axial direction for ULM and P-ULM, respectively.

6.3.2 Experimental comparison of the range verification accuracy of ULM and P-ULM

The experimental detection and localization performances of ULM and P-ULM were compared by interleaving the two imaging sequences during proton irradiation. Table 6.2 shows, for each Carbopol phantom, the total number of vaporization events detected and localized using the two methods. Interestingly, P-ULM detected twice as many vaporization events as ULM at 50 °C, but only 30% more events at 37 °C. For P-ULM, only 37-47% of the detected vaporization events could be accurately ($r^2 > 0.96$) localized using the TDOA fitting approach. For ULM, 100% of the detected events were also localized. The number of localized events was 30 to 60% higher for ULM compared to P-ULM. Surprisingly, the position of the majority of the localized events differed for the two detection methods, as only 21-31% of the events detected by ULM had a corresponding event detected by P-ULM.

Temperature	Number of events			Number of corresponding events
	P-ULM Detected	P-ULM Localized	ULM Localized	
50 °C	2929	1095 (37%)	1432	449 (31%)
50 °C	1915	733 (38%)	964	268 (28%)
37 °C	1615	758 (47%)	1219	281 (23%)
37 °C	1071	473 (44%)	794	163 (21%)

Table 6.2: Experimental detection and localization efficiency of ULM and P-ULM.

Vaporization events localized by ULM and P-ULM are overlaid on a post-irradiation B-mode image in figure 6.7 (a) and (c), for different irradiations of the same phantom at 50 °C. The event locations qualitatively correspond to the expected spatial distribution, with an entrance plateau (vaporization by secondary particles) followed by an enhancement at the end of the proton range (vaporization by primary protons). However, most of the events localized with ULM and P-ULM do not match, and the passively-located events appear to be more dispersed in the ultrasound axial direction compared to events located using ULM. The associated event counts are displayed in figure 6.7 (b) and (d), as a function of the proton fluence. The distributions of lateral and axial localization differences between corresponding ULM and P-ULM events are depicted in figure 6.7 (e) and (f), respectively. The offset and dispersion of the distribution of localization differences between corresponding events, averaged over the two phantoms irradiated at 50 °C, were ($\mu \pm \sigma$): 0.20 ± 2.00 mm for the lateral direction and 0.87 ± 3.52 mm for the axial direction.

Figure 6.8 shows results obtained in a phantom irradiated at 37 °C. Due to the higher LET threshold at 37 °C, nanodroplet vaporization is only induced by high

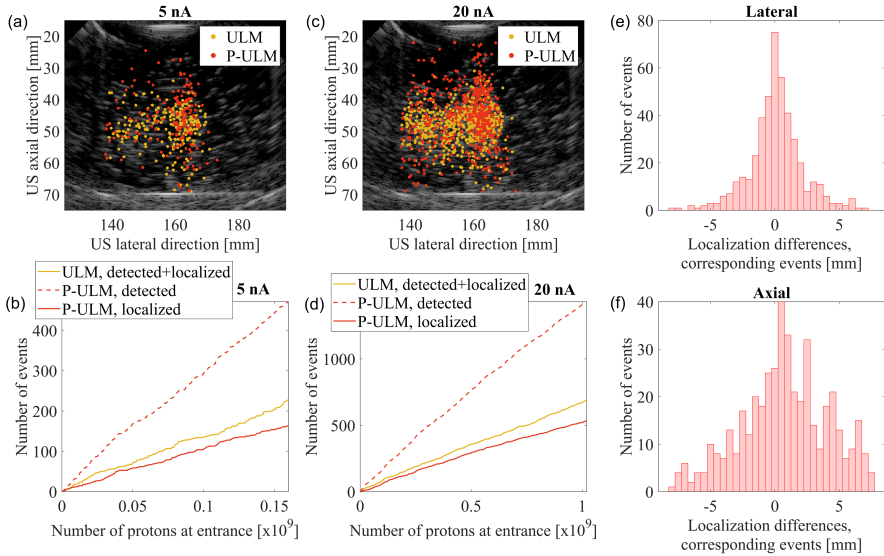


Figure 6.7: Comparison of vaporization event localization using ULM and P-ULM for a Carbopol phantom irradiated at 50 °C. (a), (c) Event localization overlaid on a post-irradiation B-mode image and (b),(d) event count as a function of the number of incoming protons for two different irradiations using a beam current at extraction of 5 nA (a-b) and 20 nA (c-d). Distribution of the lateral (e) and axial (f) localization differences between corresponding events using ULM and P-ULM in identical frames. Subplots (e) and (f) combine the three irradiations of the same phantom (see table 6.1).

LET secondary particles, leading to a relatively uniform vaporization density proximal to the Bragg peak (figure 6.8 (a) and (c)). Similarly to observations at 50 °C, vaporization events detected using P-ULM appear to be more dispersed in the axial direction, with a higher density of events close to the ultrasound probe. The distributions of lateral and axial localization differences between corresponding events, figure 6.8 (e) and (f), were similar to the ones observed at 50 °C, with offset and dispersion values of $-0.08 \text{ mm} \pm 2.25 \text{ mm}$ and $0.14 \text{ mm} \pm 3.35 \text{ mm}$, respectively.

The ability of P-ULM to specifically localize vaporization events in the presence of flow was tested by continuously stirring a dispersion of nanodroplets in water during irradiation, at 50 °C. The position of vaporization events localized using P-ULM are displayed in figure 6.9 (a), overlaid on a post-irradiation image of the phantom. The 1D experimental and fitted profiles derived from vaporization events localized using P-ULM are represented in figure 6.9 (b), showing an

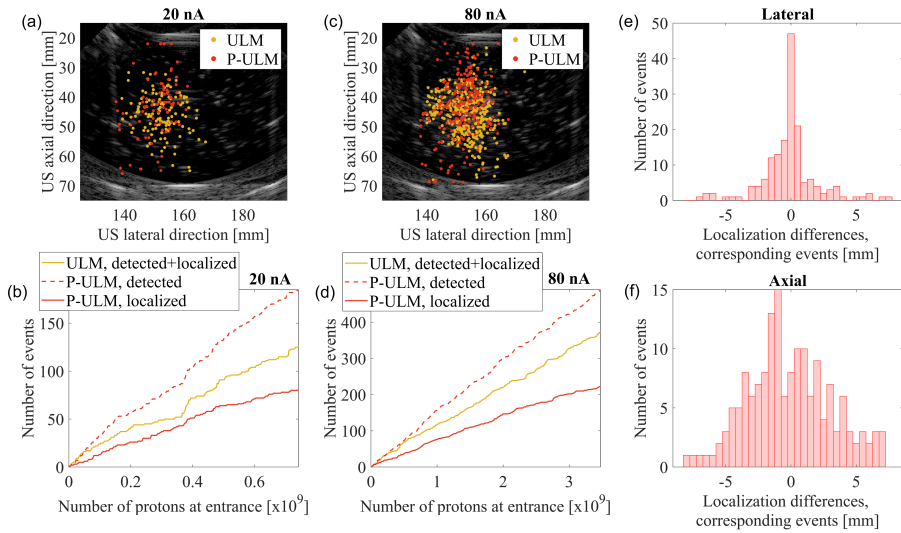


Figure 6.8: Comparison of vaporization event localization using ULM and P-ULM for a Carbopol phantom irradiated at 37 °C. (a), (c) Event localization overlaid on a post-irradiation B-mode image and (b),(d) event count as a function of the number of incoming protons for two different irradiations using a beam current at extraction of 20 nA (a-b) and 80 nA (c-d). Higher beam currents were used at 37 °C to obtain similar vaporization counts than at 50 °C. Distribution of the lateral (e) and axial (f) localization differences between corresponding events using ULM and P-ULM in identical frames. Subplots (e) and (f) combine the three irradiations of the same phantom (see table 6.1).

excellent correspondence between the proton range and the peak in vaporization events.

The shifts between the reference (derived from the beam modelling) and the estimated proton range, the reference and the estimated range dispersion, and the reference and the estimated spot size are reported in table 6.3 for all phantoms, for vaporization events localized using ULM and P-ULM. When the droplets are directly sensitive to protons (50 °C), both localization methods provide submillimeter estimates of the proton range and range dispersion. When the droplets are only sensitive to high LET secondaries (37 °C), the estimated range using ULM remains satisfactory, while P-ULM underestimates the range by several millimeters. The lateral spot size is largely overestimated (by more than 50%) by P-ULM at both temperatures, while the error using ULM is below 2 mm.

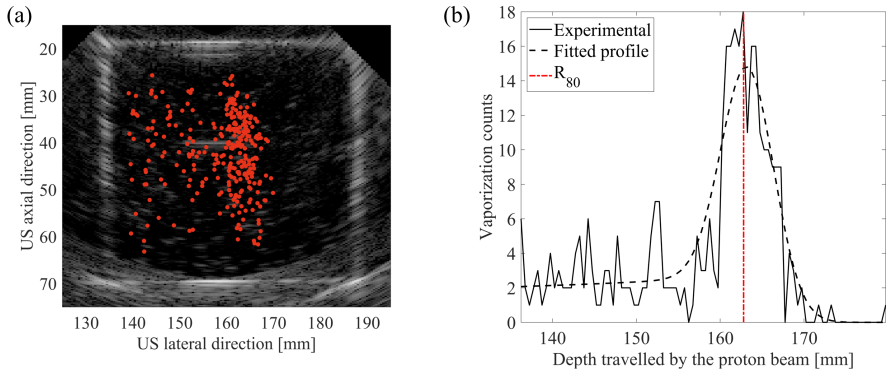


Figure 6.9: (a) Vaporization events localized using P-ULM overlaid on a post-irradiation image of a dispersion of PVA-PFB nanodroplets in water at 50 °C. The phantom was continuously stirred during proton irradiation. (b) The 1D P-ULM vaporization profile was fitted to a predicted curve in order to determine the shift between the predicted and true proton range (vertical line).

Phantom	Temperature	$R_{80}-R_{80,est}$ [mm]		$\sigma_R-\sigma_{R,est}$ [mm]		$\sigma_{lat}-\sigma_{lat,est}$ [mm]	
		ULM	P-ULM	ULM	P-ULM	ULM	P-ULM
Carbopol	50 °C	-0.17	-0.37	-0.13	0.44	1.66	-4.00
Carbopol	50 °C	0.08	0.00	-0.42	0.61	-1.15	-3.97
Water	50 °C	-	-0.59	-	0.33	-	-5.01
Carbopol	37 °C	1.08	4.35	-	-	-0.69	-4.18
Carbopol	37 °C	0.50	2.92	-	-	-1.72	-3.25

Table 6.3: Comparison of proton beam parameter estimation using vaporization events localized with ULM and P-ULM.

6.4 Discussion

In this chapter, we investigated the feasibility of passively localizing acoustic signals generated by vaporizing nanodroplets for proton range verification, and compared the precision with conventional Ultrasound Localization Microscopy. The theoretical resolution limits of P-ULM were determined by following the formalism introduced in [270]. For an experimentally determined $\sigma_{\tau,exp}$ of 37 ns and a field of view of 5 cm (lateral) by 7 cm (axial), the theoretical lateral and axial resolution limits are below 0.6 and 2 mm, respectively (figure 6.5). Assuming that the vaporization event position determined by ULM is taken as ground truth, figures 6.8 and 6.7 show experimentally-determined localization

errors for P-ULM, whose standard deviations (~ 2 mm laterally and ~ 3 mm axially) exceed these theoretical resolution limits. However, the actual resolution of ULM is far worse than theoretical predictions, especially for bubbles located at different elevational positions, as illustrated in figure 6.6, which shows that axial localization errors can reach 1 mm even in the absence of noise. Moreover, the axial resolution of ULM can be strongly affected by the variability in microbubble acoustic response [274]. Therefore, we attribute the relatively high differences in vaporization event positions observed experimentally for ULM and P-ULM to their *combined* localization errors.

As both imaging techniques can suffer from relatively large (\sim mm) localization errors, their ability to accurately retrieve proton beam features was compared in table 6.3. In the ultrasound lateral direction (parallel to the beam direction), the proton range position and dispersion (R_{80} and σ_R) were estimated with submillimeter accuracy by ULM and P-ULM at 50°C , demonstrating that the lateral localization accuracy of both methods is sufficient for the intended application. Surprisingly, however, P-ULM could not accurately determine the location of the vaporization profile fall-off at 37°C , and the resulting range estimation error was as high as 3-4 mm. We attribute this to two factors. First, the number of localized events for P-ULM was lower at 37°C than at 50°C , while this difference was less pronounced for ULM. Second, vaporization profiles are intrinsically asymmetrical at 37°C , with vaporization events only occurring in the first half of the lateral field of view. At 50°C , this asymmetry is less pronounced as the range is determined by localizing the peak in vaporization events. We hypothesize that the localization performances of P-ULM can be affected by asymmetry, due to phase aberrations occurring mostly for the first half of the wavefront. In the ultrasound axial direction (perpendicular to the beam direction), neither ULM nor P-ULM could estimate the spot size with submillimeter accuracy. The spot size was strongly overestimated by P-ULM, which we attribute to the degraded axial localization accuracy of P-ULM compared to ULM. Consequently, we anticipate that proton range verification with P-ULM should only be performed with the ultrasound probe positioned perpendicular to the beam direction, in order to benefit from the high lateral localization accuracy of P-ULM.

As far as the detection efficiency is concerned, the number of vaporization events detected by P-ULM exceeded by far those detected by ULM, although a minority (37-47%) of those detected events could be localized (table 6.2). Importantly, P-ULM could only detect vaporization events during a fraction of the total irradiation time (77%, due to the interleaved sequence), while ULM was covering the entire irradiation time. When accounting for this effect, the number of localized events is almost equivalent for both methods. We postulate that the higher detection efficiency of P-ULM is due to the higher sensitivity

of the passive method, as the RF data is not contaminated by reflections of the transmitted wave, and the vaporization signal only travels one-way, leading to a reduced attenuation. However, the low center frequency (0.1-1 MHz) of the majority of the vaporization signals is relatively far from the center frequency of the P4-2v probe (-6dB bandwidth: 1.71-3.73 MHz). The imaging volume definition also differs between the two methods: in ULM, the elevational dimension is determined by the two-way propagation of the transmitted waves, whereas in P-ULM the acoustic wave only propagates one-way. Therefore, we assume that P-ULM can detect vaporization events occurring further away from the center of the elevational plane. Finally, the localization efficiency of P-ULM is also expected to decrease as the axial distance of the source increases, due to a lower SNR and reduced localization efficiency. In contrast, ULM can benefit from a higher SNR as it is performed on beamformed images. This hypothesis was confirmed by running the active imaging dataset through the P-ULM localization algorithm, assuming an unknown transmit time (figure 6.10). The axial location of microbubbles detected by P-ULM was lower than ULM (panel a-b), and the distribution of axial and lateral localization differences between corresponding events (panel c-d) was similar to observations on real passive data (figures 6.8 and 6.7 (e-f)). The decrease of the localization efficiency of P-ULM with axial depth might explain the observed differences in axial bubble positions in figures 6.8 and 6.7 (a),(c).

While this study was a first step in demonstrating the feasibility of P-ULM in the context of proton range verification, it was limited regarding clinical translation aspects. To facilitate the comparison between ULM and P-ULM, nanodroplets were immobilized in Carbopol phantoms, in a configuration very different from physiological conditions. Nanodroplet entrapment might affect the amplitude and shape of the vaporization signals, and the high density of static neighbouring bubbles is expected to alter the localization accuracy of P-ULM. Since the foreseen advantage of P-ULM is its ability to specifically detect vaporizing nanodroplets in the presence of flowing microbubbles, P-ULM was applied to nanodroplets dispersed in a water phantom with constant stirring, as a proof-of-concept. Even though the specificity of P-ULM was confirmed, its performances should be compared to ULM combined with appropriate microbubble tracking algorithms. Therefore, future work should focus on comparing the two imaging techniques in conditions as close to the envisioned clinical application as possible, *i.e.* in the presence of flow (using vessel-mimicking phantoms, for instance). The performances for volumetric imaging and conventional 2D ultrasound imaging should also be assessed, together with the impact of attenuation and speed of sound mismatch introduced by different tissue compositions located between the transducer and the acoustic sources.

The algorithms employed to detect and localize vaporization events in P-ULM

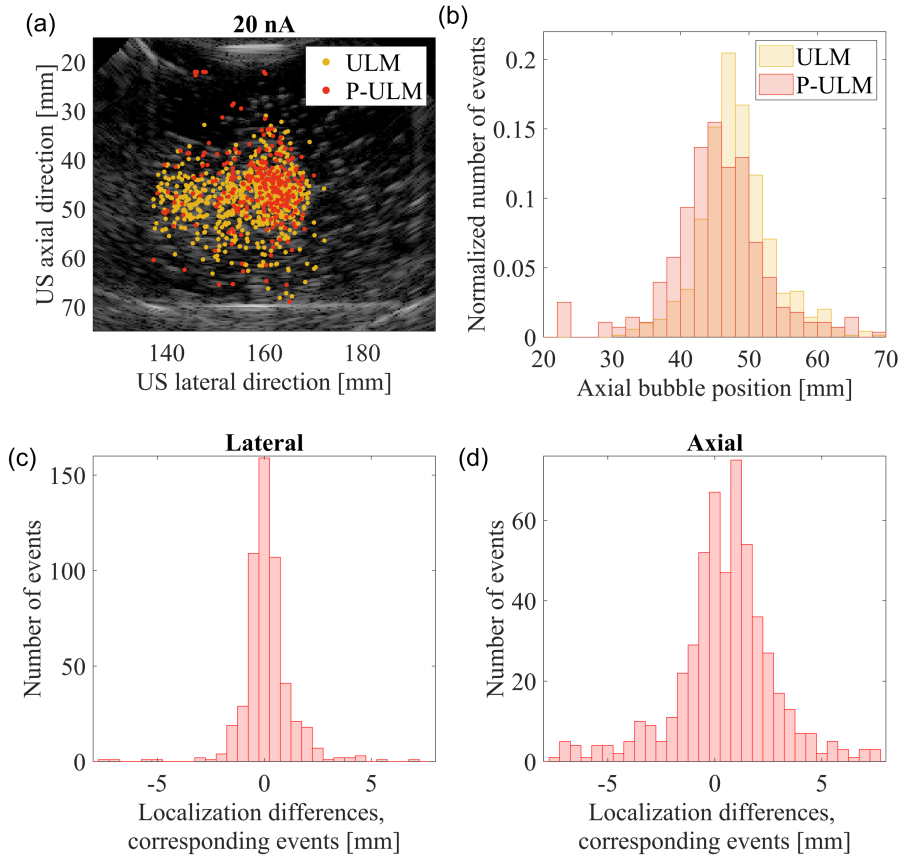


Figure 6.10: Comparison of ULM and P-ULM performances on an identical active imaging dataset (phantom at 50 °C). (a) Vaporization events localized using ULM and P-ULM overlaid on a post-irradiation image. (b) Distribution of the axial position of vaporization events in the phantom. (c) Lateral and (d) axial distribution of the localization differences between corresponding events located with ULM and P-ULM.

should be optimized in future studies. Currently, multiple (and potentially overlapping) vaporization events cannot be detected in a single frame. This limitation did not impede P-ULM for the proton beam currents and nanodroplet concentrations used in this study, but higher vaporization rates might require more complex algorithms. The fraction of successfully localized vaporization events was relatively low, which suggests that the localization process can be improved. Various methods for time delay estimation [275,276] and acoustic source localization based on TDOAs [269,277] are described in the literature, and could be explored to improve the efficiency and accuracy of the localization algorithm. Furthermore, the SNR could be enhanced by employing transducer elements with a higher sensitivity in the low frequency (0.1-1.5 MHz) region. Ideally, dual-frequency or wideband ultrasound arrays could be envisioned for clinical use, allowing to combine passive detection of the vaporization signals with anatomical imaging of the target [278–280]. Additionally, the localization precision highly depends on the probe geometry. For these experiments, a commercially available probe with a short 2 cm aperture was used. Longer apertures, or elements out of plane, can drastically affect the localization precision, thus bespoke probes are desirable for the final application.

The detection and localization of individual vaporization events also offers the opportunity to investigate the temporal and spectral characteristics of acoustic signatures of the polymeric nanodroplets used in this study. By coherently delaying and summing vaporization traces detected on each channel, the SNR of acoustic signatures can be greatly enhanced. To the best of our knowledge, acoustic signatures reported in the literature consisted exclusively of nanodroplets encapsulated by a phospholipidic shell [234,263,281]. The acoustic signatures of polymeric nanodroplets might contain information on the behavior of the shell during vaporization and on the impact of the degree of superheat on the vaporization dynamics. Some typical examples of observed radiation-induced vaporization signals of PVA-PFB nanodroplets are displayed in figure 6.11. The vaporization event in the top row starts with a relatively broadband spike, followed by narrowband, exponentially-decaying oscillations. In some cases (middle row), the oscillations are nonlinear, with a pronounced harmonic content. Interestingly, differences between vaporization signals at the two tested temperatures were observed, as the fraction of vaporization signals with a center frequency above 1 MHz decreased from 16% at 37 °C to 3% at 50 °C. Another area of investigation is whether the type and LET of charged particle vaporizing the nanodroplet (*e.g.* proton or heavy ion) might influence the nanodroplet vaporization dynamics, as different particles are characterized by different energy deposition patterns at the nanoscale.

Importantly, P-ULM was performed on samples irradiated with a continuous proton beam, leading to a relatively low vaporization rate (500-1000 events/s).

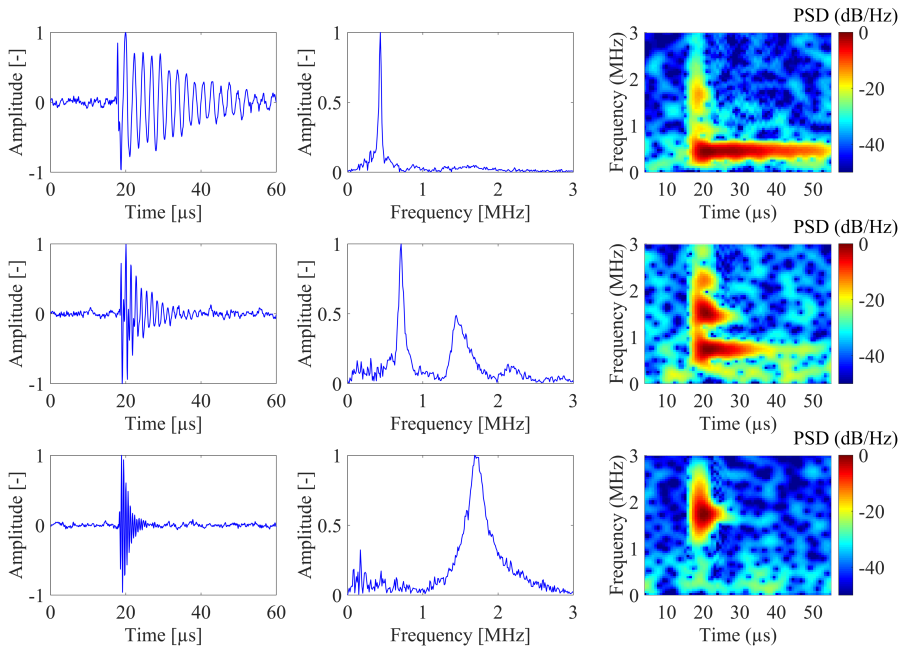


Figure 6.11: Typical observed radiation-induced vaporization signals of PVA-PFB nanodroplets in the time domain (left), frequency domain (middle), and associated power spectral density (right). The majority of the vaporization signals had a center frequency between 0.1 and 1 MHz, although some vaporization signals were also observed at higher frequencies (1-2 MHz). The mean center frequency of all localized vaporization signals was 0.5 MHz.

Some proton therapy facilities employ pulsed proton beams instead (*e.g.* IBA's Proteus One [282]), delivering proton packs in a few μs , with a repetition rate of 1 kHz. In such a situation, the vaporization event sparsity condition might not be met for high beam currents and/or nanodroplet concentrations, and the use of less accurate localization techniques, such as Passive Acoustic Mapping (PAM) [283, 284], might be necessary. On the other hand, synchronization of the ultrasound system with the delivery of individual proton packs might allow to determine the one-way time of flight of vaporization signals (with an accuracy strongly dependent on the proton pulse duration). Therefore, the preferred active or passive ultrasound imaging sequence for clinical applications will strongly depend on the temporal features of the proton therapy beam.

6.5 Conclusion

This chapter introduced an alternative method to detect and localize radiation-induced vaporization events, based on the passive detection of acoustic signatures emitted by vaporizing nanodroplets, followed by the fitting of the time differences of arrival between channels of the ultrasound array. The method was proven feasible with commercially available transducer arrays. The localization accuracy of P-ULM and ULM was compared using nanodroplet phantoms irradiated with protons at different temperatures, showing an excellent resolution in the lateral ultrasound direction. However, since the axial localization accuracy of P-ULM was limited, the proton axis should be parallel to the ultrasound probe in order to achieve sub-millimeter accuracy for range verification. Due to the high dependence of the resolution of P-ULM on the axial position of the vaporization events, we anticipate that P-ULM might only be applicable to relatively shallow tumors, although the final precision will be determined by the probe geometry. Future studies should compare the vaporization event detection specificity of ULM and P-ULM in relevant physiological conditions, to evaluate the impact of microbubble motion on the achievable performance for proton range verification.

6.6 Acknowledgments

The authors thank R. Beurskens (Erasmus MC), A. A. Brouwer (Erasmus MC) and H. Den Bok (TU Delft) for their work on the design and manufacturing of the experimental setup. The authors also thank Dr. Yosra Toumia and Prof. Gaio Paradossi (University of Rome Tor Vergata) for their help regarding nanodroplet preparation and handling, and Bram Carlier (KU Leuven) for the nanodroplet concentration assessment using NMR spectroscopy, and for stimulating discussions.

“Realists do not fear the results of their study.”

Fyodor Dostoevsky

7

A statistical model to predict superheated droplet vaporization in a proton beam: experimental validation and resolution limits for range verification

*Gonzalo Collado-Lara**, *Sophie V. Heymans**, *Marta Rovituso*, *Edmond Sterpin*,
Hendrik J. Vos, *Jan D’hooge*, *Koen Van Den Abeele*, *Nico de Jong*

In preparation for submission

The safety and efficacy of proton therapy is currently hampered by range uncertainties. A novel technique with potential for *in vivo* proton range verification, relying on the use of injectable radiation-sensitive superheated nanodroplets, was recently introduced. High frame rate ultrasound imaging during proton irradiation enabled to count and localize individual droplet vaporization events triggered by charged particles. In the present contribution, we develop a simple statistical model to predict the number and spatial

*joint first author

distribution of vaporization events as a function of the droplet size, concentration, and proton fluence. Theoretical predictions are compared to event counts from phantom experiments. While a reasonable agreement is observed for large droplet sizes, the number of events in phantoms with small droplets ($\sim 2\mu\text{m}$ diameter) is significantly lower than expected. Moreover, the inter-phantom variability is considerably larger than the variability predicted by the statistical model. Next, simulations and experiments are performed to investigate the achievable precision for range verification. The range estimates from vaporization maps in phantoms are within the uncertainty window ($\pm 0.5\text{ mm}$) of reference range measurements. Simulations predict a theoretical range retrieval precision below $\pm 0.5\text{ mm}$ for single proton spots at low energy (70 MeV) and below $\pm 1\text{ mm}$ after delivery of a full layer at high energies (150-240 MeV), for droplet concentrations higher than 10 and 30 μM , respectively. While discrepancies between the model and experimental observations should be further investigated to improve the predictive power of the model, the reported range verification performances are an incentive to move towards preclinical studies, which are critical to assess the achievable droplet distribution in and around the tumor.

7.1 Introduction

Radiation therapy is evolving towards increasingly complex treatment plans, aiming at reducing the radiation exposure of healthy tissues and organs at risk. Amongst the emerging new technologies, proton therapy is rapidly expanding and the number of treatment centers continues to grow worldwide. The main advantage of protons is their finite, tunable range within the body: they deposit a low entrance dose, followed by a narrow peak, called the Bragg peak, and a sharp dose fall-off. While such high dose gradients have the potential to improve the tumor conformity, proton therapy is also particularly vulnerable to range uncertainties [30, 104, 181]. To prevent tumor miss or unacceptable doses to organs at risk, sub-optimal beam configurations and large safety margins are adopted, thereby limiting the potential improvements of the therapeutic index [30, 181, 206]. Range uncertainties arise from multiple sources in the treatment planning and delivery phases, and can only be fully verified by means of *in vivo* range verification [30, 181]. The proton range can be indirectly measured *in vivo* by localizing secondary particles resulting from nuclear reactions, such as positron emitters or prompt gamma rays, using PET imaging or Prompt Gamma Imaging, respectively [31, 37, 39, 182, 285]. Alternatively, the detection of thermoacoustic waves induced by pulsed proton beams at the Bragg peak was proposed [40, 41, 210]. However, none of these technologies has become a gold standard for routine use in the clinic [104].

Superheated nanodroplets are investigated as an ultrasound contrast agent benefitting from extravasation capabilities, long circulation times [65,66,286–288] and able to undergo liquid to gas transition [71–74, 289]. In this process, the droplets, previously invisible to ultrasound, become echogenic gaseous microbubbles. While radiation-induced nucleation in superheated liquids is well established [113,115,149,153], the capability of ionizing radiation to induce phase-change in superheated encapsulated nanodroplets was only recently revealed [124,244] and proposed as a new method for *in vivo* proton range verification and dosimetry. The use of ultrasound imaging and superheated nanodroplets for proton range verification would offer several advantages such as the accessibility, real-time capabilities, and portability of ultrasound imaging as well as the inherently strong contrast generated by ultrasound contrast agents. Furthermore, the ability to couple range verification with anatomical ultrasound imaging could enable real-time image-guided proton therapy of moving targets [40].

Nanodroplet vaporization by ionizing radiation takes place through direct energy deposition in the superheated liquid core. Charged particles slowing down in matter locally deposit energy along their track, leading to intense heating in a confined region, called "thermal spikes". Such extreme temperatures (>300 K in a 1 nm radius around the ion track [109]) will induce explosive boiling along the tracks made by a charged particle traversing a superheated liquid. The semi-empirical thermal spike theory, first introduced by Seitz [108], is based on the homogeneous nucleation barrier: if the energy deposited by the charged particle is sufficient to generate a gas embryo with a radius greater than the critical radius, then this embryo will grow; else it will shrink back to the liquid state. The nucleation condition can be written as [146]

$$\left\langle \frac{dE}{dx} \right\rangle_{L_{eff}} \geq \frac{W_{tot}}{aR_c}, \quad (7.1)$$

with $\langle \frac{dE}{dx} \rangle_{L_{eff}}$ the particle density of energy deposition, called Linear Energy Transfer (LET) in radiation physics, averaged over an effective length, L_{eff} , which is proportional to the critical radius: $L_{eff} = aR_c$. The nucleation parameter, a , is an empirical constant varying between 2 and 13 [146], and W_{tot} is the nucleation energy of a gas embryo of critical radius. The LET threshold (right hand side of equation above) is inversely related to the degree of superheat of the liquid. When compared in terms of reduced superheat, defined as $s = (T - T_b)/(T_c - T_b)$, with T_b the boiling temperature and T_c the critical temperature, the sensitization thresholds to different types of charged particles were found to coincide for a wide range of halocarbons [113]. Protons, which reach a LET of 70-90 keV/ μ m at their individual Bragg peak [149], can only vaporize highly superheated nanodroplets ($s \geq 0.35$ -0.42), while high-LET particles (alpha, recoil ions with LETs of 200-1000 keV/ μ m) are able to vaporize moderately superheated liquids ($s \geq \sim 0.2$) [113, 114, 150]. The

influence of the degree of superheat has been evaluated experimentally for perfluorobutane (PFB) nanodroplets by comparing their vaporization response to proton irradiation at 25 °C, 37 °C and 50 °C using offline ultrasound B-mode imaging, and confirmed that a high degree of superheat (50 °C, $s = 0.45$) is required to achieve proton-induced vaporization (chapters 3 and 4) [244]. At lower temperatures, vaporization is only induced by high-LET secondary particles, resulting from rare nuclear reactions between primary protons and atomic nuclei.

Even though the proton range could be verified indirectly by detecting vaporization events induced by nuclear reaction products at physiological temperature, similarly to what is achieved by PET and Prompt Gamma Imaging, direct nanodroplet vaporization by primary protons would provide substantial advantages. Firstly, the required nanodroplet injection dose would be reduced by two orders of magnitude, as nuclear reactions are scarce events [203]. Secondly, uncertainties related to the nuclear reaction cross sections, especially in biological media [30, 207], may negatively affect the proton range estimates inferred from the distribution of secondary particles. Moreover, the correspondence between the treatment plan and the high-LET secondary particles distribution needs to be carried out by means of computationally expensive Monte Carlo simulations, which might hamper real-time implementation of proton range verification. In contrast, proton-induced vaporization can be directly related to the proton range, as protons vaporize nanodroplets at their individual Bragg peaks. Therefore, for a monoenergetic beam (such as in Pencil Beam Scanning), the peak in vaporization counts is expected to coincide with the proton range (commonly referred to as R_{80}) [256]. Conventional nanodroplets with a PFB liquid core are not sensitive to primary protons at physiological temperature, however, sensitivity to primary protons could be reached by using more volatile perfluorocarbons or through acoustic modulation of the degree of superheat of PFB NDs (chapter 8).

In a recent contribution (chapter 5), online high frame rate ultrasound imaging during proton irradiation was proposed in view of real-time treatment monitoring. Single vaporization events were localized from ultrasound recordings by applying differential imaging [256]. The obtained spatial distribution of vaporization events was found to correlate with the proton range, as the distance between the vaporization peak and the proton range was less than 1 mm (and this difference could further be attributed to measurement uncertainties). Additionally, the axial and lateral standard deviation of vaporization events corresponded to the range straggling dispersion and the spot width, respectively. Since proton-induced vaporization is in essence a stochastic process, the achievable precision for range verification depends on the detected number of vaporization events. In this study, we present a statistical model which predicts the number and

spatial distribution of proton-induced nanodroplet vaporization events, based on the probability of interaction between a droplet and a primary proton. This model is subsequently validated by comparing the predicted number of vaporization events to vaporization counts measured in aqueous phantoms irradiated with a proton beam, using online ultrasound imaging [256]. Through differential centrifugation, we isolate nanodroplet sub-populations of different sizes, and investigate the impact of the droplet size and concentration on the vaporization response. Then, the presented model is employed to predict, through simulations, the range verification precision limits as a function of the nanodroplet concentration and clinically-relevant beam parameters, such as the number of protons per spot and the beam energy. Finally, simulated range verification precision limits are compared to phantom measurements.

7.2 Materials and Methods

7.2.1 Statistical model

The model presented in this section assumes that the nanodroplets degree of superheat is sufficiently high for them to be vaporized by primary protons, i.e. the LET threshold is inferior to the peak LET reached by single protons. Only primary protons stopping by Coulomb-type interactions are considered, as these provide direct information about the proton range. Vaporization by primary protons is expected to be largely dominant as (i) only $\sim 1\%$ of primary protons undergo a nuclear reaction per traversed cm [203], and (ii) the contribution of nuclear reactions at the Bragg peak is even lower, as most protons have a residual energy below the Coulomb barrier. According to the thermal spike theory, if a proton traverses a droplet and deposits an energy superior to the nucleation energy, within an effective length comparable to the critical radius, it will induce the vaporization of the nanodroplet. Here, we simplify the model assuming that both the effective length, and the part of the track where the proton has an energy above the threshold (which we call the proton interaction length, L_p) are much shorter than the droplet radius. This hypothesis has two consequences: first, each proton can only vaporize one droplet, and second, the probability of a proton vaporizing a single nanodroplet becomes the probability of the proton stopping within a droplet core, which can be mathematically expressed as:

$$P(vap) = \sum_i \frac{4}{3}\pi R_i^3 n_i = \frac{4}{3}\pi \hat{R}^3 \hat{n}, \quad (7.2)$$

where R_i is the droplet radius and n_i is the number concentration of droplets of radius R_i . Using the above assumption, the probability of vaporization is thus equal to the fraction of the irradiated volume occupied by the superheated liquid. The sum can be removed by using the mean volume-weighted radius \hat{R} and the mean volume-weighted number concentration \hat{n} .

During proton therapy delivery, a high proton fluence ($\sim 10^8$ protons/cm²) is used. Each proton can lead to two possible outcomes: it either stops within a droplet and vaporizes it, or not. Thus, a probability distribution can be built for the irradiation of a target with a given number of protons (N_p). Since each droplet can be vaporized only once, each vaporization event decreases the local droplet concentration, and therefore the probability of a subsequent event. The probability of the k^{th} vaporization can therefore be written as:

$$P(vap_k) = \frac{4}{3}\pi\hat{R}^3\left(\hat{n} - \frac{k-1}{V_{eff}}\right), \quad (7.3)$$

where V_{eff} represents the effective volume over which a droplet vaporization has an influence on the local droplet concentration. The effective volume is related to the average distance between stopping protons. If the distance is large, a vaporization induced by a first proton will have a negligible influence on the concentration of droplets at the stopping region of another proton. However, if the stopping distribution of protons is densely packed, the vaporization of a droplet decreases the probability of vaporization by subsequent protons. In the following, we assume that $\hat{n} \gg (k-1)/V_{eff}$, so that the vaporization of a droplet has virtually no influence on the probability of a new vaporization. This assumption is reasonable for the droplet concentrations and proton fluences used in this study, as the number of vaporization events was several orders of magnitude lower than the total number of droplets. The vaporization probability distribution in this case follows a binomial distribution, with an expected number of events given by:

$$E(vap) = N_p \cdot P(vap) = N_p \cdot \frac{4}{3}\pi\hat{R}^3\hat{n}. \quad (7.4)$$

This model allows to predict the expected number of vaporization events induced by primary protons, assuming that the nanodroplet concentration, size distribution, and number of protons are known. Combined with the knowledge that the spatial distribution of vaporization events follows the proton stopping distribution [256], the model can predict, for a given treatment plan, the shape and amplitude of the nanodroplet vaporization profiles. Additionally, when used in the other way around, such a model can be used to infer the nanodroplet concentration required in the tumor to achieve a given precision for range verification (see section 7.2.3).

7.2.2 Experimental validation

Data collection

Localization of individual radiation-induced droplet vaporization events was performed by means of online ultrasound imaging as described in [256]. Briefly, perfluorobutane nanodroplets encapsulated in a polyvinyl alcohol shell (PVA-PFB) were prepared following the protocol described in [244,290]. Nanodroplets were pipetted and mixed manually in an aqueous matrix (0.1% w/v Carbopol 2050, Lubrizol, Wickliffe, USA, [245]) heated to the desired temperature of 50 °C. The phantoms were immersed in a water tank, controlled at the same temperature of 50 °C, and irradiated in the experimental room of the Holland Proton Therapy Center (Delft, the Netherlands, figure 7.1(a)). Each phantom was irradiated using a monoenergetic proton pencil beam (horizontally oriented), while the total number of incident protons was measured by a transmission ionization chamber (beam monitor, DE.TEC.TOR, Turin, Italy). The beam was aligned to the center of the phantom cross-section, and the range was located approximately in the middle of the phantom length. The phantom dimensions (54x26x51 mm) were sufficient to encompass the complete proton Gaussian spot (>98%).

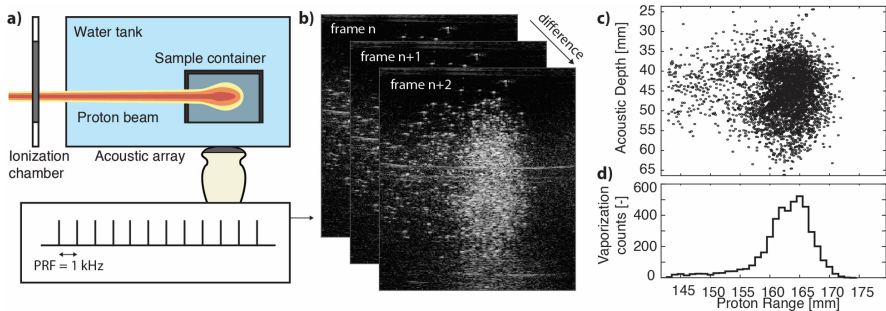


Figure 7.1: a) Schematic of the setup used for the acoustic localization of proton vaporization. b) Stack of B-mode frames used for differential imaging. c) Sample of 2D "accumulated" distribution of vaporization events after differential imaging. d) Distribution of vaporizations along the proton axis.

The phantoms were imaged during irradiation with an ultrasound linear array (ATL L12-5, 9 MHz pulses) positioned parallel to the beam direction, using a programmable ultrasound research unit (Verasonics Vantage 256, Kirkland, USA). High frame rate (1 kHz), low amplitude plane wave imaging was performed during the whole irradiation duration. The ultrasound frames were

beamformed offline on the Verasonics platform, and differential imaging was applied (figure 7.1(b)) in order to count and localize individual vaporization events, as in Ultrasound Localization Microscopy [77, 78]. 2D (figure 7.1(c)) and 1D vaporization maps were extracted for each phantom by accumulating vaporization events in time (figure 7.1(d)). The absolute position of the ultrasound probe was determined using ultrasound images of a point reflector placed at a known position, which allowed to translate the ultrasound image coordinates to absolute positions.

Study design

a) Droplet sub-populations:

In order to validate the statistical model presented in section 7.2.1, the influence of droplet size and concentration was assessed separately. Size isolation through differential centrifugation [291] was performed on the polydisperse native distribution of droplets (figure 7.2(a)). The size distribution and concentration were measured using a Coulter Counter Multisizer 3 (Beckman Coulter, Mijdrecht, the Netherlands) with a 50 μm aperture tube. Since the smallest diameter that could be measured in this configuration was 1 μm , we isolated three different size distributions in the range 1-10 μm . The required centrifugation speed ω for complete sedimentation of several cut-off diameters d_c were computed based on the centrifuge settings (Heraeus Biofuge Primo, Waltham, Massachusetts, USA, maximum rotor radius $R_{max} = 14.5$ cm), applying the following equation [291]:

$$\omega^2 = \sqrt{\frac{18\mu_w}{d_c^2 t \Delta\rho} \ln \frac{R_{max}}{R_{min}}} \quad (7.5)$$

The minimum rotor radius R_{min} is given by $R_{min} = R_{max} - L$, with $L = 5$ cm corresponding to the height of the liquid column in the nanodroplet vials, while t is the centrifugation time. $\Delta\rho = \rho_l - \rho_w$ is the difference between the nanodroplet density and the dispersion liquid (water) density, and μ_w is the dynamic viscosity of the dispersion liquid. Three cut-off sizes were defined: $d_c = 4$ μm (ND-L), 2.5 μm (ND-M), and 1.5 μm (ND-S).

The complete size sorting procedure is schematically represented in figure 7.2(e). Six days after preparation, the pellets of eight 5 ml vials of native nanodroplets were recombined after high speed centrifugation (1000g, 5 min). The time interval between nanodroplet preparation and size sorting allowed an increase of the fraction of large droplets in the native population, as seen in figure 7.2(a). The combined vial was then centrifuged 5 times using the 4 μm cut-off settings (223g, 1 minute). After each centrifugation step, the supernatant containing

droplets $<4 \mu\text{m}$ was transferred to another vial, and the pellet with the droplets $>4 \mu\text{m}$ was redispersed in Milli-Q water. Subsequently, all supernatants were centrifuged at high-speed (1000g, 5 min) and recombined. The combined vial was then centrifuged 5 times using the $2.5 \mu\text{m}$ cut-off settings (286 g and 2 min), and the same protocol was followed to collect the droplets between $2.5\text{--}4 \mu\text{m}$. After recombination of the supernatants, the vial was centrifuged 8 times using the $1.5 \mu\text{m}$ cut-off settings (529g, 3 minutes) to collect the droplets between $1.5\text{--}2.5 \mu\text{m}$. After completion of the size-isolation procedure, the headspace ($\sim 5 \text{ml}$) of each size-sorted vial (one per size range) was filled with PFB, and the vials were stored at 4°C . The size distributions of the three droplet sub-populations are shown in figure 7.2(b-d). The mean volume-weighted diameters and standard deviations were $5.8 \mu\text{m} \pm 2.2 \mu\text{m}$, $3.5 \mu\text{m} \pm 1.1 \mu\text{m}$ and $2.0 \mu\text{m} \pm 0.7 \mu\text{m}$ for sizes ND-L, ND-M and ND-S, respectively. As the Coulter Counter was not located at the proton therapy facility, the nanodroplet concentration and size distribution at the time of the proton experiment was estimated by averaging the vial concentrations and size distributions measured 4 hours before the start and 1 hour after the end of the irradiation experiments ($n=3$ at each time point). The estimated nanodroplet concentration in the vial during the irradiation experiment was 36.9, 30.6 and 16.4 mM for ND-L, ND-M and ND-S, respectively.

In order to evaluate the ability to detect a shift in proton range, phantoms with native nanodroplets (ND-native) were also irradiated at different beam energies. Irradiation experiments were performed two days after droplet preparation. The PFB concentration was assessed with NMR spectroscopy (400 MHz Avance II, Bruker Biospin GmbH, Rheinstetten, Germany) on the day following the proton experiments.

b) Irradiation parameters:

In order to study the influence of size and concentration, we irradiated different phantoms with dispersions of the size-sorted sub-populations. Additionally, phantoms with native nanodroplets were irradiated at different concentrations up to $50 \mu\text{M}$ and energies between 154 and 153 MeV to assess the ability to detect a shift in the proton range from the vaporization maps. Table 7.1 summarizes the experimental conditions for each phantom.

Characterization and modelling of the proton beam

a) Distribution of proton stopping positions:

The proton depth-dose distribution, range, and lateral spot spreading were measured and modelled following the procedure described in [256], and summarized in figure 7.3. Briefly, the proton range was obtained by an analytical

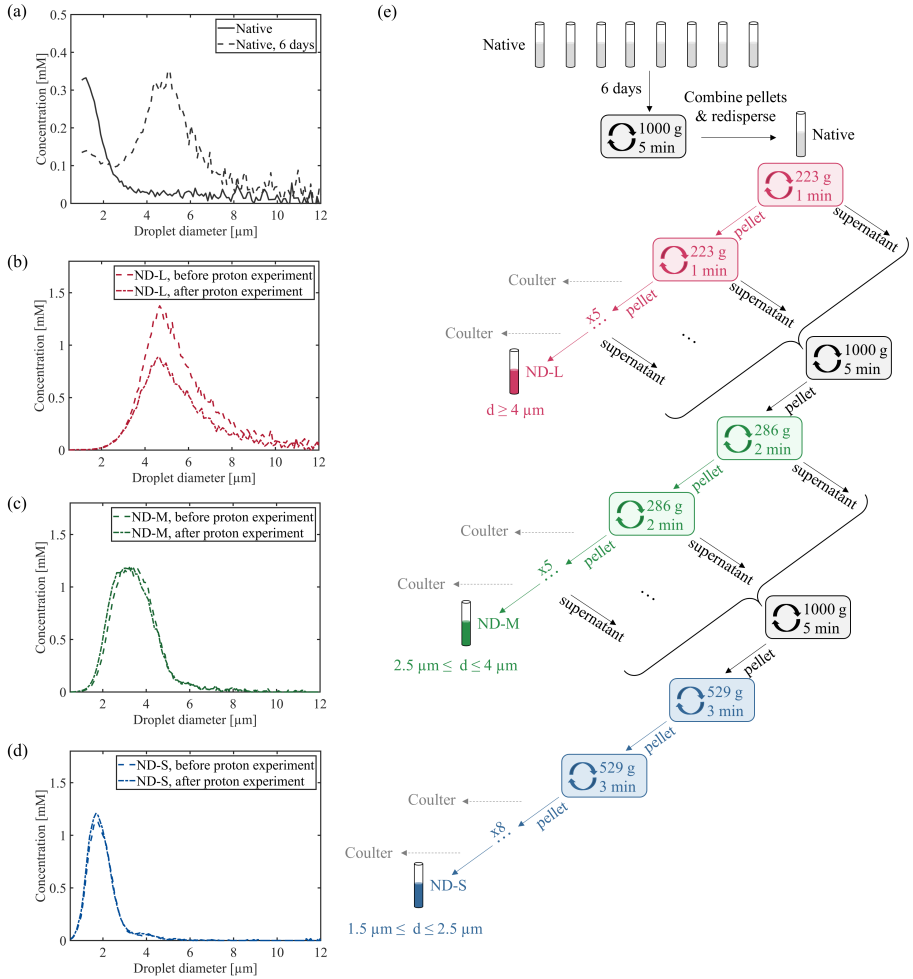


Figure 7.2: Overview of the size sorting procedure and corresponding size distributions for ND-native, ND-L, ND-M and ND-S.

fit [194] of the depth dose distribution (figure 7.3(a)) measured in a separate experiment with a multi-layer ionization chamber (QubeNext, 2.43 mm spacing, DE.TEC.TOR, Turin, Italy). The water-equivalent thickness (WET) of the different materials in the proton path, such as the water tank entrance wall and phantom entrance wall, were computed and accounted for in the range estimation [247]. The entrance lateral spot size was measured (LynxPT, IBA dosimetry, Schwarzenbruck, Germany, figure 7.3(b)) and spot spreading in water

Droplet type	Droplet concentration [μM]	Number of phantoms	Beam energy [MeV]	Beam current at extraction [nA]	Irradiation duration [s]
ND-S	20.9	3	154	40	5
ND-M	10.3	2			
	20.6	3	154	40	5
	30.9	2			
ND-L	17.3	3	154	40	5
	17.5	2	154		
ND-native	35	3	154		
	52.3	2	154	40	7
	52.3	2	153.7		
	52.3	2	153.5		
	52.3	2	153		

Table 7.1: Irradiation parameters for all phantoms under study.

was modelled with the Highland formula [15, 248]. The knowledge of the 2D Gaussian lateral spot spreading and the proton range and range dispersion (extracted from the analytical fit) allowed to compute the 3D distribution of stopping positions of primary protons. We made the distinction between primary protons stopping due to nuclear reactions (and thus indirectly leading to nanodroplet vaporization by high LET reaction products, figure 7.3(c)) and primary protons stopping in the Bragg peak, which directly vaporize nanodroplets when reaching their maximal LET (figure 7.3(d)). The stopping positions of protons lost due to nuclear interactions were obtained by using the total non-elastic interaction cross-section of protons in oxygen [200]. The stopping positions of primary protons in the Bragg peak were modelled by a Gaussian with a standard deviation equal to the fitted range spread value (σ in [194]) and centered on the range (R_{80}).

b) Estimation of the number of protons stopping in the imaged volume:

In order to compare theoretical predictions to the number of detected vaporization events, an estimation of the number of stopping protons in the imaging volume was necessary. The ultrasound images encompassed the full phantom length (parallel to the beam direction) and depth (ultrasound axial direction). However, only a slice of the phantom width was imaged, corresponding to the effective width of the ultrasound field of view. The determination of the effective width of the field of view is described in appendix 7.6. The distribution of scattered intensities was related to the droplet size distribution, assuming that the 99% quantile corresponded to a vaporized droplet of mean radius located at the center of the elevational plane. Once the ultrasound imaging volume was known, the number of protons stopping within this volume was determined from the 3D proton stopping distribution described above (figure 7.3(c-d)).

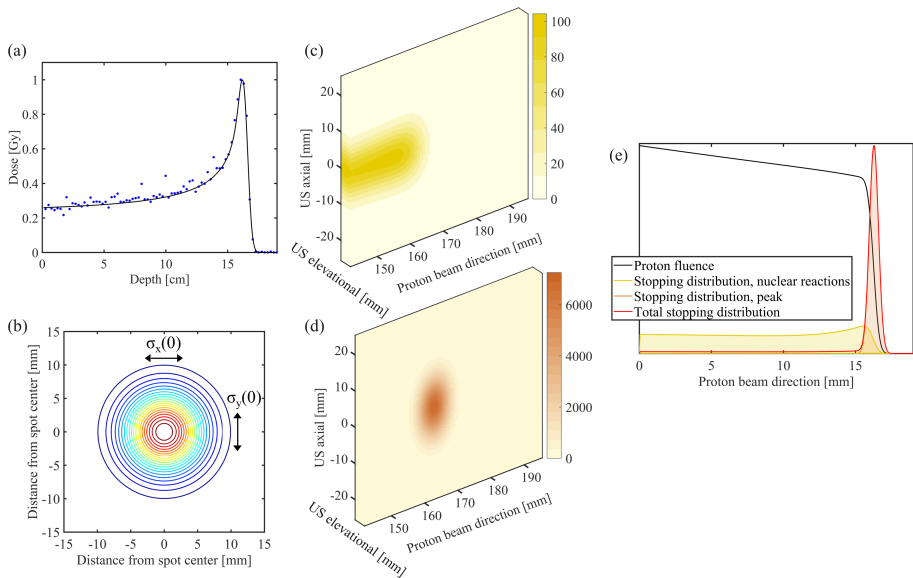


Figure 7.3: Overview of the beam characterization and modelling. Measurements of (a) the entrance spot size and (b) the depth-dose profile at 154 MeV, together with an analytical fit of the Bragg curve. Using the Highland formula, the fitted range and range dispersions, and the non-elastic cross section of protons in oxygen, 3D stopping distributions of protons lost to nuclear reactions (c) and of protons stopping at the end of their range, in the Bragg peak (d) were obtained. (e) 1D projections in the beam direction of the stopping positions of protons lost due to nuclear reactions (yellow) and protons stopping at the end of their range (orange). Note that the amplitude of the nuclear reactions curve (yellow) was enlarged by a factor 10 for visibility purposes.

Data analysis

a) Estimation of the proton range:

Individual vaporization events were binned along the direction of the proton beam propagation, using a 0.5 mm bin width. A least-squares algorithm was used to fit the 1D experimental vaporization profiles to a modelled vaporization profile (figure 7.4(a)) which consists of the sum of 1D projections of the stopping positions of protons lost due to nuclear interactions (entrance plateau) and the stopping positions of protons reaching the end of their range (Gaussian peak), derived in section 7.2.2 (figure 7.3(e)). The amplitude of both curves were used as fitting parameters, together with the shift of both profiles in the beam direction, which allowed to compute the deviation between the predicted and measured range. Additionally, in order to retrieve the number of vaporization

events due to primary protons, the number of vaporization events attributed to secondary particles, estimated through the fitting procedure, was subtracted from the total event counts.

b) Compensation for decrease in the vaporization rate:

The rate of vaporization was found to decrease over the course of irradiation, even though the model assumes a constant vaporization probability. The curves representing vaporization counts as a function of the number of incident protons were fitted to the Michaelis-Menten saturation curve, figure 7.4(b):

$$N_{vap} = \frac{a \cdot N_p}{b + N_p} \quad (7.6)$$

In order to compare experimental to predicted event counts, the initial slope, given by a/b , was used to estimate the number of vaporization events in the absence of saturation effects:

$$N_{vap,lin} = \frac{a}{b} N_p \quad (7.7)$$

c) Statistical analysis:

The measured event counts were compared to event counts predicted by the model from section 7.2.1. Experimental event counts were grouped by droplet size (ND-L, ND-M and ND-S) after normalization with the number of protons, and tested for normality with a Kolmogorov-Smirnov test, using Matlab (The Mathworks, Natick, MA, USA). The binomial distribution predicted by the model can be approximated to a normal distribution for large number of events, following the Central Limit Theorem [292]. Two-sided Student's t-tests (95% confidence level) were employed to test for differences between the observed mean number of counts for each nanodroplet size distribution and the expected value given by the statistical model, as well as pairwise differences between size groups. The linearity of the vaporization response with nanodroplet concentration was evaluated for phantoms with dispersed ND-M and dispersed ND-native, by applying a linear regression with zero intercept. For ND-M, a Student's t-test was employed to compare the fitted slope to the slope predicted by the model.

7.2.3 Simulation of the vaporization response in a clinically-relevant treatment plan

In order to investigate the impact of different factors (number of protons per spot, nanodroplet size, nanodroplet concentration) on the theoretical range retrieval precision, the nanodroplet vaporization response was simulated based

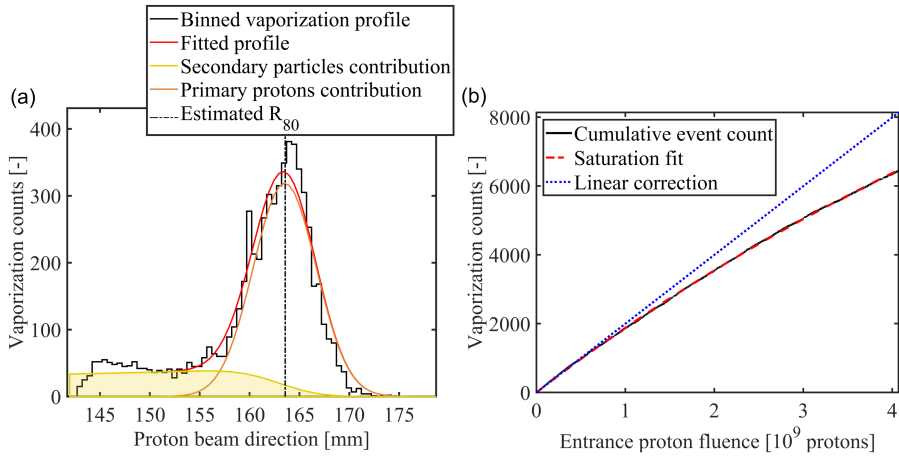


Figure 7.4: (a) Fitting of 1D vaporization profiles to a modelled profile, consisting in the sum of the expected vaporizations due to secondary particles (yellow) and due to primary protons (orange). The area under the secondaries curves was used to estimate the number of events due to secondary particles, which was subtracted from the total event count. The range error was found by estimating the shift between the fitted and experimental profiles, in the beam direction. (b) The cumulated vaporization counts were fitted to a saturation curve, and the initial slope estimate was used to derive the number of vaporization events in the absence of saturation.

on the model described in section 7.2.1, using clinically-relevant proton beam parameters. For online ultrasound imaging of a proton therapy plan delivered with Pencil Beam Scanning, the nanodroplet vaporization events would be counted and localized online, in principle allowing range verification to be performed on a spot-per-spot basis. Therefore, individual pencil beams were simulated.

In a first step, the range retrieval precision as a function of the number of vaporization events N_{vap} was evaluated for different proton energies (70, 150 and 240 MeV). One hundred synthetic vaporization distributions of $N_{max} = 10.000$ events were built using a Monte Carlo approach with a probability density function following the 1D profiles of stopping protons distributions computed as shown in figure 7.4(a), using the fitted experimental weights for the secondaries and primaries. The number of stopping protons in the US imaging volume was established by assuming a 5 cm^3 ultrasound imaging volume whose center point coincides with the proton range (R_{80}) position and the spot center. For each synthetic curve, the range estimates were computed using increasing number of

events (from 1 to N_{max}). Both the convergence to the final range estimated value (difference between range estimate $\hat{R}(N_{vap})$ and final range estimate $\hat{R}(N_{max})$) and precision (variability of the difference between the range estimates $\hat{R}(N_{vap})$ and the true proton range R_{80}) were evaluated. The precision on the range estimates was taken as $\pm 2\sigma$, in order to encompass 95% of the range estimates values, and evaluated as a function of the number of events N_{vap} .

In a second step, the initial conditions, such as the nanodroplet concentration and the number of protons per spot, were linked to the number of vaporization events. The mean and standard deviation of the total number of events were extracted for droplet concentrations ranging from 5 to 200 μM and values between $5 \cdot 10^5$ and $7 \cdot 10^9$ protons per spot, using the binomial probabilistic model of section 7.2.1. The events distribution as a function of initial conditions were then combined with the precision data to yield the expected range retrieval precision for different combinations of droplet concentration and proton intensities. Precision values for each combination were obtained by weighting the precision obtained in step 1 by the binomial distribution of event counts from step 2. To evaluate the achievable precision for clinical situations, precision values were computed for typical proton fluences of individual spots as well as full layers, extracted from clinical proton therapy treatment plans (2 Gy dose per fraction).

7.3 Results

7.3.1 Validation of the statistical model

Influence of droplet size on the vaporization response

After applying corrections to remove events attributed to secondary particles and the effect of saturation, the experimental event counts attributed to vaporization by primary protons were (mean \pm std) 950 ± 68 events for phantoms with dispersed ND-S, 4622 ± 1486 events for ND-M, and 4435 ± 1577 events for ND-L ($n=3$ for each size distribution). The reported values are normalized for 10^9 protons stopping in the ultrasound imaging volume, as the irradiation time was slightly different for each phantom. The experimental event counts were further normalized with respect to the nanodroplet concentration in each phantom. Figure 7.5(a) shows the dependency of the normalized number of vaporization events on the mean droplet radius, for the three size distributions. The dashed-dotted line represents the theoretical prediction from the statistical model. When normalized with respect to the nanodroplet number concentration, the expected number of vaporization events is proportional to

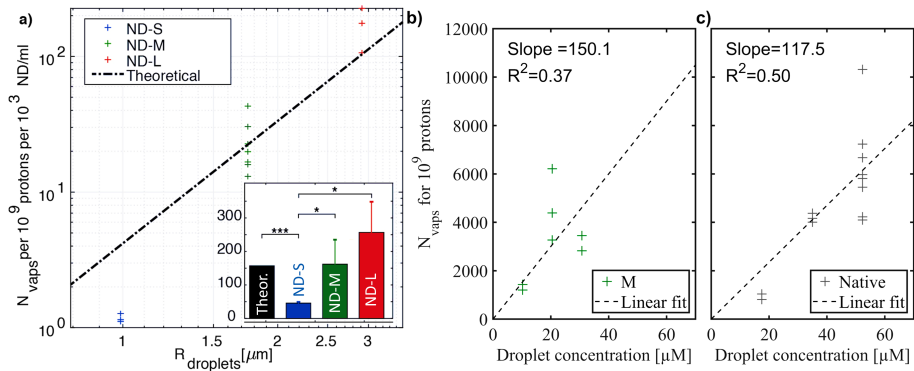


Figure 7.5: Comparison between experimental vaporization event counts from 3 different nanodroplet populations and predicted values using the statistical model. (a) Evolution of the number of vaporization events, normalized with respect to the number of protons and the droplet number concentration, as a function of the mean volume-weighted droplet radius. The dashed-dotted line represents the prediction from the model. The histogram insert compares the predicted (black) and measured (colored, mean+standard deviation) number of vaporization events normalized with respect to the number of protons and the droplet volume concentration. Statistical significance is indicated by the presence of stars: $p < 0.05$ (*) and $p < 0.001$ (***). (b-c) Evolution of the measured number of vaporization events for ND-M (b) and ND-native (c) droplets, normalized with respect to the number of protons, as a function of the droplet concentration. Dashed lines represent linear regression fits.

R^3 , hence to the mean nanodroplet volume. Therefore, when normalized with respect to the nanodroplet volume concentration, expressed in μM , the statistical model predicts that the vaporization yield is independent of the nanodroplet size distribution, as shown in the insert of figure 7.5(a). Except for ND-S, experimental event counts display a high inter-phantom variability. The Kolmogorov-Smirnov tests applied to each size group did not reject the hypothesis that the experimental data were sampled from a normal distribution. Using parametric t-tests, we observe a statistically significant difference ($p < 0.001$) between the mean number of events observed in phantoms dispersed with ND-S and the expected number of vaporization events given by the statistical model. No significant difference is found between the experimental mean of phantoms dispersed with ND-M and ND-L and the expected value. Comparing between size groups, the mean number of events for phantoms with ND-S is significantly different from the mean number of events for phantoms with ND-M and ND-L ($p < 0.05$).

Influence of droplet concentration on the vaporization response

Apart from the effect of droplet size, the influence of droplet concentration on the vaporization yield was investigated, using two different size distributions (ND-M and ND-native). Figure 7.5(b-c) shows the measured vaporization yield (number of events divided by the number of primary protons stopping in the imaging volume) as a function of the droplet volume concentration in μM , for ND-M (b) and ND-native (c), together with the associated linear regression curve. Similar to size-sorted droplets, a high inter-phantom variability is observed for native droplets (6222 ± 1975 events, $n=8$). The coefficient of determination is 0.37 for ND-M and 0.50 for ND-native, indicating that the variability in the number of events cannot be fully attributed to the concentration of droplets in the phantom. No statistically significant difference is found between the fitted slope for ND-M phantoms and the slope predicted by the statistical model: 149.2 and 157 events for 10^9 protons per μM of droplets, respectively. In contrast to the size-sorted ND populations, the number of vaporization events for ND-native was not compared to predicted values as (i) the droplet concentration could not be measured on the same day, and (ii) the polydisperse nature of native droplets prevented an accurate estimation of the effective ultrasound imaging volume.

7.3.2 Range verification performance

Theoretical range verification precision limits for different nanodroplet concentrations and number of protons

The influence of the number of vaporization events on the convergence to the final range estimated value (a) and precision with respect to the true range (b) extracted from simulations at three different energies are represented in figure 7.6. The number of vaporization events necessary to achieve a ± 0.5 mm precision on the range estimates are 70, 310 and 790 events for 70, 150, and 240 MeV, respectively (crossing between the 0.5 mm dashed line and the colored dotted curves in figure 7.6(b)). The method used to fit the vaporization events profiles and extract the position of the proton range does not introduce any constant bias (i.e., the mean error on the range estimate was <0.02 mm (figure 7.6(b))).

Using the statistical model, the expected precision ($\pm 2\sigma$, see section 7.2.3) as a function of the number of incident protons and droplet concentration is calculated and presented in figure 7.7 for the three simulated energies. The precision decreases with increasing energy, and increases with increasing

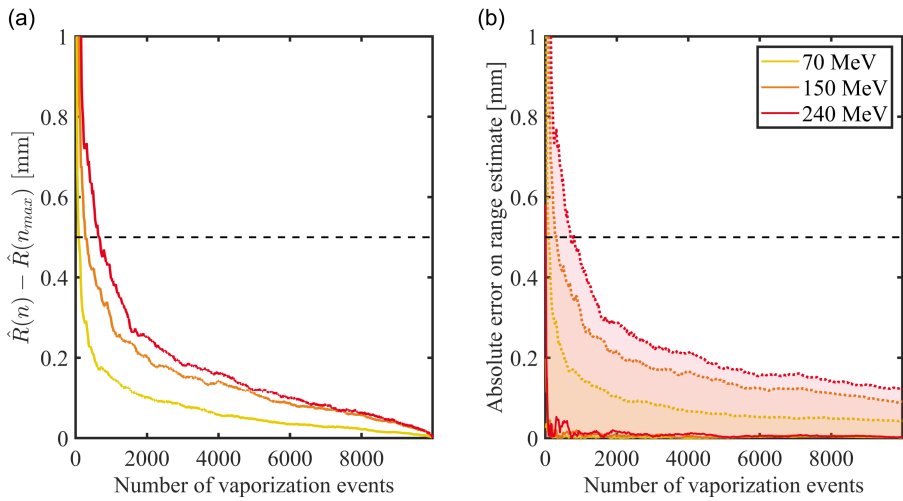


Figure 7.6: (a) Convergence to the final range estimated value $\hat{R}(n_{max})$, represented as the $+2\sigma$ limits (full lines), extracted from simulations at 70, 150 and 240 MeV. (b) Absolute error represented as the mean (line) and $+2\sigma$ (dashed lines) derived from simulations at the same abovementioned beam energies.

nanodroplet concentration and number of protons. Typical proton numbers for individual spots or full layers at different positions in the treatment plan (proximal to the tumor, in the tumor, distal to the tumor) are represented by vertical dashed (layer) and dashed-dotted (single spot) lines. At 70 MeV, the precision on range verification is below 0.5 mm for droplet concentrations as low as 12 μM and for a number of protons corresponding to individual spots distal or in the tumor. At 150 MeV, precisions below 0.5 mm can be achieved at any position in the treatment plan if the range is verified after the delivery of a full layer for concentrations of 16 μM . For single spot range verification, the precision is below 1 mm for concentrations above 38 μM . At 240 MeV, the precision on layer-based range verification is below 1 mm for concentrations above 31 μM , while for single spots, depending on the dose, the precision might be too limited (i.e. exceeding 2 mm).

Experimental validation of the range verification accuracy

The ability to detect a shift in proton range was investigated experimentally by irradiating phantoms at different beam energies. The R_{80} values measured with a multi-layer ionization chamber (QubeNext) and inferred from vaporization maps are shown in figure 7.8(a). Error bars of ± 0.5 mm were added to the

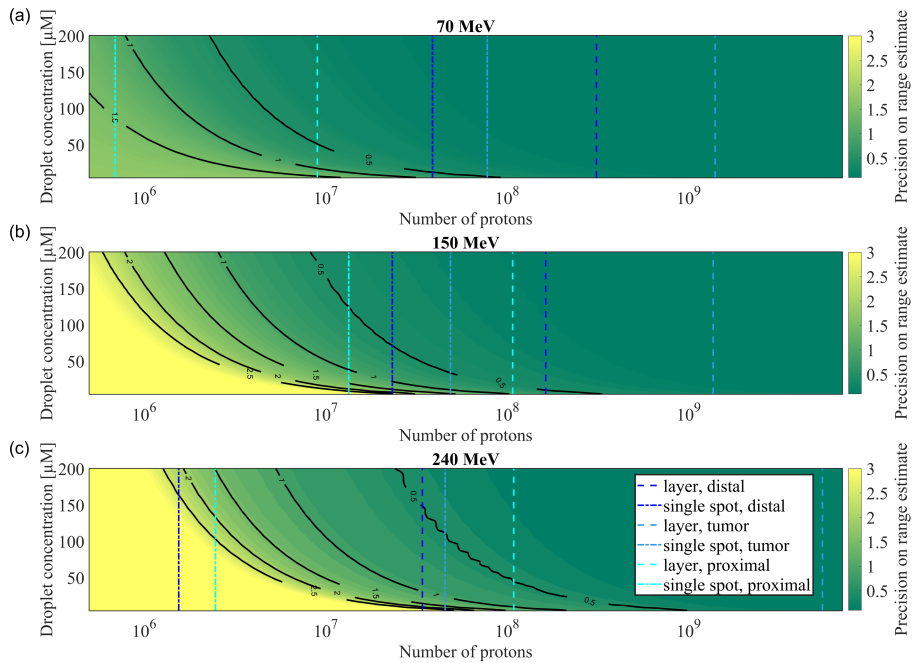


Figure 7.7: Simulated precision on range estimation from vaporization maps (yellow - worse than 2.5 mm - to dark green - better than 0.5 mm) as a function of the droplet concentration and number of incident protons, for entrance energies of 70 (a), 150 (b) and 240 (c) MeV. Vertical lines are clinically-relevant values of number of protons per spot (dashed-dotted) or per layer (dashed) located distal (dark blue), proximal (light blue), or inside (medium blue) the tumor.

QubeNext measurements, as it corresponds to the resolution limit of the detector. Except for the highest energy, where one measurement substantially deviates, all range estimates extracted from the vaporization maps are within the uncertainty window of the reference range measurements. The mean difference between the estimations of range decrease (compared to the 154 MeV value) from the vaporization maps and from QubeNext measurements is below 0.31 mm, and has a standard deviation of 0.30 mm (figure 7.8(b)).

The convergence to the final range estimated value as a function of event counts derived from the experiments at energies between 153 and 154 MeV is in good agreement with simulated values at 150 MeV (figure 7.9(a)). On the contrary, the experimental range deviation is found to be much higher than the simulated values, as shown on figure 7.9(b) ($\pm 2\sigma = 0.53$ mm versus ± 0.22 mm for event counts superior to 1770, figure 7.6(b)). The average bias between the range

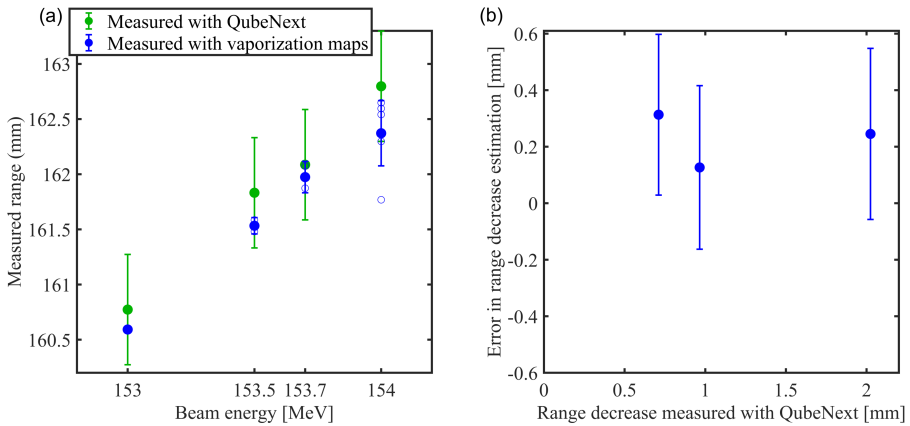


Figure 7.8: (a) Comparison between the range measured with a multi-layer ionization chamber (QubeNext, DE.TEC.TOR) and inferred from nanodroplet vaporization maps ($n=7$ at 154 MeV and $n=2$ for other energies). (b) Difference between the range decrease (with respect to the range measured at 154 MeV) measured with QubeNext and estimated from the nanodroplet vaporization maps. Dots and error bars represent mean \pm std.

estimated from vaporization maps and measured with QubeNext is 0.32 mm (figure 7.9(b)). From 1620 events on, the range accuracy limits (bias + precision, $\bar{X} \pm 2\sigma$) remain within ± 0.85 mm from the true range value.

7.4 Discussion

7.4.1 Comparison between model predictions and experimental observations

In this manuscript, we presented a statistical model to estimate the number and distribution of proton-induced vaporization events in a solution of superheated droplets. The probability of a proton vaporizing a droplet was hypothesized to be equivalent to the probability of the proton stopping within the droplet core. The distribution of event counts was then assumed to follow a binomial distribution, considering that the vaporization probability was constant (i.e., the vaporization density was orders of magnitude lower than the nanodroplet concentration). In this model, the expected number of vaporization events is linearly related to the volume concentration of nanodroplets in the phantoms, and to the number of protons stopping in the ultrasound imaging volume. To validate the model,

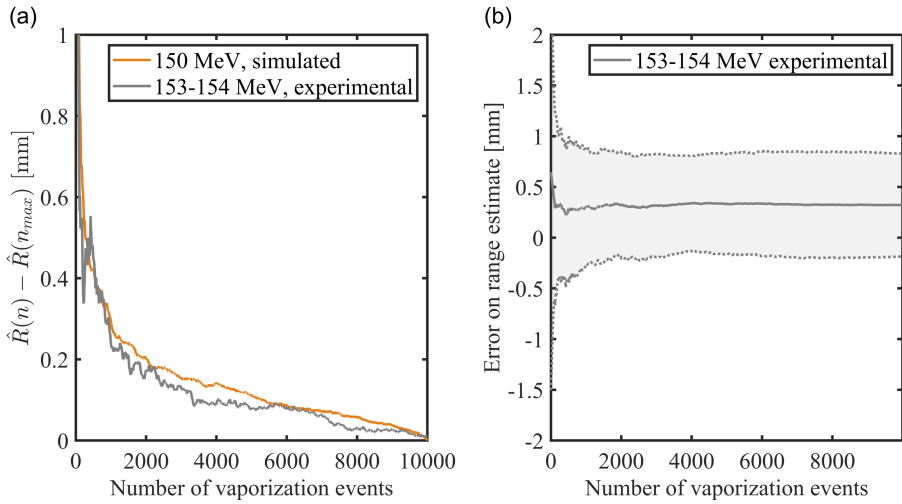


Figure 7.9: (a) Convergence to the final range estimated value $\hat{R}(n_{max})$, represented as the $+2\sigma$ limits (full lines), extracted from phantom experiments at energies between 153 and 154 MeV and compared to simulated values at 150 MeV. (b) Absolute error represented as the mean (line) $\pm 2\sigma$ (dashed lines) derived from experiments at energies between 153 and 154 MeV.

experimental event counts using different droplet sizes and concentrations were compared to theoretical estimates. A relatively high variability was observed for phantoms irradiated with similar parameters, with standard deviations reaching values up to 1577 events (ND-L). This inter-phantom variability cannot fully be explained by statistical variability, as the statistical standard deviation from the binomial distribution was between 41 to 70 events, but could originate from experimental factors. Despite this high variability, the predicted and measured number of events were in good agreement for sizes ND-M and ND-L. For ND-S, the number of events was significantly lower than expected. The observed differences between model predictions and experimental observations can arise from a series of factors, discussed below.

First of all, the model assumed that a proton has to stop within a droplet in order to vaporize it, as individual protons reach their maximum LET at the end of their range. In reality, for a vaporization to occur, a proton needs to deposit the energy necessary to nucleate a critical gas embryo within a finite distance (L_{eff}) in the superheated droplet core. Thus, the probability of vaporization depends on the droplet radius (R_i), the length over which the proton LET exceeds the LET threshold for vaporization (defined as the proton interaction length L_p) and L_{eff} . The vaporization probability increases both with R_i and

L_p , and decreases with L_{eff} . As proton energy depositions at such small scales ($L_{eff} = 44$ nm at 50°C) are stochastic, the maximum LET and therefore the interaction length L_p cannot be represented by a single value. Furthermore, the LET threshold is highly dependent on the droplet temperature, as shown by the sigmoid curves typically reported in the literature [151, 154]. Consequently, temperature differences in the order of 1°C could partially explain the large inter-phantom variability in event counts. Our model neglects these effects for the sake of simplification. A more precise prediction would require an improved and more dedicated modelling of the influence of these parameters for different droplet sizes, probably coupled with detailed Monte Carlo simulations of proton energy deposition at the nm scale.

Secondly, the model predicts only vaporization events induced by primary protons stopping at the end of their range, excluding vaporization events induced by nuclear reaction products. In order to account only for vaporization events due to primary protons, the vaporization events attributed to secondary particles were estimated by fitting the vaporization profiles to predicted responses, and subtracted from the total vaporization count. However, by using such a method, we assumed that (i) nuclear reactions are exactly following the $p+^{16}\text{O}$ nonelastic cross section of the modelled beam, neglecting other atoms such as C and F, present in the droplet core, and (ii) the vaporization probability is simply proportional to the non-elastic nuclear cross-section profile, while the dependency is in reality given by the production cross section of relevant secondary particles and their respective LET. Therefore, the separation of events due to primaries and secondaries suffers from some uncertainties.

Thirdly, the impact of the droplet shell was neglected in this model. Shell properties such as viscosity, elasticity and surface tension can influence the LET threshold, and hence the vaporization probability, especially for smaller droplets (Chapter 2). Therefore, the vaporization probability might not be simply proportional to the droplet volume, but rather decrease for smaller droplets. This hypothesis is supported by findings on the fraction of vaporization counts attributed to secondary particles and primary protons. As explained in section 7.2.2, 1D experimental vaporization profiles were fitted to an expected vaporization profile, consisting of the sum of primary protons and secondary particles contributions. Both the magnitude of the plateau contribution (secondary particles) and Gaussian end-of-range contribution (primary protons) were allowed to vary. In figure 7.10, the peak to plateau ratios extracted from such fitted vaporization profiles are presented for the three size-sorted nanodroplet distributions, as well as for native (polydisperse) nanodroplets. The peak to plateau ratio of ND-S phantoms was lower than that of ND-M and ND-L, which, combined to the reduced number of events attributed to primary protons for ND-S (figure 7.5), might indicate that the LET threshold increases

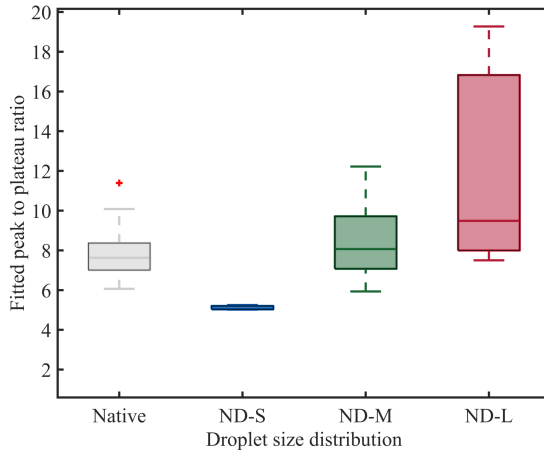


Figure 7.10: Peak to plateau ratio of experimental vaporization curves fitted to expected vaporization profiles, for the 4 different size distributions used in this study.

for smaller droplets, lowering the probability of vaporization by primary protons. The polydisperse nature of the ND-native distribution might explain why their peak to plateau ratio is higher than for ND-S, as the native distribution contains a small proportion of large (diameter $>2\mu\text{m}$) droplets, which were removed from the ND-S sample through differential centrifugation. Interestingly, for all size distributions, the peak to plateau ratio resulting from the fitted vaporization profiles was far below the ratio between the peak of the primary protons stopping distribution and the stopping distributions of protons involved in nuclear reactions ($=72$). This might indicate that some nuclear reactions could potentially lead to several vaporization events, and that the vaporization probability is higher for secondary particles than for primary protons, owing to their elevated LET (from 100-200 keV/ μm for alpha particles up to ~ 1000 keV/ μm for oxygen recoils, compared to 70-90 keV/ μm for protons).

Importantly, the model does not account for the observed decrease of the probability of vaporization over the course of irradiation (figure 7.4(b)). Several reasons can be suggested for this decrease. First, the probability could decrease due to a local decrease in the concentration and subsequent change in the size distribution of droplets, as larger droplets have a higher probability of vaporization. Second, the nanodroplet concentration can decrease due to other effects such as dissolution [67] and mass transfer to neighbor bubbles [293]. Finally, droplet vaporization into microbubbles will increase the acoustic attenuation, and therefore decrease the measured intensity of new events over

the course of irradiation, hampering their detection and decreasing the effective width of the ultrasound imaging volume. Although a dedicated model accounting for all the aforementioned effects could have led to a matching prediction of the observed saturation of the vaporization counts over time, we opted to compensate for the decrease by fitting a saturation curve and correcting the number of events by a linear extrapolation using the initial slope estimates (figure 7.4(b)). We do not expect this factor to have a major influence on the observed deviation between the predicted and experimental event counts.

The estimation of the number of protons stopping in the ultrasound imaging volume is critical to compare experimental results to theoretical predictions. In 2D ultrasound imaging, the ultrasound field of view is well-defined in the ultrasound axial and lateral directions, but not in the direction perpendicular to the ultrasound array (i.e., the elevational direction). While an elaborate method (Appendix 7.6) was employed to estimate the effective width of the field of view (FOV), uncertainties arise relating the measured intensities to the different droplet sizes. Such uncertainty sources could be removed by using volumetric ultrasound imaging with an ultrasound probe able to cover the entire irradiated volume.

Finally, uncertainties related to the measurements of the size distribution and concentration might have affected the experimental results in two ways. First, the nanodroplet size distribution was extracted from measurements acquired with a Coulter Counter Multisizer 3, which measures the outer diameter of nanodroplets. However, for radiation-induced nanodroplet vaporization, the inner diameter should be considered, as only energy depositions within the superheated liquid core may lead to vaporization. Therefore, the reported volume nanodroplet concentrations (in μM) might have been overestimated, especially for smaller sizes as the shell then takes on a relatively bigger proportion of the total droplet volume. While the shell thickness was not measured for the droplets used in this study, shell thicknesses of up to 15-40% of the outer radius were reported for PVA microbubbles [162,294]. Second, the nanodroplet concentration was measured hours before and after proton irradiation, which might have induced errors for ND-L, where a decrease of nanodroplet concentration was observed between the two measurements. This hypothesis is supported by the fact that the total number of events in phantoms with dispersed ND-L was inversely related to the order in which the phantoms were irradiated, indicating that the nanodroplet concentration in the vial might have decreased during the experiment.

Regarding clinical translation, the experimental conditions used to validate the statistical model were not directly representative of clinical conditions, as large droplets (diameter $> 1 \mu\text{m}$) and a physiologically too high temperature (50°C) were employed. As far as the temperature is concerned, the choice of 50°C

was motivated by the need to work at degrees of superheat sufficiently high for proton-induced nanodroplet vaporization. Clinical translation can be achieved through the use of nanodroplet formulations with a similar degree of superheat at 37°C, or by using other means to increase the degree of superheat of PFB droplets at 37°C, such as acoustic modulation (Chapter 8). A similar statistical model could be applied at 37°C as long as proton sensitivity is achieved. Importantly, the degree of superheat should be carefully tuned to avoid a strong dependence of the vaporization event counts on the local temperature *in vivo*. Regarding the droplet diameter, relatively large droplets were used to allow their characterization with a Coulter Counter. The option to use Dynamic Light Scattering (DLS) to evaluate the nanodroplet size distribution was abandoned, as DLS does not provide the droplet concentration, and conversion from intensity-weighted size distributions to number or volume-weighted size distributions requires the knowledge of the diffraction coefficient of liquid PFB at ambient temperature (i.e. the temperature used for DLS measurements) [204]. While values have been reported in the literature [73, 295], they might not hold when PFB is maintained in a superheated state and encapsulated in a shell. Future studies should determine the safe droplet diameter range for *in vivo* use. While smaller droplets might be beneficial to enhance the droplet distribution homogeneity in the tumor through extravasation, our experimental results revealed that a compromise might be required to preserve the vaporization efficiency.

7.4.2 Range verification performances

Once the ability to estimate the number of vaporization events based on the statistical model was confirmed experimentally, simulations were carried out to investigate the achievable theoretical range verification precision for different experimental conditions (single proton spot or full layer, beam energy, nanodroplet concentration). Range estimates were found to rapidly converge towards the true range value, reaching a precision of ± 0.5 mm with less than 1000 vaporization events (figure 7.6(b)). The convergence speed and achievable precision decreased as the proton energy increased, which can be explained by the increased fluence loss due to nuclear reactions at high energies (leading to a decrease in the number of stopping protons in the ultrasound imaging volume), as well as a broader range dispersion. Estimations for the number of protons corresponding to single spot or single layer irradiation of a clinical treatment plan indicate that range verification on a single spot basis might be achievable at low energies, if nanodroplet concentrations in the range 5-30 μM can be achieved in the tumor. For high energies and similar concentrations, irradiation of a full layer might be necessary to achieve a ± 0.5 mm range verification

precision. Next, the ability to experimentally detect a shift in proton range was verified, and range estimates extracted from vaporization maps were found to lie within the uncertainty range of the absolute range measurements performed with a multi-layer ionization chamber.

Experimental precision values were found to be approximately doubled compared to theoretical precision limits. This can be explained by the fact that simulations do not account for multiple uncertainty sources affecting experimental range estimates. Small variations in the local droplet concentration (from improper mixing) and phantom positioning could degrade the experimental reproducibility of range estimates. Moreover, ultrasound-based range estimates may also be affected by image distortion (from artifacts, speed of sound mismatch, attenuation, etc.) and by errors related to the image-based registration of the ultrasound probe position (<0.2 mm). Importantly, the "ground truth" range values also suffered from uncertainties arising from the multi-layer ionization chamber measurements (± 0.5 mm) and the WET calculations. Therefore, the simulated precision values reported in figure 7.7 represent a best-case scenario, to which uncertainties encountered in clinical conditions must be added. Future *in vivo* studies will be instrumental to determine the extent of such uncertainties, particularly those related to the achievable nanodroplet distribution homogeneity *in vivo*, and the registration between anatomical/range verification ultrasound images with the planning CT.

To infer the proton range from vaporization maps, vaporization counts were projected on the beam propagation axis, and 1D vaporization profiles were fitted to predicted profiles. The fitted parameters were the amplitude of the contributions from secondary particles and primary protons, and the shift between the predicted curves and obtained vaporization map (i.e., the estimated range shift). This method was the most performant for range estimation, both for experiments and simulations, compared to methods where other parameters (e.g. the Bragg peak width) are allowed to vary. However, in a clinical scenario, not only the amplitude and position but also the shape of vaporization profiles may differ from predicted profiles, due to e.g. range mixing induced by tissue heterogeneities or anatomical changes. In an ideal clinical workflow, a more complex fitting method might be required, allowing for variations of both the proton treatment plan and the daily patient anatomy (which could be estimated by ultrasound imaging using the same system as that used for ultrasound-based range verification) to precisely match experimental vaporization profiles. A 3D fit might also be more appropriate than a 1D fit to assess potential deviations in the lateral beam profile as well.

While the present contribution was focused on the use of the developed statistical model to predict the number of vaporization events in the Bragg peak and assess the range verification performance, the ability to quantitatively match

the expected vaporization event counts with predictions from a simple model has implications for real-time *in vivo* dosimetry, as the delivered dose could be estimated using information on the local density of vaporization events. Critical requirements for *in vivo* dosimetry are to achieve (i) a reproducible and/or quantifiable nanodroplet concentration and spatial distribution at the target, and (ii) a reasonable reproducibility of the vaporization response itself. Assessing the reproducibility, amount, and homogeneity of nanodroplet uptake in different organs/tumors of interest should therefore be the priority of preclinical studies. Alternatively, to compensate for inhomogeneities in nanodroplet distribution, which are very likely *in vivo*, techniques allowing to quantify the local nanodroplet concentration *in vivo*, through e.g. acoustic vaporization and counting of remaining nanodroplets after proton therapy delivery, should be explored.

7.5 Conclusion

This study presented a simple statistical model to predict the number and spatial distribution of vaporization events induced by primary protons and the range verification precision for a given droplet concentration and proton dose. Even though model predictions of event counts were relatively close to experimental counts, discrepancies higher than the expected statistical variability were observed, especially for the smallest droplet distribution (ND-S). The impact of temperature and of droplet-dependent parameters should be further investigated. Another important source of discrepancy on the event counts was related to the high proportion of vaporization events induced by nuclear reaction products. Conversely, the high "plateau" contribution, when properly accounted for in the fitting procedure, did not have a detrimental impact on range estimates. Ultimately, as the vaporization probability exhibits a complex dependence on many parameters, the most appropriate approach might consist of using a semi-empirical model combining theoretical predictions with ad-hoc parameters determined from a thorough experimental measurement campaign.

7.6 Appendix: Effective thickness of the acoustic imaging plane

Ultrasound B-mode images are constructed using the time-of-flight of the individual echoes to each individual transducer element. When a linear array is used (i.e. all the elements lay within a single axis), only information of the

axial and lateral position of the acoustic scatterers is preserved [251]. Thus, all the scatterers appear compressed in a single plane, and consequently, the information of the elevational direction is lost. This represents a problem for quantification of the number of protons stopping in the field of view (FOV). Indeed, the number of protons in the FOV depends on the effective thickness of the acoustic volume, defined as the maximum distance in the elevational direction at which a scatterer can be acoustically detected [296]. Radiation-induced vaporization events were detected on differential images using intensity thresholding. Since the intensity decreases with distance in the elevational direction, the effective thickness of the FOV can be found as the maximum distance that will result in a registered backscattered intensity above the set threshold. This effective thickness depends on the acoustic transducer, the acoustic properties of the vaporized droplets, and their axial position (the lateral position can be disregarded if plane waves are used). Here, we propose an experimental and numerical method (using field-ii [272, 273]) to determine the effective thickness of the FOV as a function of axial position and droplet size. The method consists of four steps: (i) hydrophone measurement of the 1-way acoustic response of the linear array, (ii) fitting simulations of the 1-way acoustic response to hydrophone measurements, (iii) simulation of the 2-way acoustic response of the linear array, and (iv) convolution with the acoustic response of the vaporized droplets.

First, the 1-way acoustic response of the linear array was measured. Using the same acoustic excitation as in the experiments, the acoustic elevational plane field was measured (figure 7.11(b1)) using a 0.2 mm needle-hydrophone (0.2 mm, Precision Acoustics, Dorchester, UK). Furthermore, the acoustic impulse response of the transducer elements was measured at the focus of each individual element, assuming that acoustic diffraction was negligible. The impulse response of all elements was averaged (figure 7.11(b2-b3)). Next, the 1-way acoustic response of the linear array was simulated using field-ii. The geometrical properties of the array provided by the manufacturer (Verasonics, Kirkland, USA) were used, in combination with the measured impulse response. Importantly, the properties of the acoustic lens built in the probe are not provided, but are critical in the geometry of the acoustic field. Thus, in order to simulate the effect of the lens, we conducted a three parameter study in the simulations, by modifying: the geometrical focus of the elements in the elevational direction (R_f), the elements height (E_H), and the elements apodization factor (A_f). In order to find the optimal set of parameters, a least-squares fitting was performed, using both the peak-pressure and the -6dB elevational width at each axial depth. The resulting optimal parameters were $R_f = 32$ mm, $E_H = 5.5$ mm, $A_f = 0.52$, and the fitting is shown in figure 7.11(c), compared to the case where only the reference geometry (no lens) is used.

Once the simulations and experiments of the 1-way field were matched, the 2-way field could be simulated. For this, the pulse-echo response of individual scatterers positioned at different axial depths and elevational position was studied. The simulated RF-data was then adapted to the format and sampling frequency in order to be beamformed using the Verasonics toolbox. This allowed to reconstruct the intensity in the B-mode image as a function of the axial and elevational position (figure 7.11(d1)). Since the variation in the axial position of the events was low ($\sigma = 5.5$ mm), we used the curve at the axial position of the proton beam axis (45 mm, figure 7.11(d2)).

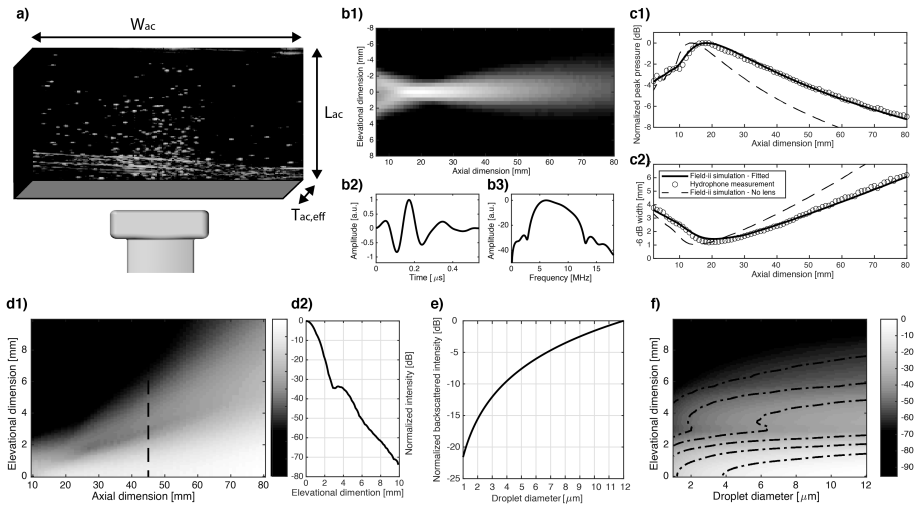


Figure 7.11: a) Schematic of the acoustic volume: the acoustic width (W_{ac}) and length (L_{ac}) are unequivocally defined, whereas the effective acoustic thickness ($T_{ac,eff}$) needs to be characterized. b) Hydrophone measurements: b1) 1-way acoustic field in the elevational and axial direction, b2) time trace of acoustic impulse, and b3) corresponding frequency spectrum. c) Comparison of the experimental and simulated acoustic field with and without the lens modelling, for both the c1) peak pressure and c2) -6dB width. d1) Received backscattered intensity as a function of axial and elevational position, and d2) profile at the axial position corresponding to the proton beam axis. e) Normalized backscattered pressure from a vaporized droplet as a function of the size assuming linearity with radius. f) Convolution of the intensity curve as a function of the elevational dimension and droplet size. The iso-level curves define the effective widths for different droplet sizes assuming different intensity thresholds.

Finally, the dependence of the scattered intensity on the vaporized droplet radius was addressed. When the acoustic frequency is much higher than the resonance frequency of a bubble, it can be shown that the scattered pressure is proportional to the bubble radius almost independently of the shell [297].

With a 5.4 fold increase in radius due to vaporization [190], the bubble radius in these measurements is in the 5-30 μm range, and since the acoustic frequency employed was 9 MHz, linearity in the scattered intensity was assumed, yielding the normalized backscattered intensity curve shown in figure 7.11(e). The intensity profile as a function of the elevational position was convolved with the intensity expected for each droplet size, giving a normalized map as a function of elevational position and droplet size (figure 7.11(f)). The effective width of the plane for each droplet size can be then found from the iso-intensity curves.

Note that this procedure yields a normalized backscattered intensity. The actual beamformed intensity is necessary to define the actual effective width for each experimental acquisition, and depends on many factors, such as the acoustic pressure, amplification factor, attenuation, etc. In our experiments, a statistical approach has been used, assuming that the 99% quantile of the experimental intensity distributions corresponded to the scattered intensity of a droplet of average radius located at the center of the acoustic plane. While we consider this hypothesis accurate enough for the purpose of this manuscript, more detailed strategies could be adopted if a more precise match is required.

7.7 Acknowledgments

The authors would like to thank Dr. Yosra Toumia and Prof. Gaio Paradossi (University of Rome Tor Vergata) for their support regarding the nanodroplet formulation, Bram Carlier (KU Leuven) for stimulating discussion, and Dr. Kevin Souris (UCLouvain) for providing clinical proton therapy treatment plans. The authors also thank A.A. Brouwer (ErasmusMC), R. Beurskens (Erasmus MC), and H. den Bok (TU Delft) for their contribution to the design and manufacturing of the experimental apparatus.

“Imagination is a form of seeing.”

Philip Pullman

8

Acoustic modulation of nanodroplet superheat enables proton detection at body temperature

*Sophie V. Heymans**, *Gonzalo Collado-Lara**, *Marta Rovituso*, *Hendrik J. Vos*, *Jan D’hooge*, *Nico de Jong*, and *Koen Van Den Abeele*

Submitted to *IEEE Transactions on Ultrasonics, Ferroelectrics, and Frequency Control*.

Superheated nanodroplet vaporization by proton radiation was recently demonstrated, opening the door to ultrasound-based *in vivo* proton range verification. However, at body temperature and physiological pressures, perfluorobutane nanodroplets (PFB-NDs), which offer a good compromise between stability and radiation sensitivity, are not directly sensitive to primary protons. Instead, they are vaporized by infrequent secondary particles, which limits the precision for range verification. The radiation-induced vaporization threshold can be reduced by lowering the pressure in the droplet such that nanodroplet vaporization by primary protons can occur. Here, we propose to use an acoustic field to lower the proton sensitization threshold of PFB-

*joint first author

NDs. Simultaneous proton irradiation and sonication with a 1.1 MHz focused transducer, using increasing peak negative pressures (PNPs), were applied on a dilution of PFB-NDs flowing in a tube, while vaporization was acoustically monitored with a linear array. Sensitization to primary protons was achieved at temperatures between 29 °C and 40 °C using acoustic PNPs of relatively low amplitude (from 800 kPa to 200 kPa, respectively), while sonication alone did not lead to ND vaporization at those PNPs. Sensitization was also measured at the clinically relevant body temperature (i.e., 37 °C) using a PNP of 400 kPa. These findings confirm that acoustic modulation lowers the sensitization threshold of superheated nanodroplets, enabling a direct proton response at body temperature.

8.1 Introduction

Proton therapy is an advanced radiotherapy modality which has gained popularity in the past decade [239]. In contrast to high energy photons, which traverse the entire patient's body, protons deliver most of their dose in a very localized region, called the Bragg peak, before abruptly stopping at a position known as the proton range [104]. The proton range can be tuned to correspond to the tumor location [15], thus enabling to better conform the dose distribution to the tumor and spare healthy tissues. However, the accuracy at which the range can be determined *in vivo* is limited by several sources of uncertainties, either with a physical or biological/anatomical origin [30,181]. To prevent severe under- or over-dosages that may result from those uncertainties, safety margins and sub-optimal beam arrangements are currently adopted, compromising the tumor dose conformality [30,206]. Therefore, *in vivo* range verification is critical to optimize the treatment precision and to allow proton therapy to reach its full potential.

The vaporization of superheated liquids by charged particles is a promising candidate for proton range verification. This technique was initially discovered in the 1950s in the context of bubble chambers [108,298], and later expanded to superheated drop detectors [113,147]. Recently, the concept was further extended to injectable superheated nanodroplets and proposed as a new solution for ultrasound-based *in vivo* proton range verification [124]. In their liquid form, droplets are effectively invisible to ultrasound, but protons can induce nanodroplet vaporization through direct energy deposition, or by reactions that produce secondary charged particles (heavy recoil nuclei, alpha particles, etc.), turning them into echogenic microbubbles [124]. The stochastic distribution of nanodroplet vaporization events can be then acoustically measured, using

either offline [244] or online [256] ultrasound imaging, and related to the spatial distribution of charged particles.

The sensitization threshold, i.e. the threshold which determines if a charged particle can trigger droplet vaporization, to each of these particles depends both on the density of energy deposition of the particle, called linear energy transfer (LET) in radiation physics, and on the degree of superheat of the nanodroplet core, which is the temperature excess above its boiling point [155]. The degree of superheat can be tuned by the nanodroplets internal temperature and pressure, and as it increases, nanodroplets become sensitive to lower LET particles [154]. In a proton beam and at low degrees of superheat, only high LET secondary particles lead to nanodroplet vaporization [124,244]. While the proton range can be indirectly inferred from the distribution of secondaries (using an approach similar to other range verification methods such as PET [33, 182, 183] and Prompt Gamma Imaging [37, 39, 285]), the precision of this method would be reduced. Firstly, the fluence of high-LET secondary particles is two orders of magnitude lower than that of primary protons [203], requiring a higher droplet concentration to achieve the same number of vaporizations. Secondly, the process to infer the range suffers from uncertainties related to the nuclear reaction cross-sections [30, 207]. Therefore, in order to obtain a precise and unambiguous measurement of the range, direct proton-induced nanodroplet vaporization is desirable.

One of the most common superheated liquids used to produce nanodroplets is perfluorobutane (PFB, C_4F_{10} , boiling temperature of -2°C at 1 atmosphere). Perfluorocarbons are biocompatible [299], and numerous studies have reported a good *in vivo* stability of coated PFB nanodroplets [122, 287, 288, 300], making this liquid core a good candidate for clinical translation. Unfortunately, the degree of superheat of PFB is below the sensitization threshold for protons at the physiological temperature of 37°C [244]. Previously, the degree of superheat of bubble chambers and superheated drop detectors was tuned by modifying the ambient temperature [151, 153], the static ambient pressure [150], or by using superheated liquids with different boiling temperatures [114, 149]. While the first two options are unfeasible in an *in vivo* application, the last option also suffers from several limitations. On the one hand, most of the superheated liquids used in *in vitro* detectors might not be biocompatible [67]. On the other hand, the lower molecular weight perfluorocarbon, namely perfluoropropane (C_3F_8 , boiling temperature of -37°C), (i) has a reduced stability due to a higher dissolution rate [119, 287], and (ii) is expected to lead to a large number of spontaneous vaporization events as the limit of superheat of perfluoropropane is very close to the physiological temperature [119, 123, 204, 287]. Thus, for *in vivo* range verification, a different approach to achieve direct vaporization of PFB nanodroplets by protons is preferred.

In the context of sono-photoacoustic imaging, the simultaneous use of ultrasound and pulsed laser radiation was shown to facilitate the vaporization of nanodroplets coated with optical absorbers [301–303]. The sensitization threshold was reduced by the rarefactional phase of the acoustic wave compared to scenarios where ultrasound or pulsed laser illumination was used alone. Here, we propose a similar approach, in which an acoustic wave is used to dynamically increase and decrease the nanodroplets degree of superheat during proton irradiation, reducing the energy required to trigger proton-induced vaporization during the rarefactional phase of the acoustic wave. Based on the homogeneous nucleation theory, we hypothesized that acoustic modulation would allow PFB nanodroplet vaporization by protons at 37 °C, enabling direct *in vivo* proton range verification. In this study, we used an acoustic imaging platform to detect nanodroplet vaporization during proton irradiation in combination with a low-frequency acoustic modulation field, covering a range of acoustic amplitudes, at different temperatures. This allowed to demonstrate the feasibility of acoustic modulation and to estimate the range of negative pressures which enable proton sensitization at each temperature, including the physiological case (i.e. 37 °C).

8.2 Materials and Methods

8.2.1 Nanodroplet formulation

Perfluorobutane nanodroplets with a polyvinyl alcohol shell (PVA-PFB) were prepared according to the protocol detailed in [244]. The intensity-weighted mean diameter of the nanodroplets, measured by Dynamic Light Scattering, was 842 nm \pm 12 nm, with a polydispersity index of 0.25 [244]. Nanodroplets were stored at 4 °C and used within 4 days post preparation.

8.2.2 Acoustic modulation transducer

In order to achieve a quasi-static pressure modulation with respect to the time scales of radiation-induced vaporization, a 1.1 MHz acoustic frequency was used. The quarter period of MHz waves is several orders of magnitude longer than the time necessary for an ion to nucleate a critical embryo, which was estimated to be in the order of tens of picoseconds [108]. This low frequency also ensures a relatively uniform pressure distribution within the droplet, whereas higher frequencies would lead to unwanted effects such as droplet resonance [173] or acoustic focusing [172]. A custom-made high-intensity focused transducer was used (center frequency 1.1 MHz), built from a spherically-focused PZT element

(48 mm, Meggit Ferroperm, Coventry, UK) and air-backed to ensure a high transmission efficiency. The steady-state pressure field (figure 8.7) and peak negative pressure (PNP) at focus were characterized using a calibrated needle hydrophone (0.2 mm, Precision Acoustics, Dorchester, UK), while driving the transducer with a 30-cycles sine wave. The acoustic focus was located at 48 mm, and the -6 dB length and width at focus were 15 mm and 1.8 mm, respectively.

8.2.3 Experimental setup

Proton irradiation experiments were carried out at the research beam line of the Holland Proton Therapy Center (Delft, the Netherlands). The beam line provides a continuous horizontal pencil beam, with clinical settings (proton energies ranging from 70 to 250 MeV and beam intensities from 1 to 800 nA at beam extraction). A clinically-relevant beam energy of 158 MeV was used for the current experiments (corresponding to a range in water of 17 cm). A water tank equipped with resistive heaters and a temperature control unit was positioned with its entrance wall located at the isocenter (i.e. the reference point in the proton beam path) (figure 8.1(a)). The irradiation target was a cellulose tube (6 mm diameter, 75 μm wall thickness, Serva, Heidelberg, DE), in which a nanodroplet solution was flowing. The tube was positioned vertically and perpendicular to the proton beam direction. To ensure inflation of the cellulose tube, a moderate overpressure (0.36 bar) was achieved by connecting a 30G needle to the tube outlet. In order to avoid variations in overpressure with temperature, the outlet of the tube was cooled down in a water reservoir at room temperature (not drawn in figure 8.1(a)).

The modulation transducer was located inside the water tank, at the same height as the proton beam axis, and focused at the center of the cellulose tube. The transducer was driven with signals generated by an arbitrary waveform generator (AWG) (ww2571a, Tabor Electronics, Neshan, IL) and amplified by 53 dB (150A100B, Amplifier Research, Souderton, USA). An L12-5 linear array was used to image the tube and capture nanodroplet vaporization events. The linear array was fixed outside the water tank and connected to a Vantage 256 system (Verasonics, Kirkland, USA). Acoustic coupling was ensured by a 20 μm -thin polyester window attached to the wall of the water tank. The linear array was positioned parallel to the tube, providing a long axis cross-sectional image in the flow direction. In order to co-align the modulation transducer and the linear array, the tube was temporarily replaced with a 1 mm diameter steel rod fixed at the location corresponding to the center of the tube and the pulse-echo signals of both acoustic probes were maximized.

In order to reduce unwanted vaporization events owing to high-LET particles,

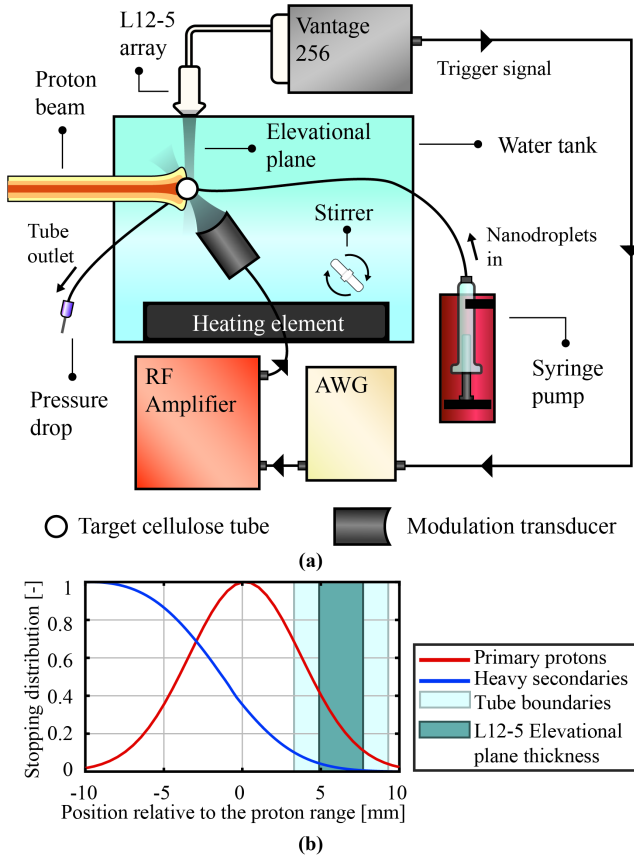


Figure 8.1: (a) Schematic diagram of the setup (top view). The proton beam, modulation transducer, and linear array were co-aligned to the target tube in which nanodroplets were flowing. (b) Position of the cellulose tube with respect to the stopping distribution of charged particles. The tube area is shown together with the -6dB elevational plane thickness of the L12-5 probe.

the center of the tube was positioned at the wake of the proton stopping distribution (figure 8.1(b)). Indeed, the fluence of high-LET secondaries drops proximal to the primary proton fluence due to the Coulomb barrier [4]. While this choice of tube position also led to a reduction in the number of stopping protons, the ratio of primary protons to secondary particles increased by one order of magnitude. The exact position of the tube with respect to the proton range was measured independently using the technique presented in [256], and the tube was found to be located 6.1 mm behind the position at which 50% of the primary protons have stopped (i.e., the proton range).

8.2.4 Acoustic modulation experiment

Nanodroplet dilutions were prepared by mixing 800 μl of native suspension with 60 ml of Milli-Q water. The dilution was driven through the tube at 1.8 ml/min using a syringe pump (AL-1000, World Precision Instruments, Sarasota, USA) and irradiated with a proton flux of 2.22×10^8 protons/s at the center of the tube (400 nA beam current at extraction). The water tank was heated to 50 °C and allowed to reach gas equilibrium overnight. During the experiments, the heating system was turned off and proton-induced nanodroplet vaporization was monitored during cooling down, while a magnetic stirrer kept the temperature homogeneous inside the tank. A thermal infrared (IR) camera (i7, FLIR, Wilsonville, USA) facing the cellulose tube recorded the temperature. The nanodroplet solution was refreshed every 20 to 30 min to compensate for any decay in droplet concentration. This resulted in the solution being refreshed before the measurements at 43 °C, 39 °C, and 35 °C.

Two different sets of recordings were acquired, depending on whether the temperature was above or below the proton sensitization threshold for the nanodroplets used:

1) *Sensitivity to protons at ambient conditions:*

First, the temperature at which the droplets lost sensitivity to protons at ambient pressure was determined. Acoustic recordings were performed during proton irradiation, without acoustic modulation, at different temperatures during cooling down of the water tank.

2) *Acoustically-induced sensitivity to protons:*

Once a drastic decrease of the number of vaporization events during proton irradiation was observed, we concluded that the temperature was below the sensitization threshold to protons. Consequently, the sensitization in the presence of an acoustic modulation field was studied. Acoustic recordings with and without acoustic modulation and proton irradiation were performed at different temperatures, during cooling down of the water tank.

8.2.5 Ultrasound sequence

The acoustic modulation and ultrasound imaging sequences are depicted in figure 8.2(a). Interferences between the modulation field and the monitoring sequences were avoided during the experiments by introducing a delay between the imaging sequence and modulation pulse. The acoustic modulation transducer was triggered by the Vantage system 40 μs after each image acquisition with the L12-5 array (8.9 MHz, plane waves, 0°angle). Effectively, each acquired image showed the effect of the previous modulation pulse. Long pulses (910 μs) at 1.1 MHz were used for acoustic modulation; such long pulses were chosen to maximize the

chance that a proton stops in a droplet while located in the rarefactional phase of the modulation beam. The pulse repetition frequency (PRF) for a single sequence (modulation + imaging) was 800 Hz. For each acquisition, 10 different pressures were investigated, starting from 0 to 900 kPa PNP, and 200 pulses were sent for each pressure step, leading to a total acquisition time of 2.5 seconds. The irradiation was always started before the ultrasound acquisition sequence and stopped once the acquisition was finished, providing a continuous proton beam during the whole sequence. For each temperature, three acquisitions were performed: (i) proton irradiation, no acoustic modulation, (ii) proton irradiation and simultaneous acoustic modulation, and (iii) acoustic modulation alone, without proton irradiation.

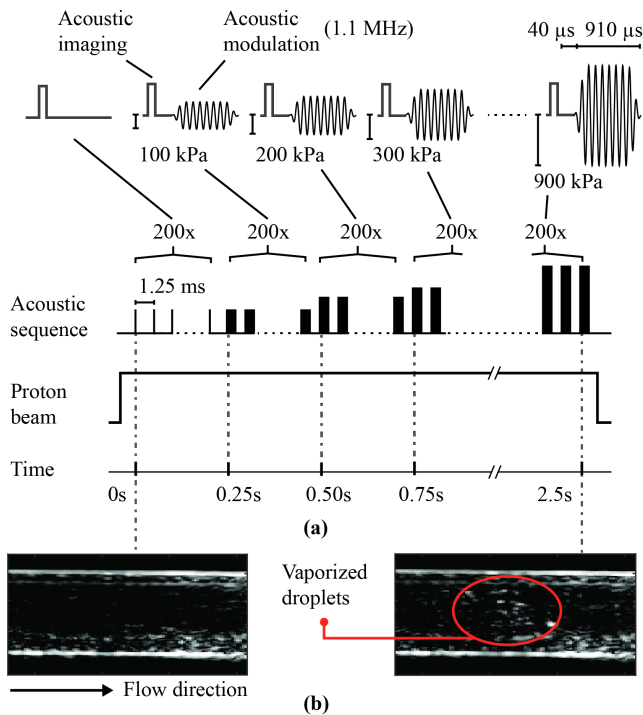


Figure 8.2: (a) Timeline of the acoustic modulation experiments. (b) Example of a B-mode image of the tube at the start (left) and end (right) of an acquisition. The bright spots at the center of the tube are vaporized nanodroplets.

8.2.6 Data processing

The radiofrequency data recorded with the Vantage system was stored to a disk and processed offline. First, B-mode images were reconstructed using the built-in Verasonics beamformer (figure 8.2(b)). Then, two regions of interest (ROI) were defined, one comprising the intersection of the proton beam cross section and the tube, and the other marking the -6dB limits of the acoustic modulation field. The boundaries of the first ROI were marked as the high vaporization density area on ultrasound recordings at 50 °C during proton irradiation. In order to determine the boundaries of the second ROI, the focus of the modulation field within the B-mode images was located using an acquisition in which the delay between the acoustic modulation and imaging pulses was removed. In this acquisition, the acoustic modulation field led to a change in the medium acoustic impedance which increased the backscatter intensity. The weighted centroids of the bright regions were used to locate the focus position in the lateral direction (figure 8.8), and the -6dB width measured with the hydrophone was then added.

Vaporization events in the ROI were measured and localized using the same principles as in [77]. Briefly, the frames were zero-phase filtered in slow time using a Butterworth high-pass filter (order 10, 300 Hz cut-off frequency, 25% pass-bandwidth). This step aimed at removing the slow changes in intensity between frames, only retaining the fast changes due to nanodroplet vaporization. Then, any image region whose intensity exceeded a given threshold, defined above the noise level in the frames without events, was localized and counted as a vaporization event. Finally, the vaporization counts were compared at different temperatures, in the presence and absence of acoustic modulation and proton irradiation.

8.3 Results

8.3.1 Sensitivity to protons at ambient conditions

figure 8.3(a) shows the vaporization events distribution as a function of the lateral position in the tube and recording time for different relevant temperatures in the absence of acoustic modulation. We chose such representation -where the axial positions of the events inside the tube are stacked- to make more compact graphs, as the axial distribution of vaporization events was not relevant for this study. Each yellow dot represents an individual event. Since the beam spot size in the lateral direction (13.3 mm FWHM) covered most of the ultrasound field of view (20 mm), the counts were distributed within the region of interest.

The total number of counts (figure 8.3(b)) was used as an indication of the sensitivity to protons at ambient conditions. The counts peaked at the highest investigated temperature (50 °C), and decreased with the temperature of the medium. This decreasing trend continued until the counts flattened below 43 °C. At this point, very few counts were measured (between 40 and 230 events during the 2.5 s recording), thus sensitivity to primary protons was assumed to be lost. Note that the 2D spatial distributions of vaporization events for the entire temperature range are shown in figure 8.9.

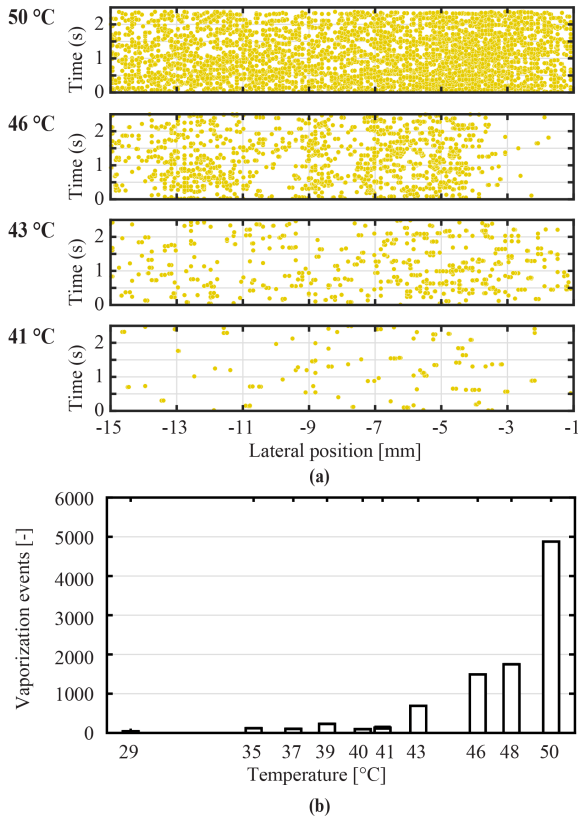


Figure 8.3: (a) Vaporization maps during proton irradiation without acoustic modulation as a function of lateral position and time within the ROI for different temperatures. All axial positions within the ROI are included. (b) Total number of counts for recordings with proton irradiation only (no acoustic modulation) for all recorded temperatures.

8.3.2 Acoustically modulated sensitivity to protons

When nanodroplet vaporization by protons was no longer observed at ambient conditions, the use of acoustic modulation to restore sensitivity to protons was investigated. The role of acoustic droplet vaporization (ADV) was also assessed during a second acquisition performed using the same acoustic modulation sequence but without proton irradiation. Figure 8.4 displays vaporization events again, but the vertical axis now represents the steps in acoustic modulation PNP. Each graph shows the data for one temperature. The full 2D spatial distribution of vaporization events in the tube, for all pressure steps, is presented in figure 8.10. Blue dots in figure 8.4 represent the vaporization events during proton irradiation with simultaneous acoustic modulation, while black dots represent the vaporization events for acoustic modulation alone (no irradiation). In the absence of acoustic modulation (0 kPa), the vaporization counts were negligible. A similar vaporization rate was observed until the PNP exceeded a certain threshold, which increased with decreasing temperatures. At low PNP, vaporization started at the acoustic modulation focus, represented by the two red dashed lines in figure 8.4. A further increase in modulation pressure amplitude resulted in a larger area where vaporization occurred. For all tested temperatures, the pressure at which vaporization occurred when the acoustic field was applied during proton irradiation was much lower than when the acoustic field was used alone (more than 500 kPa lower at the temperatures at which ADV was observed), thus showing a pressure range where vaporization events were induced by the combination of acoustic modulation and proton irradiation.

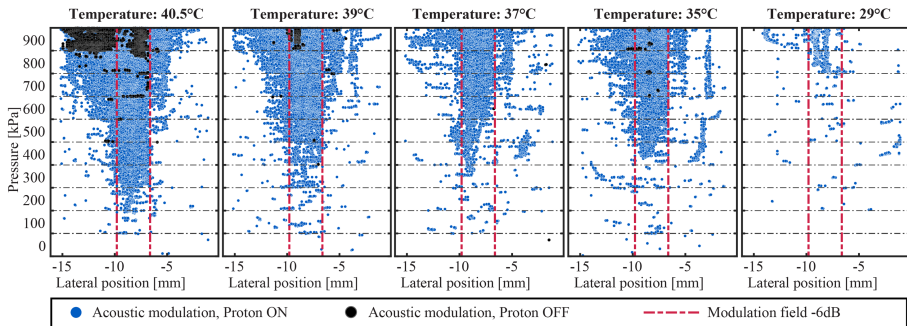


Figure 8.4: Vaporization maps within the region of interest as a function of lateral position and acoustic pressure for different temperatures at which the droplets were not initially sensitive to protons. All axial positions within the ROI are included. The blue dots represent the counts during simultaneous proton irradiation and acoustic modulation, whereas the black dots correspond to acquisitions without proton irradiation (pure acoustic droplet vaporization due to the modulation field).

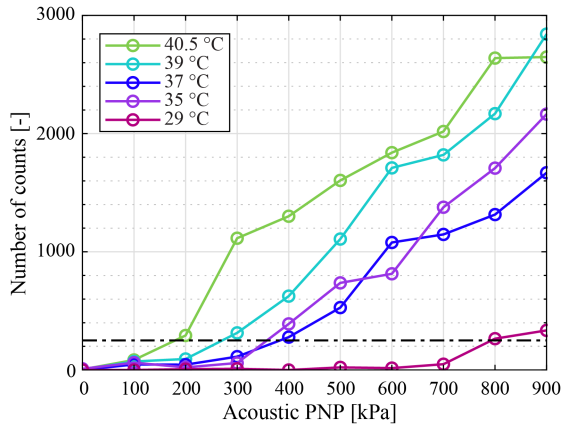


Figure 8.5: Number of vaporization events during simultaneous proton irradiation and acoustic modulation after completing each pressure step for different temperatures. The horizontal dashed-dotted line represents the sensitization threshold defined as 250 events. Note that the acoustic PNP was increased by discrete steps of 100 kPa; the lines between individual points only aim at guiding the eye.

The number of counts at each pressure step is shown in figure 8.5. A threshold at 250 counts was used to estimate the sensitization pressure. Near this threshold value, an increase in the slope of the count curves can be observed for all temperatures, and after the threshold, the counts increased at each pressure step. In addition, the counts at each pressure decreased with temperature, except for 35 °C. Note that the nanodroplets solution was replenished just before the acquisition at this temperature. The PNP threshold varied between 200 kPa at 40.5 °C and 800 kPa at 29 °C, with 400 kPa at 37 °C.

8.4 Discussion

In this study, we have investigated the use of an acoustic modulation field to lower the radiation-induced vaporization threshold of PFB nanodroplets, in order to achieve direct sensitivity to protons. At ambient pressure (1.36 bar in our experiment), proton-induced vaporization events were observed at elevated temperatures (50 °C) and their number gradually decreased with temperature, until sensitivity to protons was lost between 43 and 41 °C. These observations are in agreement with previous findings for superheated drop detectors, which showed a smooth, sigmoidal sensitization to charged particles, rather than a steep change in vaporization count [151, 154]. We attribute the

few residual vaporization counts observed for irradiations at temperatures below 41 °C to vaporizations due to high LET secondary particles. A low-frequency acoustic field was then applied during proton irradiation, enabling proton-induced vaporization at acoustic PNPs ranging from 200 kPa (40.5 °C) to 800 kPa (29 °C), well below the Acoustic Droplet Vaporization threshold. The use of an acoustic modulation field thus sensitized the nanodroplets to protons at temperatures for which, at ambient pressure, such nanodroplets would be vaporized by higher LET secondaries only [244]. While the energy sources differ, these observations are similar to findings reported for sono-photoacoustics, where nanodroplet vaporization was facilitated by the combination of laser heating of nanodroplets coated with a plasmonic absorber and the rarefactional pressure from an acoustic wave [301, 302].

We hypothesize that a transient increase in the nanodroplet degree of superheat during the rarefactional phases of the pulse is the mechanism leading to proton sensitization. Charged particles trigger the vaporization of superheated droplets through homogeneous nucleation. In this context, the energy deposited by the charged particle in the superheated liquid must exceed the energy required to create a critical embryo, and must be deposited within a distance comparable to the critical embryo size, as described by the thermal spike theory [108, 113]. This condition is mathematically expressed as:

$$\left\langle \frac{dE}{dx} \right\rangle_{L_{eff}} \geq \frac{W_{tot}}{aR_c} \quad (8.1)$$

where $\left\langle \frac{dE}{dx} \right\rangle_{L_{eff}}$ is the ion track-averaged LET, W_{tot} is the critical embryo nucleation energy, R_c is the critical radius, a is known as the nucleation parameter, and the product of a by R_c defines the effective length L_{eff} . W_{tot} and R_c can be calculated from the thermodynamic properties of the superheated liquid [113, 124]. The nucleation parameter, a , is an empirical constant for which values between 2 and 12 have been reported depending on the radiation type [113, 146, 154]. The ratio $W_{tot}/(aR_c)$ represents the LET threshold, which decreases with increasing degree of superheat. A decrease of the pressure inside the superheated liquid leads to a lower boiling temperature, and consequently an increased degree of superheat. During the rarefactional phase of an acoustic wave, the LET threshold is reduced compared to its value at ambient conditions, and could thus reach values below the maximum LET of protons, allowing the latter to vaporize nanodroplets.

The sensitization thresholds reported in this study were defined based on the vaporization counts. Importantly, three conditions are required for the counting method to accurately quantify the number of vaporization events: vaporizations are sparse; microbubbles do not subsequently disappear; and flowing bubbles do not enter or leave the imaging plane. Due to limitations

of the experimental setup used in our study, these conditions could not be entirely satisfied, as a large density of vaporization events was observed at high pressures, and some of the resulting microbubbles flowed in and out of the ultrasound field of view, likely resulting in an overestimation of vaporization events. However, we do not expect these limitations to significantly affect the sensitization threshold detection, as it is associated with low vaporization counts. A threshold corresponding to 250 vaporization counts was chosen as it qualitatively matches with a change in the slope of the count curves (figure 8.5). The measured sensitization thresholds were compared to theoretical values obtained by applying the thermal spike theory. First, the experimental proton sensitization curve at the ambient pressure (1.36 bar, figure 8.3(b)) was used to estimate the nucleation parameter. The theoretical peak proton LET in PFB is $74.5 \text{ keV}/\mu\text{m}$ [304]. Since sensitization occurred between 41°C and 43°C , the nucleation parameter had an upper and lower limit of 3.4 and 2.9, close to values previously reported in the literature for protons (i.e. $a=2.1\text{--}2.9$) [113, 149]. Then, the theoretical LET threshold was determined as a function of temperature and acoustic pressure (figure 8.6), assuming that the acoustic pressure is added quasi-statically to the ambient pressure. The blue region represents the theoretical sensitization threshold to protons for nucleation parameters between the limits reported above. The theoretical prediction is compared to the experimental values, shown as black markers. Importantly, the uncertainties affecting these thresholds should be assessed. Thermal heating due to ultrasound was estimated to be $<0.01^\circ\text{C}$ during an acquisition, and therefore, was assumed to be negligible. However, the large pressure increments used (100 kPa) and the hydrophone calibration uncertainty ($2\sigma \approx 15\%$ of PNP) must be taken into account. Thus, uncertainties of $\pm 50 \text{ kPa}$ and $\pm 15\%$ were added to the experimental points. Since the effective time interval during which the actual peak pressure is reached is negligible, the RMS pressure (reached during 50% of the rarefactional phase) is reported instead. Linear fits of the upper and lower limits of the experimental values were used to define the boundaries of the uncertainty region. The experimentally-determined acoustic pressures required for proton sensitization exceed the values predicted by the thermal spike theory, and the mismatch increases as the temperature decreases. In all cases, the differences are larger than the estimated uncertainties.

The discrepancy between theory and experiments could be due to limitations both in the model and in the sensitivity of the method. The thermal spike model used to estimate the effect of the acoustic modulation field is static, neglecting dynamic effects, such as the radial oscillations that the acoustic modulation wave induces to a vapor embryo. These could result in shrinkage and disappearance of the embryo during the consecutive compressional phase [172, 305]. Such an effect would be highly frequency-dependent and would raise the acoustic pressure needed for vaporization, in comparison to a static change in ambient

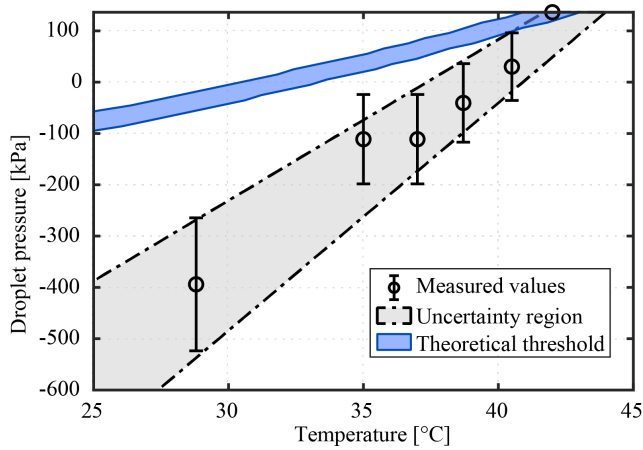


Figure 8.6: Vaporization LET threshold as a function of temperature and pressure inside the droplet. The blue region represents the theoretical sensitization curve assuming a quasi-static effect of the acoustic pressure. The black markers are the values obtained experimentally, including the uncertainty associated with the 100 kPa pressure steps and hydrophone measurement.

pressure assumed by the model. Moreover, the thermal spike model was shown to deviate from experimental observations, especially at low degrees of superheat [150, 154], and does neither account for the additional energy required to expand the viscoelastic shell during vaporization, nor for the effect of the Laplace pressure. Regarding the sensitivity of the method employed in this study, the number of vaporization counts depends on the probability for a droplet to be simultaneously exposed to the PNP of the modulation wave and traversed by a proton at the end of its range. Spatially, the calibrated PNPs are only reached in a confined spot, and the effective width of the acoustic sensitization region grows together with the applied pressure, increasing the vaporization probability. This is observed in figure 8.4, as initially the vaporization region was confined to a small area near the transducer focus, and increased with the applied acoustic pressure. Temporally, the vaporization probability increases with the effective time during which the rarefactional pressure is lower than the sensitization threshold. Once the proton sensitization threshold is reached, the proton-induced vaporization probability also increases with the degree of superheat [151, 154]. For these three reasons (spatial uniformity of the pressure field, temporal variation of the pressure, and effect of the degree of superheat), the number of vaporization events are expected to increase with increasing PNP above the sensitization threshold. This might have led to an overestimation in the reported sensitization threshold values. Consequently, the sensitization

thresholds shown in figure 8.6 should be interpreted as a trend rather than an accurate assessment of the required acoustic pressure for proton sensitization. While this study shows the feasibility of modulating the nanodroplets degree of superheat with a focused acoustic pressure field, the precise proton sensitization threshold should be determined in future studies. Ideally, a spatially-uniform modulation field would be used, and longer recordings should be acquired for each modulation PNP, allowing a relevant statistical analysis and preventing the need to define an arbitrary value (e.g., 250 vaporization event counts) to determine the sensitization threshold. Here, a center frequency of 1.1 MHz was used to modulate the pressure, but the temporal behavior of the field could play an important role. The effect of the driving frequency is an important point for future studies.

The PNPs necessary for ADV were much higher than the PNPs necessary for proton sensitization at all investigated temperatures, as seen in figure 8.4. In recordings made using acoustic modulation alone, ADV was mostly observed at 40.5 °C for PNPs above 800 kPa, while only very few vaporization events were recorded for lower temperatures within the investigated PNPs (0-900 kPa). A wide range of ADV thresholds have been reported in the literature for PFB nanodroplets, ranging from 1.2 to 3.5 MPa at 37 °C [122, 126, 306–308]. Such a large variation reflects the dependence of the ADV threshold on the ambient conditions, the acoustic pulse, and the droplet size, composition and concentration. A recent study investigated the effect of most of these parameters on the ADV threshold of PFB nanodroplets, showing that it decreases with increasing pulse length, PRF, temperature, droplet size and concentration, and with decreasing frequency [126]. Our study employed long pulses (1000 cycles), high PRF (800 Hz), and a high droplet concentration, together with a low ultrasound (US) frequency (1.1 MHz), which could explain the relatively low pressure (800 kPa) at which the onset of ADV was observed at 40.5 °C.

We envision that acoustic modulation could enable proton-induced vaporization of PFB nanodroplets for *in vivo* range verification and dosimetry. Although indirect nanodroplet vaporization induced by secondary particles at physiological temperature could be used [124, 244], such an approach suffers from severe constraints. The presented technique allows direct proton detection while employing the popular PFB liquid as the nanodroplet core. The threshold PNP for proton-induced nanodroplet vaporization at 37 °C was as low as 400 kPa, which means that proton sensitization could be achieved *in vivo* with a mechanical index of 0.29, well below the values that might lead to harmful bioeffects. Furthermore, this acoustic pressure can be easily achieved by commercial imaging arrays, which could be used both for acoustic modulation (ideally using a spatially-uniform pressure field, so that no prior knowledge about the proton range would be required) and imaging, reducing the setup

complexity. In the present proof-of-concept study, a continuous proton beam was used together with an acoustic modulation field with a long pulse length and a high PRF (1000 cycles, 800 Hz), to maximize the effective time during which nanodroplets were simultaneously exposed to protons and ultrasound. These long pulses did not lead to a temperature increase in water during this experiment; however, tissue heating should be prevented in physiological applications. Therefore, although the acoustic modulation approach is suitable for all proton therapy systems, in our opinion, the optimal clinical translation would be achieved for proton accelerators delivering a pulsed proton beam. In such a scenario, acoustic modulation can be applied for the duration of the proton spill, allowing a relatively short pulse length, while using the time in between proton bursts to image and localize nanodroplet vaporization events.

8.5 Conclusion

This manuscript reports on the feasibility of achieving direct vaporization of PFB nanodroplets by protons at physiological temperature by combining proton irradiation with a dynamic pressure modulation using an acoustic field. PVA-PFB nanodroplets flowing in a tube were simultaneously irradiated with a proton beam and sonicated with acoustic waves of increasing pressure amplitudes, while nanodroplet vaporization was monitored by an ultrasound array positioned parallel to the tube. Proton-induced nanodroplet vaporization was observed at temperatures below the sensitization temperature corresponding to ambient pressure conditions and using acoustic pressures below the ADV threshold. We attribute this effect to an increase of the nanodroplets degree of superheat during the rarefactional phase of the ultrasound wave, hence lowering the radiation-induced vaporization threshold. Importantly, the required PNP at 37 °C for proton sensitization was low (400 kPa), which suggests that acoustic modulation could be implemented clinically to enable *in vivo* proton range verification and dosimetry with the popular PFB nanodroplets.

8.6 Acknowledgments

The authors would like to thank Dr. Varya Daeichin for stimulating discussions and support, Dr. Yosra Toumia and Prof. Gaio Paradossi (University of Rome Tor Vergata) for their support regarding the nanodroplet formulation, and Bram Carlier (KU Leuven) for technical discussions. The authors also thank A.A. Brouwer (Erasmus MC), R. Beurskens (Erasmus MC) and H. den Bok (TU Delft) for their help in designing and building the experimental apparatus.

8.7 Supplementary materials

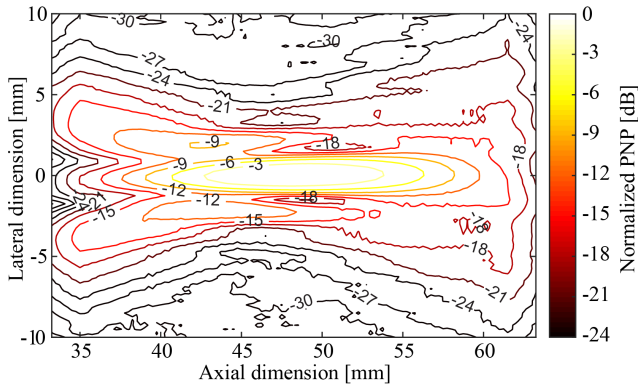


Figure 8.7: Peak negative pressure map of the 1.1 MHz acoustic modulation transducer.

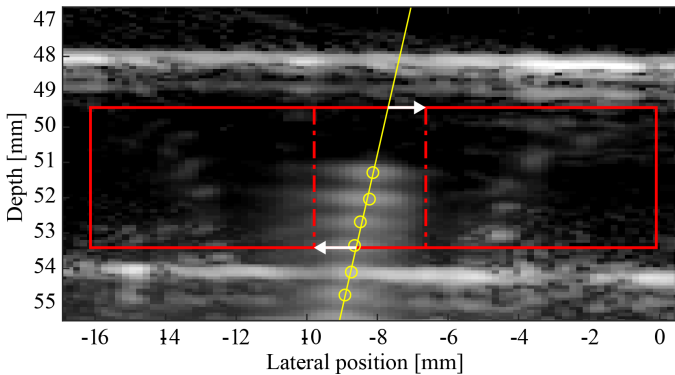


Figure 8.8: B-mode acquisition of the tube cross-section during acoustic modulation, with no delay between the imaging and modulation pulses, for alignment purposes. Two regions of interest (ROI) were defined: the vaporization region (red solid line), where the proton beam crosses the tube, and the acoustic modulation focus (red dash-dotted line). The center line of the modulation field was found from the weighted centroid of the modulation regions (yellow solid line). The white arrows correspond to the -6dB width of the beam, which were added at the two points where the center line crossed the vaporization region to create the acoustic modulation focus region. This accounts for the fact that the field was oblique with respect to the tube, including every lateral position where the pressure was above -6dB.

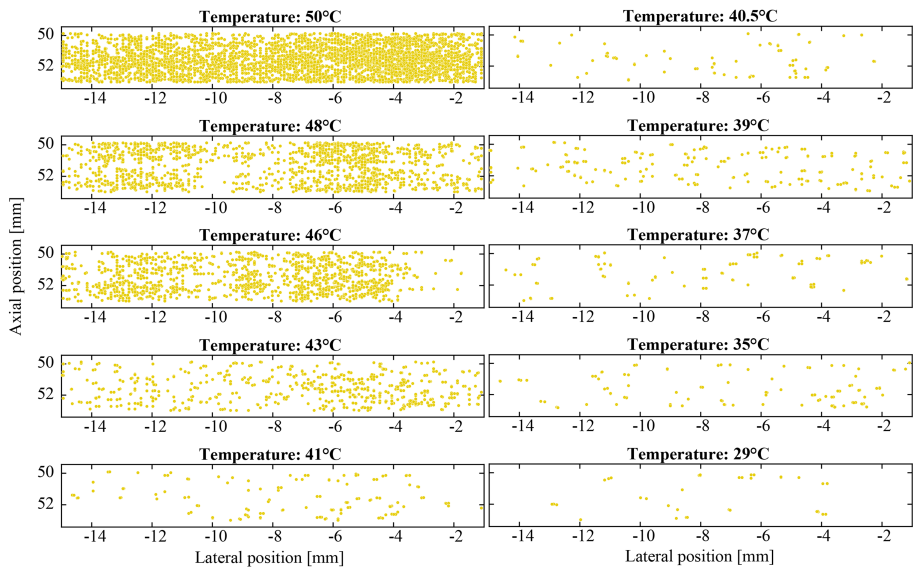


Figure 8.9: Vaporization maps obtained at all tested temperatures during proton irradiation, in the absence of acoustic modulation. The vaporization events shown are cumulated over the entire recording time (2.5 s).

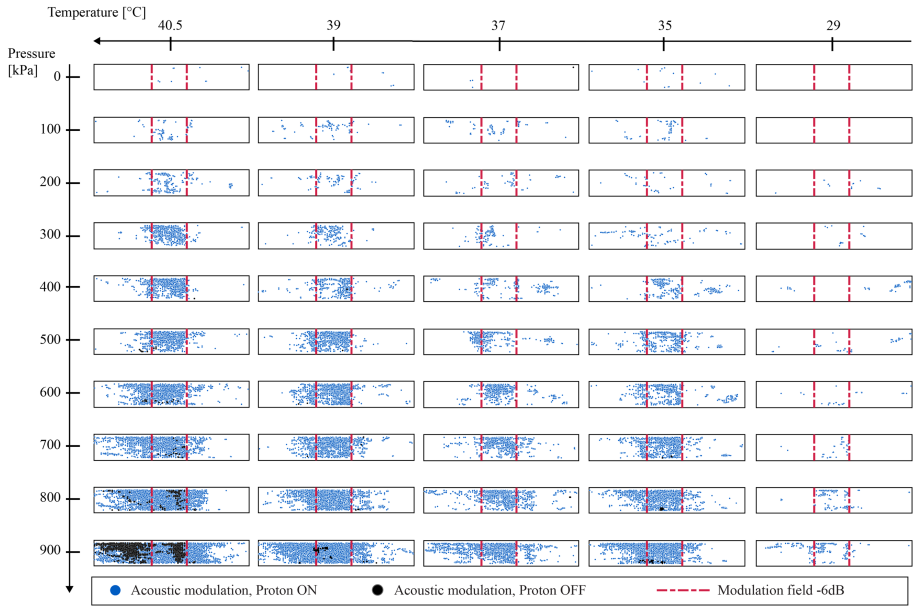


Figure 8.10: Spatial distribution of vaporization events in the tube, for all applied PNPs and for the five tested temperatures. The horizontal axis is the lateral ultrasound axis (parallel to the tube), while the vertical axis is the axial ultrasound axis. The blue dots represent counts during simultaneous proton irradiation and acoustic modulation, while the black dots correspond to acquisitions with acoustic modulation alone.

“Not all those who wander are lost.”

J. R. R. Tolkien

9

Real-time ultrasound imaging of nanodroplet vaporization in a clinical photon radiotherapeutic beam: proof-of-concept

Sophie V. Heymans, Bram Carlier, Sjoerd Nooijens, Gonzalo Collado-Lara, Yosra Toumia, Laurence Delombaerde, Gaio Paradossi, Uwe Himmelreich, Edmond Sterpin, Hendrik J. Vos, Nico de Jong, Jan D’hooge, Koen Van Den Abeele

While the previous chapters have been devoted to the characterization of nanodroplet vaporization in a proton beam, investigating the nanodroplet response to a photon beam is also of interest. Indeed, the vast majority of cancer patients prescribed with radiotherapy are treated using conventional external beam radiotherapy (EBRT), particularly because proton therapy is much more expensive and less common, and only a handful of clinical indications will be reimbursed for proton therapy. EBRT typically consists in delivering high energy photons (or electrons) using linear accelerators. To achieve high tumour conformity while maintaining minimal healthy tissue exposure, treatment delivery systems are becoming increasingly complex and

very sharp dose gradients are used. Therefore, there is a growing need for *in vivo* patient dosimetry during conventional radiotherapy delivery. In this chapter, we study the nanodroplet response to a radiotherapeutic photon beam, using online ultrasound imaging as a means to monitor single radiation-induced vaporization events.

9.1 Introduction

Radiotherapy is, together with chemotherapy and surgery, a crucial weapon in the fight against cancer, as more than 50% of all cancer patients receive radiotherapy as part of their treatment [8]. Even though radiotherapy can be delivered with different modalities (photon, electron, proton or heavy ion beams, or using implanted radioactive sources in brachytherapy), megavoltage (MV) external beam radiotherapy delivering photons is by far the most common. The objective of radiotherapy is to kill tumoral cells through DNA damage induced by radiation exposure, while keeping the exposure of organs at risk (OAR) and healthy tissues to a minimum, thereby maximizing the therapeutic efficacy. Traditionally, radiotherapy was delivered using only a few gantry angles and fixed collimators, but in the past 20-30 years, advances in beam delivery techniques and computerised treatment planning enabled the adoption of increasingly complex geometric (3D conformal radiotherapy) and intensity-modulated field shapes to optimize the conformity to the target (IMRT, Intensity Modulated Radiotherapy, VMAT, Volumetric Modulated Arc Therapy) [3]. This improvement of the spatial distribution of the delivered dose also opened the door for dose escalation at the tumour site while maintaining an acceptable healthy tissue exposure. Consequently, moderately hypofractionated radiotherapy, characterized by a higher dose per fraction (2-4 Gy) and a lower total number of fractions, is becoming increasingly popular, and its adoption is ongoing for some very common malignancies, such as prostate or breast cancer [309–311]. Clinical trials are also being conducted for extreme hypofractionation (6-30 Gy dose per fraction, delivered in five or fewer fractions [3]), for which a higher dose escalation is made possible by the use of stereotactic body radiotherapy (SBRT) [312, 313].

Although this current trend towards very steep dose gradients and tumour dose escalation has clear economical (shortening of the total treatment time) and clinical gains, it needs to be accompanied by strengthened quality assurance (QA) and patient-specific verification protocols, as deviations in treatment delivery can result in tumour miss or unacceptable radiation dose to healthy tissues or OAR [20]. Those deviations can arise from numerous sources, such as machine calibration, treatment planning, plan transfer, and patient positioning

errors (due to misalignment, motion, or anatomical changes) [20]. Despite the very thorough implementation of pretreatment QA procedures, radiotherapy accidents have led to numerous deaths and radiation overdoses [314–316]. The use of *in vivo* dosimetry techniques (defined as "the measurement of the radiation dose received by the patient during treatment, as opposed to *ex vivo* dosimetry" [20]) can act as the final barrier to detect errors in treatment delivery, and would detect errors otherwise unnoticed by pretreatment verification [21,22]. Additionally, measuring the dose distribution *in vivo* would provide clinicians with a (potentially real-time) feedback on the treatment delivery, and could facilitate the adoption of adaptive radiotherapy [23]. *In vivo* dosimetry would also be valuable for the validation and clinical implementation of new radiotherapy techniques [20]. Despite being recommended by several national and international (IAEA, WHO) organizations and societies [20], the routine use of *in vivo* dosimetry is not widespread [23,317], and is often limited to a few fractions and point/surface measurements.

The *in vivo* delivered dose can be verified using different types of passive (thermoluminescent dosimeters, optically stimulated luminescent dosimeters) or real-time (silicon diodes, plastic scintillation detectors, MOSFETs) point detectors, either located on the patient's skin (to measure the entrance or exit dose), implanted, or inserted in natural orifices [14,20,23]. Those detectors are typically used at most for a few fractions, as their use is workflow intensive and, in some cases, can impact the dose distribution [23,318,319]. Moreover, the added value of such point measurements for IMRT and VMAT treatments, with high dose gradients, is very limited [8], and detector mispositioning can lead to significant uncertainties [23]. Apart from point detectors, radiographic or radiochromic films can also provide 2D entrance or exit dose measurements [20]. Modern radiotherapy treatment plans, such as VMAT, IMRT or SBRT, are typically verified using *in vivo* dosimetry based on Electronic Portal Imaging Devices (EPID), as those can be used to infer 2D or 3D patient dose distributions from transmission measurements of the therapeutic beam [14]. EPIDs consist of an amorphous silicon flat panel located on the gantry, facing the linac head, and are available on most modern linear accelerators. Therefore, EPIDs can be used to acquire MV portal images in real-time during treatment delivery. The reconstruction of the delivered dose to the patient from EPID images can be performed with specific software tools [8]. A prediction of the portal dose images can be derived from the planning CT, by means of a physics model, and can be compared to the portal dose images acquired during treatment [20]. However, the information provided by this method cannot be straightforwardly converted to relevant metrics for clinicians (e.g., dose volume histograms) [23]. Alternatively, back-projections algorithms have been developed to fully reconstruct the 3D delivered dose distribution, based on dose calculation engines and a patient model using either the planning CT or a megavoltage cone beam CT (MV-CBCT) scan

acquired on the day of the treatment [320]. While the clinical implementation of those methods is currently performed offline, *in vivo* dosimetry can also be achieved in real-time (i.e., faster than the EPID frame rate), allowing to interrupt the treatment before a significant overdose has been reached [24,25]. A recent study demonstrated the possibility to account for intra-fractional motion by performing 4D *in vivo* dosimetry using a model-based reconstruction of the 4D patient dose from 4D-CT data [321] (which assumes, however, that the breathing/motion pattern is perfectly reproducible). As an alternative to EPID based *in vivo* dosimetry, the detection of the acoustic waves induced by pulsed radiation beams through the photoacoustic effect was proposed [26]. The potential of X-ray Acoustic Computed Tomography (XACT) for *in vivo* dosimetry was demonstrated in water [27] and soft tissue [322] phantoms, and further backed by a recent simulation study [323] and *in vivo* evaluation in a rabbit liver model [28]. While XACT is attractive as it can be combined with real-time ultrasound imaging of the tumour motion, its clinical translation faces several challenges such as the low signal-to-noise ratio (SNR) of acoustic signals and the need for specific low frequency ultrasound transducers [40].

In the context of the FET-Open Amphora project, the potential of injectable superheated nanodroplets to perform *in vivo* proton range verification and dosimetry was recently demonstrated in previous chapters [124,244,256]. When their liquid core is traversed by a charged particle with a sufficient linear energy transfer (LET, i.e. density of energy deposition), those nanodroplets can vaporize into echogenic microbubble contrast agents, easily detectable by ultrasound imaging. Nanodroplets can be synthesized to be sufficiently small to extravasate [68], and can be functionalized by attaching specific ligands to their lipidic or polymeric shell, enabling molecular imaging of different pathologies involving inflammatory processes (e.g. atherosclerosis, inflammatory bowel disease) or angiogenesis (cancer) [189,281,324]. If dense and homogeneous nanodroplet distributions can be achieved in (and around) the tumour, the use of volumetric ultrasound imaging would provide a direct (online or offline) *in situ* 3D-4D measurement of the delivered radiation dose *in vivo*, contrarily to EPID-based methods, which rely on models. Moreover, the ultrasound acquisition of dosimetric and anatomical information could be performed simultaneously, allowing to overlay dosimetric maps on intrafractional images (thus enabling real-time tumour tracking, similarly to XACT). The soft tissue contrast would be improved on ultrasound images compared to MV imaging [3], which could be beneficial for certain tumour sites in the abdominal or pelvic region. Contrarily to XACT, the use of ultrasound contrast agents ensures a high SNR, and *in vivo* dosimetry could be performed with conventional ultrasound imaging probes. Finally, as nanodroplets can be used for molecular imaging, such an *in vivo* dosimetry system could also facilitate the adoption of biologically guided radiation therapy (BGRT) strategies [20].

Since photons are not charged particles, nanodroplet vaporization is expected to be induced by secondary electrons (created by photon interactions such as the photoelectric effect, Compton scattering, and pair production [3]) rather than by the primary photon beam. For high photon energies (> 10 MeV [3, 325]), photodisintegration can also lead to vaporization by the resulting high-LET heavy particles, and produces secondary neutrons which can also trigger nuclear reactions. A proof-of-concept study with PVA-PFB nanodroplets showed that at physiological temperature, the majority of the nanodroplet population is insensitive to photons, as their degree of superheat is not sufficient to allow vaporization by low LET particles [290] (see the lack of radiation response in figure 9.1(b), evidenced by a low bubble density in B-mode images). In the same experimental study, we also investigated the influence of the beam energy on the radiation response, and found that high-LET particles generated by secondary neutrons can induce nanodroplet vaporization, as shown in figure 9.1(e), where nanodroplet vaporization was observed for phantoms irradiated with 15 MV photons (figure 9.1(d)) but not for phantoms irradiated with 6 MV photons (figure 9.1(b)), which is below the energy threshold for neutron generation. However, both the absolute contribution of those particles to the total dose (0.1 to 20.4 mSv/Gy [325]) and their presence outside of the main treatment field makes their use impractical for dosimetry purposes, although superheated drop detectors have been proven useful for in-field and out-of-field neutron dose estimation [117, 326]. Moreover, such a method would not apply to low energy photon beams. Therefore, direct nanodroplet vaporization by secondary electrons would be beneficial for *in vivo* dosimetry applications.

The sensitization of superheated drop detectors to photon beams has been demonstrated at elevated degrees of superheat [116, 153, 154]. Indeed, as the density of energy deposition is much lower for electrons than for heavier particles, the superheated liquid needs to be very close to its limit of superheat. When expressed in units of reduced superheat, defined as:

$$s = \frac{T - T_b}{T - T_c}, \quad (9.1)$$

where T_b and T_c are the boiling temperature and critical temperature, respectively, the onset of sensitization was found to correspond to $s=0.51$ for many light halocarbons [153], while the limit of superheat corresponds to $s=0.65$. Once photon sensitization is initiated, the vaporization count rate was found to rapidly increase with reduced superheat. For perfluorobutane, the core material used in the PVA-PFB formulation, $s=0.51$ corresponds to a temperature of 57°C . In a preliminary study, the response of PVA-PFB nanodroplets dispersed in polyacrylamide aqueous gel was therefore tested at 65°C ($s=0.58$) and a very high microbubble density was observed on ultrasound images post-irradiation, confirming that nanodroplets were vaporized by secondary electrons [290], as

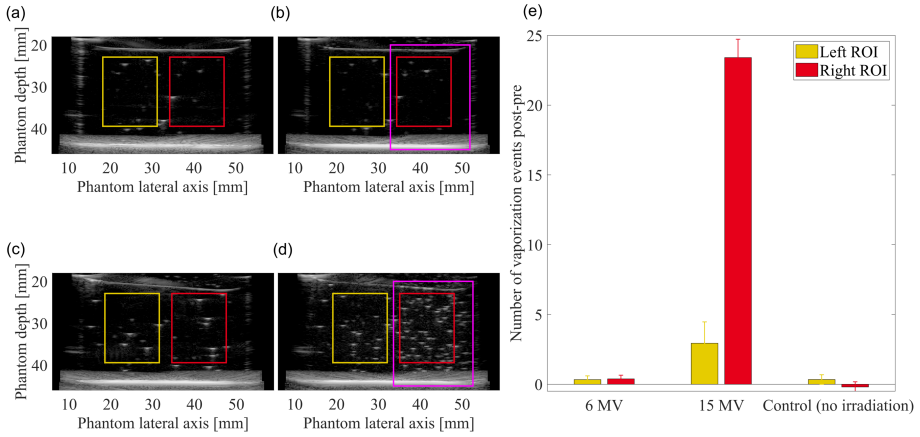


Figure 9.1: (a)-(d) Ultrasound images of polyacrylamide phantoms with 50 μM dispersed PVA-PFB nanodroplets before (left) and after (right) irradiation with radiotherapy photons (10 Gy, 4 Gy/min) at 37°C. Four phantoms were irradiated, two with a beam energy of 6 MV (b) and two with a beam energy of 15 MV (d), while two phantoms were used as controls (non irradiated, data not shown). Only the right side of the phantoms was irradiated, as shown by the radiation field boundaries in magenta. (e) Increase in the number of microbubbles (vaporized nanodroplets) for the group irradiated with 6 MV, with 15 MV, and the control group, for the left ROI (outside of the radiation field) and the right ROI (inside the radiation field).

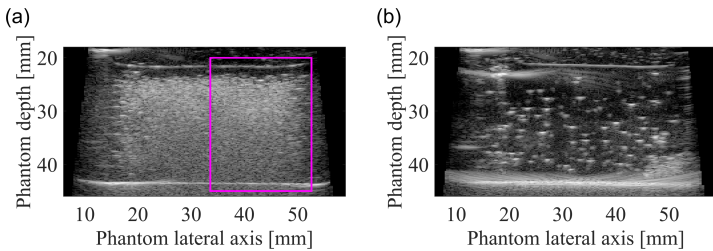


Figure 9.2: (a) Ultrasound image of a polyacrylamide phantom with 25 μM dispersed PVA-PFB nanodroplets heated to 65°C and irradiated with 6 MV photons (10 Gy, 4 Gy/min). The magenta rectangle represents the boundaries of the radiation field. (b) Ultrasound image of a similar non-irradiated (control) phantom at 65°C.

shown in figure 9.2(a). However, no difference between the in-field and out-of-field (right and left side of the phantom in figure 9.2, respectively) radiation response could be observed, which we believe was due to contrast saturation.

In the present study, we transition to online ultrasound imaging, similarly to what has been achieved for proton irradiation [256], during photon irradiation of phantoms with dispersed PVA-PFB nanodroplets by a clinical linac. The objective is to accurately quantify the temporal and spatial nanodroplet vaporization response to radiation, by means of individual vaporization events counting on differential images acquired during irradiation. If the frame rate is sufficiently high compared to the vaporization rate, differential frames will only contain sparse vaporization events (as the contrast agents are immobilized in an aqueous matrix), which can be super-localized using the same methodology as in Ultrasound Localization Microscopy (ULM) [78, 235]. Our hypothesis is that this method will allow to evaluate different characteristics of the nanodroplets' dosimetric response, such as for instance the reproducibility, dose and dose rate dependence, or droplet concentration dependence, and can be used to calibrate the nanodroplet-based dosimeter.

9.2 Materials and Methods

9.2.1 Nanodroplet and phantom synthesis

Nanodroplets with a poly(vinyl) alcohol (PVA) shell and a decafluorobutane core (C_4F_{10} , b.p. -2°C) were employed in this study. The nanodroplet size distribution was measured previously by Dynamic Light Scattering, yielding a mean diameter of 799 nm and a polydispersity index of 0.3 [244]. The perfluorobutane concentration was measured by NMR spectroscopy (400 MHz Avance II, Bruker, Biospin GmbH, Rheinstetten, Germany) on the same day as the irradiation experiments.

Carbomer (Carbopol ETD 2050, Lubrizol, Wickliffe, USA) phantoms were prepared following the protocol described in [256]. The Carbomer solution is semi-rigid and can be mixed manually, while the shear threshold of the aqueous matrix was sufficiently high to immobilize the nanodroplets and microbubbles resulting from nanodroplet vaporization. The uniformity of the nanodroplet dispersion and the absence of microbubble motion was verified by performing Acoustic Droplet Vaporization on Carbomer phantoms with dispersed nanodroplets and observing the resulting contrast distribution. Phantom preparation was performed as follows (figure 9.3(a)): first, the Carbomer solution was heated to the desired temperature (65°C) by immersion in a heated water bath. The temperature in the Carbomer matrix was verified with a thermocouple. Then, the solution was poured into phantom containers (also heated to 65°C) and a given volume of nanodroplets was injected and manually dispersed in the solution. To prevent inter-phantom variability due to

nanodroplet dissolution in the phantom, the time between phantom preparation and irradiation was kept constant (9 min).

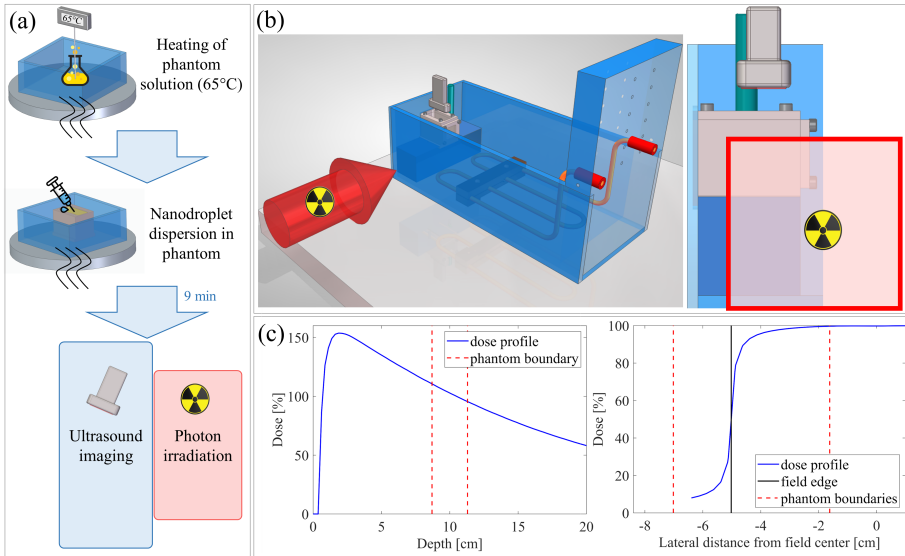


Figure 9.3: Schematic representation of the experimental procedure (a) and experimental setup (b) for photon irradiation of Carbomer phantoms with dispersed nanodroplets. (c) Dose profiles along the photon beam direction (left) and lateral axis (right), displayed together with the boundaries of the phantom. The lateral edge of the radiation field was chosen to lie within the phantom, in order to potentially observe a correlation between the lateral dose gradient and the vaporization response.

9.2.2 Irradiation protocol

Phantom irradiations were carried out at the clinical radiotherapy facility of UZ Leuven (Belgium), using a 6 MV photon beam (TrueBeam, Varian Medical Systems, Palo Alto, USA). After nanodroplet dispersion and mixing, individual phantoms were brought to the radiotherapy treatment room and immersed in a temperature-controlled water tank heated to 65 °C (figure 9.3(b)). Phantoms were irradiated from the side, using a gantry angle of 90°, with a square field of 10x10 cm² at isocenter. The Source to Skin Distance (SSD) was 90 cm and the center of the phantom was at a depth corresponding to the isocenter plane, at a 10 cm distance from the beam entrance point. The top left boundary of the radiation field, defined as the position where the radiation dose dropped to 50% of its maximum, was located within the phantom, as represented in figure

9.3(b). Phantoms were aligned with the radiation beam using the light field and markings on the water tank delimiting the phantom position. The delivered radiation doses ranged from 0.12 to 4 Gy, and the dose rates varied between 0.12 and 4 Gy/min. Experiments were performed on two different days, and the irradiation conditions for all phantoms are summarized in Table 9.1.

Experiment	Number of phantoms	Phantom number	Nanodroplet concentration [μM]	Dose [Gy]	Dose rate [Gy/min]
1	1	1	/	4	4
1	1	2	10	/	/
1	1	3	10	0.12 0.72	0.12 0.64
1	1	4	10	2.4	2.4
1	1	5	10	2.4	0.8
1	1	6	10	2.4	4
2	1	7			
	5	8-12	20	6	2.4
2	1	13	40	6	2.4
2	1	14	40	2	0.8
				2	2.4
2	1	15	20	2	4
				2	0.8
				2	4
2	1	16	20	2	0.8
				2	2.4
				2	0.8
2	1	17	20	2	2.4
				2	4

Table 9.1: Irradiation parameters for all phantoms

9.2.3 Online ultrasound imaging

The phantoms were imaged during photon irradiation using a 7.5 MHz linear array (L7-XTech, Vermon, France) mounted on a motorized linear stage (Velmex, Inc., NY, USA), and connected to a research ultrasound system (DiPhAs, Fraunhofer IBMT, Germany). The probe was positioned orthogonal to the direction of the radiation beam, and imaged a cross-section of the center of the phantom (figure 9.3(b)). The top surface of the immersed phantom was covered with an acoustically-transparent window (20 μm polyester). Plane wave imaging was employed (5 angles compounding), at pressures sufficiently low to avoid Acoustic Droplet Vaporization at 65 °C. To avoid overheating of the transducer elements, the ultrasound probe was kept outside of the 65 °C water tank while not in use, and brought down into the water using a motorized stage a few seconds before imaging. Ultrasound imaging of the phantom started 60 seconds

before irradiation, and images were acquired continuously at a frame rate of 10 Hz. Approximately 60 s after the end of beam delivery, the ultrasound imaging was stopped and the probe was lifted out of the heated water.

9.2.4 Data processing

Detection of vaporization events

The acquired ultrasound beamformed images (figure 9.4(a)) were processed by subtracting subsequent frames, followed by applying a Wiener 2D spatial filter and 2D Gaussian smoothing filter. This resulted in a sequence of differential images, with each frame (i) displaying only the microbubbles resulting from newly vaporized nanodroplets between frame (i) and (i-1). Those microbubbles appeared as bright spots in the differential images, and as their number was sparse, they could be localized beyond the diffraction limit by finding the weighted average centroid of their Point Spread Function [77, 78]. The result of this super-localization process is shown in figure 9.4(b).

Spatial quantification of the vaporization events and comparison with the radiation dose distribution

The vaporization events were cumulated over time (see figure 9.4(c)) and binned in 2D (cell of 0.8 mm by 0.8 mm), and projections on the lateral and axial ultrasound axis were obtained by summing the event counts axially and laterally, respectively, as illustrated in figure 9.4(d). A sigmoid fit was applied to those 1D vaporization profiles, using the following equation:

$$N_{vap} = N_{vap,L} + \frac{N_{vap,H} - N_{vap,L}}{1 + e^{-4 \log 3 \frac{x-x_m}{x_b}}}, \quad (9.2)$$

with N_{vap} the vaporization count, x the lateral or axial coordinate, $N_{vap,H}$ and $N_{vap,L}$ the upper and lower values, respectively, x_m the position of the middle of the ramp-up phase and x_b an indicator of the sharpness of the ramp.

The estimated middle point of the vaporization counts transition zone, \hat{x}_m , was compared to the location of the 50% boundaries of the radiation field. To transform the ultrasound image coordinates into absolute coordinates in the lateral direction, a fiducial object with a point reflector of known position was imaged at the beginning of the experiment. In the axial direction, the location of the reflection of the bottom wall of the phantom on the ultrasound images was compared to its known position. Spatial quantification was only performed for the second experiment, as the fiducial object was not imaged during the first experiment.

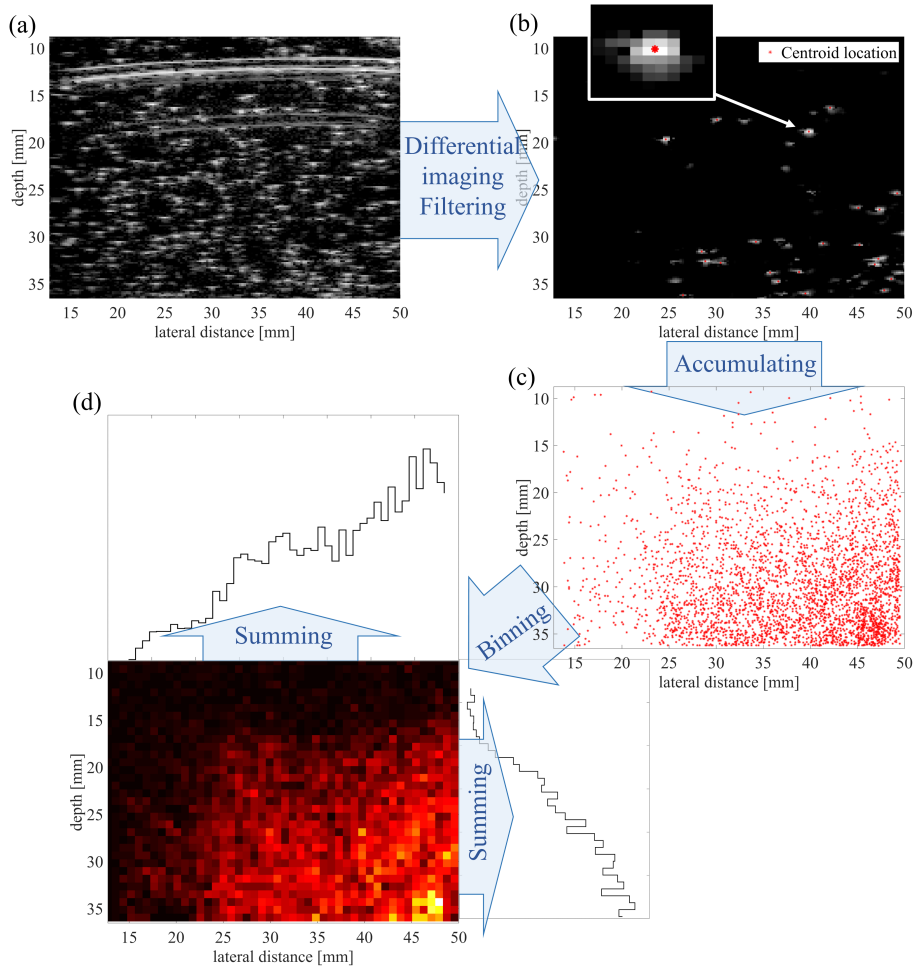


Figure 9.4: Overview of the image processing steps. Differential imaging was applied on beamformed images (a) and, after an additional filtering step, individual vaporization events were super-localized on the differential images (b). The vaporization events were accumulated throughout the irradiation (c) and binned to obtain vaporization density maps (d). Summing in each direction yielded 1D profiles of the vaporization counts.

Temporal quantification of the vaporization events and comparison with the dose delivery

The vaporization events were cumulated over time, and the start and end of the irradiation were identified as the first and last ultrasound frame for which

vaporization events were counted. The time points were then converted to radiation dose using the known dose and dose rate delivered by the linear accelerator. The curves representing the vaporization counts N_{vap} as a function of radiation dose D were fitted to a saturation curve of the form:

$$N_{vap} = \frac{aD}{b + D} \quad (9.3)$$

The initial slope parameter, $\frac{a}{b}$, was used to estimate the number of vaporization events per Gy in the absence of saturation. The saturation effect was quantified as the normalized difference between the number of counts that would have been obtained in the absence of saturation (linear response) and the observed number of counts:

$$\frac{\frac{a}{b}D_{tot} - N_{vap,tot}}{\frac{a}{b}D_{tot}}$$

9.3 Results

Figure 9.5 shows ultrasound images before (a) and after (b) irradiation of a control phantom (phantom 1, no nanodroplets), for which no visible effect of irradiation was observed. An unirradiated phantom with dispersed nanodroplets (phantom 2) is also displayed before (c) and after (d) immersion and online ultrasound imaging in the 65 °C water bath, indicating that only very limited spontaneous or ultrasound-induced vaporization took place (<10 events). Finally, figure 9.5 (e) and (f) depict an irradiated phantom with dispersed nanodroplets (phantom 6), for which a clear increase in the number of microbubbles can be observed post-irradiation. The majority of the vaporization events seemed to be located within the boundaries of the radiation field (marked by red lines).

Among the 15 phantoms with dispersed nanodroplets that were irradiated during the two experiments (see table 9.1), only 7 exhibited a clear, significant response to radiation (colored in table 9.1), while the remaining 8 phantoms showed little or no vaporization upon irradiation, even though great care was given to ensure that all phantoms were handled in the same way. The presence or absence of radiation response did not seem to be linked to any phantom or irradiation parameter, and appeared to be random. This high variability in the phantom response is illustrated in figure 9.6, showing three phantoms irradiated with the same conditions (a-c: phantoms 7, 9, and 12 and a phantom irradiated with different conditions (d: phantom 14). The lack of reproducibility in the radiation response hindered the validation of our hypothesis and inhibits the

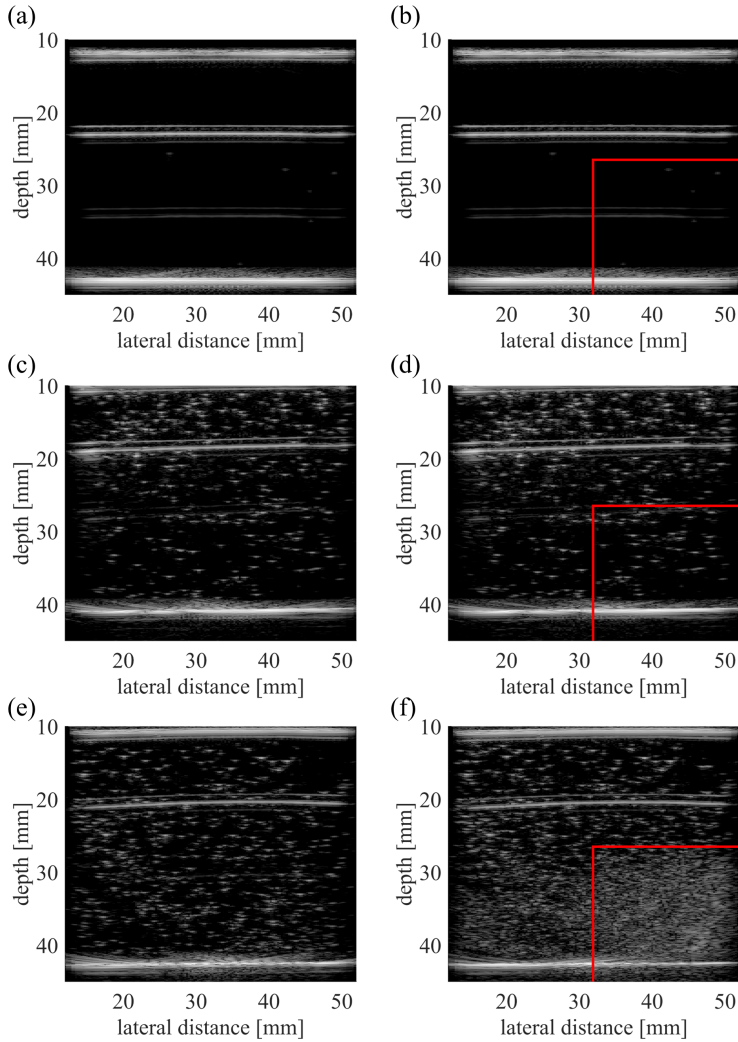


Figure 9.5: Ultrasound images of Carborer phantoms before (left) and after (right) irradiation or immersion in a warm water bath coupled with online ultrasound imaging. (a-b) Phantom with no nanodroplets (phantom 1), dose of 4 Gy and dose rate of 4 Gy/min. (c-d) Unirradiated phantom (phantom 2) with 10 μM nanodroplets. (e-f) Phantom 6 (10 μM nanodroplets irradiated with a dose of 2.4 Gy, dose rate of 4 Gy/min). The red lines indicate the radiation field boundaries (50% isodose lines).

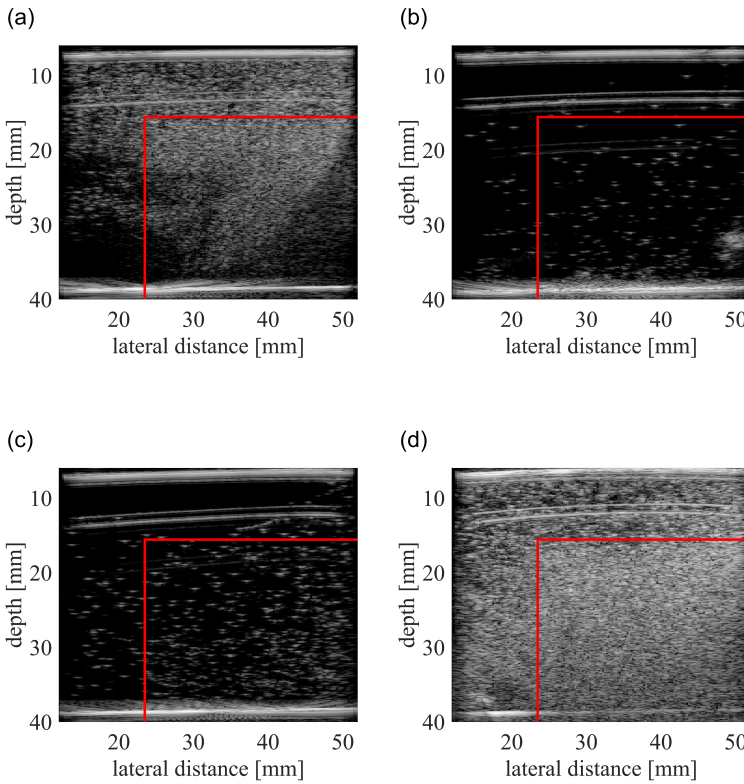


Figure 9.6: Ultrasound images of Carborer phantoms after irradiation, showing a high variability in the radiation response. (a-c) 6 Gy, 2.4 Gy/min, 20 μ M nanodroplets (phantoms 7, 9 and 12) and (d) 2 Gy, 0.8 Gy/min, 40 μ M nanodroplets (phantom 14). The red lines indicate the radiation field boundaries. The dark zones at the bottom left and right of panel (a) are attributed to improper mixing of the nanodroplets.

dosimeter calibration. In the next sections, only phantoms that exhibited a significant radiation response were further analyzed.

9.3.1 Spatial quantification

The spatial distribution of the vaporization events were compared to the radiation dose profiles within the phantoms. An example is shown in figure 9.7 for phantom 13 (table 9.1). Projections of the vaporization counts in the lateral and axial dimensions (red) are qualitatively in good agreement with the spatial dose gradients (blue), while, in comparison, gray value profiles extracted

from post-irradiation images (magenta) did not follow the dose profile, probably due to artifacts caused by the high microbubble density (see figure 9.6(d)). The spike in the axial projection is caused by a reverberation artifact (visible on all phantoms in figures 9.5 and 9.6). The effect of acoustic shadowing is also clearly observed as a contrast decrease with depth in the axial projection. The 1D vaporization count profiles were fitted to a sigmoid curve in the axial and lateral direction, and the distance between the radiation field boundaries and the estimated position of the 50% drop in vaporization counts, \hat{x}_m , was -0.22 mm in the lateral direction and 0.75 mm in the axial direction. The relatively high variability in the vaporization density in the irradiated region is attributed to inhomogeneities in the nanodroplet distribution. The distance between the radiation field boundaries and the estimated position of the 50% drop in vaporization counts was higher than 1 mm for the other phantom with a significant radiation response (phantom 14, not shown here), which could be due to an insufficient number of vaporization events or an inhomogeneous dispersion of the nanodroplets.

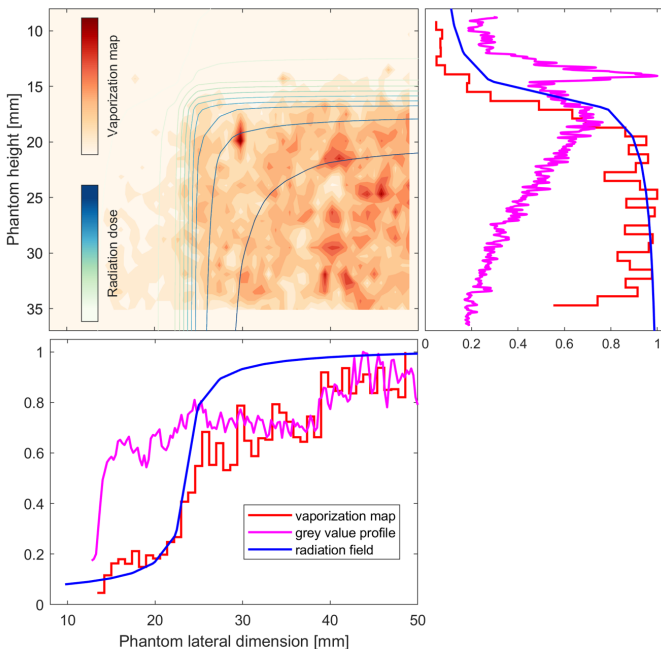


Figure 9.7: Top left: 2D spatial distribution of the vaporization counts (red) for phantom 13, binned over a 0.8 mm by 0.8 mm grid, overlaid on the 2D radiation isodose lines (blue). Axial and lateral projections of the vaporization counts (red) are compared to projections of the dose distribution (blue) and to gray value profiles extracted from post-irradiation images (magenta).

9.3.2 Temporal quantification

As the nanodroplet concentration and the position of the radiation field varied between the two experiments, the number of detected vaporization events was normalized with respect to the nanodroplet concentration and area of the radiation field for each phantom. The vaporization counts are thus reported with units of counts per cm^2 and per μM in figure 9.8. The normalized vaporization counts are displayed as a function of time in panel (a), and as a function of dose in panel (b). Dashed lines correspond to phantoms from experiment 2, while solid lines are for phantoms from the first experiment. The variability in the radiation response was relatively high, but did not follow a clear trend relative to one or several parameters (such as the dose rate, the total dose, the phantom concentration or the nanodroplet batch). All phantoms exhibited a certain degree of saturation of the vaporization count over time/dose. The curves representing the normalized vaporization events as a function of the radiation dose were fitted to a saturation curve, and the initial slope parameters, together with an estimate of the extent of the saturation behaviour, are reported in Table 9.2.

Initial slope [$\frac{\text{events}}{\mu\text{Mcm}^2\text{Gy}}$]	Saturation [%]	Phantom number	ND concentration [μM]	Dose [Gy]	Irradiation time [s]	Number of events
79.11	65	14	40	2	150	11 893
51.63	75	13	40	6	150	16 741
88.53	84	5	10	2.4	180	884
26.45	56	4	10	2.4	60	733
81.26	67	6	10	2.4	36	1712
40.99	48	3	10	0.12 0.72	60 67.5	125 348

Table 9.2: Results of the saturation curve fit: initial slope and saturation behaviour, together with the corresponding irradiation parameters

9.4 Discussion

In this study, online ultrasound imaging was employed in an attempt to quantify the nanodroplet vaporization response to a radiotherapeutic photon beam. A strong vaporization response was observed in some phantoms, for 10-40 μM nanodroplet concentrations and radiation doses in the clinical range. For those phantoms, the vaporization response was found to be well correlated with the radiation dose distribution (figure 9.7), although the vaporization events were not completely uniformly distributed. Compared to grey value profiles obtained on post-irradiation ultrasound images of the phantoms, online imaging drastically improved the accuracy of the radiation field boundaries

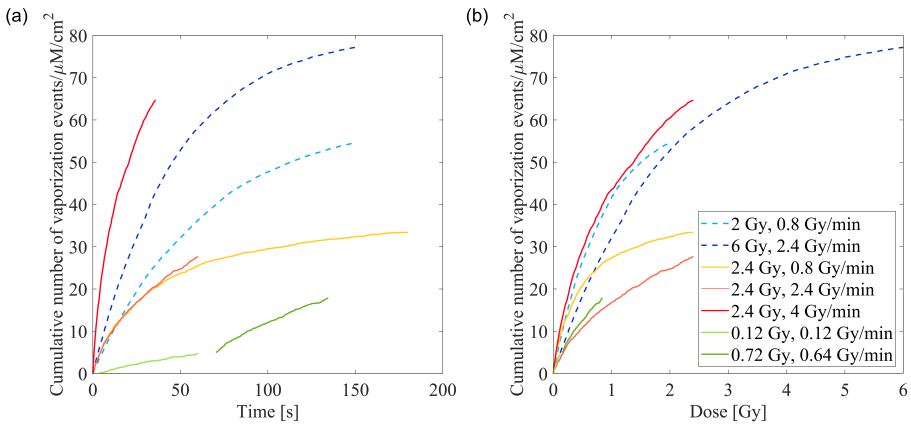


Figure 9.8: Evolution of the number of detected vaporization events as a function of (a) time and (b) radiation dose for all phantoms exhibiting a sufficient radiation response. The event counts are normalized by the nanodroplet concentration and the irradiated cross-section of the phantom. Dashed lines correspond to results for phantoms obtained in the second experiment, and solid lines in the first experiment.

estimation based on vaporization maps. However, this radiation response was not reproducible, as little or no vaporization was observed in more than half of the irradiated phantoms (table 9.1). Even among the phantoms with a satisfactory radiation response, the inter-phantom variability of the number of detected vaporization events was very high, as reflected in the estimates of the initial slope of the dose response curves, which ranged from 26 to 88 [events/ $\mu\text{M}/\text{cm}^2/\text{Gy}$]. The experimental variability of the nanodroplet response to proton radiation was also found to be relatively high (as detailed in chapter 7), but the reproducibility was notably superior to the one observed for photon irradiation. The nanodroplet response to proton irradiation was in good agreement with a simple statistical model and general trends regarding concentration dependence, dose rate dependence, and dose response could be extracted.

Variability of the nanodroplet radiation response

Several combined factors could explain the large variability observed in the nanodroplet vaporization response to photons. Firstly, inter-phantom temperature differences cannot be completely excluded, as maintaining a temperature of 65°C throughout all experimental steps was challenging. Even though the Carbomer solution, phantom containers, and irradiation water tank were controlled to be at 65°C , the temperature could have slightly decreased during dispersion and mixing of the nanodroplets (as the phantom

top surface was in contact with the ambient air for 2 min) and while being hand held during transport of the phantom to the radiotherapy room (< 1 min). Theoretically, the chosen temperature of 65 °C was largely above the expected sensitization temperature of 57 °C (corresponding to a reduced superheat of $s=0.51$ [153]). However, the presence of both non-responsive and highly responsive phantoms might suggest that the sensitization temperature for perfluorobutane nanodroplets is higher than theoretical estimations, and might be closer to 65 °C. In that case, inter-phantom temperature fluctuations could explain the extreme variability in nanodroplet radiation response. Moreover, even above the sensitization threshold, the temperature dependence of the vaporization response was found to be very steep [153].

The sensitization threshold of $s=0.51$ reported in the literature was evaluated in superheated drop detectors. Those detectors differ from encapsulated superheated nanodroplets, for which the energy barrier for nucleation might be higher due to the viscoelastic properties of the nanodroplet shell, as developed in chapter 2, and potentially the Laplace pressure. However, both the effect of the shell encapsulation and the surrounding matrix were estimated to be relatively low at such elevated degrees of superheat. Additionally, the exact LET threshold required for vaporization by electrons is not well characterized, as for such high degrees of superheat, both the critical energy (0.46 keV at 65 °C) and critical radius (10 nm) are very low. At such a small scale, the energy loss along the electron track is no longer well approximated by the stopping power [153]. Moreover, the stopping power of electrons at such low energies cannot be measured experimentally [304]. The Bethe equation for the collisional stopping power for electrons is [304]:

$$\left(-\frac{dE}{dx}\right)_{col} = \frac{4\pi k_0^2 e^4 n_e}{m_e c^2 \beta^2} \left[\ln \frac{m_e c^2 \tau \sqrt{\tau + 2}}{\sqrt{2} I} + \frac{1 - \beta^2}{2} \left[1 + \frac{\tau^2}{8} - (2\tau + 1) \ln 2 \right] \right] \quad (9.4)$$

with $k_0 = 8.99 \times 10^9 [\text{Nm}^2/\text{Cb}^2]$, e the magnitude of the electron charge, n the number of electrons per unit volume in the medium, m_e the electron rest mass, c the speed of light, $\beta = v_e/c$ with v_e the speed of the electron, $\tau = \frac{T}{m_e c^2}$ with T the kinetic energy of the electron, and I the mean excitation energy of the medium. The latter can be estimated by the Bragg additivity rule [153, 327], with Z_j the atomic number of compound j , A_j its atomic weight, and r_j its relative contribution to the total weight of the molecule:

$$\ln I = \frac{\sum_j (\ln(I_j) r_j Z_j / A_j)}{\sum_j (r_j Z_j / A_j)} \quad (9.5)$$

The collisional stopping power of C_4F_{10} for electrons estimated by the Bethe equation is displayed in 9.9. It peaks at 20.2 keV/ μm , which could be used

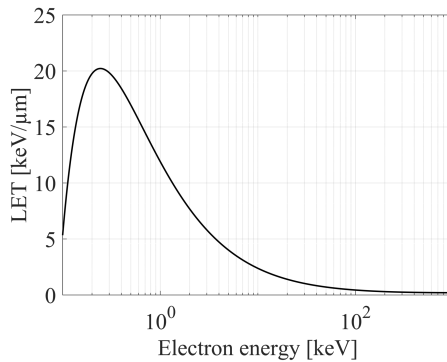


Figure 9.9: Collisional stopping power of C_4F_{10} for electrons (equivalent to the unrestricted LET), estimated by the Bethe equation.

as an estimate of the LET threshold that needs to be overcome for electron sensitization. However, comparison between the stopping power of liquid water calculated with an electron transport code (NOREC, [328]) and with the Bethe equation indicates that stopping powers predicted by the Bethe equation underestimate the peak stopping power by approximately 20% [153, 304]. Therefore, the LET threshold for electron sensitization probably lies in the interval 20-25 keV/ μm , which, for C_4F_{10} , corresponds to a sensitization temperature interval of 63 °C-67 °C (assuming a nucleation parameter equal to 2). This emphasizes the need to determine the temperature at which nanodroplets become sensitive to electrons experimentally, using a dedicated setup in which the temperature can be easily varied, similarly to the setup used in chapter 8.

A second source of variability might be due to the phantom preparation step, as nanodroplets were mixed manually in the Carbomer solution. Combined with the relatively high viscosity of the phantom matrix, this could have led to inhomogeneous nanodroplet distributions, as illustrated in figure 9.6(a). Achieving homogeneous nanodroplet distributions is desirable for accurate dosimetric measurements, and is one of the major concerns regarding the *in vivo* applicability of this technique, as tumours typically have disorganised, leaky, tortuous or misformed blood vessels, and sometimes a hypoxic core. While automated nanodroplet mixing could be used for phantom studies and dosimeter calibration, the nanodroplet distribution homogeneity in different tumour types remains to be assessed *in vivo*. Nanodroplet penetration into the tumour could be enhanced by size-selecting only nanodroplets with a sufficiently small diameter to pass through inter-endothelial gaps (380-780 nm dimensions [329]), and by actively pushing the nanodroplets deeper into tumoral tissues using the

Acoustic Radiation Force or cavitation from neighbouring microbubbles [330]. Nanodroplet distribution inhomogeneities could also be assessed prior to or after beam delivery, using acoustic vaporization of all nanodroplets at the tumour site and detection of resulting microbubbles via ultrasound imaging, or by making use of the fluorine present in the nanodroplet liquid core with ^{19}F MRI.

Finally, a third source of variability could be attributed to fast nanodroplet dissolution in the phantom, through diffusion of the perfluorocarbon core into the surrounding matrix and existing microbubbles. Nanodroplet dissolution at such elevated degrees of superheat is expected to be significantly faster than at lower temperatures, as high vapor pressures act as a driving force for dissolution [67]. A nanodroplet dissolution model was developed in [119] and provides the differential equation for the molar rate of change inside a nanodroplet of radius R , assuming that the surrounding medium (water) is saturated with the perfluorocarbon:

$$-\frac{dn_i}{dt} = \frac{4\pi R D_i \rho_w P_{i,s}}{M_w H_i} \left(e^{\frac{2M_i \sigma_s}{R_g T R \rho_i}} - 1 \right) \quad (9.6)$$

with n_i the number of moles of perfluorocarbon inside the nanodroplet, D_i the diffusivity of the perfluorocarbon, $P_{i,s}$ the saturation pressure, H_i Henry's law constant, and σ_s the nanodroplet surface tension, R_g the ideal gas constant, T the temperature in [K], M_w , ρ_w and M_i , ρ_i the molar mass and mass density of water and the perfluorocarbon core, respectively [119]. Nanodroplet dissolution accelerates with temperature, as the vapor pressure and diffusivity increase, while Henry's law constant decreases. Figure 9.10 shows the evolution of the nanodroplet radius at 37 °C, 50 °C and 65 °C, for a nanodroplet of 400 nm initial radius and assuming a surface tension of 0.01 N/m. As the surface tension of PVA-PFB nanodroplets was not measured, the dissolution times shown here are arbitrary, but illustrate the strong influence of temperature on the nanodroplet dissolution dynamics.

Additionally, the phantom contained background microbubbles that were already present in the vial or formed by spontaneous vaporization during the injection and mixing process. The presence of microbubbles in the vicinity of nanodroplets has been shown to lead to perfluorocarbon transfer from the nanodroplets into neighbouring microbubbles [293], causing rapid nanodroplet dissolution and bubble inflation. The rate of mass transfer, driven by the concentration gradient, is proportional to $P_{i,s} - y_{B_i} P_0$, with y_{B_i} the mole fraction of perfluorocarbon in the microbubble and P_0 the atmospheric pressure [293]. At 65 °C, the saturation pressure of perfluorobutane is very high ($P_{i,s}=820$ kPa) and rapid diffusion of perfluorobutane from nanodroplets to neighbouring microbubbles is expected. For lipid-shelled ultrasound contrast agents, bubble inflation was observed within seconds following the addition of perfluorobutane nanodroplets. While

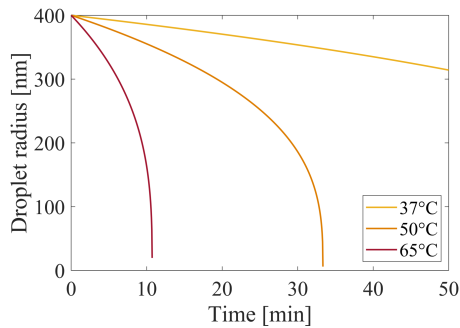


Figure 9.10: Evolution of the radius of a perfluorobutane nanodroplet immersed in water at different temperatures. The surface tension is assumed to be equal to 0.01 N/m.

the thick shell of the PVA-PFB nanodroplet formulation might hinder the PFB diffusion, significant diffusion might still occur during the relatively long time (9 min) before irradiation and over the course of irradiation (~ 3 min). This could cause a local decrease in the nanodroplet concentration at the vicinity of background microbubbles, and partly explain spatial inhomogeneities in vaporization counts in the irradiated region.

Limitations of the ultrasonic readout

The radiation-induced phase-change behaviour was monitored using online ultrasound imaging with a 7.5 MHz linear array. Applying ULM to the recorded ultrasound movies enabled to detect individual vaporization events, even in the presence of a very large microbubble concentration (figure 9.6(d)). This led to an accurate quantification of the spatial distribution of the nanodroplet vaporization events (figure 9.7). However, the ultrasound imaging and data processing steps suffered from some limitations. As 2D ultrasound imaging was employed, vaporization could only be assessed for a thin phantom slice, and a single angle radiation field. Future studies should validate the ability of online volumetric ultrasound imaging to assess the spatial distribution of the vaporization events in 3D, and to correlate the latter to a complex, highly conformal radiotherapy plan. The volume rate should be sufficiently high compared to the vaporization rate, in order to meet the condition of sparse microbubbles required to apply ULM.

The number of detected vaporization events was shown to saturate over time in all phantoms (albeit with variable severity). It is important to determine whether this observed decline of the vaporization rate simply reflects the gradual

decrease of the nanodroplet concentration in the phantom over the course of irradiation (due to vaporization and dissolution), or if it should be imputed on the vaporization events detection method. On the one hand, the impact of dissolution could not be easily quantified, and radiation-induced vaporization is not expected to significantly affect the nanodroplet concentration, as the observed number of vaporization events was several orders of magnitude below the number of nanodroplets present in the ultrasound imaging volume. On the other hand, the ultrasound-based vaporization detection method can be influenced by the number of microbubbles in the phantom. Indeed, microbubbles strongly attenuate the ultrasound waves, which results in an inverse relationship between the microbubble density and the effective elevational plane width. Therefore, for phantoms with high microbubble densities, the effective imaging volume might have decreased over the course of irradiation, as the signal of newly formed microbubbles was attenuated sufficiently to drop below the noise level. Moreover, microbubble identification on differential frames was performed by simple intensity thresholding, which is far from ideal considering that the microbubble signal could have decreased over the course of irradiation. However, lowering the threshold only led to the detection of false vaporization events due to noise or imaging artifacts.

In the context of Amphora, an alternative microbubble detection method based on deep learning, BubbleNet, was developed, aiming at improving bubble detection performances in phantoms with high microbubble densities. BubbleNet was applied to the two phantoms with the highest microbubble counts (phantoms 13 and 14), and detected 20% and 50% more vaporization events than the thresholding method [331], as shown in figure 9.11. However, BubbleNet detected more vaporization events already at the start of the irradiation, and did not suppress the observed saturation effect. As a high saturation effect was also observed in phantoms with a lower number of vaporization events (Table 9.2), the origin of the observed saturation is likely to be multifactorial.

Another shortcoming of the detection of vaporization events by thresholding was its sensitivity to artifacts. Although differential imaging strongly reduced the reverberation artifacts seen on the unprocessed ultrasound images (figure 9.4(a) and (b)), the latter was not entirely suppressed, and an exclusion zone had to be defined around the artifact to avoid erroneous bubble detections due to the artifact. Advanced signal processing techniques or deep learning methods could help discriminate between such artifacts and microbubble signals.

Preliminary trends regarding dosimeter calibration

Even though the high inter-phantom variability restricted the usability of the data, some preliminary conclusions can still be drawn. In the absence of saturation, the vaporization response seems to be proportional to the total

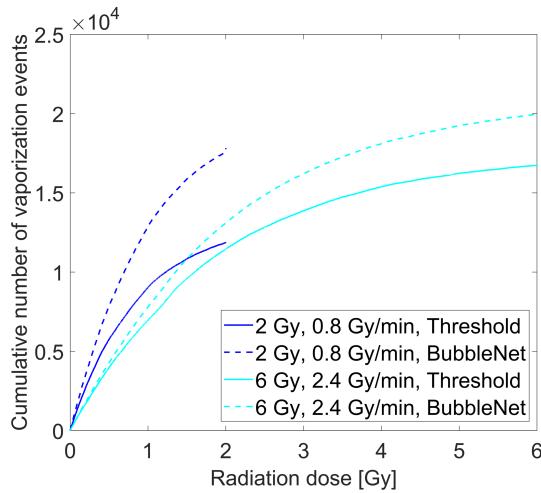


Figure 9.11: Comparison between thresholding and BubbleNet.

radiation dose (or the photon fluence), in agreement with observations in proton beams. However, at such high degrees of superheat, saturation seems to play an important role and will have to be accounted for in order to achieve quantitative dosimetry. This requires a detailed understanding of the nanodroplets dissolution dynamics and the impact of the ultrasound-based readout on the vaporization count statistics. When normalized with respect to the nanodroplet concentration and the irradiated phantom surface, the initial slope estimates vary from 26 to 88 bubbles/cm²/Gy/ μ M. In comparison, Apfel [118] reported a yield of 2.7 million bubbles per Gy and per mg of superheated liquid. After unit conversion, the initial slope estimates were 0.87 - 2.96 million bubbles/Gy/mg, in close agreement with values reported by Apfel. As the vaporization yield is expected to be highly temperature dependent, however, the effect of temperature should be carefully evaluated in future experiments. The estimation of the minimum number of vaporization events required to accurately quantify the radiation dose distribution should also be a priority, as combining it with the vaporization yield discussed above will provide a rough estimation of the nanodroplet concentration required in and around the tumour.

An important requirement for *in vivo* dosimeters is dose rate independence, as modern radiotherapy techniques employ highly variable dose rates [14, 332]. Theoretically, radiation-induced nanodroplet vaporization should not be affected by the dose rate, as the likelihood of vaporization solely depends on the probability of an electron traversing a droplet while depositing sufficient energy

to nucleate a critical gas embryo (hence, it depends on the total electron fluence/radiation dose and nanodroplet concentration). The only impact of the dose rate could be related to the ultrasound readout, as higher frame rates might be required for high dose rates (and hence high vaporization rates). In our study, one phantom was irradiated twice (phantom 3), with different dose rates (0.12 and 0.64 Gy/min), and the two vaporization responses appeared to follow the same curve (figure 9.8(b)), which seems to indicate that the nanodroplet response does not depend on the dose rate. The dose response is also represented in figure 9.8(b) for three phantoms (phantoms 4-6) irradiated with different dose rates (yellow, orange and red curves), with the same total delivered dose. Here, the inter-phantom variability was too high to demonstrate dose rate independence.

9.5 Conclusion and future directions

In this chapter, we reported on the use of online ultrasound imaging to quantify the nanodroplet vaporization response in a photon radiotherapeutic beam. Phantoms with dispersed PVA-PFB nanodroplets were heated to 65 °C and irradiated with different parameters while simultaneously being imaged with plane wave, low intensity ultrasound. Although several phantoms exhibited a strong vaporization response, the inter-phantom variability was extremely high, impairing the reproducibility of the results. Possible reasons for this high variability were discussed, amongst which the strong dependence on temperature, uncertainties relative to the exact sensitization threshold, and the accelerated nanodroplet dissolution. Clearly, this illustrates the difficulties associated with operating nanodroplets at an extreme degree of superheat, as their stability is compromised by their elevated vapor pressure. The importance of shell composition was already stressed in previous chapters, and can act as a barrier against perfluorocarbon diffusion.

Despite the shortcomings of this study, the potential of nanodroplets for *in vivo* dosimetry of conventional radiotherapy was confirmed, and no insurmountable obstacle has been identified at this stage. As operating the nanodroplets at 65 °C is technically challenging, impractical, and irrelevant with respect to the intended application, there is an urgent need for lower boiling point nanodroplet formulations that would be sensitive to low-LET radiation at physiological temperature. A potential candidate is octafluoropropane (C_3F_8 , b.p. -36.6 °C), although careful engineering of the nanodroplet shell will be required to prevent unacceptable amounts of spontaneous vaporization, since its theoretical and experimental limits of superheat are ~37 °C and 38 °C-40 °C, respectively [113, 119, 123]. Nevertheless, octafluoropropane nanodroplets

are currently being investigated for clinical use [281, 333]. Nanodroplet cores composed of mixtures of octafluoropropane and decafluorobutane have also been reported in the literature, but the rapid diffusion of octafluoropropane out of the droplet core might be problematic [334]. Regardless of the final nanodroplet formulation, there is a need for a better understanding of the behavior of nanodroplets dispersed in water and physiological media at such elevated degrees of superheat, as well as the impact of neighbouring microbubbles on their dissolution dynamics.

An alternative to the numerous challenges associated with operating nanodroplets at extreme degrees of superheat is the use of acoustic modulation to transiently increase the degree of superheat, as demonstrated in chapter 8 for the case of proton beams. The theoretical ultrasound negative pressure required to sensitize PFB nanodroplets to electrons at physiological temperature is 950 kPa, but the real pressure value should be determined experimentally, as significant deviations between theoretical predictions and experimental results were revealed in chapter 8. Moreover, the exact LET threshold for electron sensitization suffers from uncertainties, as previously pointed out.

Online ultrasound imaging was proven to be a reliable tool to quantify radiation-induced vaporization, as vaporization count maps representative of the spatial dose distribution could be extracted. However, a transition to volumetric imaging is necessary to allow for quantification of realistic radiotherapy plans. Additionally, the impact of microbubble density on the detection of vaporization events should be minimized through the use of artificial intelligence or advanced image processing techniques.

To conclude, further *in vitro* and *in vivo* characterization work is required to establish whether *in vivo* nanodroplet-based dosimetry during radiotherapy is a viable application. Although the use of injectable nanodroplets might appear more complex and workflow-intensive than EPID based dosimetry systems, which are increasingly being adopted, we expect that their capability to directly measure the *in vivo* delivered dose, combined with their versatile use will make them attractive theranostic candidates in the future, more patient-oriented radiotherapy landscape.

“One never notices what has been done; one can only see what remains to be done.”

Marie Curie

10

Discussion and conclusion

This thesis explored the feasibility and potential of radiation-induced nanodroplet vaporization for *in vivo* dosimetry, and particularly proton range verification. Through several *in vitro* studies, we determined the conditions for nanodroplet vaporization by charged particles, compared different ultrasound imaging methods to quantify the vaporization events, investigated the possibility to obtain direct proton detection at body temperature by acoustic modulation, and tested the applicability for conventional radiotherapy dosimetry. In this final chapter, the findings of this thesis are combined, discussed, and put in the current clinical context of radiotherapy and proton therapy. Finally, we elaborate on potential research and development paths towards the envisioned short and long term clinical applications.

10.1 Summary, discussion, and future research actions

***In vitro* evaluation of the nanodroplets response to proton and photon radiation:**

After introducing the superheat limits and the thermal spike model in **Chapter**

2, the response of perfluorobutane (PFB) nanodroplets to proton radiation was evaluated at different temperatures in **Chapters 3** and **4**. At 25 °C and 37 °C, the observed uniform nanodroplet vaporization profiles, falling proximal to the Bragg peak, were attributed to nanodroplet vaporization by high-LET secondary particles. The distance between the fall-off of the vaporization profiles and the proton range decreased from 2.8 to 0.17 mm, which was due to a reduction in the theoretical LET threshold from 370 (at 25 °C) to 145 keV/ μm (at 37 °C), enabling vaporization by lower-LET secondaries. At 50 °C, a high density of vaporization events was observed at the end of the proton range, which is consistent with the theoretical LET threshold (60 keV/ μm) predicting nanodroplet vaporization by primary protons at the end of their path. In **Chapter 9**, a similar proof of principle experiment was conducted where the temperature was raised to 65 °C to assess vaporization by secondary electrons produced by a radiotherapy photon beam. Despite the high inter-phantom variability, the strong vaporization response observed in several phantoms seems to confirm that the LET threshold was sufficiently low (20-25 keV/ μm) to enable vaporization by electrons.

Overall, the experimental observations reported in Chapters 3, 4, and 9 appear to be in agreement with the thermal spike theory developed for bubble chambers and superheated drop detectors. However, the radiation response was evaluated only at four discrete temperatures and in the presence of two radiation sources, namely protons and photons. To fully and accurately characterize the LET threshold of superheated nanodroplets, irradiations with different charged particles of known LET combined with a full temperature sweep would be necessary [113, 148, 151]. Indeed, when a superheated liquid becomes sensitive to a given charged particle, the vaporization response typically follows a sigmoid curve as a function of temperature [151, 154], which should be measured experimentally to accurately determine the sensitization temperature. The proton sensitization temperature of PVA-PFB droplets was roughly estimated in **Chapter 8** by observing the vaporization response in the range 40-50 °C, but this preliminary result should be confirmed. The experimental tube setup with a constant flow of a nanodroplet dilution in a temperature-controlled water tank (Chapter 8) is suitable for such a study, although the methods used for quantifying the radiation response should be improved as the setup suffered from several limitations. Moreover, a careful control of the nanodroplet concentration in the tube is required, as it directly impacts the number of vaporization events.

Even though the thermal spike theory predicts that the superheated liquid core predominantly determines the vaporization threshold, the comparison of PCDA and PVA-shelled PFB nanodroplets (Chapter 4) revealed that the **role of the shell** should not be neglected. We hypothesize that the low stability of PCDA-PFB droplets is due to the presence of heterogeneous nucleation sites,

leading to spontaneous vaporization at temperatures well below the predicted limit of superheat of 76.5 °C, contrarily to PVA-PFB nanodroplets. In that respect, assessing the thermal vaporization threshold, *e.g.* using Differential Scanning Calorimetry as in Chapter 2, is critical to determine the actual limit of superheat of a given nanodroplet formulation.

Apart from influencing the thermal stability, the impact of the viscoelastic shell on the energy required for vaporization was modelled in Chapter 2, and the model predicts a significant effect of the shell at low degrees of superheat, especially for small nanodroplets (diameter < 800 nm). To validate this model, the onset of the radiation response to high-LET particles at low degrees of superheat (15-25 °C) should be evaluated for different shell types, such as PCDA and PVA, and for nanodroplet populations of different sizes. However, establishing a correspondence with the **shell models** will be challenging as it requires the knowledge of various shell parameters such as its elasticity, viscosity, surface tension and thickness. While the shell thickness can probably be determined by transmission electron microscopy [294], other shell properties are often inferred from optical or acoustic measurements of the response of oscillating microbubbles [165, 168, 224, 335–337], but there is no guarantee that the shell retains its physical integrity and viscoelastic properties after vaporization. Direct approaches, such as transmission electron microscopy [176], atomic force microscopy [177–179], or fluorescence lifetime imaging microscopy [180], have also been employed to characterize microbubbles, and might be applicable to droplets.

The effect of pressure on radiation-induced vaporization of PVA-PFB nanodroplets was assessed in **Chapter 8** by modulating the nanodroplet degree of superheat using an acoustic field. On the basis of the thermal spike theory, we assumed that the decrease in pressure within the droplet core during the rarefactional phase of the ultrasound pulse would raise the degree of superheat. Experimental observations of nanodroplet vaporization by primary protons at temperatures lower than the proton sensitization temperature (43 °C) and acoustic pressures well below the threshold for Acoustic Droplet Vaporization seem to confirm this hypothesis. The reported rarefactional pressures for proton sensitization were higher than those predicted by the thermal spike theory, which is probably due to the combined effect of experimental conditions and model oversimplifications. The exact acoustic pressures leading to proton sensitization at different temperatures should be determined with an optimized experimental setup, using a spatially-uniform pressure field and improved methods to detect the onset of vaporization.

Ultrasound imaging methods to quantify nanodroplet vaporization:

Radiation-induced nanodroplet vaporization was monitored by offline ultrasound

imaging in Chapters 3 and 4. Even though the shift between vaporization profiles and the proton range was measured with a sub-millimeter reproducibility, the ability to quantify the vaporization response was limited due to various image artifacts caused by the high bubble density. In **Chapters 5** and **6**, we transitioned to online active or passive high frame rate ultrasound imaging, which enabled to detect and super-localize individual vaporization events using active or passive Ultrasound Localization Microscopy (ULM or P-ULM). The obtained vaporization maps allowed to retrieve the proton range and range dispersion with sub-millimeter accuracy, while the spot size was largely overestimated by P-ULM due to its degraded axial resolution. We could also extract the number of vaporization events as a function of the proton fluence. As processing operations such as beamforming, (P-)ULM, and range retrieval from the vaporization maps were currently performed offline, future work should focus on developing an online implementation in order to enable real-time range verification.

A comparison between **active and passive microbubble detection** revealed that the passive method detects approximately twice as many events as the active methods, however, the localization efficiency of P-ULM was limited ($\approx 40\%$). Surprisingly, although both methods allowed to retrieve the proton range with comparable accuracy, the position of those vaporization events did not fully match, which indicates that each method might be sensitive to different vaporization events. The algorithms used for P-ULM were not optimal, and should be improved by harvesting the abundant literature on acoustic source localization methods [269, 275, 277]. Moreover, the efficiency of P-ULM could be increased by employing a probe made of transducer elements with a high sensitivity in the low frequency region (100 kHz - 1.5 MHz). The passive method generally detected vaporization events located closer to the probe, which was expected as the resolution of P-ULM rapidly worsens as the source depth increases. Therefore, for deep targets, ULM is expected to be more accurate, especially if quantification of the radiation response in the axial ultrasound direction is required. The major advantage of P-ULM was its ability to specifically detect vaporization events, without being affected by flowing microbubbles. As an important next step, the performance of the two methods should be compared in a physiologically-relevant setup, using volumetric imaging (coupled with bubble-tracking algorithms for the active case). Ultimately, the choice of the imaging method will depend on the contrast agents dynamics *in vivo*, e.g. the extent of spontaneous vaporization, the lifetime of vaporized nanodroplets (preliminary *in vivo* tests seem to indicate a lifetime of 15-30 min under continuous imaging), and whether nanodroplets and resulting microbubbles will remain immobile (as in the case of extravasation and/or targeting) or will be subject to flow.

Development of a predictive model:

Chapter 7 took a step further towards the implementation of real-time range verification by developing a simple statistical model allowing to predict the number and spatial distribution of vaporization events induced by primary protons. The interaction of the proton beam with a dispersion of droplets was assumed to follow a binomial probability law, and the developed model was compared to experimental results obtained with different droplet sizes and concentrations. Although a relatively good agreement was observed between model predictions and experimental observations, the inter-phantom variability was higher than expected and the measured number of vaporization events was significantly lower than predicted for the smallest droplets (diameter $< 2.5 \mu\text{m}$). The latter suggests that the vaporization probability might not be proportional to the droplet volume concentration, as assumed by the model. We attribute the reduced vaporization counts observed for small droplets to a higher relative impact of the droplet shell on the vaporization threshold. This hypothesis should be further investigated and included in the model, to yield accurate predictions of the behaviour of submicron droplets.

The vaporization counts were found to saturate over time. In addition to droplet depletion [114], this behaviour probably strongly depends on the imaging system (2D versus 3D ultrasound) and on the attenuation of vaporization signals by high densities of static bubbles, and should be evaluated in conditions as close to the envisioned clinical application. Once again, the next logical step appears to be the transition from static phantoms to systems more representative of dynamic physiological conditions, coupled with the use of volumetric imaging. Indeed, encompassing the whole irradiated volume in the ultrasound field of view would make the burdensome and error-prone assessment of the elevational plane width unnecessary.

The statistical model developed in Chapter 7 also enabled to establish, through simulations, lower bounds for the achievable **range retrieval precision** in a clinical Pencil Beam Scanning treatment scenario. If nanodroplet concentrations in the tumor can reach values in the range 5-50 μM , single spot verification might be sufficiently accurate at low energy to trigger the interruption of the beam before the delivery of a full layer, while the scanning of a full layer might be required to extract accurate range estimates at high energies. However, these simulations represent a best-case scenario and do not account for uncertainties related to ultrasound imaging, inter- and intramodality image registration errors, or potential inhomogeneities in nanodroplet concentration. A range-shifting experiment was also performed in phantoms, and the range retrieved from vaporization maps lay within the uncertainty window of reference range measurements, which demonstrates the excellent accuracy of this method in an *in vitro* setting.

The ability to predict the number of vaporization events also offers perspectives

for *in vivo* dosimetry. To reach that goal, the major obstacle to overcome is the high variability in the vaporization response, both for phantoms irradiated with protons (Chapter 7) and with photons (Chapter 9), as it would immediately lead to high uncertainties on the inferred dose. This variability could not be fully attributed to the stochastic nature of proton-droplet interactions, but was rather postulated to come from (i) variations in nanodroplet concentration and spatial distribution in the phantoms, and (ii) a steep dependence of the vaporization response on temperature. To reduce the first source of variability, the development of means to quantify the nanodroplet concentration and spatial distribution in and around the tumor appears to be critical. As far as the temperature dependence is concerned, the degree of superheat should be carefully tuned to minimize the sensitivity to temperature. Assuming that the high variability and saturation behavior can be properly compensated, the linearity and dose-rate independence of the nanodroplet vaporization response are favorable properties for *in vivo* dosimetry of intensity-modulated radiation fields.

10.2 Future perspectives

10.2.1 Envisioned path towards clinical applications

In order to successfully translate the concept of injectable superheated nanodroplets for radiation detection into a viable clinical application, several research and development steps should be undertaken.

Optimization of the nanodroplet response:

The vaporization response to proton or photon radiation, depending on the application, should be optimized for the physiological temperature of 37 °C. For proton therapy, PVA-PFB nanodroplets vaporize through interactions with secondary particles at 37 °C, allowing to indirectly infer the proton range. This strategy, although similar to the one used in PET and Prompt Gamma Imaging, suffers from two major drawbacks. Firstly, high nanodroplet concentrations are required at the tumor, since nuclear reactions are rare events. Secondly, the correspondence between vaporization maps and the proton range is not straightforward and is impacted by uncertainties on the nuclear reaction cross sections in biological media [30]. Therefore, in our opinion, targeting a degree of superheat sufficiently high to allow direct nanodroplet vaporization by protons is essential, as it would offer this technology competitive advantages compared to PET and PGI and relax the requirements on the *in vivo* droplet concentration. As far as conventional radiotherapy is concerned, the use of highly superheated

droplets (reduced superheat $s > 0.51$) is mandatory to enable vaporization by low-LET electrons.

Two different approaches can be investigated to increase the nanodroplets degree of superheat at 37°C. The first one requires a **modification of the nanodroplet liquid core** to include more volatile compounds. The two major factors to consider when designing the nanodroplet liquid core are the biocompatibility and boiling temperature. Although many liquids with suitable boiling temperatures have been used in superheated drop detectors [113], injectable superheated nanodroplets reported in the literature are almost exclusively made of biologically inert perfluorocarbons for the liquid core: dodecafluoropentane (C_5F_{12} , b.p. 29°C), decafluorobutane (C_4F_{10} , b.p. -2°C), and octafluoropropane (C_3F_8 , b.p. -37°C) [66]. While the degree of superheat of octafluoropropane (OFP) would be sufficiently high at 37°C for nanodroplet vaporization by protons and electrons, the *in vivo* stability is compromised as the limit of superheat of OFP is 38°C [119]. Several studies have investigated the use of OFP nanodroplets at physiological temperature [122, 123, 260, 287, 306, 333, 338, 339], with a large variability in the reported stability performances. A careful engineering of the nanodroplet shell might slightly enhance the stability of OFP droplets, through the use of long acyl-chain phospholipids [123, 288] or polymeric shells, such as PVA [290, 340]. However, as shown in chapter 2, the impact of the shell on the limit of superheat remains limited. Nanodroplet cores containing mixtures of OFP and PFB have also been used as a means to modulate the degree of superheat [333, 334]. However, in an open system, the mixture behaved similarly to pure PFB as OFP diffused rapidly out of the lipidic shell [334]. Finally, endoskeletal droplets with a tunable vaporization temperature have recently been reported [238]. A preliminary proton irradiation experiment (not detailed in this thesis) was performed with endoskeletal droplets operated a few degrees below their spontaneous vaporization threshold. Radiation-induced droplet vaporization was not observed, presumably due to the vaporization mechanism of endoskeletal droplets being different than homogeneous nucleation, as it is triggered by the melting of the solid phase. Further experimental work should be conducted to evaluate whether those endoskeletal droplets can be vaporized by ionizing radiation.

The second approach to raise the degree of superheat is **acoustic modulation**, as proposed in Chapter 8. The acoustic pressure required for sensitization of PVA-PFB nanodroplets to protons at 37°C was 400 kPa at 1.1 MHz, well within the safety limits for diagnostic ultrasound. Sensitization of PVA-PFB nanodroplets to lower LET particles, such as electrons, remains to be assessed. While the theoretically required static pressure decrease is 600-900 kPa, experimentally determined sensitization thresholds exceeded theoretical

predictions by far. If the sensitization pressure to electrons approaches the Acoustic Droplet Vaporization threshold, the use of acoustic modulation in conventional radiotherapy might be compromised. For range verification and dosimetry applications, the acoustic modulation pressure field should be as uniform as possible and encompass the entire irradiated volume, *e.g.* using plane waves. In order to minimize interference with the radiation beam, acoustic modulation and nanodroplet vaporization detection should be performed with a single array. For medical accelerators delivering pulsed radiation beams (such as radiotherapy linacs and proton therapy synchrocyclotrons), the ultrasound system could alternate between the acoustic modulation pulse (synchronized with the beam delivery) and high frame rate imaging of vaporization events. For continuous proton beams produced by *e.g.* isochronous cyclotrons, transducer elements used for modulation and imaging could be interleaved [280, 341, 342], although their simultaneous use might induce significant crosstalk. The impact of ultrasound frequency on the acoustic modulation effect should be further investigated to determine whether dual-frequency arrays are required. Importantly, if the modulation frequency overlaps with the frequency range of nanodroplet vaporization signals (200 kHz - 2 MHz), tissue reflections from the modulation wave might hinder the passive detection of vaporization signals. Compared to the droplet composition approach, acoustic modulation enables a finer tuning of the degree of superheat, at the cost of increased technological complexity.

Development and validation of a predictive model:

While the statistical approach presented in Chapter 7 was a first step, further research is required to develop fast and accurate predictive models. As a complementary tool to better predict the nanodroplet vaporization behaviour, detailed Monte Carlo simulations are also required. Although out of the scope of this thesis, a simulation framework was implemented within the Amphora project, allowing to simulate energy depositions by primary protons and secondary particles and predict vaporization using the thermal spike model [343, 344]. Such an approach will be essential to elucidate some of the remaining open questions, namely the estimation of the value of the nucleation parameter, a , or the reasons for the relatively low peak to plateau ratios observed on vaporization maps. Moreover, Monte Carlo simulations can help determine the exact value of the maximum LET reached by protons and other particles at the end of their range, as analytical formulas are generally inaccurate for energy depositions at the nanoscale. Ideally, Monte Carlo simulation results would provide parameter values which could be incorporated into the fast analytical model of Chapter 7, yielding an accurate, real-time implementation. Finally, extensive *in vitro* measurement campaigns are required to calibrate the nanodroplet response in various clinically-relevant irradiation conditions and

validate the developed predictive model.

Achievable performances assessment in preclinical studies:

The feasibility of range verification and dosimetry with superheated nanodroplets strongly depends on the achievable nanodroplet concentrations and uniform accumulation at the target. Tumors are heterogeneous, with a disorganized architecture made of highly vascularized regions (angiogenesis) with enhanced permeability due to large inter-endothelial gaps, and avascular, often hypoxic, regions [79,329]. The lymphatic drainage is typically reduced in tumors, which leads to longer retention times of extravasated particles, a phenomenon called the enhanced permeability and retention (EPR) effect [69]. Due to the complexity of the tumor microenvironment, transitioning to *in vivo* animal studies with different tumor models is critical to assess the achievable performances in a clinically-relevant situation. Such studies will provide decisive answers to crucial aspects such as (i) the *in vivo* biocompatibility of the nanodroplet formulation, (ii) the achievable nanodroplet concentrations at the tumor, (iii) the relevant time frames for accumulation and clearance, and (iv) the effectiveness of passive targeting (through the EPR effect) compared to active targeting. Moreover, the nanodroplet behaviour in a physiological environment, particularly the amount of spontaneous vaporization, the lifetime of vaporized droplets, and whether they remain static at the target site or not, will determine which ultrasound imaging strategy should be adopted and optimized. We suggest to start by investigating organs where nanodroplets naturally accumulate, such as the liver, and then move on to different tumor models with non-targeted droplets, before evaluating the behaviour of targeted droplets. As a large body of research is already dedicated to the use of ultrasound contrast agents for molecular imaging and therapeutic applications in oncology [75,79], synergies with different research groups should be exploited.

In order to minimize the impact of nanodroplet distribution inhomogeneities on dosimetry and range verification performances, **methods to determine the nanodroplet concentration and *in vivo* distribution** should be developed. Moreover, assessing the concentration at the target is a prerequisite for dosimetry. Nanodroplets could be detected *in vivo* by means of ^{19}F MRI imaging, as their core contains Fluorine. A second approach, potentially more time-efficient and easy to integrate in the clinical workflow, would be to transform the droplets into microbubbles by means of Acoustic Droplet Vaporization and detect them with the ultrasound system used for dosimetry. If the nanodroplet *in vivo* distribution is sufficiently reproducible, this operation could be performed using a first injection for calibration purposes, followed by a second injection for dosimetry after clearance of the microbubbles or application of a destructive burst. Alternatively, vaporization of remaining nanodroplets can be performed after treatment delivery. However, this approach only allows to correct the

dose/range estimation after irradiation, which limits the potential for real-time monitoring.

Finally, range verification and dosimetry performances should be assessed *in vivo*. As the required ultrasound frequency depends on the target size and depth, ultrasound probes for animal imaging should be used, ideally enabling real-time volumetric imaging during irradiation. Relatively large animals such as rats or rabbits might be more suitable than mice to deliver and measure dose gradients around the tumor.

System integration in the radiotherapy workflow:

Despite its established advantages, the emergence of **ultrasound image guidance** in radiotherapy has been relatively slow and timid. The widespread adoption of ultrasound imaging in the radiotherapy workflow, traditionally dominated by X-ray and CT imaging, faces a number of barriers that should also be overcome to introduce ultrasound-based *in vivo* dosimetry. To that aim, prior and ongoing research not only in the field of ultrasound image-guided radiotherapy but also in ultrasound technology in general should be leveraged, ideally in collaboration with major ultrasound equipment vendors.

Quantitative ultrasound imaging requires a reduction of the inter-operator variability [48]. This can be achieved by **automating** both the acquisition process, through the use of passive or robotic probe holders, and the interpretation and processing of images, through *e.g.* machine learning [50]. As far as probe holders are concerned, robotic systems for real-time ultrasound imaging of different organs in the abdominopelvic region during radiotherapy are being developed and commercialized [55, 345–347]. Some of those solutions allow to monitor and control the pressure induced by the probe on the patient skin, to properly manage the resulting soft tissue motion [346]. Regarding image processing automation, research efforts in the field of segmentation [348–351] and motion estimation [352–354] could be used for treatment planning and image guidance [48, 49]. Additionally, inter- and/or intra- modality image registration methods will be required to overlay the dose distribution inferred from nanodroplet vaporization maps on the reference treatment plan, and are being developed in the field of image guidance [48, 355–357]. In parallel to automation, the radiotherapy staff should be thoroughly trained in ultrasound imaging to facilitate its successful adoption [50].

Potential **interferences** between the radiation beam and the ultrasound probe should also be accounted for during plan optimization. As an alternative approach to beam avoidance [55, 358], ultrasound probe designs that can minimize the impact on beam delivery, such as radiolucent probes [58] and/or flexible arrays, should be developed. Also, new **software interfaces**, designed

in partnership with radiation therapy companies, should integrate the novel functionalities offered by image guidance and dosimetry into the radiotherapy workflow, to facilitate image registration procedures, treatment replanning decisions, and real-time interruption and/or modification of the beam delivery process.

10.2.2 Integration of this technology in the current and future radiotherapy and oncology landscape

Short term vision:

In the short term, we foresee that ultrasound detection of radiation-induced nanodroplet vaporization could be a viable clinical solution for *in vivo* proton range verification, and dosimetry of both proton and conventional radiotherapy. However, considering that (i) proton beams contain higher LET particles than photon beams, and (ii) sensitivity to low LET particles requires high degree of superheat, which comes at the cost of degraded droplet stability, we argue that **proton therapy should be targeted in priority**. In addition to the reduced technological complexity, the clinical benefits conferred by *in vivo* monitoring are potentially greater, as it may help reduce range uncertainty margins and safely adopt beam angles more favorable to sparing organs at risk. Moreover, as only a few beam angles are typically used in proton therapy, the risk of interference between the ultrasound system and the radiation beam is not as severe as for conventional radiotherapy, where the dose is often delivered during a full gantry rotation. Finally, no gold standard solution currently exists for *in vivo* range verification, and this ultrasound-based approach would provide substantial advantages compared to competitors such as PET or PGI.

By combining range verification with real-time ultrasound image guidance, this technique could also become a powerful tool to facilitate the safe use of proton therapy for moving targets in the abdomen or pelvis. Cancers located in the abdominopelvic region are particularly deadly as they account for more than 48% of all cancer fatalities [359]. Currently, except for pediatric patients for which clinical indications are broader, proton therapy is mainly used to treat static targets such as brain or head and neck tumors. In the abdomen, range uncertainties can reach values of several millimeters, and are further increased due to large (approximately 2 cm [49]) intrafractional motion aggravated by the interplay effect with scanned proton beams [254, 255]. These excessive uncertainties can lead to unacceptable toxicity and push clinicians to adopt non-optimal, conservative treatment planning strategies, with limited benefits compared to conventional radiotherapy. Ultrasound-based range verification and intrafractional motion management can **increase the**

safety and efficacy of proton therapy for those tumor locations, which may in turn **broaden the panel of clinical indications** for proton therapy and favor higher reimbursement rates for a larger fraction of patients.

In conventional radiotherapy, EPID-based *in vivo* dosimetry has the potential to be broadly adopted, as EPIDs are available on the vast majority of modern linacs. Image guidance solutions are also well developed: cone-beam CT can be used to scan the patient in treatment position prior to beam delivery, and Magnetic Resonance Imaging is being integrated to linacs to offer offline and online image guidance [360,361]. Nevertheless, the technique introduced in this thesis would still benefit from competitive advantages, by simultaneously providing anatomical images with soft tissue contrast, on which the measured delivered dose could be superimposed during treatment delivery. To the best of our knowledge, the only other technology able to achieve these combined performances using a single imaging modality is XACT (X-Ray Acoustic Computed Tomography), whose development is still in its infancy [28]. Hypothetically, the technology developed by Amphora and subsequent projects could be initially targeted to applications where **high doses per fraction** are used. An example is Stereotactic Body Radiation Therapy of soft tissue tumors such as the liver, the pancreas, or the prostate [3,312].

Long term vision:

Despite the growing need for *in vivo* treatment monitoring of radiation therapy and the intensive research efforts undertaken, the adoption of relatively mature techniques, such as EPID-based dosimetry for radiotherapy and PET or PGI range verification for proton therapy, remains relatively slow and limited. In addition to previously discussed barriers impeding the widespread adoption of ultrasound image guidance, the demanding requirements regarding throughput and cost-efficiency of radiotherapy/proton therapy facilities might inhibit the integration of any treatment verification technique in the radiotherapy workflow, especially if the sole short term gain is the prevention of rare serious accidents and, more frequently, minor dose delivery errors. Moreover, demonstrating indirect clinical benefits such as the improvement of treatment efficacy and potential extension of clinical indications for proton therapy is neither fast nor straightforward.

Fortunately, ongoing trends in radiotherapy will provide a strong impetus to the development of *in vivo* monitoring techniques in the future. The adoption of offline and particularly **real-time adaptive radiotherapy** in the clinical workflow will require intrafractional image guidance and *in vivo* dosimetry systems to guide decisions on plan adaptation. Currently, in proton therapy, the delivered dose can be estimated by combining a pretreatment cone-beam CT scan of the patient with log files of the proton therapy delivery system [362,363],

but this indirect approach requires high imaging doses and ignores intrafractional motion. The ability to perform real-time image guidance and dosimetry would open the door to online adaptive radiotherapy, which would be particularly useful in combination with extreme hypofractionation.

In the longer term, the emergence of technologies employing **ultra high dose rates** (FLASH, >40 Gy/s [364]) and **spatially-fractionated micro-or minibeam** therapy [365,366], separately or in combination, will further favor **dose escalation** strategies owing to improved healthy tissue sparing effects [367,368]. Preclinical research on FLASH and mini/microbeam techniques has rapidly grown in the past years, and is expected to be applied to electron/X-ray therapy as well as proton therapy [369]. The extremely fast delivery (ms range) of high doses (~ 10 Gy) in only a few pulses requires online image guidance and treatment verification on a pulse by pulse basis [367], and a solution based on the detection of thermoacoustic waves has been already proposed [370]. The high temporal (ms) and spatial (μm) resolution achievable by ULM of nanodroplet vaporization makes this technique potentially applicable to *in vivo* dosimetry/range verification in FLASH and minibeam therapy. To maximize and demonstrate the potential benefits of such ground-breaking techniques, their integration with novel advanced methods for real-time treatment monitoring by pioneering research-oriented radio/proton therapy centers will be decisive.

Finally, we expect the versatility of ultrasound contrast agents to be their strongest asset in the long run, *i.e.* the one able to tilt the scale in their favor. By providing **functional and molecular imaging** of the tumor, ultrasound contrast agents can allow clinicians to adopt biologically-guided adaptive radiotherapeutic strategies [14], where the dose within the tumor is varied as a function of its inner characteristics (microvasculature, hypoxic regions, etc.). Additionally, a large body of research is currently devoted to **therapeutic applications** of ultrasound contrast agents in oncology [79]. Powerful synergies between radiotherapy and microbubble bioeffects were recently unveiled, such as oxygen delivery to hypoxic regions, cavitation-induced damage, and targeted release of chemotherapeutic drugs [90,94]. Therefore, in the future, a single nanodroplet injection might be able to provide anatomical and functional information about the tumor, perform real-time dosimetry and/or range verification combined with intrafractional motion monitoring, and help eradicate the tumor in synergy with radiotherapy, by leveraging one or several bioeffects that ultrasound contrast agents can unleash (Figure 10.1).

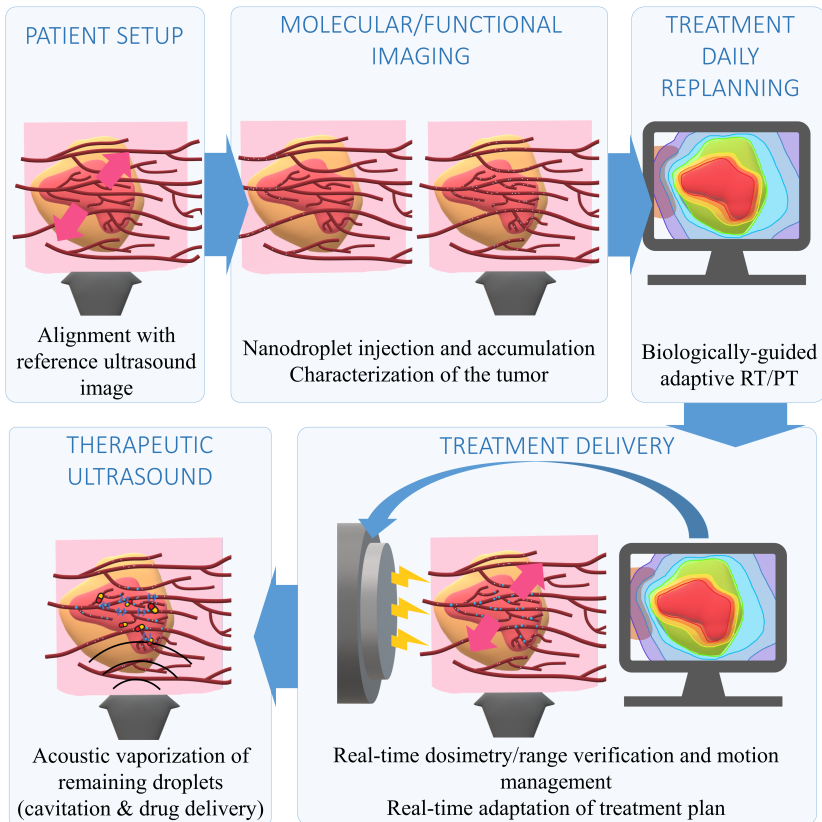


Figure 10.1: Envisioned long-term radiotherapy or proton therapy workflow with ultrasound imaging and nanodroplets. Following the order of the arrows: (1) ultrasound imaging of the tumor can be performed to guide patient setup by comparing daily anatomical images to a reference. (2) By injecting targeted nanodroplets, functional characteristics of the tumor can be better refined and its microvascular architecture can be assessed through e.g. acoustic angiography [371] or ULM [235] (3) Treatment plan adaptation can be triggered at this stage if large anatomical (1) or functional (2) changes in the tumor environment are detected. (4) During treatment delivery, ultrasound imaging allows to detect intrafractional motion and to measure the proton range and delivered dose, which potentially enables to adapt treatment delivery in real-time. (5) At the end of treatment delivery, remaining nanodroplets can be vaporized acoustically to generate bioeffects through cavitation and/or to trigger drug delivery.

10.3 Conclusion

This thesis introduced a novel method for *in vivo* treatment monitoring of radiation therapy using superheated nanodroplets. Phantom experiments revealed that superheated nanodroplets vaporize when irradiated by proton and photon beams, and that their response to radiation can be predicted using the thermal spike theory. The proton range was inferred from vaporization profiles with sub-millimeter reproducibility. Several offline and online ultrasound detection methods were developed, and their performance for range verification and dosimetry were compared. Future studies should investigate the impact of the nanodroplet shell on the vaporization threshold, optimize the nanodroplet degree of superheat at physiological temperature, and proceed to animal experiments in order to elucidate the achievable nanodroplet concentration and homogeneity in and around the tumor, as well as investigate the *in vivo* performance of the technology. In addition, the integration of ultrasound imaging in the radiotherapy environment should be facilitated by ongoing technological developments. By bringing together real-time image guidance, dosimetry, molecular imaging, and therapeutic capabilities, ultrasound contrast agents can become a valuable - if not essential - asset to broaden the horizons of proton therapy and, globally, assist the transition towards dose-escalated, safe, and automatically adaptable radiotherapy treatment strategies.

Bibliography

- [1] World Health Organization, “Cancer overview.” Available at <https://www.who.int/health-topics/cancer>, page consulted 18/10/2021.
- [2] International Agency for Research on Cancer, “The global cancer observatory.” Available at <https://gco.iarc.fr/tomorrow/en>, page consulted 18/10/2021.
- [3] F. M. Khan and J. P. Gibbons, *The Physics of Radiation Therapy*. Wolters Kluwer, 2014.
- [4] W. D. Newhauser and R. Zhang, “The physics of proton therapy,” *Physics in Medicine and Biology*, vol. 60, pp. 155–209, 2015.
- [5] F. Tommasino and M. Durante, “Proton radiobiology,” *Cancers*, vol. 7, no. 1, pp. 353–381, 2015.
- [6] J. Thariat, J.-M. Hannoun-Levi, A. S. Myint, T. Vuong, and J.-P. Gérard, “Past, present, and future of radiotherapy for the benefits of patients,” *Nature Reviews Clinical Oncology*, vol. 10, no. 1, pp. 52–60, 2013.
- [7] The International Atomic Energy Agency, “Dirac, directory of radiotherapy centres.” Available at <https://dirac.iaea.org/>, page consulted 18/10/2021.
- [8] N. D. MacDougall, M. Graveling, V. N. Hansen, K. Brownsword, and A. Morgan, “In vivo dosimetry in UK external beam radiotherapy: current and future usage,” *The British Journal of Radiology*, vol. 90, p. 20160915, 2017.
- [9] J. Vlayen, L. G. Fernandez, T. Boterberg, and L. S. Miguel, “Proton beam therapy in adults - a systematic review,” Tech. Rep. KCE Report 307, Health Technology Assessment (HTA) Brussels: Belgian Health Care Knowledge Center (KCE), 2019.
- [10] N. Zientara, E. Giles, H. Lee, and M. Short, “A scoping review of patient selection methods for proton therapy,” *Journal of Medical Radiation Sciences*, vol. 68, no. 4, 2021.
- [11] Particle Therapy Co-Operative Group, “Patient statistics.” Available at <https://www.ptcog.ch/index.php/patient-statistics>.
- [12] B. Glimelius, A. Ask, G. Bjelkengren, T. Björk-Eriksson, E. Blomquist, B. Johansson, M. Karlsson, and B. Zackrisson, “Number of patients potentially eligible for proton therapy,” *Acta Oncologica*, vol. 44, no. 8, pp. 836–849, 2005.
- [13] G. Gordon Steel, T. McMillan, and J. H. Peacock, “The 5Rs of radiobiology,” *International Journal of Radiation Biology*, vol. 56, no. 6, pp. 1045–1048, 1989.
- [14] B. Mijnheer, ed., *Clinical 3D Dosimetry in Modern Radiation Therapy*. Imaging in Medical Diagnosis and Therapy, Boca Raton: CRC Press, 2017.
- [15] H. Paganetti, ed., *The Physics of Proton Therapy*. Boca Raton: CRC Press, second ed., 2019.

- [16] J. Seco, G. Gu, T. Marcelos, H. Kooy, and H. Willers, "Proton arc reduces range uncertainty effects and improves conformality compared with photon volumetric modulated arc therapy in stereotactic body radiation therapy for non-small cell lung cancer," *International Journal of Radiation Oncology Biology Physics*, vol. 87, no. 1, pp. 188–194, 2013.
- [17] X. Ding, X. Li, J. M. Zhang, P. Kabolizadeh, C. Stevens, and D. Yan, "Spot-scanning proton arc (SPArc) therapy: The first robust and delivery-efficient spot-scanning proton arc therapy," *International Journal of Radiation Oncology Biology Physics*, vol. 96, no. 5, pp. 1107–1116, 2016.
- [18] A. Carabe-Fernandez, A. Bertolet-Reina, I. Karagounis, K. Huynh, and R. G. Dale, "Is there a role for arcing techniques in proton therapy?," *British Journal of Radiology*, vol. 93, p. 20190469, 2020.
- [19] D. Rodin, B. Tawk, O. Mohamad, S. Grover, F. Y. Moraes, M. L. Yap, E. Zubizarreta, and Y. Lievens, "Hypofractionated radiotherapy in the real-world setting: An international ESTRO-GIRO survey," *Radiotherapy and Oncology*, vol. 157, pp. 32–39, 2021.
- [20] B. Mijnheer, S. Beddar, J. Izewska, and C. Reft, "In vivo dosimetry in external beam radiotherapy," *Medical Physics*, vol. 40, no. 7, p. 070903, 2013.
- [21] C. Bojchko, M. Phillips, A. Kalet, and E. Ford, "A quantification of the effectiveness of EPID dosimetry and software-based plan verification systems in detecting incidents in radiotherapy," *Medical Physics*, vol. 42, no. 9, pp. 5363–5369, 2015.
- [22] A. Mans, M. Wendling, L. N. McDermott, J.-J. Sonke, R. Tielenburg, R. Vijlbried, B. Mijnheer, M. van Herk, and J. C. Stroom, "Catching errors with in vivo EPID dosimetry," *Medical Physics*, vol. 37, no. 6, pp. 2638–2644, 2010.
- [23] I. Olaciregui-Ruiz, S. Beddar, P. Greer, N. Jornet, B. McCurdy, G. Paiva-Fonseca, B. Mijnheer, and F. Verhaegen, "In vivo dosimetry in external beam photon radiotherapy: Requirements and future directions for research, development, and clinical practice," *Physics and Imaging in Radiation Oncology*, vol. 15, pp. 108–116, 2020.
- [24] H. C. Woodruff, T. Fuangrod, E. Van Uytven, B. M. C. McCurdy, T. van Beek, S. Bhatia, and P. B. Greer, "First experience with real-time EPID-based delivery verification during IMRT and VMAT sessions," *International Journal of Radiation Oncology - Biology - Physics*, vol. 93, no. 3, pp. 516–522, 2015.
- [25] H. Spreeuw, R. Rozendaal, I. Olaciregui-Ruiz, P. Gonzalez, A. Mans, and B. Mijnheer, "Online 3D EPID-based dose verification: Proof of concept," *Medical Physics*, vol. 43, no. 7, pp. 3969–3974, 2016.
- [26] L. Xiang, B. Han, C. Carpenter, G. Prax, Y. Kuang, and L. Xing, "X-ray acoustic computed tomography with pulsed x-ray beam from a medical linear accelerator," *Medical Physics*, vol. 40, no. 1, 2013.
- [27] S. Hickling, H. Lei, M. Hobson, P. Léger, X. Wang, and I. E. Naqa, "Experimental evaluation of x-ray acoustic computed tomography for radiotherapy dosimetry applications," *Medical Physics*, vol. 44, no. 2, pp. 608–617, 2017.
- [28] W. Zhang, I. Oraiqt, H. Lei, P. L. Carson, I. E. Naqa, and X. Wang, "Dual-modality X-ray-induced radiation acoustic and ultrasound imaging for real-time monitoring of radiotherapy," *BME Frontiers*, vol. 2020, p. 10, 2020.
- [29] J.-J. Sonke, M. Aznar, and C. Rasch, "Adaptive radiotherapy for anatomical changes," *Seminars in Radiation Oncology*, vol. 29, pp. 245–257, 2019.
- [30] H. Paganetti, "Range uncertainties in proton therapy and the role of Monte Carlo simulations," *Physics in Medicine and Biology*, vol. 57, no. 11, pp. R99–R117, 2012.

- [31] K. Parodi and W. Enghardt, "Potential application of PET in quality assurance of proton therapy," *Physics in Medicine and Biology*, vol. 45, no. 11, pp. N151–N156, 2000.
- [32] A. Knopf, K. Parodi, T. Bortfeld, H. A. Shih, and H. Paganetti, "Systematic analysis of biological and physical limitations of proton beam range verification with offline PET/CT scans," *Physics in Medicine and Biology*, vol. 54, pp. 4477–4495, 2009.
- [33] C. H. Min, X. Zhu, B. A. Winey, K. Grogg, M. Testa, G. E. Fakhri, T. R. Bortfeld, H. Paganetti, and H. A. Shih, "Clinical application of in-room PET for in vivo treatment monitoring in proton radiotherapy," *International Journal of Radiation Oncology Biology Physics*, vol. 86, no. 1, pp. 183–189, 2013.
- [34] X. Zhu, S. España, J. Daartz, N. Liebsch, J. Ouyang, H. Paganetti, T. R. Bortfeld, and G. E. Fakhri, "Monitoring proton radiation therapy with in-room PET imaging," *Physics in Medicine and Biology*, vol. 56, no. 13, pp. 4041–4057, 2011.
- [35] S. Helmbrecht, A. Santiago, W. Enghardt, P. Kuess, and F. Fiedler, "On the feasibility of automatic detection of range deviations from in-beam PET data," *Physics in Medicine and Biology*, vol. 57, no. 5, pp. 1387–1397, 2012.
- [36] V. Ferrero, E. Fiorina, M. Morrocchi, F. Pennazio, G. Baroni, G. Battistoni, N. Belcari, N. Camarlinghi, M. Ciocca, A. D. Guerra, M. Donetti, S. Giordanengo, G. Giraud, V. Patera, C. Peroni, A. Rivetti, M. D. da Rocha Rolo, S. Rossi, V. Rosso, G. Sportelli, S. Tempellini, F. Valvo, R. Wheadon, P. Cerello, and M. G. Bisogni, "Online proton therapy monitoring: clinical test of a silicon-photodetector-based in-beam PET," *Scientific Reports*, vol. 8, p. 4100, 2018.
- [37] Y. Jongen and F. Stichelbaut, "Verification of the proton beams position in the patient by the detection of prompt gamma-rays emission," in *39th Meeting of the Particle Therapy Co-Operative Group*, (San Francisco, CA), 2003.
- [38] J. Smeets, F. Roellinghoff, D. Prieels, F. Stichelbaut, A. Benilov, P. Busca, C. Fiorini, R. Peloso, M. Basilavecchia, T. Frizzi, J. C. Dehaes, and A. Dubus, "Prompt gamma imaging with a slit camera for real-time range control in proton therapy," *Physics in Medicine and Biology*, vol. 57, no. 11, pp. 3371–3405, 2012.
- [39] Y. Xie, E. H. Bentefour, G. Janssens, J. Smeets, F. V. Stappen, L. Hotoiu, L. Yin, D. Dolney, S. Avery, F. O'Grady, D. Prieels, J. McDonough, T. D. Solberg, R. A. Lustig, A. Lin, and B.-K. K. Teo, "Prompt Gamma imaging for in vivo range verification of pencil beam scanning proton therapy," *International Journal of Radiation Oncology Biology Physics*, vol. 99, no. 1, pp. 210–218, 2017.
- [40] S. Hickling, L. Xiang, K. C. Jones, K. Parodi, W. Assmann, S. Avery, M. Hobson, and I. E. Naqa, "Ionizing radiation-induced acoustics for radiotherapy and diagnostic radiology applications," *Medical Physics*, vol. 45, no. 7, pp. 707–721, 2018.
- [41] S. Lehrack, W. Assmann, D. Bertrand, S. Henrotin, J. Herault, V. Heymans, F. V. Stappen, P. G. Thirolf, M. Vidal, J. Van de Walle, and K. Parodi, "Submillimeter ionoacoustic range determination for protons in water at a clinical synchrotron," *Physics in Medicine and Biology*, vol. 62, pp. L20–L30, 2017.
- [42] S. K. Patch, D. E. Hoff, T. B. Webb, L. G. Sobotka, and T. Zhao, "Two-stage ionoacoustic range verification leveraging Monte Carlo and acoustic simulations to stably account for tissue inhomogeneity and accelerator-specific time structure - A simulation study," *Medical Physics*, vol. 45, no. 2, pp. 783–793, 2018.
- [43] S. K. Patch, C. Nguyen, D. Dominguez-Ramirez, R. Labarbe, G. Janssens, D. Cammarano, J. Lister, C. Finch, J. Lambert, J. Pandey, C. Bennett, E. Porteous, C. Chirvase, M. Cohilis, K. Souris, S. Ono, and T. Lynch, "Thermoacoustic range verification during pencil beam delivery of a clinical plan to an abdominal imaging phantom," *Radiotherapy and Oncology*, vol. 159, pp. 224–230, 2021.

- [44] J. Lascaud, P. Dash, M. Würfl, H.-P. Wieser, B. Wollant, R. Kalunga, W. Assman, D.-A. Clevert, A. Ferrari, P. Sala, A. S. Savoia, and K. Parodi, "Enhancement of the ionoacoustic effect through ultrasound and photoacoustic contrast agents," *Scientific Reports*, vol. 11, no. 1, p. 2725, 2021.
- [45] A. L. Klibanov and J. A. Hossack, "Ultrasound in radiology: from anatomic, functional, molecular imaging to drug delivery and image-guided therapy," *Investigative Radiology*, vol. 50, no. 9, pp. 657–670, 2015.
- [46] S. Banerjee, T. Kataria, D. Gupta, S. Goyal, S. S. Bisht, T. Basu, and A. Abhishek, "Use of ultrasound in image-guided high-dose-rate brachytherapy: enumerations and arguments," *Journal of Contemporary Brachytherapy*, vol. 9, no. 2, pp. 146–150, 2017.
- [47] C. Western, D. Hristov, and J. Schlosser, "Ultrasound imaging in radiation therapy: From interfractional to intrafractional guidance," *Cureus*, vol. 7, no. 6, pp. 1–19, 2015.
- [48] D. Fontanarosa, S. van der Meer, J. Bamber, E. Harris, T. O'Shea, and F. Verhaegen, "Review of ultrasound image guidance in external beam radiotherapy: I. treatment planning and inter-fraction motion management," *Physics in Medicine and Biology*, vol. 60, pp. R77–R114, 2015.
- [49] T. O'Shea, J. Bamber, D. Fontanarosa, S. van der Meer, F. Verhaegen, and E. Harris, "Review of ultrasound image guidance in external beam radiotherapy part II: intra-fraction motion management and novel applications," *Physics in Medicine and Biology*, vol. 61, pp. R90–R137, 2016.
- [50] E. Harris, D. Fontanarosa, and C. Baldock, "In the future, ultrasound guidance in radiotherapy will become a clinical standard," *Physical and Engineering Sciences in Medicine*, vol. 44, pp. 347–350, 2021.
- [51] D. Mah, G. Freedman, B. Milestone, A. Hanlon, E. Palacio, T. Richardson, B. Movsas, R. Mitra, E. Horwitz, and G. E. Hanks, "Measurement of intrafractional prostate motion using magnetic resonance imaging," *International Journal of Radiation Oncology Biology Physics*, vol. 54, no. 2, pp. 568–575, 2002.
- [52] A. Grimwood, H. A. McNair, T. P. O'Shea, S. Gilroy, K. Thomas, J. C. Bamber, A. C. Tree, and E. J. Harris, "In vivo validation of Elekta's Clarity Autoscan for ultrasound-based intrafraction motion estimation of the prostate during radiation therapy," *International Journal of Radiation Oncology Biology Physics*, vol. 102, no. 4, pp. 912–921, 2018.
- [53] E. A. Omari, B. Erickson, C. Ehlers, F. Quiroz, G. Noid, D. T. Cooper, and M. Lachaine, "Preliminary results on the feasibility of using ultrasound to monitor intrafractional motion during radiotherapy for pancreatic cancer," *Medical Physics*, vol. 43, no. 9, pp. 5252–5260, 2016.
- [54] D. J. Fraser, P. Wong, K. Sultanem, and F. Verhaegen, "Dosimetric evolution of the breast electron boost target using 3D ultrasound imaging," *Radiotherapy and Oncology*, vol. 96, no. 2, pp. 185–191, 2010.
- [55] J. Schlosser, R. H. Gong, R. Bruder, A. Schweikard, S. Jang, J. Henrie, A. Kamaya, A. Koong, D. T. Chang, and D. Hristov, "Robotic intrafractional US guidance for liver SABR: System design, beam avoidance, and clinical imaging," *Medical Physics*, vol. 43, no. 11, pp. 5951–5963, 2016.
- [56] N. Bourbakis and M. Tsakalakis, "A 3-D ultrasound wearable array prognosis system with advanced imaging capabilities," *IEEE Transactions on Ultrasonics, Ferroelectrics, and Frequency Control*, vol. 68, no. 4, pp. 1062–1072, 2021.
- [57] Pulsify Medical, "The ultrasound monitoring patch." <https://pulsify-medical.com/>, 2021. page consulted on 21/20/2021.

- [58] J. Schlosser and D. Hristov, "Radiolucent 4D ultrasound imaging: System design and application to radiotherapy guidance," *IEEE Transactions on Medical Imaging*, vol. 35, no. 10, pp. 2292–2300, 2016.
- [59] L. Wei, G. Wahyulaksana, B. Meijlink, A. Ramalli, E. Noothout, M. Verweij, E. Boni, K. Kooiman, A. F. W. van der Steen, P. Tortoli, N. de Jong, and H. J. Vos, "High frame rate volumetric imaging of microbubbles using a sparse array and spatial coherence beamforming," *IEEE Transactions on Ultrasonics, Ferroelectrics, and Frequency Control*, vol. 68, no. 10, pp. 3069–3081, 2021.
- [60] P. Santos, G. U. Haugen, L. Løvstakken, E. Samset, and J. D'hooge, "Diverging wave volumetric imaging using subaperture beamforming," *IEEE Transactions on Ultrasonics, Ferroelectrics, and Frequency Control*, vol. 63, no. 12, pp. 2114–2124, 2016.
- [61] K. Ferrara, R. Pollard, and M. Borden, "Ultrasound Microbubble Contrast Agents : Fundamentals and application to gene and drug delivery," *Annual Review of Biomedical Engineering*, vol. 9, pp. 415–447, 2007.
- [62] A. Stanziola, M. Toulemonde, Y. O. Yildiz, R. J. Eckersley, and M.-X. Tang, "Ultrasound imaging with microbubbles," *IEEE Signal Processing Magazine*, vol. 33, no. 2, pp. 111–117, 2016.
- [63] N. de Jong, P. J. Frinking, A. Bouakaz, and F. J. T. Cate, "Detection procedures of ultrasound contrast agents," *Ultrasonics*, vol. 38, pp. 87–92, 2000.
- [64] N. de Jong, A. Bouakaz, and P. Frinking, "Basic acoustic properties of microbubbles," *Echocardiography*, vol. 19, no. 3, pp. 229–240, 2002.
- [65] P. S. Sheeran and P. A. Dayton, "Phase-change contrast agents for imaging and therapy," *Current Pharmaceutical Design*, vol. 18, no. 15, pp. 2152–2165, 2012.
- [66] H. Lea-Banks, M. A. O'Reilly, and K. Hynynen, "Ultrasound-responsive droplets for therapy: a review," *Journal of Controlled Release*, vol. 293, pp. 144–154, 2019.
- [67] M. A. Borden, G. Shakya, A. Upadhyay, and K.-H. Song, "Acoustic nanodrops for biomedical applications," *Current Opinion in Colloid & Interface Science*, vol. 50, no. 101383, 2020.
- [68] B. L. Helfield, K. Yoo, J. Lio, R. Williams, P. S. Sheeran, D. E. Goertz, and P. N. Burns, "Investigating the accumulation of submicron phase-change droplets in tumors," *Ultrasound in Medicine and Biology*, vol. 46, no. 10, pp. 2861–2870, 2020.
- [69] H. Maeda, J. Wu, T. Sawa, Y. Matsumura, and K. Hori, "Tumor vascular permeability and the EPR effect in macromolecular therapeutics: a review," *Journal of Controlled Release*, vol. 65, pp. 271–284, 2000.
- [70] N. Rapoport, R. Gupta, Y.-S. Kim, and B. E. O'Neil, "Polymeric micelles and nanoemulsions as tumor-targeted drug carriers: Insight through intravital imaging," *Journal of Controlled Release*, vol. 206, pp. 153–160, 2015.
- [71] P. S. Sheeran, S. H. Luois, L. B. Mullin, T. O. Matsunaga, and P. A. Dayton, "Design of ultrasonically-activatable nanoparticles using low-boiling point perfluorocarbons," *Biomaterials*, vol. 33, no. 11, pp. 3262–3269, 2012.
- [72] Y. Toumia, B. Cerroni, F. Domenici, H. Lange, L. Bianchi, M. Cociorb, F. Brasili, E. Chiessi, E. D'Agostino, K. Van Den Abele, S. V. Heymans, J. D'Hooge, and G. Paradossi, "Phase change ultrasound contrast agents with a photopolymerized diacetylene shell," *Langmuir*, vol. 35, no. 31, pp. 10116–10127, 2019.
- [73] J. D. Dove, P. A. Mountford, T. W. Murray, and M. A. Borden, "Engineering optically triggered droplets for photoacoustic imaging and therapy," *Biomedical Optics Express*, vol. 5, no. 12, pp. 4417–4427, 2014.

- [74] S. Lin, A. Shah, J. Hernández-Gil, A. Stanziola, B. I. Harriss, T. O. Matsunaga, N. Long, J. Bamber, and M.-X. Tang, "Optically and acoustically triggerable sub-micron phase-change contrast agents for enhanced photoacoustic and ultrasound imaging," *Photoacoustics*, vol. 6, pp. 26–36, 2017.
- [75] A. Kosareva, L. Abou-Elkacem, S. Chowdhury, J. R. Lindner, and B. A. Kaufmann, "Seeing the invisible - ultrasound molecular imaging," *Ultrasound in Medicine & Biology*, vol. 46, no. 3, pp. 479–497, 2020.
- [76] K. P. Hadinger, J. P. Marshalek, P. S. Sheeran, P. A. Dayton, and T. O. Matsunaga, "Optimization of phase-change contrast agents for targeting MDA-MB-231 breast cancer cells," *Ultrasound in Medicine & Biology*, vol. 44, no. 12, pp. 2728–2738, 2018.
- [77] C. Errico, J. Pierre, S. Pezet, Y. Desailly, Z. Lenkei, O. Couture, and M. Tanter, "Ultrafast ultrasound localization microscopy for deep super-resolution vascular imaging," *Nature*, vol. 527, no. 7579, pp. 499–502, 2015.
- [78] O. M. Viessmann, R. J. Eckersley, K. Christensen-Jeffries, M. X. Tang, and C. Dunsby, "Acoustic super-resolution with ultrasound and microbubbles," *Physics in Medicine and Biology*, vol. 58, no. 18, pp. 6447–6458, 2013.
- [79] K. Kooiman, S. Roovers, S. A. Langeveld, R. T. Kleven, H. Dewitte, M. O'Reilly, J.-M. Escoffre, A. Bouakaz, M. D. Verweij, K. Hynynen, I. Lentacker, E. Stride, and C. K. Holland, "Ultrasound-responsive cavitation nuclei for therapy and drug delivery," *Ultrasound in Medicine and Biology*, vol. 46, no. 6, pp. 1296–1325, 2020.
- [80] S. M. Chowdhury, L. Abou-Elkacem, T. Lee, J. Dahl, and A. M. Lutz, "Ultrasound and microbubble mediated therapeutic delivery: Underlying mechanisms and future outlook," *Journal of Controlled Release*, vol. 326, pp. 75–90, 2020.
- [81] J. Deprez, G. Lajoinie, Y. Engelen, S. C. De Smedt, and I. Lentacker, "Opening doors with ultrasound and microbubbles: Beating biological barriers to promote drug delivery," *Advanced Drug Delivery Reviews*, vol. 172, pp. 9–36, 2021.
- [82] T. Mainprize, N. Lipsman, Y. Huang, Y. Meng, A. Bethune, S. Ironside, C. Heyn, R. Alkins, M. Trudeau, A. Sahgal, J. Perry, and K. Hynynen, "Blood-brain barrier opening in primary brain tumors with non-invasive MR-guided focused ultrasound: A clinical safety and feasibility study," *Scientific Reports*, vol. 9, no. 321, 2019.
- [83] J. J. Kwan, R. Myers, C. M. Coviello, S. M. Graham, A. R. Shah, E. Stride, R. C. Carlisle, and C. C. Coussios, "Ultrasound-propelled nanocups for drug delivery," *Small*, vol. 11, no. 39, pp. 5305–5314, 2015.
- [84] M. Aryal, C. D. Arvanitis, P. M. Alexander, and N. McDannold, "Ultrasound-mediated blood-brain barrier disruption for targeted drug delivery in the central nervous system," *Advanced Drug Delivery Reviews*, vol. 72, pp. 94–109, 2014.
- [85] N. Lipsman, Y. Meng, A. J. Bethune, Y. Huang, B. Lam, M. Masellis, N. Herrmann, C. Heyn, I. Aubert, A. Boutet, G. S. Smith, K. Hynynen, and S. E. Black, "Blood-brain barrier opening in Alzheimer's disease using MR-guided focused ultrasound," *Nature Communications*, vol. 9, no. 1, pp. 1–8, 2018.
- [86] C. Gasca-Salas, B. Fernández-Rodríguez, J. A. Pineda-Pardo, R. Rodríguez-Rojas, I. Obeso, F. Hernández-Fernández, M. del Álamo, D. Mata, P. Guida, C. Ordás-Bandera, J. I. Montero-Roblas, R. Martínez-Fernández, G. Foffani, I. Rachmilevitch, and J. A. Obeso, "Blood-brain barrier opening with focused ultrasound in Parkinson's disease dementia," *Nature Communications*, vol. 12, no. 779, pp. 1–7, 2021.
- [87] S. T. Roos, L. J. Juffermans, J. Slikkerveer, E. C. Unger, T. R. Porter, and O. Kamp, "Sonothrombolysis in acute stroke and myocardial infarction : A systematic review," *IJC Heart & Vessels*, vol. 4, pp. 1–6, 2014.

- [88] M. Smeenge, F. Tranquart, C. K. Mannaerts, T. M. de Reijke, M. J. van de Vijver, M. P. Laguna, S. Pochon, J. J. de la Rosette, and H. Wijkstra, "First-in-human ultrasound molecular imaging with a VEGFR2-specific ultrasound molecular contrast agent (BR55) in prostate cancer - A safety and feasibility pilot study," *Investigative Radiology*, vol. 52, no. 7, pp. 419–427, 2017.
- [89] J. K. Willmann, L. Bonomo, A. C. Testa, P. Rinaldi, G. Rindi, K. S. Valluru, G. Petrone, M. Martini, A. M. Lutz, and S. S. Gambhir, "Ultrasound molecular imaging with BR55 in patients with breast and ovarian lesions: First in-human results," *Journal of Clinical Oncology*, vol. 35, no. 19, pp. 2133–2140, 2017.
- [90] G. J. Czarnota, R. Karshafian, P. N. Burns, S. Wong, A. A. Mahrouki, J. W. Lee, A. Caissie, W. Tran, C. Kim, M. Furukawa, E. Wong, and A. Giles, "Tumor radiation response enhancement by acoustical stimulation of the vasculature," *Proceedings of the National Academy of Sciences of the United States of America*, vol. 109, no. 30, 2012.
- [91] J. R. Eisenbrey, F. Forsberg, C. E. Wessner, L. J. Delaney, K. Bradigan, S. Gummadi, M. Tantawi, A. Lyshchik, P. O'Kane, J. B. Liu, C. Intenzo, J. Civan, W. Maley, S. W. Keith, K. Anton, A. Tan, A. Smolock, S. Shamimi-Noori, and C. M. Shaw, "US-triggered microbubble destruction for augmenting hepatocellular carcinoma response to transarterial radioembolization: A randomized pilot clinical trial," *Radiology*, vol. 298, no. 2, pp. 450–457, 2021.
- [92] P. Lai, C. Tarapacki, W. T. Tran, A. E. Kaffas, J. Lee, C. Hupple, S. Iradj, A. Giles, A. Al-Mahrouki, and G. J. Czarnota, "Breast tumor response to ultrasound mediated excitation of microbubbles and radiation therapy in vivo," *Oncoscience*, vol. 3, pp. 98–108, 2016.
- [93] A. Daecher, M. Stanczak, J.-B. Liu, J. Zhang, S. Du, F. Forsberg, D. B. Leeper, and J. R. Eisenbrey, "Localized microbubble cavitation-based antivascular therapy for improving hcc treatment response to radiotherapy," *Cancer Letters*, vol. 411, pp. 100–105, 2017.
- [94] Q. Lacerda, M. Tantawi, D. B. Leeper, M. A. Wheatley, and J. R. Eisenbrey, "Emerging applications of ultrasound-contrast agents in radiation therapy," *Ultrasound in Medicine and Biology*, vol. 47, no. 6, pp. 1465–1474, 2021.
- [95] S. M. Fix, V. Papadopoulou, H. Velds, S. K. Kasoji, J. N. Rivera, M. A. Borden, S. Chang, and P. A. Dayton, "Oxygen microbubbles improve radiotherapy tumor control in a rat fibrosarcoma model - a preliminary study," *PLoS ONE*, vol. 13, no. 4, pp. 1–18, 2018.
- [96] J. R. Eisenbrey, R. Shraim, J.-B. Liu, J. Li, M. Stanczak, B. Oeffinger, D. B. Leeper, S. W. Keith, L. J. Jablonowski, F. Forsberg, P. O'Kane, and M. A. Wheatley, "Sensitization of hypoxic tumors to radiation therapy using ultrasound sensitive oxygen microbubbles," *International Journal of Radiation Oncology Biology Physics*, vol. 101, no. 1, pp. 88–96, 2018.
- [97] C. McEwan, J. Owen, E. Stride, C. Fowley, H. Nesbitt, D. Cochrane, C. C. Coussios, M. A. Borden, N. Nomikou, A. P. McHale, and J. F. Callan, "Oxygen carrying microbubbles for enhanced sonodynamic therapy of hypoxic tumours," *Journal of Controlled Release*, vol. 203, pp. 51–56, 2015.
- [98] J. M. Brown and W. R. Wilson, "Exploiting tumour hypoxia in cancer treatment," *Nature Reviews Cancer*, vol. 4, pp. 437–447, 2004.
- [99] S. Rockwell, I. T. Dobrucki, E. Y. Kim, S. T. Marrison, and V. T. Vu, "Hypoxia and radiation therapy: Past history, ongoing research, and future promise," *Current Molecular Medicine*, vol. 9, no. 4, pp. 442–458, 2009.
- [100] Y. Xiang, N. Bernards, B. Hoang, J. Zheng, and N. Matsuura, "Perfluorocarbon nanodroplets can reoxygenate hypoxic tumors in vivo without carbogen breathing," *Nanotheranostics*, vol. 3, no. 2, pp. 135–144, 2019.

- [101] N. Arteaga-Marrero, J. F. Mainou-Gomez, C. B. Rygh, N. Lutay, D. Roehrich, R. K. Reed, and D. R. Olsen, "Radiation treatment monitoring with DCE-US in CWR22 prostate tumor xenografts," *Acta Radiologica*, vol. 60, no. 6, pp. 788–797, 2019.
- [102] S. K. Kasoji, J. N. Rivera, R. C. Gessner, S. X. Chang, and P. A. Dayton, "Early assessment of tumor response to radiation therapy using high-resolution quantitative microvascular ultrasound imaging," *Theranostics*, vol. 8, no. 1, pp. 156–168, 2018.
- [103] L. J. Delaney, M. Tantawi, C. E. Wessner, P. Machado, F. Forsberg, A. Lyshchik, P. O'Kane, J.-B. Liu, J. Civan, A. Tan, K. Anton, C. M. Shaw, and J. R. Eisenbrey, "Predicting long-term hepatocellular carcinoma response to transarterial radioembolization using contrast-enhanced ultrasound: initial experiences," *Ultrasound in Medicine and Biology*, vol. 47, no. 9, pp. 2523–2531, 2021.
- [104] K. Parodi and J. C. Polf, "In vivo range verification in particle therapy," *Medical Physics*, vol. 45, no. 11, pp. e1036–e1050, 2018.
- [105] E. Verboven, E. D'Agostino, M. Callens, H. Pfeiffer, D. Verellen, J. D'hooge, and K. Van Den Abeele, "Ultrasound based dosimetry for radiotherapy: in-vitro proof of principle," in *IEEE International Ultrasonics Symposium*, (Chicago, IL), pp. 2265–2268, 3-6 September 2014 2014.
- [106] E. Verboven, *Development of Ultrasound Contrast Agent based Dosimetry for Radiotherapy*. PhD thesis, KU Leuven, April 2017.
- [107] Lawrence Berkeley National Laboratory, "First tracks observed in John Wood's 1-1/2 inch liquid hydrogen bubble chamber." <https://photos.lbl.gov/bp/#/folder/408304/10173689>, May 1955. Page consulted on 22/10/2021.
- [108] F. Seitz, "On the theory of the bubble chamber," *Physics of Fluids*, vol. 1, no. 1, pp. 2–13, 1958.
- [109] M. Toulemonde, E. Surdutovich, and A. Solov'yoy, "Temperature and pressure spikes in ion-beam cancer therapy," *Physical Review E - Statistical, Nonlinear, and Soft Matter Physics*, vol. 80, no. 031913, 2009.
- [110] D. A. Glaser, "Some effects of ionizing radiation on the formation of bubbles in liquids," *Physical Review*, vol. 87, no. 4, p. 665, 1952.
- [111] A. Miller, R. Machrafi, E. Benton, H. Kitamura, and S. Kodaira, "Comparison of the space bubble detector response to space-like neutron spectra and high energy protons," *Acta Astronautica*, vol. 151, pp. 1–6, 2018.
- [112] B. J. Lewis, M. B. Smith, H. Ing, H. R. Andrews, R. Machrafi, L. Tomi, T. J. Matthews, L. Veloce, V. Shurshakov, I. Tchernykh, , and N. Khoshooni, "Review of bubble detector response characteristics and results from space," *Radiation Protection Dosimetry*, vol. 150, no. 1, pp. 1–21, 2012.
- [113] F. D'Errico, "Radiation dosimetry and spectrometry with superheated emulsions," *Nuclear Instruments and Methods in Physics Research B*, vol. 184, pp. 229–254, 2001.
- [114] F. d'Errico and W. G. Alberts, "Superheated-drop (bubble) neutron detectors and their compliance with ICRP-60," *Radiation Protection Dosimetry*, vol. 54, no. 3/4, pp. 357–360, 1994.
- [115] M. Felizardo, T. Morlat, J. Marques, A. Ramos, T. Girard, A. Fernandes, A. Kling, I. Lázaro, R. Martins, and J. Puibasset, "Fabrication and response of high concentration simple superheated droplet detectors with different liquids," *Astroparticle Physics*, vol. 49, pp. 28–43, 2013.
- [116] F. D'Errico, R. Nath, M. Lamba, and S. K. Holland, "A position-sensitive superheated emulsion chamber for three-dimensional photon dosimetry," *Physics in Medicine and Biology*, vol. 43, no. 5, pp. 1147–1158, 1998.

- [117] F. D'Errico, R. Nath, G. Silvano, and L. Tana, "In vivo neutron dosimetry during high-energy Bremsstrahlung radiotherapy," *International Journal of Radiation Oncology - Biology - Physics*, vol. 41, no. 5, pp. 1185–1192, 1998.
- [118] R. E. Apfel, "Activatable infusible dispersions containing drops of a superheated liquid for methods of therapy and diagnosis." United States Patent n°5,840,276, November 1998.
- [119] P. A. Mountford and M. A. Borden, "On the thermodynamics and kinetics of superheated fluorocarbon phase-change agents," *Advances in Colloid and Interface Science*, vol. 237, pp. 15–27, 2016.
- [120] R. E. Apfel, "A novel technique for measuring the strength of liquids," *The Journal of the Acoustical Society of America*, vol. 49, no. 1, pp. 145–155, 1971.
- [121] M. Blander and J. L. Katz, "Bubble nucleation in liquids," *American Institute of Chemical Engineers Journal*, pp. 833–848, September 1975.
- [122] P. S. Sheeran, K. Yoo, R. Williams, M. Yin, F. S. Foster, and P. N. Burns, "More than bubbles: creating phase-shift droplets from commercially available ultrasound contrast agents," *Ultrasound in Medicine and Biology*, vol. 43, no. 2, pp. 531–540, 2017.
- [123] P. A. Mountford, A. N. Thomas, and M. A. Borden, "Thermal activation of superheated lipid-coated perfluorocarbon drops," *Langmuir*, vol. 31, no. 4627–4634, 2015.
- [124] B. Carlier, S. V. Heymans, S. Nooijens, Y. Toumia, M. Ingram, G. Paradossi, E. d'Agostino, U. Himmelreich, J. D'hooge, K. Van Den Abeele, and E. Sterpin, "Proton range verification with ultrasound imaging using injectable radiation sensitive nanodroplets: A feasibility study," *Physics in Medicine and Biology*, vol. 65, p. 065013, March 2020.
- [125] O. D. Kripfgans, M. L. Fabilli, P. L. Carson, and J. B. Fowlkes, "On the acoustic vaporization of micrometer-sized droplets," *The Journal of the Acoustical Society of America*, vol. 116, no. 1, pp. 272–281, 2004.
- [126] Q. Wu, C. Mannaris, J. P. May, L. Bau, A. Polydorou, S. Ferri, D. Carugo, N. D. Evans, and E. Stride, "Investigation of the acoustic vaporization threshold of lipid-coated perfluorobutane nanodroplets using both high-speed optical imaging and acoustic methods," *Ultrasound in Medicine and Biology*, vol. 47, no. 7, pp. 1826–1843, 2021.
- [127] V. P. Carey, *Liquid-Vapor Phase-Change Phenomena*. Taylor & Francis Group, second ed., 2008.
- [128] J. H. Lienhard, "The properties and behavior of superheated liquids," *Lat. Am. J. Heat Mass transf.*, vol. 10, pp. 169–187, 1986.
- [129] D. C. Johnston, "Thermodynamic properties of the van der Waals fluid." arXiv preprint, 2014.
- [130] W. Demtröder, *Mechanics and Thermodynamics*. Undergraduate Lecture Notes in Physics, Switzerland: Springer International Publishing, 2017.
- [131] J. Lekner, "Parametric solution of the van der Waals liquid-vapor coexistence curve," *American Journal of Physics*, vol. 50, pp. 161–163, February 1982.
- [132] J. H. Lienhard, N. Shamsundar, and P. O. Biney, "Spinodal lines and equations of state: a review," *Nuclear Engineering and Design*, vol. 95, pp. 297–314, 1986.
- [133] P. Atkins and J. de Paula, *Atkins' Physical Chemistry*. New York, USA: W.H. Freeman and Company, eighth ed., 2006.
- [134] J. G. Eberhart, "The many faces of van der Waals's equation of state," *Journal of Chemical Education*, vol. 66, pp. 906–909, 1989.

- [135] J. Eberhart and H. Schnyders, "Application of the mechanical stability condition to the prediction of the limit of superheat for normal alkanes, ether, and water," *The Journal of Physical Chemistry*, vol. 77, no. 23, pp. 2730–2736, 1973.
- [136] P. Linstrom and E. W.G. Mallard, eds., *NIST Chemistry WebBook, NIST Standard Reference Database Number 69*. Gaithersburg MD, 20899: National Institute of Standards and Technology, Retrieved May 15, 2020. <https://doi.org/10.18434/T4D303>.
- [137] The Mathworks, Inc., "Matlab." The Mathworks, Inc., 2019. R2019a.
- [138] D. R. Schreiber and K. S. Pitzer, "Equation of state in the acentric factor system," *Fluid Phase Equilibria*, vol. 46, pp. 113–130, 1989.
- [139] V. P. Skripov, *Metastable Liquids*. John Wiley & Sons, 1974.
- [140] C. Avedisian, "Effect of pressure on bubble growth within liquid droplets at the superheat limit," *Journal of Heat Transfer*, vol. 104, pp. 750–757, 1982.
- [141] J. Lienhard and A. Karimi, "Homogeneous nucleation and the spinodal line," *Journal of Heat Transfer*, vol. 103, pp. 61–64, February 1981.
- [142] C. Avedisian, "The homogeneous nucleation limit of liquids," *Journal of Physical and Chemical Reference Data*, vol. 14, no. 3, pp. 695–729, 1985.
- [143] C. D. West, "Cavitation bubble nucleation by energetic particles," Tech. Rep. ORNL/TM-13683, Oak Ridge National Laboratory, 1998.
- [144] A. G. Tenner, "Nucleation in bubble chambers," *Nuclear Instruments and Methods*, vol. 22, pp. 1–42, 1963.
- [145] A. Norman and P. Spiegler, "Radiation nucleation of bubbles in water," *Nuclear Science and Engineering*, vol. 16, pp. 213–217, 1963.
- [146] H. Ing, R. A. Noulty, and T. D. McLean, "Bubble detectors - a maturing technology," *Radiation measurements*, vol. 27, no. 1, pp. 1–11, 1997.
- [147] R. E. Apfel, "The superheated drop detector," *Nuclear Instruments and Methods*, vol. 162, pp. 603–608, 1979.
- [148] F. D'Errico, R. E. Apfel, G. Curzio, E. Dietz, E. Egger, G. F. Gualdrini, S. Guldbakke, R. Nath, and B. R. L. Siebert, "Superheated emulsions: neutronics and thermodynamics," *Radiation Protection Dosimetry*, vol. 70, no. 1-4, pp. 109–112, 1997.
- [149] A. R. Green, H. R. Andrews, L. G. I. Bennett, E. T. H. Clifford, H. Ing, G. Jonkmans, B. J. Lewis, R. A. Noulty, and E. A. Ough, "Bubble detector characterization for space radiation," *Acta Astronautica*, vol. 56, pp. 949–960, 2005.
- [150] H. R. Andrews, R. A. Noulty, H. Ing, F. d'Errico, B. J. Lewis, L. G. I. Bennett, and A. R. Green, "LET dependence of bubble detector response to heavy ions," *Radiation Protection Dosimetry*, vol. 120, no. 1-4, pp. 480–484, 2006.
- [151] S. Archambault, F. Aubin, M. Auger, M. Beleshi, E. Behnke, J. Behnke, B. Beltran, K. Clark, X. Dai, M. Das, A. Davour, F. Debris, J. Farine, M.-H. Genest, G. Giroux, R. Gornea, R. Faust, H. Hinnefeld, A. Kamaha, C. Krauss, M. Lafrenière, M. Laurin, I. Lawson, C. Leroy, C. Lévy, L. Lessard, I. Levine, J.-P. Martin, S. Kumaratunga, R. MacDonald, P. Nadeau, A. Noble, M.-C. Piro, S. Pospisil, N. Starinski, I. Stekl, N. V. Werf, U. Wichoski, and V. Zacek, "New insights into particle detection with superheated liquids," *New Journal of Physics*, vol. 13, no. 043006, p. 25, 2011.
- [152] S.-L. Guo, L. Li, B.-L. Chen, T. Doke, J. Kikuchi, K. Terasawa, M. Komiyama, K. Hara, and T. Fuse, "Proton tracks in bubble detector," *Nuclear Instruments and Methods in Physics Research B*, vol. 198, pp. 135–141, 2002.
- [153] F. D'Errico, R. Nath, and R. Nolte, "A model for photon detection and dosimetry with superheated emulsions," *Medical Physics*, vol. 27, no. 2, pp. 401–409, 2000.

- [154] F. D'Errico, "Fundamental properties of superheated drop (bubble) detectors," *Radiation Protection Dosimetry*, vol. 84, no. 1-4, pp. 55–62, 1999.
- [155] S. C. Roy, "Superheated liquid and its place in radiation physics," *Radiation Physics and Chemistry*, vol. 61, no. 271-281, 2001.
- [156] A. A. Doinikov and A. Bouakaz, "Review of shell models for contrast agent microbubbles," *IEEE Transactions on Ultrasonics, Ferroelectrics, and Frequency Control*, vol. 58, no. 5, pp. 981–993, 2011.
- [157] M. Versluis, E. Stride, G. Lajoinie, B. Dollet, and T. Segers, "Ultrasound contrast agent modeling: A review," *Ultrasound in Medicine and Biology*, vol. 46, no. 9, pp. 2117–2144, 2020.
- [158] P. Marmottant, S. van der Meer, M. Emmer, and M. Versluis, "A model for large amplitude oscillations of coated bubbles accounting for buckling and rupture," *The Journal of the Acoustical Society of America*, vol. 118, no. 6, pp. 3499–3505, 2005.
- [159] C. C. Church, "The effects of an elastic solid surface layer on the radial pulsations of gas bubbles," *The Journal of the Acoustical Society of America*, vol. 97, pp. 1510–1521, 1995.
- [160] T. Leighton, *The acoustic bubble*. Academic Press, Harcourt Brace & Company, Publishers, 1994.
- [161] F. Brau and G. Kozyreff, "Mécanique des milieux continus." Online: <https://www2.ulb.ac.be/sciences/nlpc/documents/Math-F426-2021-01-26.pdf>, University Libre de Bruxelles, Belgium, 2019.
- [162] D. Grishenkov, C. Pecorari, T. B. Brismar, and G. Paradossi, "Characterization of acoustic properties of PVA-shelled ultrasound contrast agents: linear properties (part I)," *Ultrasound in Medicine and Biology*, vol. 35, no. 7, pp. 1127–1138, 2009.
- [163] M. Poehlmann, D. Grishenkov, S. V. V. N. Kothapalli, J. Härmak, H. Hebert, A. Philipp, R. Hoeller, M. Seuss, C. Kuttner, S. Margheritelli, and G. Paradossi, "On the interplay of shell structure with low- and high-frequency mechanics of multifunctional magnetic microbubbles," *Soft Matter*, vol. 10, no. 1, pp. 214–226, 2014.
- [164] D. Grishenkov, C. Pecorari, T. B. Brismar, and G. Paradossi, "Characterization of acoustic properties of PVA-shelled ultrasound contrast agents: ultrasound-induced fracture (part II)," *Ultrasound in Medicine and Biology*, vol. 35, no. 7, pp. 1139–1147, 2009.
- [165] S. M. van der Meer, B. Dollet, M. M. Voormolen, C. T. Chin, A. Bouakaz, N. de Jong, M. Versluis, and D. Lohse, "Microbubble spectroscopy of ultrasound contrast agents," *The Journal of the Acoustical Society of America*, vol. 121, no. 1, pp. 648–656, 2007.
- [166] M. Overvelde, V. Garbin, J. Sijl, B. Dollet, N. de Jong, D. Lohse, and M. Versluis, "Nonlinear shell behavior of phospholipid-coated microbubbles," *Ultrasound in Medicine and Biology*, vol. 36, no. 12, pp. 2080–2092, 2010.
- [167] J. Sijl, B. Dollet, M. Overvelde, V. Garbin, T. Rozendael, N. de Jong, D. Lohse, and M. Versluis, "Subharmonic behavior of phospholipid-coated ultrasound contrast agent microbubbles," *The Journal of the Acoustical Society of America*, vol. 128, no. 5, pp. 3239–3252, 2010.
- [168] J. S. Lum, J. D. Dove, T. W. Murray, and M. A. Borden, "Single microbubble measurements of lipid monolayer viscoelastic properties for small-amplitude oscillations," *Langmuir*, vol. 32, pp. 9410–9417, 2016.
- [169] T. Segers, N. de Jong, and M. Versluis, "Uniform scattering and attenuation of acoustically sorted ultrasound contrast agents: Modeling and experiments," *The Journal of the Acoustical Society of America*, vol. 140, no. 4, pp. 2506–2517, 2016.

- [170] M. M. Nguyen, S. Zhou, J.-L. Robert, V. Shamdasani, and H. Xie, "Development of oil-in-gelatin phantoms for viscoelasticity measurement in ultrasound shear wave elastography," *Ultrasound in Medicine and Biology*, vol. 40, no. 1, pp. 168–176, 2014.
- [171] R. Apfel, "The tensile strength of liquids," *Scientific American*, pp. 58–71, 1972.
- [172] O. Shpak, M. Verweij, H. J. Vos, N. de Jong, D. Lohse, and M. Versluis, "Acoustic droplet vaporization is initiated by superharmonic focusing," *Proceedings of the National Academy of Sciences of the United States of America*, vol. 111, no. 5, pp. 1697–1702, 2014.
- [173] G. Lajoinie, T. Segers, and M. Versluis, "High-frequency acoustic droplet vaporization is initiated by resonance," *Physical Review Letters*, vol. 126, no. 3, p. 034501, 2021.
- [174] G. Soave, "Equilibrium constants from a modified Redlich-Kwong equation of state," *Chemical Engineering Science*, vol. 27, no. 6, pp. 1197–1203, 1972.
- [175] S. Velasco, M. Santos, and J. White, "Extended corresponding states expressions for the changes in enthalpy, compressibility factor and constant-volume heat capacity at vaporization," *Journal of Chemical Thermodynamics*, vol. 85, pp. 68–76, 2015.
- [176] J. Owen and E. Stride, "Technique for the characterization of phospholipid microbubbles coatings by Transmission Electron Microscopy," *Ultrasound in Medicine and Biology*, vol. 41, no. 12, pp. 3253–3258, 2015.
- [177] V. Sboros, E. Glynos, S. D. Pye, C. M. Moran, M. Butler, J. Ross, R. Short, W. N. McDicken, and V. Koutsos, "Nanointerrogation of ultrasonic contrast agent microbubbles using Atomic Force Microscopy," *Ultrasound in Medicine and Biology*, vol. 32, no. 4, pp. 579–585, 2006.
- [178] E. B. Santos, J. K. Morris, E. Glynos, V. Sboros, , and V. Koutsos, "Nanomechanical properties of phospholipid microbubbles," *Langmuir*, vol. 28, pp. 5753–5760, 2012.
- [179] E. Glynos, V. Koutsos, W. N. McDicken, C. M. Moran, S. D. Pye, J. A. Ross, and V. Sboros, "Nanomechanics of biocompatible hollow thin-shell polymer microspheres," *Langmuir*, vol. 25, no. 13, pp. 7514–7522, 2009.
- [180] N. A. Hosny, G. Mohamedi, P. Rademeyer, J. Owen, Y. Wu, M.-X. Tang, R. J. Eckersley, E. Stride, and M. K. Kuimova, "Mapping microbubble viscosity using fluorescence lifetime imaging of molecular rotors," *Proceedings of the National Academy of Sciences of the United States of America*, vol. 110, no. 23, pp. 9225–9230, 2013.
- [181] A.-C. Knopf and A. Lomax, "In vivo proton range verification: a review," *Physics in Medicine & Biology*, vol. 58, pp. 131–160, 2013.
- [182] K. Parodi, H. Paganetti, E. Cascio, and J. B. Flanz, "PET/CT imaging for treatment verification after proton therapy: a study with plastic phantoms and metallic implants," *Medical Physics*, vol. 34, no. 2, pp. 419–435, 2007.
- [183] A. C. Kraan, G. Battistoni, N. Belcari, N. Camarlinghi, G. A. P. Cirrone, G. Cuttone, S. Ferretti, A. Ferrari, G. Pirrone, F. Romano, P. Sala, G. Sportelli, K. Straub, A. Tramonta, A. D. Guerra, and V. Rosso, "Proton range monitoring with in-beam PET: Monte Carlo activity predictions and comparison with cyclotron data," *Physica Medica*, vol. 30, pp. 559–569, 2014.
- [184] C.-H. Min, C. H. Kim, M.-Y. Youn, and J.-W. Kim, "Prompt gamma measurements for locating the dose falloff region in the proton therapy," *Applied Physics Letters*, vol. 89, no. 18, pp. 2–5, 2006.
- [185] H. Rohling, M. Priegnitz, S. Schoene, A. Schumann, W. Enghardt, F. Hueso-Gonzalez, G. Pausch, and F. Fiedler, "Requirements for a Compton camera for in vivo range verification of proton therapy," *Physics in Medicine & Biology*, vol. 62, no. 2795, 2017.

- [186] M. Mumot, C. Algranati, M. Hartmann, J. M. Schippers, E. Hug, and A. J. Lomax, "Proton range verification using a range probe: Definition of concept and initial analysis," *Physics in Medicine & Biology*, vol. 55, pp. 4771–4782, 2010.
- [187] T. Plautz, V. Bashkurov, V. Feng, F. Hurley, R. P. Johnson, C. Leary, S. Macafee, A. Plumb, V. Rykalin, H. F.-W. Sadrozinski, K. Schubert, R. Schulte, B. Schultze, D. Steinberg, M. Witt, and A. Zatserkmyaniy, "200 MeV proton radiography studies with a hand phantom using a prototype proton CT scanner," *IEEE Transactions on Medical Imaging*, vol. 33, no. 4, pp. 875–881, 2014.
- [188] R. Sarkar, B. K. Chatterjee, B. Roy, and S. C. Roy, "Radiation detection by using superheated droplets," *Radiation Physics and Chemistry*, vol. 75, no. 12, pp. 2186–2194, 2006.
- [189] N. Deshpande, A. Needles, and J. Willmann, "Molecular ultrasound imaging: current status and future directions," *Clinical radiology*, vol. 65, no. 7, pp. 567–581, 2010.
- [190] P. S. Sheeran, S. Luo, P. A. Dayton, and T. O. Matsunaga, "Formulation and acoustic studies of a new phase-shift agent for diagnostic and therapeutic ultrasound," *Langmuir*, vol. 27, no. 17, pp. 10412–10420, 2011.
- [191] W. Porteous and M. Blander, "Limits of superheat and explosive boiling of light hydrocarbons, halocarbons, and hydrocarbon mixtures," *AIChE*, vol. 21, pp. 560–566, 1975.
- [192] M. Takada, H. Kitamura, T. Koi, T. Nakamura, and K. Fujikata, "Measured proton sensitivities of bubble detectors," *Radiation Protection Dosimetry*, vol. 111, no. 2, pp. 181–189, 2004.
- [193] M. O. Culjat, D. Goldenberg, P. Tewari, and R. S. Singh, "A review of tissue substitutes for ultrasound imaging," *Ultrasound in Medicine and Biology*, vol. 36, no. 6, pp. 861–873, 2010.
- [194] T. Bortfeld, "An analytical approximation of the Bragg curve for therapeutic proton beams," *Medical Physics*, vol. 24, no. 12, pp. 2024–2033, 1997.
- [195] G. Zhang, S. Harput, S. Lin, K. Christensen-Jeffries, C. H. Leow, J. Brown, C. Dunsby, R. J. Eckersley, and M.-X. Tang, "Acoustic wave sparsely activated localization microscopy (AWSALM): Super-resolution ultrasound imaging using acoustic activation and deactivation of nanodroplets," *Applied Physics Letters*, vol. 113, no. 014101, 2018.
- [196] C. Grassberger and H. Paganetti, "Elevated LET components in clinical proton beams," *Physics in Medicine & Biology*, vol. 56, pp. 6677–6691, 2011.
- [197] A. Koning, D. Rochman, S. C. van der Marck, J. Kopecky, J. C. Sublet, S. Pomp, H. Sjostrand, R. Forrest, E. Bauge, and H. Henriksson, "TENDL-2014: TALYS-based evaluated nuclear data library." Database available from: <http://www.talys.eu/tendl-2012>, 2014.
- [198] M. J. Berger, J. S. Coursey, M. A. Zucker, and J. Chang, "ESTAR, PSTAR and ASTAR: Computer programs for calculating stopping-power and range tables for electrons, protons and helium ions (version 2.0.1)." National Institute of Standards and Technology, Gaithersburg, MD., 2005.
- [199] S. M. Seltzer, "An assessment of the role of charged secondaries from nonelastic nuclear interactions by therapy proton beams in water," tech. rep., National Institute of Standards and Technology Report, Gaithersburg, MD 20899, July 1993.
- [200] International Commission on Radiation Units & Measurements, "Nuclear data for neutron and proton radiotherapy and for radiation protection," Report 63, ICRU, Bethesda, MD, 2000.
- [201] J. F. Ziegler, "SRIM-2013 software package." available at <http://www.srim.org>, 2013.

- [202] E. Unger and T. O. Matsunaga, *Handbook of Materials for Nanomedicine*, ch. Lipid Coated Microbubbles and Nanodroplets as Tools for Biomedical Nanotechnology, p. 38. Jenny Stanford Publishing, 1st ed., 2011.
- [203] M. Durante and H. Paganetti, “Nuclear physics in particle therapy: A review,” *Reports on Progress in Physics*, vol. 79, no. 9, p. 096702, 2016.
- [204] P. S. Sheeran, N. Matsuura, M. A. Borden, R. Williams, T. O. Matsunaga, P. N. Burns, and P. A. Dayton, “Methods of generating submicrometer phase-shift perfluorocarbon droplets for applications in medical ultrasonography,” *IEEE Transactions on Ultrasonics, Ferroelectrics and Frequency Control*, vol. 64, no. 1, pp. 252–263, 2017.
- [205] M. Moteabbed, S. España, and H. Paganetti, “Monte Carlo patient study on the comparison of prompt gamma and PET imaging for range verification in proton therapy,” *Physics in Medicine & Biology*, vol. 56, no. 4, pp. 1063–1082, 2011.
- [206] J. C. Polf and K. Parodi, “Imaging particle beams for cancer treatment,” *Physics Today*, vol. 68, no. 10, pp. 28–33, 2015.
- [207] S. España, X. Zhu, J. Daartz, G. E. Fakhri, T. Bortfeld, and H. Paganetti, “The reliability of proton-nuclear interaction cross-section data to predict proton-induced PET images in proton therapy,” *Physics in Medicine & Biology*, vol. 56, no. 9, pp. 2687–2698, 2011.
- [208] K. C. Jones, W. Nie, J. C. H. Chu, J. V. Turian, A. Kassaei, C. M. Sehgal, and S. Avery, “Acoustic-based proton range verification in heterogeneous tissue: simulation studies,” *Physics in Medicine & Biology*, vol. 63, no. 025018, 2018.
- [209] K. C. Jones, F. V. Stappen, C. R. Bawiec, G. Janssens, P. A. Lewin, D. Prieels, T. D. Solberg, C. M. Sehgal, and S. Avery, “Experimental observation of acoustic emissions generated by a pulsed proton beam from a hospital-based clinical cyclotron,” *Medical Physics*, vol. 42, no. 12, pp. 7090–7097, 2015.
- [210] S. K. Patch, M. K. Covo, A. Jackson, Y. M. Qadadha, K. S. Campbell, R. A. Albright, P. Bloemhard, A. P. Donoghue, C. R. Siero, T. L. Gimpel, S. M. Small, B. F. Ninemire, M. B. Johnson, and L. Phair, “Thermoacoustic range verification using a clinical ultrasound array provides perfectly co-registered overlay of the Bragg peak onto an ultrasound image,” *Physics in Medicine & Biology*, vol. 61, pp. 5621–5638, 2016.
- [211] S. Kellnberger, W. Assmann, S. Lehrack, S. Reinhardt, P. Thirolf, D. Queirós, G. Sergiadis, G. Dollinger, K. Parodi, and V. Ntziachristos, “Ionoacoustic tomography of the proton Bragg peak in combination with ultrasound and optoacoustic imaging,” *Scientific Reports*, vol. 6, no. 29305, 2016.
- [212] M. F. Gensheimer, T. I. Yock, N. J. Liebsch, G. C. Sharp, H. Paganetti, N. Madan, P. E. Grant, and T. Bortfeld, “In vivo proton beam range verification using spine MRI changes,” *International Journal of Radiation Oncology Biology Physics*, vol. 78, no. 1, pp. 268–275, 2010.
- [213] Y. Yuan, O. C. Andronesi, T. R. Bortfeld, C. Richter, R. Wolf, A. R. Guimaraes, T. S. Hong, and J. Seco, “Feasibility study of in vivo MRI based dosimetric verification of proton end-of-range for liver cancer patients,” *Radiotherapy and Oncology*, vol. 106, no. 3, pp. 378–382, 2013.
- [214] F. d’Errico, “Status of radiation detection with superheated emulsions,” *Radiation Protection Dosimetry*, vol. 120, no. 1-4, pp. 475–479, 2006.
- [215] P. S. Sheeran, Y. Daghighi, K. Yoo, R. Williams, E. Cherin, F. S. Foster, and P. N. Burns, “Image-guided ultrasound characterization of volatile sub-micron phase-shift droplets in the 20–40 MHz frequency range,” *Ultrasound in Medicine and Biology*, vol. 42, no. 3, pp. 795–807, 2016.

- [216] N. Reznik, R. Williams, and P. N. Burns, "Investigation of vaporized submicron perfluorocarbon droplets as an ultrasound contrast agent," *Ultrasound in Medicine & Biology*, vol. 37, no. 8, pp. 1271–1279, 2011.
- [217] W. Crijns, F. Maes, U. A. van der Heide, and F. Van den Heuvel, "Calibrating page sized Gafchromic EBT3 films," *Medical Physics*, vol. 40, no. 1, p. 012102, 2013.
- [218] F. Fiorini, D. Kirby, J. Thompson, S. Green, D. J. Parker, B. Jones, and M. A. Hill, "Under-response correction for EBT3 films in the presence of proton spread out Bragg peaks," *Physica Medica*, vol. 30, no. 4, pp. 454–461, 2014.
- [219] K. Soetanto and M. Chan, "Fundamental studies on contrast images from different-sized microbubbles: analytical and experimental studies," *Ultrasound in Medicine & Biology*, vol. 26, no. 1, pp. 81–91, 2000.
- [220] A. L. Klibanov, "Targeted delivery of gas-filled microspheres, contrast agents for ultrasound imaging," *Advanced Drug Delivery Reviews*, vol. 37, pp. 139–157, 1999.
- [221] J. N. Marsh, M. S. Hughes, C. S. Hall, S. H. Lewis, R. L. Trousil, G. H. Brandenburger, H. Levene, and J. G. Miller, "Frequency and concentration dependence of the backscatter coefficient of the ultrasound contrast agent Albutex®," *The Journal of the Acoustical Society of America*, vol. 104, no. 3, pp. 1654–1666, 1998.
- [222] A. Muraleedharan, A. Bertrand, and J. D'hooge, "A linear least squares based estimation of spatial variation of the attenuation coefficient from ultrasound backscatter signals," in *Proceedings of Meetings on Acoustics* (T. A. S. of America, ed.), vol. 38, International Conference on Ultrasonics, 3-6 September 2019.
- [223] P. Kruizinga, F. Mastik, N. de Jong, A. F. W. van der Steen, and G. van Soest, "Plane-wave ultrasound beamforming using a nonuniform fast Fourier transform," *IEEE Transactions on Ultrasonics, Ferroelectrics, and Frequency Control*, vol. 59, no. 12, pp. 2684–2691, 2012.
- [224] N. de Jong, M. Emmer, A. van Wamel, and M. Versluis, "Ultrasonic characterization of ultrasound contrast agents," *Medical and Biological Engineering and Computing*, vol. 47, pp. 861–873, 2009.
- [225] N. de Jong and L. Hoff, "Ultrasound scattering properties of Albutex microspheres," *Ultrasonics*, vol. 31, no. 3, pp. 175–181, 1993.
- [226] T. G. Leighton, *The Acoustic Bubble*. San Diego, CA, USA: Academic Press Inc., 1994.
- [227] L. Hoff, P. C. Sontum, and J. M. Hovem, "Oscillations of polymeric microbubbles: Effect of the encapsulating shell," *The Journal of the Acoustical Society of America*, vol. 107, no. 4, pp. 2272–2280, 2000.
- [228] J. L. Raymond, K. J. Haworth, K. B. Bader, K. Radhakrishnan, J. K. Griffin, S.-L. Huang, D. D. McPherson, and C. K. Holland, "Broadband attenuation measurements of phospholipid-shelled ultrasound contrast agents," *Ultrasound in Medicine & Biology*, vol. 40, no. 2, pp. 410–421, 2014.
- [229] G. Montaldo, M. Tanter, J. Bercoff, N. Benech, and M. Fink, "Coherent plane-wave compounding for very high frame rate ultrasonography and transient elastography," *IEEE Transactions on Ultrasonics, Ferroelectrics, and Frequency Control*, vol. 56, no. 3, pp. 489–506, 2009.
- [230] M. Haji-Saeid, M. R. A. Pillai, T. J. Ruth, D. J. Schlyer, P. Van den Winkel, M. M. Vora, R. N. Capote, L. Carroll, J. C. Clark, J. Comor, M. Dehnel, R. Ferrieri, R. D. Finn, J. S. Fowler, M. J. Schueller, and F. Tárkányi, "Cyclotron produced radionuclides: Physical characteristics and production methods," Tech. Rep. Technical Reports Series no.468, International Atomic Energy Agency, Vienna, Austria, 2009.

- [231] J. V. Jokerst, T. Lobovkina, R. N. Zare, and R. S. Gambhir, "Nanoparticle pegylation for imaging and therapy," *Nanomedicine*, vol. 6, no. 4, pp. 715–728, 2011.
- [232] Y. Cao, Y. Chen, T. Yu, Y. Guo, F. Liu, Y. Yao, P. Li, D. Wang, Z. Wang, Y. Chen, and H. Ran, "Drug release from phase-changeable nanodroplets triggered by low-intensity focused ultrasound," *Theranostics*, vol. 8, no. 5, pp. 1327–1339, 2018.
- [233] Y. Desailly, O. Couture, M. Fink, and M. Tanter, "Sono-activated ultrasound localization microscopy," *Applied Physics Letters*, vol. 103, no. 174107, 2013.
- [234] P. S. Sheeran, T. O. Matsunaga, and P. A. Dayton, "Phase change events of volatile liquid perfluorocarbon contrast agents produce unique acoustic signatures," *Physics in Medicine and Biology*, vol. 59, no. 2, pp. 379–401, 2014.
- [235] K. Christensen-Jeffries, O. Couture, P. A. Dayton, Y. C. Eldar, K. Hynynen, F. Kiessling, M. O'Reilly, G. F. Pinton, G. Schmitz, M.-X. Tang, M. Tanter, and R. J. Van Sloun, "Super-resolution ultrasound imaging," *Ultrasound in Medicine and Biology*, vol. 46, no. 4, pp. 865–891, 2020.
- [236] B. Cerroni, R. Cicconi, L. Oddo, M. Scimeca, R. Bonfiglio, R. Bernardini, G. Palmieri, F. Domenici, E. Bonanno, M. Mattei, and G. Paradossi, "In vivo biological fate of poly(vinylalcohol) microbubbles in mice," *Heliyon*, vol. 4, no. e00770, 2018.
- [237] W. Assmann, S. Kellnberger, S. Reinhardt, S. Lehrack, A. Edlich, P. G. Thirolf, M. Moser, G. Dollinger, M. Omar, V. Ntziachristos, and K. Parodi, "Ionoacoustic characterization of the proton Bragg peak with submillimeter accuracy," *Medical Physics*, vol. 42, no. 2, pp. 567–574, 2015.
- [238] G. Shakya, S. E. Hoff, S. Wang, H. Heinz, X. Ding, and M. A. Borden, "Vaporizable endoskeletal droplets via tunable interfacial melting transitions," *Science Advances*, vol. 6, no. 14, p. eaaz7188, 2020.
- [239] C. Grau, M. Durante, D. Georg, J. A. Langendijk, and D. C. Weber, "Particle therapy in Europe," *Molecular Oncology*, vol. 14, pp. 1492–1499, 2020.
- [240] T. Kubiak, "Particle therapy of moving targets - the strategies for tumour motion monitoring and moving targets irradiation," *British Journal of Radiology*, vol. 89, no. 20150275, 2016.
- [241] A. Meijers, O. C. Seller, J. Free, D. Bondesson, C. S. Oria, M. Rabe, K. Parodi, G. Landry, J. A. Langendijk, S. Both, C. Kurz, and A. C. Knopf, "Assessment of range uncertainty in lung-like tissue using a porcine lung phantom and proton radiography," *Physics in Medicine & Biology*, vol. 65, no. 155014, 2020.
- [242] A. Raldow, J. Lamb, and T. Hong, "Proton beam therapy for tumors of the upper abdomen," *British Journal of Radiology*, vol. 93, no. 20190226, 2020.
- [243] J. Shimizu, R. Endoh, T. Fukuda, T. Inagaki, H. Hano, R. Asami, K. ichi Kawabata, M. Yokoyama, and H. Furuhashi, "Safety evaluation of superheated perfluorocarbon nanodroplets for novel phase change type neurological therapeutic agents," *Perspectives in Medicine*, vol. 1, pp. 25–29, 2012.
- [244] S. V. Heymans, B. Carlier, Y. Tournia, S. Nooijens, M. Ingram, A. Giammanco, E. d'Agostino, W. Crijns, A. Bertrand, G. Paradossi, U. Himmelreich, J. D'hooge, E. Sterpin, and K. Van Den Abele, "Modulating ultrasound contrast generation from injectable nanodroplets for proton range verification by varying the degree of superheat," *Medical Physics*, vol. 48, no. 4, 2021.
- [245] A. M. V. Putz and T. I. Burghelca, "The solid-fluid transition in a yield stress shear thinning physical gel," *Rheologica Acta*, vol. 48, pp. 673–689, 2009.
- [246] T. Brunet, S. Raffy, B. Mascaro, J. Leng, R. Wunenberger, O. Mondain-Monval, O. Poncelet, and C. Aristégui, "Sharp acoustic multipolar-resonances in highly monodisperse emulsions," *Applied Physics Letters*, vol. 101, no. 011913, 2012.

- [247] R. Zhang and W. D. Newhauser, "Calculation of water equivalent thickness of materials of arbitrary density, elemental composition and thickness in proton beam irradiation," *Physics in Medicine and Biology*, vol. 54, no. 6, pp. 1383–1395, 2009.
- [248] B. Gottschalk, A. M. Koehler, R. J. Schneider, J. M. Sisterston, and M. S. Wagner, "Multiple Coulomb scattering of 160 MeV protons," *Nuclear Instruments and Methods in Physics Research B*, vol. 74, pp. 467–490, 1993.
- [249] P. S. Sheeran, V. P. Wong, R. J. McFarland, W. D. Ross, S. G. Feingold, T. O. Matsunaga, and P. A. Dayton, "Efficacy of perfluorobutane as a phase-change contrast agent for low-energy ultrasonic imaging," in *2010 IEEE International Ultrasonics Symposium Proceedings*, pp. 904–907, 11–14 October 2010.
- [250] V. Hingot, M. Bézagu, C. Errico, Y. Desailly, R. Bocheux, M. Tanter, and O. Couture, "Subwavelength far-field ultrasound drug-delivery," *Applied Physics Letters*, vol. 109, no. 194102, 2016.
- [251] R. S. C. Cobbold, *Foundations of Biomedical Ultrasound*. Oxford University Press, 2007.
- [252] A. Ramalli, A. Dallai, F. Guidi, L. Bassi, E. Boni, L. Tong, G. Fradella, J. D'hooge, and P. Tortoli, "Real-time high frame rate cardiac B-mode and tissue Doppler imaging based on multiline transmission and multiline acquisition," *IEEE Transactions on Ultrasonics, Ferroelectrics, and Frequency Control*, vol. 65, no. 11, pp. 2030–2041, 2018.
- [253] A. Ramalli, S. Harput, S. Bézy, E. Boni, R. J. Eckersley, P. Tortoli, and J. D'hooge, "High-frame-rate tri-plane echocardiography with spiral arrays: From simulation to real-time implementation," *IEEE Transactions on Ultrasonics, Ferroelectrics, and Frequency Control*, vol. 67, no. 1, pp. 57–69, 2020.
- [254] C. Bert, S. O. Grözinger, and E. Rietzel, "Quantification of interplay effects of scanned particle beams and moving targets," *Physics in Medicine and Biology*, vol. 53, pp. 2253–2265, 2008.
- [255] K. Dolde, Y. Zhang, N. Chaudhri, C. David, M. Kachelrieß, A. J. Lomax, P. Naumann, N. Saito, D. C. Weber, and A. Pfaffenberger, "4DMRI-based investigation of the interplay effect for pencil beam scanning proton therapy of pancreatic cancer patients," *Radiation Oncology*, vol. 14, no. 30, 2019.
- [256] G. Collado-Lara, S. V. Heymans, M. Rovituso, B. Carlier, Y. Toumia, M. Verweij, G. Paradossi, E. Sterpin, H. J. Vos, J. D'hooge, N. de Jong, K. Van Den Abeele, and V. Daeichin, "Spatiotemporal distribution of nanodroplet vaporization in a proton beam using real-time ultrasound imaging for range verification," *Ultrasound in Medicine and Biology*, 2021.
- [257] O. Couture, B. Besson, G. Montaldo, M. Fink, and M. Tanter, "Microbubble ultrasound super-localization imaging (MUSLI)," in *2011 IEEE International Ultrasonics Symposium Proceedings*, pp. 1285–1287, 2011.
- [258] M. A. O'Reilly and K. Hynynen, "A super-resolution ultrasound method for brain vascular mapping," *Medical Physics*, vol. 40, no. 11, pp. 1–7, 2013.
- [259] O. Couture, V. Hingot, B. Heiles, P. Muleki-Seya, and M. Tanter, "Ultrasound Localization Microscopy and super-resolution: A state of the art," *IEEE Transactions on Ultrasonics, Ferroelectrics, and Frequency Control*, vol. 65, no. 8, pp. 1304–1320, 2018.
- [260] G. Zhang, S. Harput, H. Hu, K. Christensen-Jeffries, J. Zhu, J. Brown, C. H. Leow, R. J. Eckersley, C. Dunsby, and M.-X. Tang, "Fast Acoustic Wave Sparsely Activated Localization Microscopy: Ultrasound super-resolution using plane-wave activation of nanodroplets," *IEEE Transactions on Ultrasonics, Ferroelectrics, and Frequency Control*, vol. 66, no. 6, pp. 1039–1046, 2019.

- [261] G. P. Luke, A. S. Hannah, and S. Y. Emelianov, "Super-resolution ultrasound imaging in vivo with transient laser-activated nanodroplets," *Nano Letters*, vol. 16, no. 4, pp. 2256–2259, 2016.
- [262] R. M. DeRuiter, E. N. Markley, J. D. Rojas, G. F. Pinton, and P. A. Dayton, "Using low-boiling point phase change contrast agent activation signals for super resolution Ultrasound Localization Microscopy," in *2019 IEEE International Ultrasonics Symposium Proceedings*, (Glasgow, Scotland), pp. 1934–1936, October 6-9 2019.
- [263] R. M. DeRuiter, E. N. Markley, J. D. Rojas, G. F. Pinton, and P. A. Dayton, "Transient acoustic vaporization signatures unique to low boiling point phase change contrast agents enable super-resolution ultrasound imaging without spatiotemporal filtering," *AIP Advances*, vol. 10, no. 105124, 2020.
- [264] G. Zhang, S. Harput, A. Shah, J. Hernández-Gil, J. Zhu, K. Christensen-Jeffries, J. Brown, N. J. Long, R. J. Eckersley, C. Dunsby, J. Bamber, and M.-X. Tang, "Photoacoustic super-resolution imaging using laser activation of low-boiling-point dye-coated nanodroplets in vitro and in vivo," in *2019 IEEE International Ultrasonics Symposium Proceedings*, (Glasgow, Scotland), pp. 944–947, October 6-9 2019.
- [265] G. Zhang, B. Wang, A. Shah, J. Bamber, and M.-X. Tang, "Contrast-enhanced photoacoustic imaging of low-boiling-point phase-change nanodroplets," in *2019 IEEE International Ultrasonics Symposium Proceedings*, (Glasgow, Scotland), pp. 2271–2274, October 6-9 2019.
- [266] G. C. Carter, "Time delay estimation for passive sonar signal processing," *IEEE Transactions on Acoustics, Speech, and Signal Processing*, vol. 29, no. 3, pp. 463–470, 1981.
- [267] M. Gyöngy, M. Arora, J. A. Noble, and C. C. Coussios, "Use of passive arrays for characterization and mapping of cavitation activity during HIFU exposure," in *2008 IEEE International Ultrasonics Symposium Proceedings*, pp. 871–874, 2008.
- [268] M. Felizardo, R. C. Martins, T. A. Girard, A. R. Ramos, and J. G. Marques, "Acoustic spatial localization of events in superheated droplet detectors," *Nuclear Instruments and Methods in Physics Research A*, vol. 599, pp. 93–99, 2009.
- [269] X. Li, Z. D. Deng, L. T. Rauchenstein, and T. J. Carlson, "Contributed review: Source-localization algorithms and applications using time of arrival and time difference of arrival measurements," *Review of Scientific Instruments*, vol. 87, no. 041502, 2016.
- [270] Y. Desailly, J. Pierre, O. Couture, and M. Tanter, "Resolution limits of ultrafast Ultrasound Localization Microscopy," *Physics in Medicine and Biology*, vol. 60, pp. 8723–8740, 2015.
- [271] W. F. Walker and G. E. Trahey, "A fundamental limit on delay estimation using partially correlated speckle signals," *IEEE Transactions on Ultrasonics, Ferroelectrics, and Frequency Control*, vol. 42, no. 2, pp. 301–308, 1995.
- [272] J. A. Jensen and N. B. Svendsen, "Calculation of pressure fields from arbitrarily shaped, apodized, and excited ultrasound transducers," *IEEE Transactions on Ultrasonics, Ferroelectrics, and Frequency Control*, vol. 39, no. 2, pp. 262–267, 1992.
- [273] J. A. Jensen, "Field: A program for simulating ultrasound systems," in *Medical & Biological Engineering & Computing*, vol. 34, pp. 351–353, the 10th Nordic-Baltic Conference on Biomedical Imaging, 1996.
- [274] K. Christensen-Jeffries, S. Harput, J. Brown, P. N. T. Wells, P. Aljabar, C. Dunsby, and M.-X. Tang, "Microbubble axial localization errors in ultrasound super-resolution imaging," *IEEE Transactions on Ultrasonics, Ferroelectrics, and Frequency Control*, vol. 64, no. 11, pp. 1644–1654, 2017.

- [275] F. Viola and W. F. Walker, "A comparison of the performance of time-delay estimators in medical ultrasound," *IEEE Transactions on Ultrasonics, Ferroelectrics, and Frequency Control*, vol. 50, no. 4, pp. 392–401, 2003.
- [276] F. Viola and W. F. Walker, "Computationally efficient spline-based time delay estimation," *IEEE Transactions on Ultrasonics, Ferroelectrics, and Frequency Control*, vol. 55, no. 9, pp. 2084–2091, 2008.
- [277] A. V. Telichko, T. Lee, M. Jakovljevic, and J. J. Dahl, "Passive cavitation mapping by cavitation source localization from aperture-domain signals - part I: Theory and validation through simulations," *IEEE Transactions on Ultrasonics, Ferroelectrics, and Frequency Control*, vol. 68, no. 4, pp. 1184–1197, 2021.
- [278] A. Novell, C. B. Arena, O. Oralkan, and P. A. Dayton, "Wideband acoustic activation and detection of droplet vaporization events using a capacitive micromachined ultrasonic transducer," *The Journal of the Acoustical Society of America*, vol. 139, no. 6, pp. 3193–3198, 2016.
- [279] C. B. Arena, A. Novell, P. S. Sheeran, C. Puett, L. C. Moyer, and P. A. Dayton, "Dual-frequency acoustic droplet vaporization detection for medical imaging," *IEEE Transactions on Ultrasonics, Ferroelectrics, and Frequency Control*, vol. 62, no. 9, pp. 1623–1633, 2015.
- [280] K. H. Martin, B. D. Lindsey, J. Ma, M. Lee, S. Li, F. S. Foster, X. Jiang, and P. A. Dayton, "Dual-frequency piezoelectric transducers for contrast enhanced ultrasound imaging," *Sensors*, vol. 14, pp. 20825–20842, November 2014.
- [281] J. D. Rojas and P. A. Dayton, "In vivo molecular imaging using low-boiling-point phase-change contrast agents: a proof of concept study," *Ultrasound in Medicine and Biology*, vol. 45, no. 1, 2019.
- [282] S. Henrotin, M. Abs, E. Forton, Y. Jongen, W. Kleeven, J. Van de Walle, and P. Verbruggen, "Commissioning and testing of the first IBA S2C2," in *Proceedings of the 21st International Conference on Cyclotrons and their Applications*, (Zurich, Switzerland), pp. 178–180, 2016.
- [283] M. Gyöngy and C.-C. Coussios, "Passive spatial mapping of inertial cavitation during HIFU exposure," *IEEE Transactions on Biomedical Engineering*, vol. 57, no. 1, pp. 48–56, 2010.
- [284] J. J. Choi, R. C. Carlisle, C. Coviello, L. Seymour, and C.-C. Coussios, "Non-invasive and real-time passive acoustic mapping of ultrasound-mediated drug delivery," *Physics in Medicine and Biology*, vol. 59, pp. 4861–4877, 2014.
- [285] C. Richter, G. Pausch, S. Barczyk, M. Priegnitz, I. Keitz, J. Thiele, J. Smeets, F. V. Stappen, L. Bombelli, C. Fiorini, L. Hotoiu, I. Perali, D. Prieels, W. Enghardt, and M. Baumann, "First clinical application of a prompt gamma based in vivo proton range verification system," *Radiotherapy and Oncology*, vol. 118, no. 2, pp. 232–237, 2016.
- [286] R. Williams, C. Wright, E. Cherin, N. Reznik, M. Lee, I. Gorelikov, F. S. Foster, N. Matsuura, and P. N. Burns, "Characterization of submicron phase-change perfluorocarbon droplets for extravascular ultrasound imaging of cancer," *Ultrasound in Medicine & Biology*, vol. 39, no. 3, pp. 475–489, 2013.
- [287] P. S. Sheeran, J. D. Rojas, C. Puett, J. Hjelmquist, C. B. Arena, and P. A. Dayton, "Contrast-enhanced ultrasound imaging and in vivo circulatory kinetics with low-boiling-point nanoscale phase-change perfluorocarbon agents," *Ultrasound in Medicine and Biology*, vol. 41, no. 3, pp. 814–831, 2015.
- [288] K. Yoo, W. R. Walker, R. Williams, C. Tremblay-Darveau, P. N. Burns, and P. S. Sheeran, "Impact of encapsulation on in vitro and in vivo performance of volatile nanoscale phase-shift perfluorocarbon droplets," *Ultrasound in Medicine and Biology*, vol. 44, no. 8, pp. 1836–1852, 2018.

- [289] K. Wilson, K. Homan, and S. Emelianov, "Biomedical photoacoustics beyond thermal expansion using triggered nanodroplet vaporization for contrast-enhanced imaging," *Nature Communications*, vol. 3, no. 618, 2012.
- [290] Y. Toumia, R. Miceli, F. Domenici, S. V. Heymans, B. Carlier, M. Cociorb, L. Oddo, P. Rossi, R. M. D'Angellilo, E. Sterpin, E. d'Agostino, K. Van Den Abeele, J. D'hooge, and G. Paradossi, "Ultrasound-assisted investigation of photon triggered vaporization of poly(vinylalcohol) phase-change nanodroplets: A preliminary concept study with dosimetry perspective," *Physica Medica*, vol. 89, pp. 232–242, 2021.
- [291] M. A. Livshits, E. Khomyakova, E. G. Evtushenko, V. N. Lazarev, N. A. Kulemin, S. E. Semina, E. V. Generozov, and V. M. Govorun, "Isolation of exosomes by differential centrifugation: Theoretical analysis of a commonly used protocol," *Scientific Reports*, vol. 5, no. 17319, pp. 1–14, 2015.
- [292] D. D. Wackerly, W. I. M. III, and R. L. Scheaffer, *Mathematical Statistics with Applications*. Belmont, CA: Brooks/Cole, seventh ed., 2008.
- [293] C. J. Brambila, J. Lux, R. F. Mattrey, D. Boyd, M. A. Borden, and C. de Gracia Lux, "Bubble inflation using phase-change perfluorocarbon nanodroplets as a strategy for enhanced ultrasound imaging and therapy," *Langmuir*, vol. 36, pp. 2954–2965, 2020.
- [294] S. V. V. N. Kothapalli, L. Oddo, G. Paradossi, L. Åke Brodin, and D. Grishenkov, "Assessment of the viscoelastic and oscillation properties of a nano-engineered multimodality contrast agent," *Ultrasound in Medicine and Biology*, vol. 40, no. 10, pp. 2476–2487, 2014.
- [295] M. F. L'Annunziata, ed., *Handbook of Radioactivity Analysis*. Academic Press Inc, third ed., 2012.
- [296] J. H. Lee, D. S. Boning, and B. W. Anthony, "Measuring the absolute concentration of microparticles in suspension using high-frequency B-mode ultrasound imaging," *Ultrasound in Medicine & Biology*, vol. 44, no. 5, pp. 1086–1099, 2018.
- [297] J. Sijl, E. Gaud, P. J. A. Frinking, M. Arditì, N. de Jong, D. Lohse, and M. Versluis, "Acoustic characterization of single ultrasound contrast agent microbubbles," *The Journal of the Acoustical Society of America*, vol. 124, no. 6, pp. 4091–4097, 2008.
- [298] D. A. Glaser, "Bubble chamber tracks of penetrating cosmic-ray particles," *Physical Review*, vol. 91, no. 3, pp. 762–763, 1953.
- [299] G. P. Biro, P. Blais, and A. L. Rosen, "Perfluorocarbon blood substitutes," *Critical Reviews in Oncology and Hematology*, vol. 6, no. 4, pp. 311–374, 1987.
- [300] H. Lea-Banks, M. O'Reilly, C. Hamani, and K. Hynynen, "Localized anesthesia of a specific brain region using ultrasound-responsive barbiturate nanodroplets," *Theranostics*, vol. 10, no. 6, pp. 2849–2858, 2020.
- [301] B. Arnal, C. Perez, C.-W. Wei, J. Xia, M. Lombardo, I. Pelivanov, T. J. Matula, L. D. Pozzo, and M. O'Donnell, "Sono-photoacoustic imaging of gold nanoemulsions: Part I. exposure thresholds," *Photoacoustics*, vol. 3, no. 1, pp. 3–10, 2015.
- [302] B. Arnal, C.-W. Wei, C. Perez, T.-M. Nguyen, M. Lombardo, I. Pelivanov, L. D. Pozzo, and M. O'Donnell, "Sono-photoacoustic imaging of gold nanoemulsions: Part II. real time imaging," *Photoacoustics*, vol. 3, no. 1, pp. 11–19, 2015.
- [303] D. S. Li, G.-S. Jeng, J. J. P. Jr, M. Kim, L. D. Pozzo, and M. O'Donnell, "Spatially localized sono-photoacoustic activation of phase-change contrast agents," *Photoacoustics*, vol. 20, no. 100202, 2020.
- [304] J. E. Turner, *Atoms, Radiation, and Radiation Protection*, vol. Third. Weinheim, Germany: Wiley, 2007.

- [305] T. Lacour, M. Guédra, T. Valier-Brasier, and F. Coulouvrat, "A model for acoustic vaporization dynamics of a bubble/droplet system encapsulated within a hyperelastic shell," *The Journal of the Acoustical Society of America*, vol. 143, no. 1, pp. 23–37, 2018.
- [306] C. de Gracia Lux, A. M. Veziridis, J. Lux, A. M. Armstrong, S. R. Sirsi, K. Hoyt, and R. F. Mattrey, "Novel method for the formation of monodisperse superheated perfluorocarbon nanodroplets as activatable ultrasound contrast agents," *RSC Advances*, vol. 7, no. 48561, 2017.
- [307] D. S. Li, S. Schneewind, M. Bruce, Z. Khaing, M. O'Donnell, and L. Pozzo, "Spontaneous nucleation of stable perfluorocarbon emulsions for ultrasound contrast agents," *Nano Letters*, vol. 19, pp. 173–181, 2019.
- [308] J. D. Rojas, M. A. Borden, and P. A. Dayton, "Effect of hydrostatic pressure, boundary constraints and viscosity on the vaporization threshold of low-boiling-point phase-change contrast agents," *Ultrasound in Medicine & Biology*, vol. 45, no. 4, pp. 968–979, 2019.
- [309] G. N. Marta, C. Coles, O. Kaidar-Person, I. Meattini, T. Hijal, Y. Zissiadis, J.-P. Pignol, D. Ramiah, A. Y. Ho, S. H.-C. Cheng, G. Sancho, B. V. Offeren, and P. Poortmans, "The use of moderately hypofractionated post-operative radiation therapy for breast cancer in clinical practice: a critical review," *Critical Reviews in Oncology/Hematology*, vol. 156, p. 103090, 2020.
- [310] K. J. Ray, N. R. Sibson, and A. E. Kiltie, "Treatment of breast and prostate cancer by hypofractionated radiotherapy: Potential risks and benefits," *Clinical Oncology*, vol. 27, no. 420-426, 2015.
- [311] L. C. Benjamin, A. C. Tree, and D. P. Dearnaley, "The role of hypofractionated radiotherapy in prostate cancer," *Current Oncology Reports*, vol. 19, no. 30, 2017.
- [312] M. A. Gomez-Aparicio, J. Valero, B. Caballero, R. Garcia, O. Hernando-Requejo, A. Montero, A. Gomez-Iturriaga, T. Zilli, P. Ost, F. Lopez-Campos, and F. Couñago, "Extreme hypofractionation with sbrt in localized prostate cancer," *Current Oncology*, vol. 28, pp. 2933–2949, 2021.
- [313] S. Arcangeli and C. Greco, "Hypofractionated radiotherapy for organ-confined prostate cancer: is less more?," *Nature Reviews Urology*, vol. 13, pp. 400–408, 2016.
- [314] M. V. Williams, "Radiotherapy near misses, incidents and errors: Radiotherapy incident at Glasgow," *Clinical Oncology*, vol. 19, pp. 1–3, 2007.
- [315] W. Bogdanich, "Radiation offers new cures, and ways to do harm," *New York Times*, January 23 2010.
- [316] S. Derreumaux, C. Etard, C. Huet, F. Trompier, I. Clairand, J.-F. Bottolier-Depois, B. Aubert, and P. Gourmelon, "Lessons from recent accidents in radiation therapy in France," *Radiation Protection Dosimetry*, vol. 131, no. 1, pp. 130–135, 2008.
- [317] P. M. McCowan, G. Asuni, E. Van Uytven, T. VanBeek, B. M. McCurdy, S. K. Loewen, N. Ahmed, B. Bashir, J. B. Butler, A. Chowdhury, A. Dubey, A. Leyelek, and M. Nashed, "Clinical implementation of a model-based in vivo dose verification system for stereotactic body radiation therapy-volumetric modulated arc therapy treatments using the electronic portal imaging device," *International Journal of Radiation Oncology - Biology - Physics*, vol. 97, no. 5, pp. 1077–1084, 2017.
- [318] A. Sen, E. I. Parsai, S. W. McNeeley, and K. M. Ayyangar, "Quantitative assessment of beam perturbations caused by silicon diodes used for in vivo dosimetry," *International Journal of Radiation Oncology - Biology - Physics*, vol. 36, no. 1, pp. 205–211, 1996.
- [319] R. Alecu, J. J. Feldmeier, and M. Alecu, "Dose perturbations due to in vivo dosimetry with diodes," *Radiotherapy and Oncology*, vol. 42, pp. 289–291, 1997.

- [320] W. Van Elmpt, S. Nijsten, S. Petit, B. Mijnheer, P. Lambin, and A. Dekker, "3D in vivo dosimetry using megavoltage cone-beam CT and EPID dosimetry," *International Journal of Radiation Oncology*, vol. 73, no. 5, pp. 1580–1587, 2009.
- [321] S. Aftabi, D. Sasaki, T. vanBeek, S. Pistorius, and B. McCurdy, "4D in vivo dose verification for real-time tumor tracking treatments using EPID dosimetry," *Medical Dosimetry*, vol. 46, no. 1, pp. 29–38, 2021.
- [322] H. Lei, W. Zhang, I. Oraiqat, Z. Lui, J. Ni, X. Wang, and I. E. Naqa, "Toward in vivo dosimetry in external beam radiotherapy using x-ray acoustic computed tomography: A soft-tissue phantom study validation," *Medical Physics*, vol. 45, no. 9, pp. 4191–4200, 2018.
- [323] Y. Zheng, P. Samant, J. Merill, Y. Chen, S. Ahmad, D. Li, and L. Xiang, "X-ray induced acoustic computed tomography for guiding prone stereotactic partial breast irradiation: a simulation study," *Medical Physics*, vol. 47, no. 9, pp. 4386–4395, 2020.
- [324] L. Abou-Elkacem, S. V. Bachawal, and J. K. Willmann, "Ultrasound molecular imaging: Moving toward clinical translation," *European Journal of Radiology*, vol. 84, pp. 1685–1693, 2015.
- [325] R. Takam, E. Bezak, L. G. Marcu, and E. Yeoh, "Out-of-field neutron and leakage photon exposures and the associated risk of second cancers in high-energy photon radiotherapy: Current status," *Radiation Research*, vol. 176, no. 4, pp. 508–520, 2011.
- [326] F. D'Errico, R. Nath, L. Tana, G. Curzio, and W. G. Alberts, "In-phantom dosimetry and spectrometry of photoneutrons from an 18 MV linear accelerator," *Medical Physics*, vol. 25, no. 9, pp. 1717–1724, 1998.
- [327] W. H. Bragg and R. Kleeman, "On the alpha particles of radium and their loss range in passing through various atoms and molecules," *Philosophical Magazine*, vol. 10, pp. 318–340, 1905.
- [328] V. A. Semenenko, J. E. Turner, and T. B. Borak, "NOREC, a Monte Carlo code for simulating electron tracks in liquid water," *Radiation and Environmental Biophysics*, vol. 42, pp. 213–217, 2003.
- [329] N. Y. Rapoport, A. M. Kennedy, J. E. Shea, C. L. Scaife, and K.-H. Nam, "Controlled and targeted tumor chemotherapy by ultrasound-activated nanoemulsions/microbubbles," *Journal of Controlled Release*, vol. 138, no. 3, pp. 268–276, 2009.
- [330] Y. J. Zong, X. Zou, R. Wang, Y. Feng, and M. Wan, "Ultrasound-enhanced extravasation of multifunctional nanodroplets from leaky vessel," in *2015 IEEE International Ultrasonics Symposium Proceedings*, (Taipei, Taiwan), pp. 1–3, IEEE, 2015.
- [331] B. van der Heyden, "BubbleNet." software, 2021.
- [332] C. Elith, S. E. Dempsey, N. Findlay, and H. M. Warren-Forward, "An introduction to the intensity-modulated radiation therapy (IMRT) techniques, tomotherapy, and VMAT," *Journal of Medical Imaging and Radiation Sciences*, vol. 42, pp. 37–43, 2011.
- [333] T. R. Porter, C. Arena, S. Sayyed, J. Lof, R. R. High, F. Xie, and P. A. Dayton, "Targeted transthoracic acoustic activation of systemically administered nanodroplets to detect myocardial perfusion abnormalities," *Circulation Cardiovascular Imaging*, vol. 9, no. 1, pp. 1–7, 2016.
- [334] P. A. Mountford, W. S. Smith, and M. A. Borden, "Fluorocarbon nanodrops as acoustic temperature probes," *Langmuir*, vol. 31, pp. 10656–10663, 2015.
- [335] G. Renaud, J. G. Bosch, A. F. W. van der Steen, and N. de Jong, "An "acoustical camera" for in vitro characterization of contrast agent microbubble vibrations," *Applied Physics Letters*, vol. 100, no. 101911, 2012.

- [336] V. Daeichin, M. A. Inzunza-Ibarra, J. S. Lum, M. A. Borden, and T. W. Murray, "Photoacoustic impulse response of lipid-coated ultrasound contrast agents," *IEEE Transactions on Ultrasonics, Ferroelectrics, and Frequency Control*, vol. 68, no. 6, pp. 2311–2314, 2021.
- [337] B. Helfield, "A review of phospholipid encapsulated ultrasound contrast agent microbubble physics," *Ultrasound in Medicine and Biology*, vol. 45, no. 2, pp. 282–300, 2019.
- [338] S. M. Fix, A. Novell, Y. Yun, P. A. Dayton, and C. B. Arena, "An evaluation of the sonoporation potential of low-boiling point phase-change ultrasound contrast agents in vitro," *Journal of Therapeutic Ultrasound*, vol. 5, no. 7, pp. 1–11, 2017.
- [339] S.-Y. Wu, S. M. Fix, C. B. Arena, C. C. Chen, W. Zheng, O. O. Olumolade, V. Papadopoulou, A. Novell, and P. A. Dayton, "Focused ultrasound-facilitated brain drug delivery using optimized nanodroplets: Vaporization efficiency dictates large molecular delivery," *Physics in Medicine and Biology*, vol. 63, p. 035002, 2018.
- [340] J. Y. Lee, D. Carugo, C. Crake, J. Owen, M. de Saint Victor, A. Seth, C. Coussios, and E. Stride, "Nanoparticle-loaded protein-polymer nanodroplets for improved stability and conversion efficiency in ultrasound imaging and drug delivery," *Advanced Materials*, vol. 27, pp. 5484–5492, 2015.
- [341] J. S. Jeong, J. H. Chang, and K. K. Shung, "Ultrasound transducer and system for real-time simultaneous therapy and diagnosis for noninvasive surgery of prostate tissue," *IEEE Trans. Ultrason Ferroelectr Freq Control*, vol. 56, pp. 1913–1922, September 2009.
- [342] J. S. Jeong, J. M. Cannata, and K. K. Shung, "Adaptative HIFU noise cancellation for simultaneous therapy and imaging using an integrated HIFU/imaging transducer," *Physics in Medicine and Biology*, vol. 55, pp. 1889–1902, 2010.
- [343] A. Giammanco, "Radiation-induced vaporisation of superheated nanodroplets as an in vivo proton range verification technique: a Monte Carlo approach," Master's thesis, KU Leuven and Politecnico di Milano, 2019.
- [344] W. Piot, "The development of a LET-based Monte Carlo model to predict the radiation response of superheated nanodroplets for proton range verification," Master's thesis, KU Leuven, 2021.
- [345] J. Schlosser, K. Salisbury, and D. Hristov, "Telerobotic system concept for real-time soft-tissue imaging during radiotherapy beam delivery," *Medical Physics*, vol. 37, no. 12, pp. 6357–6367, 2010.
- [346] H. T. Şen, M. A. L. Bell, Y. Zhang, K. Ding, E. Boctor, J. Wong, I. Iordachita, and P. Kazanzides, "System integration and in vivo testing of a robot for ultrasound guidance and monitoring during radiotherapy," *IEEE Transactions on Biomedical Engineering*, vol. 64, no. 7, pp. 1608–1618, 2017.
- [347] S. Ipsen, D. Wulff, I. Kuhlemann, A. Schweikard, and F. Ernst, "Towards automated ultrasound imaging - robotic image acquisition in liver and prostate for long-term motion monitoring," *Physics in Medicine and Biology*, vol. 66, p. 094002, 2021.
- [348] S. Ghose, A. Oliver, R. Martí, X. Lladó, J. C. Vilanova, J. Freixenet, J. Mitra, D. Sidibé, and F. Meriaudeau, "A survey of prostate segmentation methodologies in ultrasound, magnetic resonance and computed tomography images," *Computer Methods and Programs in Biomedicine*, vol. 108, pp. 262–287, 2012.
- [349] Y. Lei, S. Tian, X. He, T. Wang, B. Wang, P. Patel, A. B. Jani, H. Mao, W. J. Curran, T. Liu, and X. Yang, "Ultrasound prostate segmentation based on multidirectional deeply supervised V-Net," *Medical Physics*, vol. 46, no. 7, pp. 3194–3206, 2019.

- [350] H. Williams, L. Cattani, W. Li, M. Tabassian, T. Vercauteren, J. Deprest, and J. D'hooge, "3D convolutional neural network for segmentation of the urethra in volumetric ultrasound of the pelvic floor," in *2019 IEEE International Ultrasonics Symposium (IUS)*, (Glasgow, Scotland), pp. 1473–1476, October 6-9 2019.
- [351] J. A. Noble, N. Navab, and H. Becher, "Ultrasonic image analysis and image-guided interventions," *Interface Focus*, vol. 1, no. 4, pp. 673–685, 2011.
- [352] P. Huang, L. Su, S. Chen, K. Cao, Q. Song, P. Kazanzides, I. Iordachita, M. A. L. Bell, J. W. Wong, D. Li, and K. Ding, "2D ultrasound imaging based intra-fraction respiratory motion tracking for abdominal radiation therapy using machine learning," *Physics in Medicine and Biology*, vol. 64, no. 185006, 2019.
- [353] E. J. Harris, N. R. Miller, J. C. Bamber, J. R. N. Symonds-Tayler, and P. M. Evans, "Speckle tracking in a phantom and feature-based tracking in liver in the presence of respiratory motion using 4D ultrasound," *Physics in Medicine and Biology*, vol. 55, pp. 3363–3380, 2010.
- [354] M. A. L. Bell, B. C. Byram, E. J. Harris, P. M. Evans, and J. C. Bamber, "In vivo liver tracking with a high volume rate 4D ultrasound scanner and a 2D matrix array probe," *Physics in Medicine and Biology*, vol. 57, pp. 1359–1374, 2012.
- [355] S. van der Meer, S. M. Camps, W. J. C. van Elmpt, M. Podesta, P. G. Sanches, B. G. L. Vanneste, D. Fontanarosa, and F. Verhaegen, "Simulation of pseudo-CT images based on deformable image registration of ultrasound images: A proof of concept for transabdominal ultrasound imaging of the prostate during radiotherapy," *Medical Physics*, vol. 43, no. 4, pp. 1913–1920, 2016.
- [356] Y. Chen, L. Xing, L. Yu, W. Liu, B. P. Fahimian, T. Niedermayr, H. P. Bagshaw, M. Buyyounouski, and B. Han, "MR to ultrasound image registration with segmentation-based learning for HDR prostate brachytherapy," *Medical Physics*, vol. 48, no. 6, pp. 3074–3083, 2021.
- [357] M. Kaar, M. Figl, R. Hoffmann, W. Birkfellner, J. Hummel, M. Stock, D. Georg, and G. Goldner, "Automatic patient alignment system using 3D ultrasound," *Medical Physics*, vol. 40, no. 4, 2013.
- [358] S. Gerlach, I. Kuhlemann, P. Jauer, R. Bruder, F. Ernst, C. Fürweger, and A. Schlaefer, "Robotic ultrasound-guided SBRT of the prostate: feasibility with respect to plan quality," *International Journal of Computer Assisted Radiology and Surgery*, vol. 12, pp. 149–159, 2017.
- [359] International Agency for Research on Cancer, "The global cancer observatory." Available at <https://gco.iarc.fr/today/home>, page consulted 27/10/2021.
- [360] J. M. Pollard, Z. Wen, R. Sadagopan, J. Wang, and G. S. Ibbot, "The future of image-guided radiotherapy will be MR guided," *British Journal of Radiology*, vol. 90, no. 20160667, 2017.
- [361] A. Choudhury, G. Budgell, R. MacKay, S. Falk, C. Faivre-Finn, M. Dubec, M. van Herk, and A. McWilliam, "The future of image-guided radiotherapy," *Clinical Oncology*, vol. 29, pp. 662–666, 2017.
- [362] F. Albertini, M. Matter, L. Nenoff, Y. Zhang, and A. Lomax, "Online daily adaptive proton therapy," *British Journal of Radiology*, vol. 93, p. 20190504, 2020.
- [363] M. Matter, L. Nenoff, L. Marc, D. C. Weber, A. J. Lomax, and F. Albertini, "Update on yesterday's dose - use of delivery log-files for daily adaptive proton therapy (DAPT)," *Physics in Medicine and Biology*, vol. 65, p. 195011, 2020.
- [364] B. Lin, F. Gao, Y. Yang, D. Wu, Y. Zhang, G. Feng, T. Dai, and X. Du, "FLASH radiotherapy: History and future," *Frontiers in Oncology*, vol. 11, no. 644400, 2021.

- [365] L. De Marzi, C. Nauraye, P. Lansonneur, F. Pouzoulet, A. Patriarca, T. Schneider, C. Guardiola, H. Mammar, R. Dendale, and Y. Prezado, "Spatial fractionation of the dose in proton therapy: Proton minibeam radiation therapy," *Cancer/Radiothérapie*, vol. 23, pp. 677–681, 2019.
- [366] H. Fukunaga, K. T. Butterworth, S. J. McMahon, and K. M. Prize, "A brief overview of the preclinical and clinical radiobiology of microbeam radiotherapy," *Clinical Oncology*, vol. 33, pp. 705–712, 2021.
- [367] J. D. Wilson, E. M. Hammond, G. S. Higgins, and K. Petersson, "Ultra-high dose rate (FLASH) radiotherapy: Silver bullet or fool's gold," *Frontiers in Oncology*, vol. 9, no. 1563, 2020.
- [368] A. Mazal, J. A. V. Sanchez, D. Sanchez-Parcerisa, J. M. Udias, S. España, V. Sanchez-Tembleque, L. M. Fraile, P. Bragado, A. Gutierrez-Uzquiza, N. Gordillo, G. Garcia, J. C. Novais, J. M. P. Moreno, L. M. Ortiz, A. I. Idoate, M. C. Sendino, C. Ares, R. Miralbell, , and N. Schreuder, "Biological and mechanical synergies to deal with proton therapy pitfalls: Minibeams, FLASH, arcs, and gantryless rooms," *Frontiers in Oncology*, vol. 10, no. 613669, 2021.
- [369] A. Mazal, Y. Prezado, C. Ares, L. De Marzi, A. Patriarca, R. Mirabell, and V. Favaudon, "FLASH and minibeams in radiation therapy: the effect of microstructures on time and space and their potential application to protontherapy," *British Journal of Radiology*, vol. 93, no. 20190807, 2020.
- [370] I. Oraiqat, W. Zhang, D. Litzenberg, K. Lam, N. B. Sunbul, J. Moran, K. Cuneo, P. Carson, X. Wang, and I. E. Naqa, "An ionizing radiation imaging (iRAI) technique for real-time dosimetric measurements for FLASH radiotherapy," *Medical Physics*, vol. 47, no. 10, pp. 5090–5101, 2020.
- [371] I. G. Newsome and P. A. Dayton, "Visualization of microvascular angiogenesis using dual-frequency contrast-enhanced acoustic angiography: a review," *Ultrasound in Medicine and Biology*, vol. 46, no. 10, pp. 2625–2635, 2020.

Curriculum Vitae

Work experience

Joint PhD researcher	KU Leuven Erasmus University Rotterdam	2018-2022
System Engineer - Beam Physics	Ion Beam Applications	2017-2018
Requirements & Systems Engineer	Ion Beam Applications	2015-2017
Student coach	MySherpa	2011-2014

Education

Master of Sciences Biomedical Engineering Medical Physics Stream	Imperial College London, UK	2014-2015
Master of Sciences Electromechanical Engineering Option: Energy	UCLouvain, Belgium	2012-2014
Erasmus EU student exchange	Politecnico di Torino, Italy	2014
Bachelor of engineering	UCLouvain, Belgium	2009-2012
Secondary school Option: Mathematics-Greek	Collège Notre-Dame de la Paix Erpent, Belgium	2003-2009

Awards and Grants

Postdoctoral mandate (1 year), KU Leuven Internal Funds, 2022.

Grant for a long stay abroad (3 months), Research Foundation-Flanders (FWO), 2020.

Travel award, Microbubble Summer School on Ultrasound Contrast Agents, IEEE Ultrasonics, Ferroelectrics and Frequency Control Society, 2019.

Best poster award, The 24th European symposium on Ultrasound Contrast Imaging, Rotterdam, the Netherlands, 2019. Title: "Investigation of PCDA-PFB nanodroplets for multimodal imaging and *in vivo* dosimetry of radiation therapy".

Ash Prize for the best academic performance in the MSc Programme, Imperial College London, 2015.

IPEM Prize for the best MSc project in Medical Physics, Imperial College London, 2015.

Research stays abroad

Microbubble lab of Prof. dr. M. Borden, Colorado University, Boulder, USA, May 2019.

Microbubble lab of Prof. dr. G. Paradossi, University of Rome Tor Vergata, Italy, April 2018.

List of publications

Peer-reviewed publications in this thesis

- Gonzalo Collado-Lara*, **Sophie V. Heymans***, Marta Rovituso, Bram Carlier, Yosra Toumia, Martin Verweij, Gaio Paradossi, Edmond Sterpin, Hendrik J. Vos, Jan D'hooge, Nico de Jong, Koen Van Den Abeele, and Verya Daeichin, "Spatiotemporal distribution of nanodroplet vaporization in a proton beam using real-time ultrasound imaging for range verification", *Ultrasound in Medicine and Biology*, 48(1), 2022, pp. 149-156.
- **Sophie V. Heymans***, Bram Carlier*, Yosra Toumia, Sjoerd Nooijens, Marcus Ingram, Andrea Giammanco, Emiliano d'Agostino, Wouter Crijns, Alexander Bertrand, Gaio Paradossi, Uwe Himmelreich, Jan D'hooge, Edmond Sterpin and Koen Van Den Abeele, "Modulating ultrasound contrast generation from injectable nanodroplets for proton range verification by varying the degree of superheat", *Medical Physics*, 48(4), 2021, pp. 1983-1995.
- Bram Carlier*, **Sophie V. Heymans***, Sjoerd Nooijens, Yosra Toumia, Marcus Ingram, Gaio Paradossi, Emiliano d'Agostino, Uwe Himmelreich, Jan D'hooge, Koen Van Den Abeele and Edmond Sterpin, "Proton range verification with ultrasound imaging using injectable radiation sensitive nanodroplets: a feasibility study", *Physics in Medicine and Biology*, 65, 2020, 065013.

*joint first authorship

Peer-reviewed publications not in this thesis

- Yosra Toumia, Roberto Miceli, Fabio Domenici, **Sophie V. Heymans**, Bram Carlier, Madalina Cociorb, Letizia Oddo, Piero Rossi, Rolando Maria D'Angellilo, Edmond Sterpin, Emiliano d'Agostino, Koen Van Den

- Abeele, Jan D'hooge, Gaio Paradossi, "Ultrasound-assisted investigation of photon triggered vaporization of poly(vinylalcohol) phase-change nanodroplets: A preliminary concept study with dosimetry perspective", *Physica Medica*, 89, 2021, pp. 232-242.
- Gonzalo Collado-Lara, **Sophie V. Heymans**, Jeremy Godart, Emiliano d'Agostino, Jan D'hooge, Koen Van Den Abeele, Hendrik J. Vos and Nico de Jong, "Effect of a Radiotherapeutic Megavoltage Beam on Ultrasound Contrast Agents", *Ultrasound in Medicine and Biology*, 47(7), 2021, pp.1857-1867.
 - Yosra Toumia, Barbara Cerroni, Fabio Domenici, Heiko Lange, Livia Bianchi, Madalina Cociorb, Francesco Brasili, Esther Chiessi, Emiliano d'Agostino, Koen Van Den Abeele, **Sophie V. Heymans**, Jan D'hooge, Gaio Paradossi, "Phase Change Ultrasound Contrast Agents with a Photopolymerized Diacetylene Shell", *Langmuir*, 35, 2019, pp. 10116-10127.
 - **Sophie V. Heymans**, Christine F. Martindale, Andrej Suler, Antonios N. Pouliopoulos, Robert J. Dickinson, James J. Choi, "Simultaneous Ultrasound Therapy and Monitoring of Microbubble-Seeded Acoustic Cavitation Using a Single-Element Transducer", *IEEE Transactions on Ultrasonics, Ferroelectrics and Frequency Control*, 64(8), 2017, pp. 1234-1244.

Manuscripts submitted or in preparation

- **Sophie V. Heymans***, Gonzalo Collado-Lara*, Marta Rovituso, Hendrik J. Vos, Jan D'hooge, Nico de Jong, and Koen Van Den Abeele, "Passive Ultrasound Localization Microscopy of nanodroplet vaporization during proton irradiation: a new imaging method to assist *in vivo* proton range verification", *In Preparation*.
- **Sophie V. Heymans***, Gonzalo Collado-Lara*, Marta Rovituso, Hendrik J. Vos, Jan D'hooge, Nico de Jong, and Koen Van Den Abeele, "Acoustic Modulation Enables Proton Detection with Nanodroplets at Body Temperature", *Submitted to IEEE Transactions on Ultrasonics, Ferroelectrics, and Frequency Control*.
- Gonzalo Collado-Lara*, **Sophie V. Heymans***, Marta Rovituso, Edmond Sterpin, Hendrik J. Vos, Jan D'hooge, Koen Van Den Abeele, and Nico de Jong, "Influence of droplet size, concentration, and proton fluence on the achievable precision for *in vivo* proton range verification: simulations and experimental validation", *In Preparation*.

**joint first authorship*

Communications at international conferences and symposia

- **Sophie V. Heymans**, Christine F. Martindale, Andrej Suler, Antonios N. Pouliopoulos, Robert J. Dickinson, James J. Choi, "Single-Element Transducer for Simultaneous Ultrasound Therapy and Monitoring of Microbubble-Seeded Acoustic Cavitation", presented at *The 23rd European symposium on Ultrasound Contrast Imaging*, Rotterdam, the Netherlands, 18-19 January 2018 (oral presentation).
- **Sophie V. Heymans**, Yosra Toumia, Bram Carlier, Andrea Giammanco, Gonzalo Collado, Heiko Lange, Uwe Himmelreich, Edmond Sterpin, Nico de Jong, Emiliano d'Agostino, Gaio Paradossi, Jan D'hooge, Koen Van Den Abeele, "Investigation of PCDA-PFB nanodroplets for multimodal imaging and *in vivo* dosimetry of radiation therapy", presented at *The 24th European symposium on Ultrasound Contrast Imaging*, Rotterdam, the Netherlands, 17-18 January 2019 (poster).
- **Sophie V. Heymans**, Bram Carlier, Andrea Giammanco, Yosra Toumia, Sjoerd Nooijens, Gonzalo Collado, Edmond Sterpin, Nico de Jong, Emiliano d'Agostino, Gaio Paradossi, Jan D'hooge, Koen Van Den Abeele, "Radiation-induced vaporization of nanodroplets for *in vivo* dosimetry of radiation therapy", presented at *The International Congress of Ultrasonics (ICU)*, Bruges, Belgium, 3-6 September 2019 (poster).
- **Sophie V. Heymans**, Bram Carlier, Sjoerd Nooijens, Yosra Toumia, Marcus Ingram, Gaio Paradossi, Emiliano d'Agostino, Uwe Himmelreich, Jan D'hooge, Edmond Sterpin, Koen Van Den Abeele, "Radiation-induced vaporization of PCDA-PFB nanodroplets: a feasibility study for ultrasound-based proton range verification and dosimetry", presented at *The 25th European symposium on Ultrasound Contrast Imaging*, Rotterdam, the Netherlands, 16-17 January 2020 (oral presentation).
- **Sophie V. Heymans**, Bram Carlier, Yosra Toumia, Sjoerd Nooijens, Marcus Ingram, Gaio Paradossi, Emiliano d'Agostino, Uwe Himmelreich, Jan D'hooge, Edmond Sterpin, Koen Van Den Abeele, "Ultrasound imaging of perfluorobutane nanodroplet vaporization induced by proton irradiation: towards a novel approach for proton range verification and dosimetry", presented at *IEEE International Ultrasonics Symposium (IUS)*, Online, 6-11 September 2020 (oral presentation).
- **Sophie V. Heymans**, Gonzalo Collado, Marta Rovituso, Bram Carlier, Yosra Toumia, Gaio Paradossi, Verva Daeichin, Hendrik J. Vos, Jan

D'hooge, Nico de Jong, Koen Van Den Abeele, "Passive detection and super-localization of acoustic signatures from PVA-PFB nanodroplets vaporized by protons", presented at *The 26th European symposium on Ultrasound Contrast Imaging*, Online, 14-15 January 2021 (poster presentation).

- **Sophie V. Heymans**, Bram Carlier, Yosra Toumia, Sjoerd Nooijens, Marcus Ingram, Andrea Giammanco, Gaio Paradossi, Emiliano d'Agostino, Wouter Crijns, Alexander Bertrand, Uwe Himmelreich, Jan D'hooge, Edmond Sterpin and Koen Van Den Abeele, "Towards ultrasound assisted *in vivo* proton range verification with injectable superheated nanodroplets: a feasibility study", presented at the *59th Annual Conference of the Particle Therapy Co-Operative Group*, Online, 4-7 June 2021 (oral presentation).
- **Sophie V. Heymans**, Bram Carlier, Sjoerd Nooijens, Gonzalo Collado-Lara, Laurence Delombaerde, Yosra Toumia, Nico de Jong, Jan D'hooge, and Koen Van Den Abeele, "Online monitoring of radiotherapy using ultrasound imaging of radiation-induced nanodroplet vaporization", presented at *IEEE International Ultrasonics Symposium (IUS)*, Online, 11-16 September 2021 (oral presentation).

Communications at other meetings

- **Sophie V. Heymans**, Christine F. Martindale, Andrej Suler, Antonios N. Pouliopoulos, Robert J. Dickinson, James J. Choi, "Single-element transducer for simultaneous ultrasound therapy and monitoring of microbubble-seeded acoustic cavitation", Physics seminar at Kulak, Kortrijk, Belgium (16/04/2018).
- **Sophie V. Heymans**, "Radiation-induced vaporization of nanodroplets: a feasibility study for ultrasound-based proton range verification and dosimetry, Department of Biomedical Engineering Research Meetings, Rotterdam, The Netherlands (14/04/2020).
- Gonzalo Collado-Lara, **Sophie V. Heymans**, Verya Daeichin and Marta Rovituso, "Ultrasound contrast agents for dosimetry in proton therapy", Holland Proton Therapy Center, Delft, The Netherlands (02/11/2020).
- **Sophie V. Heymans**, "Radiation-induced nanodroplet vaporization for proton range verification and radiotherapy dosimetry", Department of Biomedical Engineering Research Meetings, Rotterdam, The Netherlands (18/05/2021).

- **Sophie V. Heymans**, "Radiation-induced vaporization of phase-change ultrasound contrast agents for *in vivo* proton therapy range verification and dosimetry - Can we see radiation by popping bubbles?", Medical Imaging Research Center Seminars, Leuven, Belgium (21/05/2021).
- **Sophie V. Heymans**, "Ultrasound imaging of nanodroplet vaporization for radiotherapy monitoring", Department of Biomedical Engineering Research Meetings, Rotterdam, The Netherlands (14/12/2021).
- **Sophie V. Heymans**, "Ultrasound imaging of nanodroplet vaporization for proton therapy monitoring", Seminars of the Interdisciplinary Research Facility Life Sciences, Kulak, Kortrijk, Belgium (15/12/2021).

PhD portfolio

Courses	ECTS	Year
Seminar on Research Integrity for starting PhD researchers KU Leuven (compulsory for all new doctoral researchers)	-	2018
LabView Core I and II	1	2018
Biomedical Data Processing - KU Leuven	6	2018
Managing my PhD - KU Leuven	1	2018
Microbubble Summer School on Ultrasound Contrast Agents	1	2019
Academic Writing for junior researchers - KU Leuven	2	2020
Research seminars and journal clubs - KU Leuven	1	2018-2021

Teaching	ECTS	Year
Teaching assistant: Conceptuele Natuurkunde (KULAK)	2	2019-2020
Teaching assistant: Hot Topics in Medical Imaging - KU Leuven	2	2019
Teaching assistant: Hot Topics in Medical Imaging - KU Leuven	2	2020
Teaching assistant: Hot Topics in Medical Imaging - KU Leuven	2	2021
Teaching assistant: Medical Imaging and Analysis - KU Leuven	1	2020

Scientific Presentations and Meetings	ECTS	Year
Department of Physics Research Meetings (KULAK) <i>Kortrijk, Belgium</i> (oral presentation)	1	2018
24th European Symposium on Ultrasound Contrast Imaging <i>Rotterdam, the Netherlands</i> (poster presentation)	1	2019
International Congress of Ultrasonics (ICU) <i>Bruges, Belgium</i> (poster presentation)	1	2019
25th European Symposium on Ultrasound Contrast Imaging <i>Rotterdam, the Netherlands</i> (oral presentation)	1	2020
Department of Biomedical Engineering Research Meetings <i>Rotterdam, The Netherlands</i> (oral presentation)	1	2020
IEEE International Ultrasonics Symposium (IUS) <i>Online</i> (oral presentation)	1	2020
26th European Symposium on Ultrasound Contrast Imaging <i>Online</i> (poster presentation)	1	2021
Department of Biomedical Engineering Research Meetings <i>Rotterdam, The Netherlands</i> (oral presentation)	1	2021
Medical Imaging Research Center Seminars <i>Leuven, Belgium</i> (oral presentation)	1	2021
59th Annual Conference of the Particle Therapy Co-Operative Group <i>Online</i> (oral presentation)	1	2021
IEEE International Ultrasonics Symposium (IUS) <i>Online</i> (oral presentation)	2.1	2021
	Total	33.1

